AD-A277 680
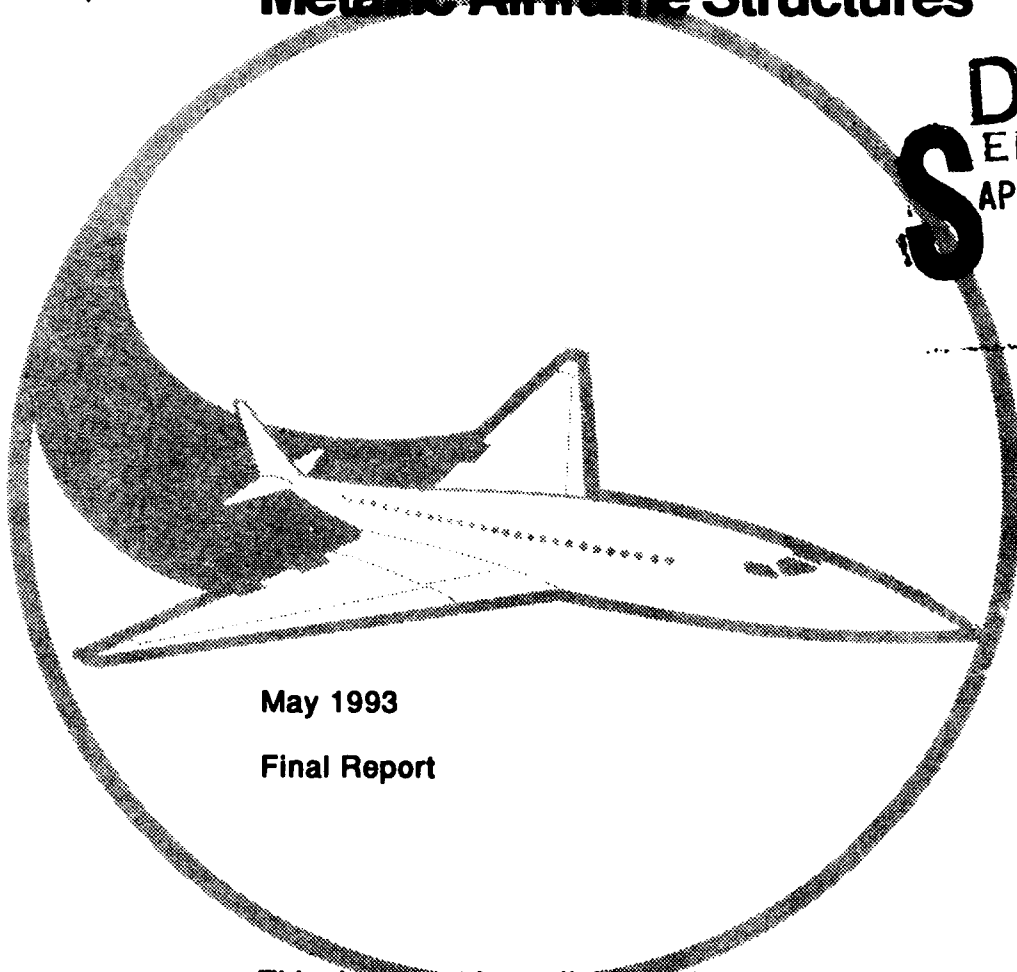
DOT/FAA/CT-92/32

FAA Technical Center
Atlantic City International Airport,
N.J. 08405

Composite Repairs of Cracked Metallic Airframe Structures

May 1993

Final Report

This document is available to the public
through the National Technical Information
Service, Springfield, Virginia 22161.

94-09921

U.S. Department of Transportation
Federal Aviation Administration

94 3 31 219

NOTICE

This document is disseminated under the sponsorship of the U. S. Department of Transportation in the interest of information exchange. The United States Government assumes no liability for the contents or use thereof.

The United States Government does not endorse products or manufacturers. Trade or manufacturers' names appear herein solely because they are considered essential to the objective of this report.

1. Report No. DOT/FAA/CT-92/32	2. Government Accession No.	3. Recipient's Catalog No.
4. Title and Subtitle COMPOSITE REPAIRS OF CRACKED METALLIC AIRCRAFT STRUCTURES		5. Report Date May 1993
		6. Performing Organization Code
7. Author's) S.N. Atluri, J.H. Park, E.F. Punch, P.E. O'Donoghue (KSI) and Rhys Jones, (ARL)		8. Performing Organization Report No.
9. Performing Organization Name and Address *Knowledge Systems Inc. *Aeronautical Research Laboratories P.O. Box 77032 P.O. Box 4331 Atlanta, GA 30357 Melbourne, Victoria, Australia 3001		10. Work Unit No. (TRAIS)
		11. Contract or Grant No. DTRS-57-89-C-00008
12. Sponsoring Agency Name and Address U.S. Department of Transportation Federal Aviation Administration Technical Center Atlantic City International Airport, NJ 08405		13. Type of Report and Period Covered Final Oct 1990 - Feb 1992
		14. Sponsoring Agency Code ACD-220

15. Supplementary Notes   *Under contract to: U.S. DOT, Research and Special Programs Administration, Volpe National Transportation Systems Center, Cambridge, MA 02142-1093
FAA Technical Monitor: Donald W. Oplinger

16. Abstract

This report summarizes work that quantifies the benefits of composite patch repairs on cracked metallic aircraft structures. The first chapter describes a data base on bonding methods and repair materials that can be used in design and analysis. In the second chapter, analytical models are derived for the stress intensity factor of cracks in metallic sheets with bonded orthotropic repairs. Specific configurations included through-the-thickness center cracks, through-the-thickness cracks at a loaded fastener hole, surface cracks, and surface cracks at a hole. These analyses can be used in calculations of crack growth life extension resulting from the bonded repairs. Four types of specimens were tested in fatigue to verify the increase in fatigue life. The four configurations were edge crack specimens, surface crack specimens, surface crack at hole specimens, and simulated lap joint specimens with multiple site damage (MSD). All experiments confirmed that bonded composite repairs could significantly increase fatigue life. An update is also included on a flight demonstration program in which composite patches were placed on undamaged sections of an in-service aircraft. Preliminary results on the durability of the patches are promising.

17. Key Words Aircraft, Composite Repairs, Fatigue, Bonded Repairs, Fuselage Cracks, Damage Tolerance, Stress Intensity Factor, Crack Growth	18. Distribution Statement Document is available to the public through the National Technical Information Service, Springfield, Virginia 22161	
19. Security Classif. (of this report) Unclassified	20. Security Classif. (of this page) Unclassified	21. No. of Pages 188	22. Price

Form DOT F 1700.7 (8-72)   Reproduction of completed page authorized

PREFACE

This final technical report covers work performed on Department of Transportation Contract DTRS-57-89-C-00008, "Composite Patches for Crack Repairs" for the Volpe National Transportation Systems Center, Department of Transportation, Cambridge MA. The funding for this program was provided by the Federal Aviation Administration's National Aging Aircraft Research Program under the direction of Dr. S. Sampath, Federal Aviation Administration Technical Center, Aircraft Safety Division, Atlantic City International Airport, NJ 08405. The program was administered by Dr. J. Brewer of the Volpe National Transportation Systems Center. Mr. D. Oplinger, of the Propulsion and Structures Branch, Federal Aviation Technical Center, acted as technical monitor for the Federal Aviation Administration.

The work was performed by Knowledge Systems Incorporated (KSI) of Atlanta, GA, with the Aeronautical Research Laboratories (ARL), Mellbourne, Australia, as subcontractor. Dr. S. Atluri was the Program Manager and Principal Investigator for KSI, while Dr. Rhys Jones served as Program Manager and Principal Investigator for ARL.

iii

Accession For

NTIS GRA&I ☑
DTIC TAB ☐
Unannounced ☐
Justification

By
Distribution/
Availability Codes

Dist	Avail and/or Special
A-1	

METRIC/ENGLISH CONVERSION FACTORS

ENGLISH TO METRIC

LENGTH (APPROXIMATE)

1 inch (in.)   = 2.5 centimeters (cm)
1 foot (ft)   = 30 centimeters (cm)
1 yard (yd)   = 0.9 meter (m)
1 mile (mi)   = 1.6 kilometers (km)

AREA (APPROXIMATE)

1 square inch (sq in, in²)   = 6.5 square centimeters (cm²)
1 square foot (sq ft, ft²)   = 0.03 square meter (m²)
1 square yard (sq yd, yd²)   = 0.8 square meter (m²)
1 square mile (sq mi, mi²)   = 2.6 square kilometers (km²)
1 acre = 0.4 hectares (he) = 4,000 square meters (m²)

MASS - WEIGHT (APPROXIMATE)

1 ounce (oz)   = 28 grams (gr)
1 pound (lb)   = .45 kilogram (kg)
1 short ton = 2,000 pounds (lb) = 0.9 tonne (t)

VOLUME (APPROXIMATE)

1 teaspoon (tsp)   = 5 milliliters (ml)
1 tablespoon (tbsp)   = 15 milliliters (ml)
1 fluid ounce (fl oz)   = 30 milliliters (ml)
1 cup (c)   = 0.24 liter (l)
1 pint (pt)   = 0.47 liter (l)
1 quart (qt)   = 0.96 liter (l)
1 gallon (gal)   = 3.8 liters (l)
1 cubic foot (cu ft, ft³)   = 0.03 cubic meter (m³)
1 cubic yard (cu yd, yd³)   = 0.76 cubic meter (m³)

TEMPERATURE (EXACT)

$[(x - 32)(5/9)]$ °F = y°C

METRIC TO ENGLISH

LENGTH (APPROXIMATE)

1 millimeter (mm)   = 0.04 inch (in)
1 centimeter (cm)   = 0.4 inch (in)
1 meter (m)   = 3.3 feet (ft)
1 meter (m)   = 1.1 yards (yd)
1 kilometer (km)   = 0.6 mile (mi)

AREA (APPROXIMATE)

1 square centimeter (cm²)   = 0.16 square inch (sq in, in²)
1 square meter (m²)   = 1.2 square yards (sq yd, yd²)
1 square kilometer (kn²)   = 0.4 square mile (sq mi, mi²)
1 hectare (he) = 10,000 square meters (m²) = 2.5 acres

MASS - WEIGHT (APPROXIMATE)

1 gram (gr)   = 0.036 ounce (oz)
1 kilogram (kg)   = 2.2 pounds (lb)
1 tonne (t) = 1,000 kilograms (kg) = 1.1 short tons

VOLUME (APPROXIMATE)

1 milliliter (ml)   = 0.03 fluid ounce (fl oz)
1 liter (l)   = 2.1 pints (pt)
1 liter (l)   = 1.06 quarts (qt)
1 liter (l)   = 0.26 gallon (gal)
1 cubic meter (m³)   = 36 cubic feet (cu ft, ft³)
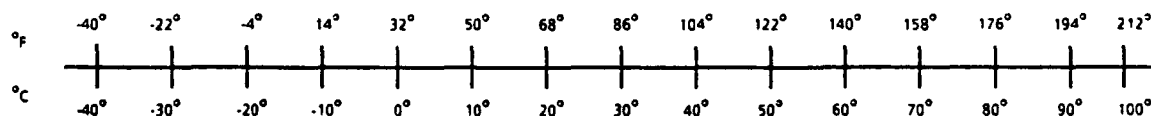1 cubic meter (m³)   = 1.3 cubic yards (cu yd, yd³)

TEMPERATURE (EXACT)

$[(9/5)y + 32]$ °C = x °F

QUICK INCH-CENTIMETER LENGTH CONVERSION

INCHES 0 1 2 3 4 5 6 7 8 9 10

CENTIMETERS 0 1 2 3 4 5 6 7 8 9 10 11 12 13 14 15 16 17 18 19 20 21 22 23 24 25

25 40

QUICK FAHRENHEIT-CELSIUS TEMPERATURE CONVERSION

°F -40° -22° -4° 14° 32° 50° 68° 86° 104° 122° 140° 158° 176° 194° 212°

°C -40° -30° -20° -10° 0° 10° 20° 30° 40° 50° 60° 70° 80° 90° 100°

For more exact and or other conversion factors, see NBS Miscellaneous Publication 286, Units of Weights and Measures. Price $2.50. SD Catalog No. C13 10286.

TABLE OF CONTENTS

vi

LIST OF ILLUSTRATIONS

LIST OF TABLES

EXECUTIVE SUMMARY

This work evaluates the concept of life enhancement of cracked metallic airframe structures through adhesively bonded boron/epoxy composite repair patches. The five-part research addresses the following principle tasks:

Development of a database for materials, surface preparation, and bonding methods in composite patch repairs.

Detailed analytical and computational treatment of four idealized problems of relevance to a repair technology, leading to a set of patch design charts.

Fabrication and testing of specimens representative of typical aircraft structural components.

Testing and analysis of a lap joint specimen with multiple site damage.

Demonstration of composite patches on an in-service commercial aircraft.

The detailed objectives were:

1. Generation of a database that contains properties of materials and adhesives, information regarding the treatment of metallic surface prior to application on composite patches, and information regarding the adhesive cure process.

2. Development of a simplified analytical method for analysis and design of composite patches. Specifically, the effect of composite patches in reducing crack tip stress intensity factors in the following cases:

   (a) Through-the-thickness crack in a metallic panel;
   (b) Surface crack in a panel;
   (c) Surface flaw near a fastener hole; and
   (d) Through-the-thickness crack near a loaded fastener hole

3. Fabrication and testing of specimens with and without composite patches. Specifically:

   (a) A panel with a through-thickness crack;
   (b) A panel with a semi-elliptical surface flaw; and
   (c) A panel with a quarter-elliptical surface flaw near a fastener hole.

1. BONDING METHODS AND MATERIALS DATA BASE

In the early 1970's the Aeronautical Research Laboratories of Melbourne, Australia, pioneered a novel method for the repair of fatigue and stress corrosion cracking in aircraft, using adhesively bonded fiber composite patches. This method has proven to be effective and highly cost effective compared to conventional repair methods. Repairs undertaken have performed well in service.

Repairs using bonded composites have numerous advantages over mechanically fastened repairs. Adhesive bonding eliminates stress concentrations at fastener holes. Composites are readily formed into complex shapes, permitting repair of irregular components. They exhibit high stiffness-to-weight and strength-to-weight, and are fatigue and corrosion resistant. In service monitoring is possible, for non-conducting fiber systems, by direct inspection through the repair using eddy current methods. The high degree of anisotropy of composites eliminates parasitic stiffening of structures other than in the desired direction.

Preliminary design methods for repairs have been covered extensively in literature. The objective of this work is to discuss the process development phase of bonded repairs.

Numerous practical repairs and experimental evidence [1-6] have shown that bonded repairs are substantially more effective in retardation of crack growth than conventional mechanically fastened repairs. The principal aim of any repair is to either eliminate the crack or reduce crack growth by reduction of stress intensity at the crack tip. Prior to the advent of bonded repairs stress intensity reduction was primarily obtained by reduction of net section stress in the vicinity of a crack. Bolted or bonded repairs of the same stiffness will effectively produce the same net section stress reduction.

The significant difference between repair methods is the behavior of the repair region adjacent to the crack.

In a fastened repair, proximity of the first set of fasteners to the crack is limited by shear out. The free length of repair between the first set of fasteners will be strained, allowing displacement of the crack faces. For a bonded repair, as crack opening occurs the adhesive adjacent to the crack is subjected to shear leading to load transfer into the repair. This load transfer modifies the local displacement behavior of the crack. As the point of load transfer is substantially closer for a bonded repair, crack face displacement is considerably smaller than for a bolted repair. The rate of crack propagation for a bonded repair is substantially below that for a conventional repair.

To perform repairs on an aircraft, several processes are required. Adhesive bond strength and durability are strongly influenced by surface preparation of the bond interfaces, in particular on metallic components. There are several suitable surface treatment processes for repair applications. Most current applications rely on the use of modified epoxy film

adhesives, which require elevated temperature and pressure during cure. Numerous methods are available for heating and pressurizing components under field conditions. In this section, the advantages and limitations of application methods will be discussed.

A consequence of the above discussion is that the wide spread practice of 'stop drilling' is not desirable, as it moves the point of load transfer further from the crack, thus allowing an increase in crack opening by increasing the free length of the repair.

1.1 CRITERIA FOR REPAIRABILITY

The bonded repair method has proven to be more effective than conventional repairs, exhibiting ease of application and excellent in-service performance. However, the method is not universally applicable. Design considerations may preclude bonded repairs, and in some cases selection of the method, although technically possible, may not be appropriate. A list of selection/rejection criteria follows:

1. Does an effective repair already exist?

In some cases where an existing repair method is performing successfully, the cost of development of a bonded repair may not be justified for other than simple cases. A value judgement is required, based on design and fabrication costs, down time for repair, and the effectiveness and frequency of existing repair methods. Component replacement may also be an option.

2. Nature and frequency of cracking.

An important aspect of repair is to determine the cause of cracking. Careful inspection of crack faces after sectioning would reveal the cause; overload cracks typically show a dimpled surface typical of rapid fracture, fatigue cracking has the characteristic lines known as striations, and stress corrosion cracking usually shows flakes of corroded matter on the crack face.

If the cracking problem in question is limited to a few aircraft the cost of development of a bonded repair may not be justified for more complex applications. Typical cases where this aspect is considered are cracks resulting from design exceedance damage, ground handling damage or incorrect maintenance procedures. If a bonded repair is feasible, the criteria listed in 1 should be addressed.

3. Is the component flight critical?

If the component is not critical to the survival of the aircraft, then this criterion is not of concern. In cases where the component is essential, the consequence of repair failure, leading to crack growth, should be considered. Where crack propagation rates and defect size are likely to produce a critical crack size between inspection intervals, or if the uncertainty in the inspection intervals is high, then the bonded repair method may not be suited.

4. Are there geometrical limitations to repair effectiveness?

The presence of protruding fasteners, corners, changes in section, holes or other components may inhibit the development of a sufficient adhesive transfer length to allow effective performance of the repair. Bonding is possible over flush fasteners, provided the repair fibers over the fasteners are continuous. Obviously, bonding over fasteners may preclude their later removal.

5. Is the crack location and orientation consistent between aircraft?

Some cracking problems, particularly those associated with vibrations may produce cracking which may not be repeated with sufficient consistency between aircraft to allow the use of unidirectional bonded repairs. Cross plied laminates may be used, but these will exhibit a lower modulus and interlaminar shear strength.

6. Is access practical for repair application?

While repair by bonded composites may be feasible in theory, access for repair processes, such as surface preparation, should be sufficient to allow the repair to be performed to an acceptable standard. Inspection requirements after repair should also be considered. Although adaptation of method to suit local conditions may be considered, quality control requirements should be of prime concern.

7. Are there environmental problems?

Adhesive bonds may be susceptible to degradation by a range of environments which may occur in service. Also, the presence of some surface contaminants may inhibit the development of an effective bond. Such environments may include high humidity, a large temperature range during service, the presence of oils, urine, fuels, etc. The location of a repair in a high traffic area, such as a walkway, may lead to damage by impact during service.

8. What type of material is to be repaired?

Consideration of the type of material to be repaired is required for the selection of surface treatment processes. A suitable surface preparation process which is practical for the specific problem must be available. Also, the material being repaired may influence the cure process and adhesive selection. For example, most aluminum alloys are solution heat treated and artificially aged. Excessive heating of these materials may lead to a loss of strength. Therefore, an adhesive system which cures at lower temperatures must be selected.

9. Would the repair processes damage surrounding components?

Consideration should be given to the effects of surface treatment materials, such as solvents, acids and grit, on materials and components adjacent to the repair region. The effect of heating on materials and components such as hydraulic fluids, greases, seals and electrical wiring must also be considered. Modification of the application process or removal of susceptible components may be required. It should be noted that a similar assessment would be required for conventionally fastened repairs, where drill penetration or contamination by the drilling tool may preclude the use of mechanical fasteners.

1.2 REPAIR DESIGN AND SELECTION ASPECTS

It is not the purpose of this work to discuss specific design methods. However, an understanding of the influence of material and geometric variables is relevant to the development of application processes.

In analysis of a repair problem three criteria are to be satisfied:

A. Shear Stresses in the adhesive must be below the shear allowables for the adhesive. Consideration of allowable shear strain, plastic strain capability, and fatigue performance is required for acceptable bonded repair design.

B. Tensile Strains in the reinforcement must be below the allowable strains for the repair composite.

C. The level of stress intensity reduction must be sufficient to justify the repair.

These criteria are dependent on the geometry of the repair and the properties of the repair materials.

1.3 REPAIR GEOMETRY

1.3.1 Geometric Variables

For complex structural repairs analysis is usually performed using the Finite Element Method, which allows evaluation of specific repairs. Other earlier methods for analysis provide informative assessments of specific geometric variables. A comprehensive analytical methodology that allows the analysis and design of composite patches using very efficient computational approaches, requiring no more than a PC, is developed in the course of the present effort, and is reported in detail in Part II of this report.

The variables of interest in the repair methodology include:

A. Location of the edge of repair patch with respect to the tip of a crack.

B. Repair thickness.

C. Repair length.

D. Repair width.

E. Adhesive thickness

4

The problem of repair location along a crack has been addressed. By considering a stringer type reinforcement applied at various locations along a crack, it was found that maximum stress intensity reduction occurs when a reinforcement is applied very near to the tip of a crack. Application of a repair over a crack will always provide some stress intensity reduction, but application ahead of a crack produces little if any reduction in stress intensity.

This is of significance to practical repair problems, indicating the importance of applying repairs over the tip of a crack. In practice, it is usual to apply repairs over as much of a crack as possible.

A major design parameter for repairs is the repair stiffness, Et, which influences the three criteria listed above. It may be seen that increasing either patch thickness or elastic modulus produces an initial rapid reduction in stress intensity, adhesive shear stress and reinforcement stress. Further increases in stiffness produce diminishing returns.

Repair length, perpendicular to the crack, is determined by adhesive stress requirements. As may be seen, for purely elastic conditions, shear stresses in the adhesive layer of a bonded repair exhibit a peak at the outer end, and adjacent to the crack. Between these points, adhesive stresses decay to zero, provided the repair length is sufficient. The distance from the maximum stress point to where the stress is effectively zero is known as the 'characteristic length', and depends on repair geometry. Baker [1] gives this length as

$$ d = \sqrt{\frac{E_p E_r t_p t_r t_a}{G_a (E_p t_p + E_r t_r)}} $$

where E_p is the modulus of the plate, E_r that of the repair patch; t_p, t_r and t_a are, respectively, the thickness of the plate, repair patch and adhesive layer; and G_a is the shear modulus of the adhesive.

An allowance of a minimum length of 4d at each side of the crack is necessary. In practice, to allow for environmental degradation and production variability, a minimum length of 6d is used. Provided the length of repair perpendicular to the crack used exceeds 6d, any increase in length above this will not alter the performance of the repair and is therefore redundant.

Adhesive stresses exhibit high values near the crack and at the outer ends of the repair. The high stresses at the crack may be reduced by increasing repair thickness. However, an increase in repair thickness increases the shear stress at the outer end of a repair. To reduce high shear stresses at outer ends and also to reduce peel stresses, repairs are usually tapered (A quantitative evaluation of the effects of taper is planned in the near future, as part of our continuing research in to the repair methodology), gradually reducing stiffness to effectively zero. Because composites are layered, it is relatively easy to taper patches by simply terminating each layer shorter than the previous layer. Common practice is to allow a

5

minimum overlap length per layer of 3 mm to maximize peel resistance of the patch. An inverse taper system is used, where the largest ply is located at the top of the layup.

In practical applications, structural features such as fastener holes, edge distances, changes in section, or the presence of other components may inhibit repairs by interference with the required transfer length. In many cases it is this requirement which causes rejection of the bonded repair method for specific applications.

Adhesive thickness directly influences adhesive stresses; thinner adhesive thicknesses produce higher shear stresses. The use of film adhesives with carrier fiber systems helps to limit the variability of adhesive thickness.

1.3.2 Crack Length Effects

A geometric peculiarity of the repair method exists in reference to the size of crack repaired. Initial theoretical work done by Atluri and Kathiresan [2] and Rose [3] indicated that the stress intensity after repair should be independent of initial crack length (This result is corroborated in the comprehensive analytical work described in Part II of this report. This result appears to hold not only for repaired cracks in center-cracked panels as in [2,3], but also for repaired cracks near loaded fastener holes, a problem which is solved for the first time in this work, and is described in Part II of this report). Therefore one would anticipate that crack propagation rates after repair would be independent of initial crack length. Experiments by Baker [4] showed that this was not always the case; crack growth for large cracks was strongly retarded following repair, while small cracks continued to propagate at a slow rate. Several factors are believed to produce this behavior. First, there appears to be a limiting crack length, above which cracks behave as if they were cracks of the limiting length. Cracks below the limiting length would continue to propagate to that limiting length. Second, for large cracks, compressive stresses resulting from the development of the plastic zone at the crack tip prior to repair inhibit reinitiation of the crack. Small cracks have smaller plastic zones, which provide reduced resistance to crack growth.

1.4 MATERIALS SELECTION

The major materials variables involved in repair cases, given that the parent materials are set, are the reinforcement elastic modulus and strength, and the adhesive shear modulus and strength.

1.4.1 Reinforcement Selection

An increase in elastic modulus, resulting in an increase in patch stiffness, will reduce stress intensity, adhesive stresses and reinforcement stresses. It is therefore apparent that reinforcement materials should be selected to have the highest elastic modulus, for minimum thickness repairs. Thinner repairs reduce residual stresses and reduce aerodynamic drag. Because repair stiffness effects diminish rapidly with increasing stiffness, the value of high

6

stiffness fiber systems is lost for other than relatively thin repairs, and cheaper more compliant fiber systems become attractive. Table 1-1 shows comparative moduli of typical repair materials.

TABLE 1-1 .   TYPICAL PROPERTIES OF UNIDIRECTIONAL COMPOSITES

Property	Graphite/ Epoxy ($V_f = 60\%$)	Boron/ Epoxy ($V_f = 50\%$)	Glass/ Epoxy ($V_f = 45\%$)	Aramid/ Epoxy ($V_f = 60\%$)
Strength, G Pa				
Longitudinal				
Tensile	1.1	1.3	1.1	1.4
Compressive	0.7	2.5	0.6	0.2
Transverse				
Tensile	0.02	0.06	0.03	0.01
Compressive	0.13	0.20	0.12	0.05
Modulus, G Pa				
Longitudinal	130	200	40	80
Transverse	7	19	8	6
Shear	6	6	4	2
Shear Strength, G Pa	0.06	0.07	0.07	0.03
Poisson's ratio, v_{12}	0.28	0.23	0.26	0.34

One problem associated with repairs, whether bonded or mechanically fastened, is that if the repair can be applied to one side only, then by offsetting the neutral axis of the repaired region, local bending results. Unfortunately, this bending acts to open the back face of the crack, leading to an increase in crack propagation. It is therefore important to minimize the amount of neutral axis offset by application of a minimum thickness repair. This phenomenum tends to negate the attraction of cheaper low modulus fiber systems, compared to boron/epoxy. A further disadvantage of thick repairs is that the effectiveness of NDI methods diminishes with increasing repair thickness.

Note that for maximum stiffness, unidirectional laminates are used for patching where possible, despite the low transverse strength of such a lay-up. Because unidirectional composites also exhibit a low transverse elastic modulus, the failure strain is high. For most repairs to metals, the transverse failure strain of a unidirectional patch is nearly the same strain as would produce failure in the metal.

While the high stiffness of boron/epoxy is suited to repairs, the material does have some disadvantages. Firstly, being a large diameter fiber, (around 0.125 mm), boron is not readily formed around sharp corners, as the bending stresses developed in the fiber may cause fracture. A radius of 75mm is about the minimum possible for a boron laminate. For applications with smaller radii, small diameter fibers such as graphite, should be used.

7

Boron fibers also exhibit extreme hardness, which leads to difficulty in cutting and handling. Usually cutting is by laser or water jet systems. Fibers in pre-preg form may by cut by glass cutting wheels, or disposable type knives, but this approach leads to some fragmentation of the fibers at the cut. For many applications boron/epoxy is preferred. This is because of its:

       A. high strength and stiffness,

       B. low electrical conductivity, and

       C. relatively high coefficient of thermal expansion.

The low electrical conductivity means that conventional eddy current Non-Destructive Inspection (NDI) techniques can be used to monitor in-service crack growth. An additional benefit is that it also avoids the problem of galvanic corrosion between the patch and the structure. Its relatively high coefficient of thermal expansion, compared to graphite/epoxy, aids in minimizing the residual thermal stresses which arise due to the thermal mismatch between the coefficients of expansion of the composite and the metal component. The high modulus of boron, in comparison with graphite epoxy, also results in thinner patches and less induced bending effects (due to offset of the neutral axis).

1.4.2 Adhesive Selection

Adhesive properties of importance have been addressed by Baker et al [5,6]. The primary selection parameters are adhesive strength and shear modulus. A high shear modulus reduces stress intensity, adhesive and patch stresses. Selection of an adhesive with a low shear modulus will result in a compliant repair, which may be durable under cyclic loading, but will not be as effective in crack retardation as an adhesive with a high shear modulus. Obviously, a high shear strain capability, including plastic strain, improves the performance of a repair.

Adhesive cure temperature is also an adhesive selection parameter. For most applications, the use of elevated temperature curing adhesives is required. Elevated temperature curing adhesives usually exhibit high strength and durability. For high temperature applications adhesives must exhibit a high Glass Transition Temperature, the temperature at which a significant loss of strength and stiffness occurs. Most epoxy systems cured at low temperatures exhibit poor environmental durability. Recently developed acrylic systems exhibit numerous advantages. They are easy to apply, requiring no control of precise mixing ratios. They also exhibit reasonable environmental resistance and moderate adhesive strengths. The adhesives may be suited to battle damage type applications and repairs to minor structure. Currently for high performance durable repairs, elevated cure epoxy systems are still preferred.

Creep and creep recovery of adhesives are also of importance in repair applications. An ideal adhesive shows little creep under sustained load, and recovers rapidly on unloading. Fatigue performance of adhesives must also be considered. The Double Overlap Fatigue

8

Specimen (DOFS) developed by ARL allows evaluation of adhesives for repair applications. In this specimen, a double overlap joint is formed by butting two segments together and bonding face sheets over the joint. Measurement of the opening displacement of the butt joint under load, and after unloading allows evaluation of creep and creep recovery. Continuous measurement of opening displacement under fatigue loading allows evaluation of adhesive fatigue performance. Fatigue damage occurs near the joint in the adhesive layer. As this damage propagates, the length of unsupported face sheet increases, leading to an increase in opening displacement. The rate of damage growth can be determined.

1.5 SURFACE TREATMENT SELECTION

There is a wide range of pre-bonding surface treatments currently in use in aircraft manufacture, in particular for aluminum alloys. Most systems aim at removal of surface oxides, and the promotion of an oxide layer which is resistant to hydration, and with a microstructure which enhances interlocking of the adhesive with the surface.

1.5.1 Surface Preparation Evaluation

The evaluation of adhesive bond surface preparations is usually performed by determination of bond durability under conditions known to be aggressive to adhesive bonds. Usually specimens are prepared by bonding panels treated with the candidate surface treatment, followed by cutting to form wedge specimen. A wedge is driven into the specimen producing an initial crack through the adhesive. Exposure to hot-wet environments (50 C, 100% R.H.), produces varying degrees of crack growth in the adhesive or through the bond interface. Measurement of crack growth with time gives a measure of the effectiveness of surface treatments. Slower growth rates, and those which do not propagate along the adhesive interface indicate good environmental durability, and therefore better in-service performance.

In the evaluation of adhesive performance, crack growth rates may not necessarily be the best criterion. Energy release rate, G, gives some indication of resistance to adhesive degradation. However, energy release rates for wedge tests are dependent on initial crack size produced when the wedge is driven into the bond. For example, an adhesive with a low peel strength may produce a large initial crack length, but not produce significant environmentally induced growth. A more realistic measure of environmental durability relates the energy release rate at a given time to the initial energy release rates at 48 hours exposure, and comparison to initial release rates, a more realistic measure of environmental degradation may be obtained.

1.5.2 Surface Treatment Processes

For all adhesive bonding procedures, surface cleanliness is imperative. The presence of contaminants severely inhibits adhesive bonding. For this reason, extensive surface

preparation is vital to bonding processes. The first and most important step in surface preparation is to degrease the surface, using a strong solvent, such as Methyl Ethyl Ketone, (MEK), or Trichlorethane. In factory processes, precleaning is usually performed by use of vapor degreasing tanks. In these systems, solvent is vaporized by heating to the boiling point. The vapor condenses on the work piece, and drips off under gravity, taking with it dissolved contaminants. Careful control of boiling temperatures ensures that solvent vapor purity is high, minimizing re-contamination of the surface.

Under field conditions, vapor processes are impractical for large components. Frequently, contaminants such as oils and fuel are present. The surface is usually highly oxidized. In such cases, degreasing is performed by use of copious amounts of solvent applied at room temperature by direct contact. Firstly, surface contaminants, such as sealants, paint or oxide films are removed by vigorous use of abrasives, such as Scotchbrite pads, lubricated with solvent. The surface is then carefully cleaned by direct application of solvent. Use of disposable tissues is the usual method.

Extreme cleanliness is required for this step. A measure of this requirement is that cleaning should continue until a clean tissue shows no indication of contaminants after strong contact with the surface. Final cleaning is then performed by one-wipe application of solvent, rejecting each tissue after a single pass over the surface. Only after this step has been stringently pursued should further surface treatment processes be undertaken.

In the development of practical repair applications, the method of surface preparation is usually predetermined by laboratory validation. Procedures for implementation under field conditions concentrate on minimization of contamination of the bond surface and protection of surrounding structure from surface treatment materials.

1.5.2.1 Surface Abrasion

The easiest form of surface preparation for adhesive bonding is mechanical abrasion by use of abrasive papers of alumina impregnated pads, (e.g. Scotchbrite). Such systems are usually recommended for low standard adhesive bonds, and are common for domestic adhesive systems. In high performance applications adhesive bonds produced using this preparation perform poorly, often exhibiting low shear strength and poor environmental durability. The use of simple abrasion alone is not recommended for bonded repairs.

1.5.2.2 Grit Blasting

Performance of simple surface treated bonds is improved by further aggressive abrasion by grit blasting. Best results are achieved by use of fine alumina grit, (50 micron) which presents a very irregular surface of hard material. In bonding applications it is essential that used grit is not recycled, as surface contaminants which are removed by grit blasting will re-contaminate the surface on contact.

10

Grit blasting involves the abrasion of a surface by an abrasive material carried in a stream of high flow rate gas. In most industrial applications, compressed air is used. As compressed air frequently carries high levels of oil from compressor systems, its use in bonding is not recommended, unless the system is highly filtered. Common practice is to use compressed dry nitrogen as the propellant gas, as this eliminates oil contamination, and also reduces oxidation of the surface by dispelling oxygen during abrasion. Oxidation will commence soon after grit blasting, but concentrations will be at atmospheric pressure, rather than at elevated blasting pressure. Nitrogen is commonly available at most air bases, where it is used to inflate shock structures, pressure accumulators and so forth.

1.5.2.3 Non-Tank Anodizing

For repair applications, most factory surface preparations are unsuited, because they usually involve immersion of components into etching or anodizing baths. This is only practical under field conditions for small components. For this reason, the phosphoric acid non-tank anodizing process, (PANTA) was developed. In this process, a phosphoric acid solution is used in gel form (see Appendix A). It is held in place by interspersion of the gel between layers of washed cotton gauze. A stainless steel mesh, which is isolated from the metal surface acts as the cathode, and a voltage is impressed between the mesh and the metal surface. A closely controlled voltage sequence is used, followed by immediate washing of the surface with water and drying. Care is required not to touch or brush the surface after anodizing, as damage to the oxide layer will result. Some process descriptions suggest that excess acid gel be carefully wiped off with a tissue prior to washing. As such a process will result in disturbance of the anodized layer, it is not recommended.

The resulting surface may be inspected by polarized light as a quality control measure. A fluorescent light is held on one side of the treated surface, and reflected light from the surface is viewed at the other side through a polarizing film. A low angle of incidence with the surface (5 to 15 degrees) is required. The surface is inspected for the presence of color. Areas which exhibit no color may not be correctly anodized.

If the polarizer is rotated through 90 degrees, all colors should change to their complementary color. Areas which exhibit no color change, or which still show no color are not correctly anodized and the surface preparation process should be repeated.

This process has been used successfully under field conditions. For applications on lower or vertical surfaces of an aircraft, the anodizing mesh may be held in place by use of rubber straps, hooked onto suction pads, of the type used to handle plate glass.

A significant problem in the use of the PANTA process is the development of bubbles of evolved gasses produced during anodizing. In extreme cases, bubbles may exclude surface contact of the gel, leading to poor surface preparation. This is usually detected during the quality control check. Use of a fairly coarse size stainless steel mesh will encourage bubbles to be expelled, and mesh spacings of about 2mm seem suitable.

Several etchant processes, usually known by trade names (eg. Alodine and Pasagel), are available and reasonably easy to use. Unpublished test results have shown that, while these treatments perform adequately, the durability of bonds using the PANTA process is superior.

1.5.2.4 Silane Primers

Recent work at ARL has concentrated on the use of silane primer (gamma-glycidoxypropyltrimethoxy silane) as a surface treatment. In this process, a 1% solution of silane in distilled water is brushed onto the bond surface. The particular silane compound used is chosen so that it chemically links with the metal surface. The other end of the compound chain is such that it forms a covalent bond with epoxy groups, thus forming a strong and stable bond. Tests have shown that results comparable with the PANTA process have been achieved on 2024-T3 aluminum and some high strength steels. The near neutral pH of the solution minimizes the chance of hydrogen embrittlement of steels.

Surface preparation using silane primers is very simple compared to anodizing. Silane solution of about 1% in distilled water, prepared one or two hours before use, is applied directly to the surface using a solvent cleaned paint brush. The surface is maintained in a moist condition for 10 minutes, and then simply dried using warm air. The process eliminates the need for complex equipment and procedures as required for the PANTA process, substantially reducing complexity and equipment cost. However, unlike the PANTA process, there is no simple quality control check on surface quality prior to bonding.

1.5.2.5 Composite Surface Preparation

In general, surface preparation of composite patches is comparatively easy. The surface is thoroughly solvent cleaned, and then lightly grit brushed. Care is required not to aggressively abrade the surface as exposure of fibers may result. It is however essential that all release agents which may be present on the composite surface are removed by the process.

Some composite manufacturing processes use a nylon release cloth or tear film as protection against surface contamination. This cloth is removed just prior to bonding, and usually no further surface preparation is used. As most repair applications are performed in less than perfect bonding conditions, the chances of surface contamination are considerably higher than for production bonding. Therefore, reliance on tear films as the only surface preparation process is not recommended.

1.6 HEATING METHODS AND ISSUES

A substantial proportion of development time for practical repairs is devoted to the establishment of correct heating procedures for the structure. The method for heating may be selected from the methods outlined in the following sections. Power requirements for heating depend on the emissivity of the materials being heated, the area of structure being heated, the

thickness of the heated zone, and the required temperature difference. Heat requirements are the sum of heat stored in the heated zone, and losses by conduction to the surrounding structure, convection to passing air currents, and radiation to the surrounding environment. Convection and radiation losses may be reduced by use of insulating blankets surrounding the heated zone.

Selection of the location of heating elements around or over the repair zone is usually done by trial and error, as the complexity of most aircraft structure negates the use of mathematical models. Some Finite Element packages may be used to determine heat flow patterns, and these could provide heater design information. To date, practical repair heating has only been developed by evaluation on the structure to be repaired.

1.6.1 Heater blankets

Heating of aircraft structure for repair may be performed in several ways. The most common of these is a heater blanket system, where resistance heating wires are imbedded in flexible heat resistant medium, such as silicone rubber. Blankets are placed in direct contact with the repair and structure, Figure 1.1. Some processes recommend a copper sheet between the blanket and repair, to promote a more even temperature distribution. Advantages of the heater blanket system are that heat is applied directly to the repair region, and the system is sufficiently flexible to be generally applicable to most aircraft structure. For repairs to thick aircraft structure, the low wattage density of heater blankets may be a limitation.

It is common practice to incorporate control thermocouples into the heater blanket. This has the advantage of ease of handling, and also avoids the danger of overheating of the blanket, as may occur for independent thermocouple systems. A disadvantage is that by controlling the temperature at the heater system and not the zone being heated, there is no guarantee that the actual structure will achieve the set point temperature due to heat losses. Calibration of a higher set temperature which achieves the correct surface temperature would
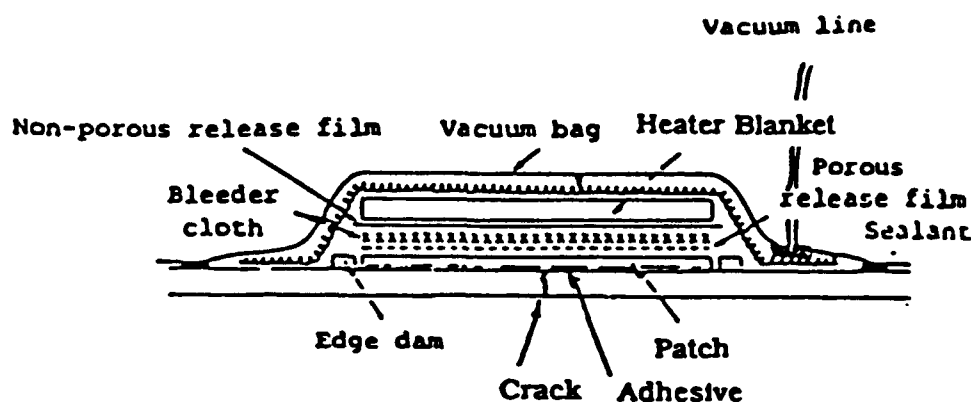
FIGURE 1-1. HEATER BLANKET METHOD FOR REPAIR APPLICATION USING VACUUM BAG FOR IN-SITU CO-CURE

13

be required prior to bonding.

A further problem with heater blankets, and also other systems which pass heat through the composite repair, is that the conductivity of composites is substantially below that of metals. Therefore if a rapid application of heat occurs, significant temperature gradients are set up through the thickness of the composite, and uneven cure will occur. For thick composite repairs heat application through the repair must be accompanied by supplementary heating of the substrate, to minimize through-thickness temperature gradients.

1.6.2 Heated Platens

A second heating method used for repairs is to electrically heat a thick caul plate, see Figure 1-2. By manipulating the location of heating elements in the caul plate some degree of thermal gradient can be maintained. This process is ideally suited to cases where some form of compliant conductive medium, such as a molded silicone rubber pad, can be used to ensure continuous contact between the heater and the heated structure. The compliant medium may also provide more uniform pressure distribution. Control thermocouples may be located in the heating plate or located on the surface under the rubber pad.
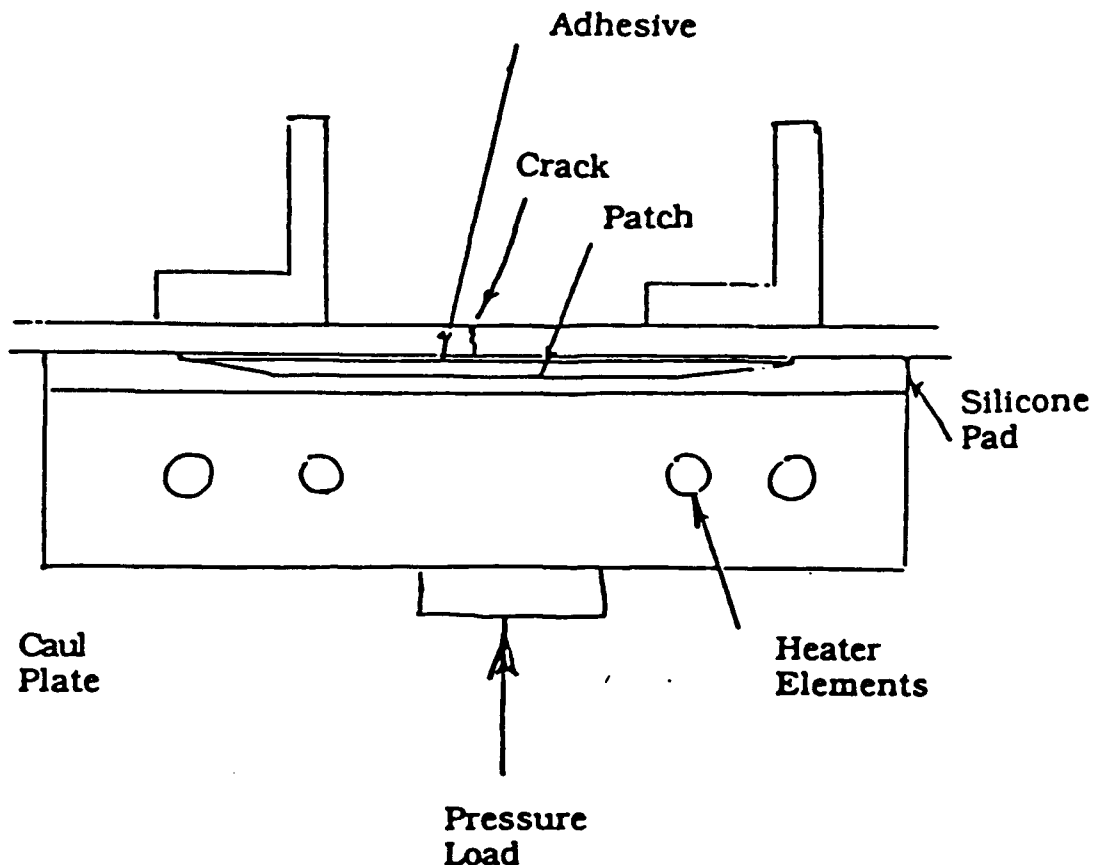
FIGURE 1-2. SET-UP FOR HEATING USING INTERNALLY HEATED CAUL PLATE.
PRESSURIZATION BY MECHANICAL OR HYDRAULIC LOADING

1.6.3 Infrared Lamps

Another method for heat application to aircraft structure during repair is by use of infrared lamps. A wide variety of such lamps is available, allowing groups of lamps to be configured for particular applications. Typically, these lamps are used to heat directly through vacuum bag systems, although protective systems such as aluminum tapes may be required to avoid burning through the bag. Some applications use lamps to provide heat around a repair, either as a heat supplementation system or as the principal heat source.

The major advantage of infrared heat lamps is that there is no direct surface contact, and therefore the system tends to be generally applicable to aircraft structure. Also the height of the lamp above the work surface provides a further control variable for the heating process. For repair to metallic structure high thermal conductivities usually minimize hot spots directly under lamps. Care is necessary for applications involving materials with low thermal conductivity.

Infrared heating relies on good conductivity to minimize thermal hot-spots. Obviously, if a region is not capable of distributing heat, high temperatures will occur. This is particularly true for thermocouple leads which may be required to measure temperatures in the heated zone. For this reason thermocouples should not be positioned under lamps, as a false reading will result. Thermocouple leads also require protection from direct radiation, as damage to leads may result.

1.6.4 Temperature Distribution

There are numerous (proprietary) examples of repair processes specified for aircraft which rely on heater blanket systems for cure of adhesives. As most of these systems are of a general nature, little if any attention is paid to actual temperature distributions on the repair surface during bonding. Thermocouples used to control heating are usually located within the heater blanket or attached to a copper heat distribution foil under the blanket.

Such a procedure is suited to structures where there are no heat sinks, as caused by conductive sub-structural elements, for example ribs or spars. In cases where sub-structural elements are present usage of a single heat source is inadvisable, and may result in poor bond strength or damage to the repaired metal. If for example the control thermocouple is located over thin section material, any adjacent material in contact with thick sub-structure may not achieve bonding temperature due to heat loss to the heat sink. If the control thermocouple is in contact with material over thick sub-structure, surrounding thin structure may be overheated. For applications where large changes in section occur, a system with multiple heat zones should be used. Acceptability of temperature distribution should be verified before bonding by use of thermocouples distributed over the surface during a dummy run of the heating system.

1.6.5 Temperature Measurement and Control

An important factor in repair applications is the control and recording of temperatures in the repair zone. Control of heating is essential to avoid overheating the structure or the repair itself, or to avoid undercure of adhesives, with subsequent loss of strength. Measurement of temperatures enables control and recording for quality control purposes.

Most common repair temperature controllers are a dedicated system by which measurement of one temperature at one location controls power supply to one heater element. These systems are ideal for simple repairs where temperature gradients are minimal. In complex applications, where significant thermal requirements exist, (eg. near large changes in section) single heat sources with a single control source may not be appropriate. This is particularly true for cases where interaction may occur between heater units.

Temperature recording systems should be selected to record more points than those used for control purposed. It is essential to record systems during repair to provide an adequate record for verification of system performance in the event of in-service failure. Usually, temperatures are measured by surface probes held in contact with the heated surface. Care must be taken that the point where temperature is measured actually is on the surface. A common problem here is that systems used to hold thermocouples firmly onto a surface also influence the measured temperature at the joint. Insulating layers over the thermocouple help to reduce errors from secondary contact.

Instruments for recording and controlling temperatures are usually expensive, with the cost increasing rapidly with the number of points measured and controlled. Modern computer systems provide a cost effective alternative to a bank of stand alone controllers and a multichannel recorder. Figure 1-3 shows a method for control and recording of a heating system using an IBM-PC. Up to 16 temperatures are measured by multiplexing input thermocouple voltages into an analog to digital converter. Software systems interpret the voltages as temperatures and assess the heating requirements for specific zones allocated to heated elements. Heating requirements are output by a digital to analog link to silicon control rectifiers or solid state relays which control either the power level to heaters or the time of operation of the heaters. Recorded temperatures and other operational functions are displayed on a VDU, and output for hard copy to a printer. Back-up and running data is continuously recorded on floppy disks during operation to enable re-start in the event of equipment malfunction.

As the above system uses only one analog to digital channel, other channels may be used for measurement and recording of other process parameters. Pressure transducers or load cells may provide information on applied pressures or jack loads during patch application.

Such a system is cost effective for larger applications, due to the high aggregate cost of controllers and recorders.
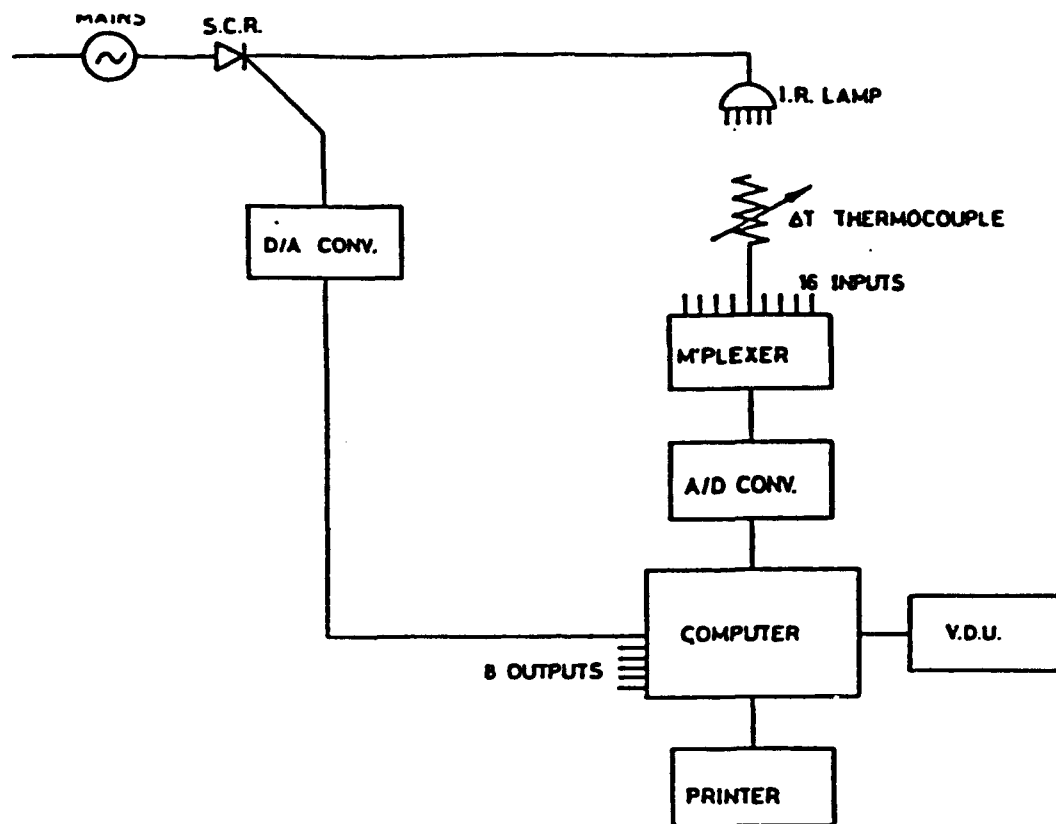
FIGURE 1-3. BLOCK DIAGRAM OF COMPUTER SYSTEM FOR REPAIR HEATING, TEMPERATURE MEASUREMENT & CONTROL

1.7 PRESSURIZATION

Pressure is required during adhesive bonding to minimize void content. Direct pressure acts to reduce the volume of trapped gasses, and to increase the vapor pressure, minimizing evolution of volatiles during cure. A pressure gradient during flow of adhesives promotes migration of voids.

1.7.1 Vacuum Bags

The most common method for repair pressurization is the vacuum bag method. An airtight sealed bag is placed over the repair region, and the region between the bag and the repair surface is evacuated. Atmospheric pressure acts on the outer surface of the bag and the back surface of the repair region, ideally providing a uniformly distributed pressure over the repair. As atmospheric pressure acts on both sides of the structure, no net load is applied; therefore the structure is not distorted by the pressurization process. Obviously, as the method relies on atmospheric pressure, the maximum pressure possible is approximately 107 kPa, (15 psi).

17

Some systems are available which provide a force multiplier effect, thereby increasing the pressure over the repair zone. In these devices, an area substantially larger than the repair region is evacuated. Atmospheric pressure acts on a stiff backing plate, which is in contact with the repair, but not with the surrounding structure. Force multiplication is provided, equal to the ratio of the evacuated area to the area of repair in contact with the backing plate. The stiffening plate tends to reduce the general applicability of the method, and customized systems may be required for irregular shapes. Also, evacuation of a large area around the repair inhibits the use of supplementary heating around the repair.

Vacuum bagging is a fast, cheap and easy method for pressurization and is in common use. It does have several disadvantages. In regions where direct pressure does not act, entrapped gasses may be subject to low pressures, causing them to expand. Similarly, pressures which are below vapor pressures for resin constituents and moisture may encourage evolution of gasses leading to void formation.

The use of vacuum over cracked components or fasteners can also lead to contaminants being drawn into the bond region. Air ingress through such areas may also lead to severe void formation, with subsequent degradation of adhesive bond integrity. These problems may be minimized by sealing cracks and fasteners from the rear prior to repair.

1.7.2 Mechanical Pressure

To avoid sealing problems associated with the use of vacuum bags, direct mechanical pressure may be used. Loading is applied over the bond area by use of hydraulic or screw jacks. A more even pressure distribution may be obtained by use of compliant pad, such as a silicone rubber. A rigid caul plate transfers load from the jack to the surface through the rubber pad. Heating elements may be incorporated in the caul plate.

This method is suited only to thick section repairs, or repairs with sufficient structural rigidity to resist deformation by the pressurization loads. For applications where access is limited to one side, the loads are applied directly to the structure, and some form of reactive system must be possible to enable application of force to the structure. For some thin section applications it may be possible to gain ready access to both sides of the structure to be repaired. In these cases, a simple screw or lever clamp system may provide a ready cheap pressurization process.

As mechanical pressure does not rely on vacuum, except as a reactive system for some applications, higher pressures than the vacuum bag method may be obtained. Care is required not to exceed design allowables for the structure.

1.7.3 Inflated Bladder Method

Recent work at ARL on repair applications to F111-C aircraft uses a mini-autoclave approach to bond boron/epoxy laminated doublers and adhesives to wing structure. Because of

large variations in the geometry of the surface to be repaired in-situ forming of the repair was required. In this application, (Figure 1-4), a rubber bladder is attached to a thick aluminum plate. Gas pressure between the plate and the bladder forces the bladder down onto the repair assembly. A frame around the repair prevents side wash of the fibers, and acts to complete the pressure region. Loads generated by the bladder pressure act against the upper plate. These must be reacted out. In the F111-C application, hard points on the wings were used in conjunction with a stiff beam reaction system.
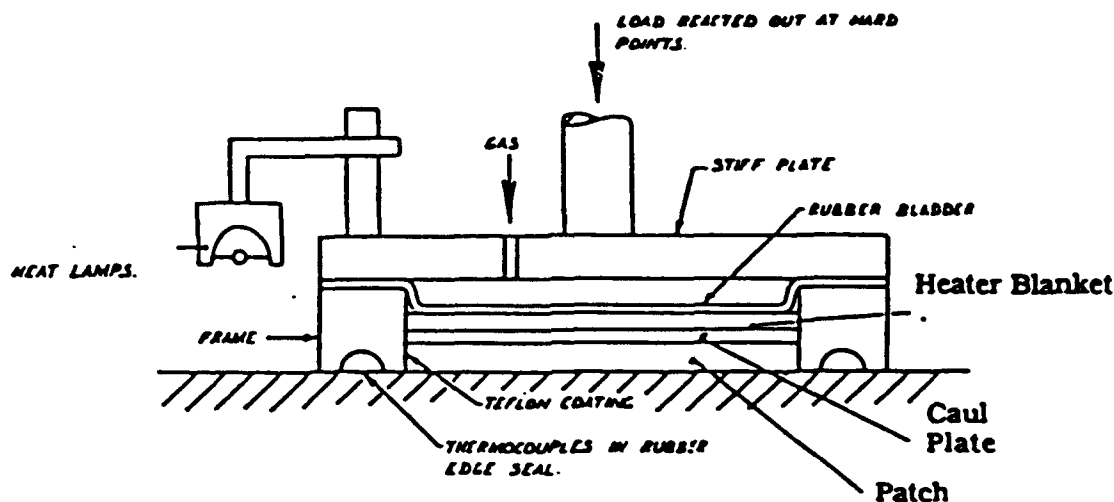
FIGURE 1-4. RUBBER BLADDER METHOD FOR PRESSURE APPLICATION. HEATING BY HEATER BLANKETS OR PERIPHERAL INFRARED LAMPS OR A COMBINATION OF BOTH.

The gas bag method provides the ease of vacuum bagging in the development of uniform pressure distribution over the bond area. It is not susceptible to alignment problems, as occur in the mechanical pressure method. Again, as this method produces a net direct force on the repair region, it is limited to thick structures, or structures with sufficient sub-structural support. Bladder pressures above those of the vacuum bag method may be used.

1.8 CURE PROCESSES

One advantage of composite materials is their formability. Complex shapes can readily be reproduced by molding composites before cure. In practice the method for curing of the patch resin system may depend on the manufacturing tolerances used to produce the component to be repaired.

1.8.1 Pre-cure the Patch

Components with close tolerances or those which are nearly flat lend themselves to repair using patches which are pre-cured under controlled autoclave processes. Patches may be formed onto molds of the component, using normal processes for laminate production. This procedure enables a high degree of quality control of the repair, including ultrasonic C-scan inspection. Because of the high standard of the component produced, pre-curing of patches is preferable to other production systems.

1.8.2 In-Situ Cure

Several procedures are available. The first method involves pre-curing of the laminate. A thin teflon film is located over the repair zone. The repair is either wet laminated, layer by layer over the region to be repaired and cured in-situ, or the pre-laminated patch is located over the area and pressurized to force it into the correct shape, prior to in-situ cure. After cure of the repair, NDI checks on laminate quality may be performed prior to bonding the repair. For applications where the area is not flat, or manufacturing tolerances exceed about 30% of the adhesive thickness over the area of the patch, formation of the repair on the actual repair site may be required.

1.8.3 Repair and Adhesive Co-cure

An alternative in-situ method involves co-cure of the resin and adhesive systems together onto the repair zone. This process has the advantage of only one cure process being performed, thus reducing the repair down time. Compatible adhesive and resin systems must be selected. Care is also required when pressure is applied. Usually, adhesives flow at lower temperatures than resin systems. Therefore, when pressure is applied, the flow of the adhesive occurs first, leading to adhesive thinning at contact points.

A major disadvantage of co-curing is that once the repair patch is bonded, quality control measures are substantially inhibited, and failure to meet required levels will necessitate removal of the cured patch from the structure.

1.8.4 Resin Staging

Co-cure under field conditions may require complex autoclave processes to be performed, including resin bleeding. Containment of resin to avoid ingress into components surrounding the region to be repaired may be difficult. To avoid this problem, it is possible to 'stage' the resin system in the laminate under autoclave conditions prior to full cure on the structure. During the staging process, the patch is molded to nearly the final shape in an autoclave, using a cure cycle which does not exceed the gel time and temperature for the resin

system. By heating to above the resin flow temperature, but below the gel temperature, close control of laminate quality can be obtained. Also, during this step excess resin may be bled off. The resulting patch will have the minimal resin flash, but will still be able to conform to the repair surface during full cure in-situ. Because of the presence of uncured resin, inspection of the repair using ultrasonics is not possible, as moisture contamination would result.

1.9 THERMAL STRESS MINIMIZATION

Unfortunately, for most structural repairs the need for high adhesive strength and durability requires the use of adhesive systems which cure at elevated temperatures. For repairs involving dissimilar materials, residual thermal stresses will result. This is particularly true for composites, when bonded to aluminum. For example, boron/epoxy has a thermal expansion coefficient of 5×10^{-6} per °C and graphite/epoxy may have a zero expansion coefficient, depending on the laminate lay-up. Aluminum has a thermal coefficient of about 24×10^{-6} per °C. Such large differences in thermal expansion strains will cause high stresses in the adhesive layer upon cooling.

Experiments also showed that crack retardation for some aluminum alloys was dependent on the curing temperature for the adhesive system used to repair cracks; higher temperature cure cycles produce lower crack growth retardation (Figure 1-5). Higher thermal residual stresses may play a part in this phenomenon. Also, metallurgical effects on the crack tip plastic zone may contribute to the lower performance of high temperature curing systems.
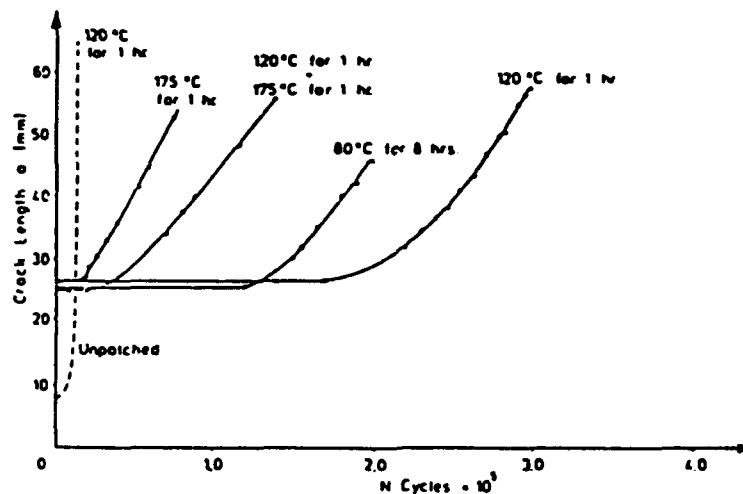
FIGURE 1-5. CRACK PROPAGATION EXPERIMENTS-INFLUENCE OF BONDING TEMPERATURE

1.9.1 Structural Restraint

In practical applications to large structures, thermal expansion of the parent material is usually lower than the natural thermal expansion coefficient for the material in the structure. If only one region of a structure is heated, then the remaining unheated structure

provides some restraint against expansion of the heated zone. Compressive stresses generated by this restraint reduce the resultant thermal expansion, leading to a lower strain in the heated region than if the entire structure had been heated.

Structural restraint may be significant. In recent trials, true thermal expansion coefficients for a wing section were shown to be up to 27% lower than for the unrestrained parent material. Thus, in applications where thermal stresses are of concern, the size of the heated zone should be kept to a minimum. Unless absolutely essential, generalized structural heating should be avoided.

1.9.2 Adhesive Cure Cycle Modification

A further parameter which directly effects thermal stresses is the temperature for adhesive cure. For this reason current studies aim at the use of room temperature curing adhesives. Some room temperature curing epoxy systems have shown promise, but do not provide the performance of higher temperature systems. Recently developed acrylic adhesives are receiving considerable attention, because of their ease of use at room temperatures. However, for most high performance applications, particularly where high service temperatures will be encountered, elevated temperature curing modified epoxies are preferred.

Studies at ARL in Melbourne, Australia, have concentrated on the development of suitable cure cycles for elevated curing epoxies, which result in reduced residual stresses. The obvious area of interest is the maximum cure temperature. For some structural adhesives, it is possible to cure at lower temperatures provided the cure time is extended. For example, adhesives AF-126 and FM-73M have a recommended cure temperature of 121°C. By spectrographic determination of the absence of unlinked epoxy molecules, it has been shown that both of these adhesives may successfully be cured at 80°C to 100°C if the cure time is extended (see Table 1-2). Cross checks on shear strength indicate acceptable performance, as shown in Table 1-3.

TABLE 1-2. TIMES FOR CONSUMPTION OF EPOXIDE FOR ADHESIVES AF126 AND FM73M

Temperature, °C		Time for Consumption of Epoxide
	AF126	
80		> 12 h
90		5.5 h
110		70 min
120		35 min
131		23 min
	FM73M	
81		6 h

TABLE 1-3. NOMINAL TENSILE SHEAR STRENGTH OF SINGLE OVERLAP JOINTS PREPARED FROM AF126 OR FM73M CURED UNDER VARIOUS CONDITIONS

Cure Schedule	Shear Strength, MPa	
	20°C	80°C
AF126		
1 h/121°C	28.4	21.3
8 h/80°C	24.6	14.0
15 h/80°C	27.4	21.3
FM73M		
1 h/121°C	39.2	30.4
8 h/80°C	37.3	27.2
15 h/80°C	38.1	30.0

A further experiment has shown that residual stresses are substantially reduced by lower cure temperatures, even if post-curing at elevated temperatures is used. Specimens were made using boron/epoxy bonded to aluminum strips, using FM-73 adhesive cured with various cycles. By measuring the radius of curvature of the resulting distorted specimen, and use of bi-metallic theory, a measure of thermal residual stress may be obtained: (the radius of a bent beam is inversely proportional to the stress in the beam). Table 1-4 show that for FM-73 a cure cycle of 80°C for 8 hours, followed by a post-cure of 1 hour at 120°C provides a large radius of curvature, and therefore a low thermal residual stress. Obviously, modification of the cure cycle has a strong influence on residual stresses.

1.9.3 Ply Layup Modification

Fiber composite material plies are highly orthotropic, with properties varying rapidly with the angle of orientation. Thermal expansion coefficients are low in the fiber direction, but are high in the transverse direction, due to the decreased influence of the fibers. By use of composite design procedures, it may be possible to produce a laminate with a thermal expansion coefficient which matches substrate material, thereby eliminating residual stresses. A consequent loss of repair stiffness will result.

TABLE 1-4. BIMATERIAL THERMAL STRESS TESTS

Time/Temp	Radius
1 hr/120°C	1861 mm
1 /120° + 1/120	1859 full cure in 1 hr
4/80 + 1/120	2105
8/80	2318
8/80 + 1/120	2450

23

1.10 PROCESS VERIFICATION

For more critical applications of the repair technology, it is essential to verify the effectiveness of process steps prior to implementation of repair programs. To ensure correct cure of adhesives for specific repair applications, temperature distribution, adhesive thickness and void content should be evaluated.

1.10.1 Pressure Verification

Verification of adhesive pressurization processes may be undertaken by use of non-bonding film systems (e.g. Verifilm) or by use of thin teflon film separators on each side of an adhesive film. The normal cure cycle is undertaken with the separator system preventing adhesion. By examination of the resulting adhesive layer, areas of excessive variations in adhesive thickness may readily be identified, and alternative measures taken to correct any problems.

As these systems rely on non-bonding films, the films themselves may enhance void movement during adhesive flow. Care is therefore required in interpretation of results in relation to void formation and distribution in adhesive bonds.

1.10.2 Temperature Distribution Verification

In applications where large changes in section occur, or where materials are poor conductors of heat, assessment of temperature distribution during cure may be required. To perform verification of temperature profiles, a number of thin thermocouples are strategically distributed within a layer of adhesive. A teflon separator film is required to prevent bonding during trials. The cure cycle is followed while temperatures at the thermocouples are recorded. Regions of high or low temperatures may be identified and corrections may be made to heater element locations or intensities. Provided care is taken with the adhesive layer containing the thermocouples, it may be used for further testing after modification of heater patterns.

1.11 SAFETY AND CONTAMINATION PRECAUTIONS

In any repair to an aircraft, precautions are required to ensure the viability of the repair and to ensure that the repair processes do not cause damage or contamination of other aircraft components. In the development of repair procedures and the specification for field implementation, care must be taken to anticipate likely eventualities. For example, under field conditions, numerous sources of surface contamination may be present during adhesive bonding, such as engine exhaust gas, hydraulic oils or fuels. A major source of contamination encountered during initial work stems from inquisitive bystanders, who handle surfaces out of interest. Obviously, many of these problems are beyond the control of the specification writer; however, they should be drawn to the attention of bonding personnel during training in repair procedures.

1.11.1 Fire Prevention

During elevated temperature curing of repairs on aircraft, it is common to apply repairs to fuel storage regions, frequently above ignition temperatures for the fuels. One practical method for minimizing fire danger is the use of a non-oxidizing gas to purge fuel tanks. By replacing atmospheric oxygen in fuel tanks with inert gas, the possibility of ignition of fuel is eliminated. Nitrogen is an ideal inert gas which is readily available at air bases. It forms an excellent fire prevention medium and has been safely used on service aircraft. Care is required not to exceed allowable pressures in aircraft fuel systems while purging is occurring.

The effects of heat on components such as electronic equipment or actuator seals should be assessed prior to repair.

1.11.2 Metallurgical Effects

For repairs involving most structural aluminum alloys, care must be exercised with elevated temperatures. Aluminum alloys are usually solution hardened and artificially aged at comparatively low temperatures. Serious loss of strength may result from even moderate exposures to elevated temperatures. Data should be assessed before repair applications at high temperatures is considered. A further effect is to reduce fatigue resistance of fasteners adjacent to the repair. It is believed that elevated temperatures relieve residual compressive stresses induced by manufacturing, allowing initiation of fatigue cracking. Similarly, elevated temperatures reduce the retardation of repaired cracks in aluminum, when compared to repairs cured at lower temperatures. It is therefore evident that higher temperature curing adhesives, such as FM300 are not suited for repair applications to aluminum.

1.11.3 Bonding Surface Contamination

A frequent source of bond failure is contamination of the bond during surface preparation. Obvious sources such as dust, oil mist or contact by personnel may be minimized by site selection or protection of the region.

A common source of contamination of bonding in aircraft repairs is fuel or volatile materials trapped in cracks or fasteners under the repair. This is of particular concern in applications which use the vacuum bag method, as a pressure gradient results in contaminants being drawn into the bond region from cracks or fasteners. It is therefore important to dispel all contaminants from cracks and fasteners prior to repair application surface preparation. Extensive use of solvents followed by heating is usually sufficient to remove volatile materials. This process has been used successfully under field conditions, in conjunction with fire prevention measures described above.

1.11.4 Contamination by Processes

Care is required during the repair process to avoid damage to adjacent structure or components. Problems relating to fire and metallurgical effects are already addressed. Most

repairs involve the use of contaminants (e.g. alumina grit, etchants or anodizing acids) for surface preparation. As these may cause damage to nearby structure, care is required to minimize egress of these from repair sites. Physical containment of surface liquids by tapes and edge dams usually is sufficient. In some cases, the use of positive pressure barriers, such as loose fitting seals which are slightly pressurized, may provide control of liquid contaminants.

Control of abrasive material such as grit is important near bearings and hydraulic gear. One method is to contain grit within a transparent loose fitting box which is held against the repair region. A vacuum cleaner is attached, maintaining a negative pressure gradient. Grit is mainly extracted or contained. Precautions such as protective coverings and thorough washing after repair would be recommended.

1.11.5 Health Aspects

In the performance of bonded repairs, operators may come in contact with minor health hazards. Surface preparation solvents such as MEK should be handled with care, to avoid skin and eye contact, and respiratory protection should be used. Adhesives which contain epoxies may cause allergic reactions and minor skin irritations. The use of disposable gloves when handling adhesives provides operators with protection, as well as minimizing adhesive contamination from skin contact.

Fiber composites present similar handling problems to timber. Splinters may penetrate skin, causing irritation. Boron fibers present a problem in that they are a large diameter hard stiff fiber. Fibers tend to be brittle, and fragment easily, making removal difficult. Boron and graphite fibers are resistant to chemical degradation in bodily fluids, and therefore are a potential hazard if they enter the blood stream.

1.12 QUALITY CONTROL

1.12.1 Qualification Testing

There is no definitive method for verification of adhesive bond integrity following repair application. In practice, poor bond quality is usually detected after in-service crack growth or debond has been observed. Therefore, quality control of repair bonds is difficult. One method for repair qualification is to infer repair integrity by production of a test coupon during the repair application, for later evaluation. For example, wedge test specimens could be prepared and bonded beside the repair. Later, these specimens would be tested in the usual manner, giving an indication if bond problems are likely. Similar tests are suitable for qualification of operators after training, or to refamiliarize operators after extended periods without repair activities.

1.12.2 Process Specification and Recording

Because bond integrity is difficult to assure by usual quality control checks, it is essential to verify the integrity of the application process, and to specify procedures such that common process errors are eliminated. For example, the use of film adhesives in preference to pre-mixed systems eliminates errors in mixing ratios. Release films from adhesives and any other protective films should be retained as proof of their removal. Specification of elapsed time for process steps may eliminate some problems. As prepared surfaces are susceptible to oxidation and contamination, it is essential to minimize the probability of occurrence by specification of maximum exposure times. Frequently, repair processes require a continuous sequence of events. It is imperative that interruptions such as lunch breaks do not impede repair application.

In the development of the repair process, equipment should be selected which provides a hard copy of process variables, in particular variation of temperature and pressure with time. This hard copy should be retained, as information may be obtained should subsequent in-service performance be unsatisfactory.

1.12.3 Materials Storage and Transport

Many adhesive systems have a limited shelf life and require special storage conditions, for example refrigeration. These are usually specified by the manufacturer, and should be followed. Adhesive batch details and date of manufacture should be recorded on receipt of supply. Large batches are best split into smaller usable packages immediately on receipt, to minimize the amount of time the adhesive is at room temperature.

Periodic revalidation of adhesive and resin systems is strongly recommended. Standard tests may be used, such as lap-shear and climbing drum peel tests for adhesives, while flexural and interlaminar shear strength tests are suited to preimpregnated composite ("prepreg") materials.

At all times sealed packages of adhesives or prepreg material should be allowed to reach room temperature before opening to prevent condensation on the material.

Where adhesive or resin materials are transported they should be kept cold if required. Materials are packed in air-tight polythene bags to prevent condensation and moisture contamination. Packaging in dry ice is sufficient to allow safe transport. An alternative is to use a portable freezer system which is capable of being connected to aircraft power systems during travel.

1.13 IN-SERVICE INSPECTION

1.13.1 Bond Integrity

Verification of bond integrity after repair application is not practical. Most NDI methods for bond inspection, such as ultrasonic methods, may detect gross debond, but there is

no method for measuring the quality of an adhesive bond. Micro-voids in the adhesive can not readily be detected.

Experience has shown that the best method to verify repair effectiveness is to monitor crack growth in service. By specification of short inspection intervals after repair, early crack growth may be used to indicate repair failure. As confidence in the performance of a repair grows, inspection intervals may be extended.

For applications of the repair method for non-cracked structures, (local stiffening to reduce stresses for example), bond integrity may be verified by regular measurement of strain distribution under standard loads. Strain gauges incorporated over the repair would show a change in strain if debonding or delamination of the repair had occurred.

1.13.2 Crack Propagation Monitoring

One major advantage of the bonded composite repair method is the ability to inspect crack behavior through the repair, in particular for boron/epoxy patches. Because boron/epoxy is non-conducting, eddy current inspection is possible directly through moderately thin repairs.

Simple "yes/no" inspection equipment is adequate for structure where the crack tip is distant from other structural features such as rivets or holes. Inspection progresses along the crack until no further indications are received, thereby locating the crack tip. Comparison with NDI and visual records prior to repair would show if propagation had occurred.

For repairs to more complex structure, simple eddy current devices provide confused information, because of interaction of eddy currents with local structural features. Inspection is possible using more sophisticated eddy current devices, which enable experienced operators to distinguish between cracks and fasteners, holes, sheet edges and other adjacent components. Characteristic curves for each structural feature are usually determined from an NDI standard model of the repaired region.

1.14 PATCH REMOVAL

Under circumstances where a repair fails to perform adequately in service, or where deficiencies in application procedures have occurred, removal of the repair may be required. Bonded repairs present problems for removal due to the inert nature of most fiber systems, and the chemical resistance and strong adhesion of epoxies. Methods for removal depend on either degradation of the resin and adhesive, or mechanical action.

1.14.1 Solvent Methods

Most composite fibers are resistant to chemical reactions, and therefore can not be readily degraded. Chemical methods are only effective for degradation of the resin and adhesive systems. Several "solvent" systems have been in use in the electrical industry for

deencapsulation of electronic components cast in epoxies. These systems are effective on room temperature cured systems but are relatively slow for high performance epoxies cured at elevated temperature. Degradation rate for repair removal may be enhanced by heating the solution, but care is required as the materials are flammable. To further enhance activation rate, the solution should be stirred, or sprayed onto the repair surface. As the process of degradation relies on diffusion through the resin system, regular mechanical removal of outer degraded layers will substantially increase the removal rate.

Use of solvent systems presents several health hazards. The solvents readily dissolve oils from skin, causing severe skin irritation, and possible loss of outer skin layers after minor contact. The potential for eye damage is high. At elevated temperature, the solvents have an unpleasant odor.

Sealing and containment of these materials is difficult, and therefore the chance of human contact is high. In general, other removal methods should be used in preference to solvent methods.

1.14.2 Mechanical Methods

A more efficient removal method for unserviceable repairs is to utilize the relatively low peel strength of composites. By driving wedges between layers, substantial amounts of the repair may be peeled off. The use of blunt chisels to crush fibers and resin systems is also effective. In all cases, where direct contact occurs with the substrate structure, soft tools made from aluminum or brass are required, to minimize the chance of scratching of the aircraft material under the repair. Removal rates are enhanced by elevated temperature, due to the reduction in peel strength with temperature. In cases where high temperature will not lead to degradation of the repaired structure, heating to temperatures sufficient to char resin and adhesives facilitates removal.

Health problems associated with mechanical removal are limited to skin penetration by fiber splinters, particularly for boron fiber systems.

1.15 IN-SERVICE PROTECTION

Damage or degradation in service may lead to premature failure of a repair. Damage has occurred to some repairs in service on RAAF aircraft, due to ignorance of maintenance staff of the presence of a bonded repair. In one instance, a bonded repair to a fuel drain hole was severely damaged by staff attempting to clear what appeared to be an obstruction in the fuel decant point. In another case, a bonded skin repair was damaged by attempts to remove what was thought to be excessive paint build-up. This type of damage may be minimized by use of warning labels on or near the repair. In particular, limitations on the use of aggressive chemicals, such as paint strippers, should be stated.

A major cause of long term durability problems with bonded repairs is moisture absorption by epoxy systems. Moisture absorbed leads to a lowering of mechanical properties, including glass transition temperature, and interlaminar shear strength. Good design practice should allow for service degradation. The use of inhibiting barriers will decrease degradation rates. One method is to cover the bonded repair with a thin aluminum foil. Sealant is used to bond the foil to the repair. Diffusion is reduced to that which occurs in the plane of the repair, considerably reducing the rate of moisture absorption.

Ultraviolet light is known to cause degradation of resin systems in composite materials. Tests conducted by ARL have shown that resin is stripped from the surface of composites exposed to direct sunlight, and initiates within days of exposure. The rate of loss is only slightly reduced for semi-shaded specimens. However, resin stripping is eliminated by painting of the surface of composites. Therefore, repairs on external surfaces of aircraft should be painted prior to service.

2. ANALYTICAL AND COMPUTATIONAL METHODS

This part of the report consists of a description of the detailed analytical and computational treatment of four idealized problems of interest in the development of a repair technology. These are:

    A. Repair of a through-the-thickness crack in a metal sheet, by using a composite patch

    B. Repair of a through-the-thickness crack near a loaded fastener hole in a metal sheet, by using a composite patch

    C. Repair of a surface-crack in a metal sheet, by using a composite patch

    D. Repair of surface flaws near a fastener hole in a metal plate, using a composite patch

2.1 THROUGH-THE-THICKNESS CRACK IN A METAL SHEET WITH A BONDED COMPOSITE PATCH

2.1.1 Basic Formulations

The problem of interest, in Figure 2-1, is considered to be a superposition of the following two problems.

Problem A: Determine the stress fields for an isotropic sheet *without a crack*, to which is bonded an orthotropic patch as in Figure 2-2.

Problem B: When the tractions at the location of the crack, as determined from the solution of Problem A above, are *erased*, determine the stress-intensity factors at the crack-tips. This problem is sketched in Figure 2-3.

The relevant material and geometric parameters from Problems A and B are as follows:

    A. The Young's modulus E, and Poisson's ratio v for the isotropic sheet.

    B. Thickness h_s of the isotropic sheet.

    C. The Young's modulus E_x and E_y of the orthotropic patch; the Poisson ratio v_{xy} and the shear modulus G_{xy} of the orthotropic patch.

    D. The height H; and thickness h_p of the orthotropic patch; and

    E. The thickness h_a, and the shear modulus h_a of the adhesive layer.

By using the Buckingham's Π theorem [7], the grouping of non-dimensional parameters that arise from the above geometric and material data is determined to be:

$$\left(\frac{G_s R}{h_s}\right), \quad \left(\frac{a}{h_s}\right), \quad \left(\frac{h_p E_y}{h_s G_s}\right), \quad (v_s), \quad \left(\frac{E_y}{E_x}\right), \quad \left(\frac{E_x}{G_{xy}}\right), \quad (v_{xy}), \quad \left(\frac{H}{a}\right)$$

It is the objective of the present analysis to determine the stress-intensity factor as a function of the above 8 non-dimensional parameters. This ensemble of curves would then lead to a design procedure to select the appropriate composite patch, and adhesive, for a given crack in a metallic sheet. This is the first comprehensive treatment of this problem in the literature.

The model Problem A is further simplified to be that of an infinite isotropic sheet to which is bonded an orthotropic sheet of height 2H and infinite width. To simulate the hoop stress in the pressurized fuselage. the isotropic sheet is assumed to be subject to uniform tensile
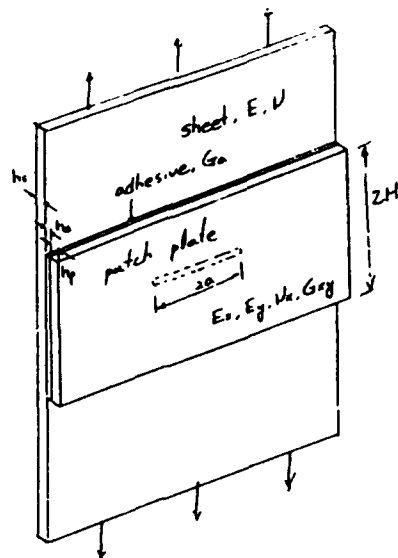
FIGURE 2-1. SCHEMATIC OF A CRACKED METAL SHEET, REPAIRED WITH A COMPOSITE PATCH (SOLVED BY SUPERPOSITION OF PROBLEMS IN FIGS. 2-2 & 2-3)
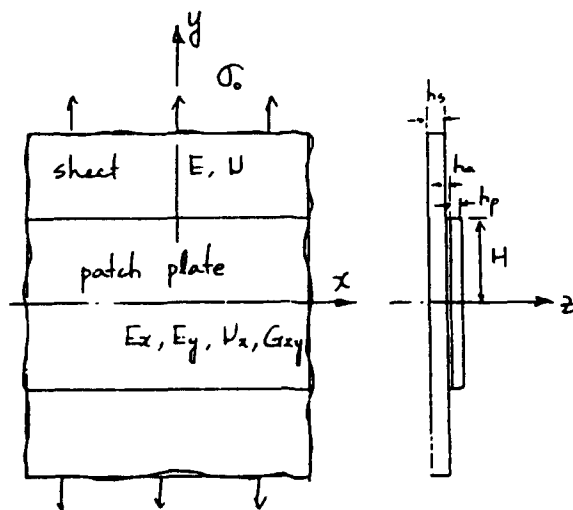
FIGURE 2-2. UNCRACKED METAL SHEET WITH A COMPOSITE PATCH LOADED IN THE FAR-FIELD (PROBLEM A)
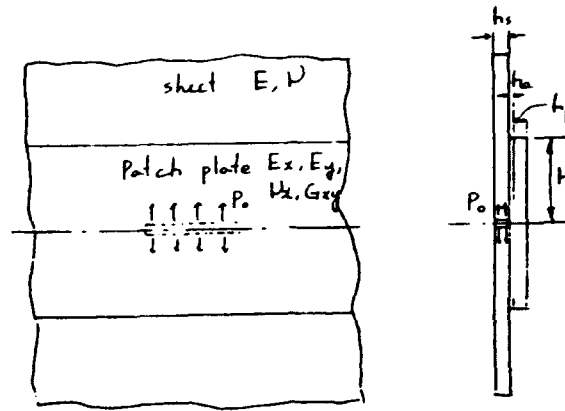
FIGURE 2-3. CRACKED METAL SHEET WITH A COMPOSITE PATCH LOADED ON THE CRACK
FACE (PROBLEM B)

stress σ_0 in the y direction (Figure 2-2). It is assumed that the adhesive layer carries only the shear stress τ_y. This adhesive layer stress τ_y, in turn, acts as a body force on the isotropic as well as the orthotropic sheets, when the free-body diagrams of these sheets are considered. It is further assumed that both   sheets are in states of generalized plane stress. Denoting by a subscript 's' the isotropic sheet; and by subscript 'p' the orthotropic patch; the equilibrium equations of the two sheets can be simplified as:

$$\frac{d\sigma_{sy}}{dy} = \frac{\tau_y}{h_s} \quad \text{and} \quad \frac{d\sigma_{py}}{dy} = \frac{-\tau_y}{h_p}$$

(2-1)

where σ_{sy} and σ_{py} are the direct stresses in the y direction in the two sheets, respectively. The strain-stress relations in the two sheets are given by:

$$\varepsilon_{sx} = \frac{1}{E_s}(\sigma_{sx} - \nu_s \, \sigma_{sy})$$

$$\varepsilon_{sy} = \frac{1}{E_s}(\sigma_{sy} - \nu_s \, \sigma_{sx})$$

(2-2)

$$\varepsilon_{px} = \frac{1}{E_x}(\sigma_{px} - \nu_x \, \sigma_{py})$$

$$\varepsilon_{py} = \frac{1}{E_y}(\sigma_{py} - \nu_y \, \sigma_{px})$$

(2-3)

The shearing stress τ_y in the adhesive is related to the y-displacements of the isotropic sheet (ie., v_s) and the orthotropic sheet (ie., v_p), in the following fashion:

$$\tau_y = \frac{v_s - v_p}{R}$$

(2-4)

33

where R is the "adhesive flexibility" coefficient. Following the experience at ARL [8,9], R is taken to be:

$$R = \left(\frac{h_a}{G_a}\right) + \left(\frac{3}{8}\frac{h_s}{G_s}\right) + \left(\frac{3}{8}\frac{h_p}{G_p}\right) \qquad (2\text{-}5)$$

To simplify the problem further, the approximations, $\varepsilon_{sx} \cong 0$ and $\varepsilon_{px} \cong 0$ are invoked. From Eqs. (2-2 and 2-3), these approximations imply:

$$\sigma_{sx} = v_s\,\sigma_{sy} \quad \text{and} \quad \sigma_{px} = v_x\,\sigma_{py} \qquad (2\text{-}6)$$

By differentiating Eq. (2-4) with respect to y, one obtains:

$$R\frac{d\tau_u}{dy} = \frac{dv_s}{dy} - \frac{dv_p}{dy} = \varepsilon_{sy} - \varepsilon_{py} \qquad (2\text{-}7)$$

By using (2-6) in Eqs. (2-2b) and (2-3b), to express ε_{sy} in terms of σ_{sx} and σ_{sy} and ε_{py} in terms of σ_{px} and σ_{py}, one obtains from Eq. (2-7):

$$R\frac{d\tau_y}{dy} = \frac{1 - v_s^2}{E_s}\,\sigma_{sy} - \frac{1 - v_x v_y}{E_y}\,\sigma_{py} \qquad (2\text{-}8)$$

or

$$R\frac{d^2\tau_y}{dy^2} = \frac{1 - v_s^2}{E_s}\frac{d\sigma_{sy}}{dy} - \left(\frac{1 - v_x v_y}{E_y}\right)\frac{d\sigma_{py}}{dy} \qquad (2\text{-}9)$$

Upon using Eq. (2-1) in Eq. (2-9), one obtains:

$$R\frac{d^2\tau_y}{dy^2} = \frac{1 - v_s^2}{E_s}\frac{\tau_y}{h_s} + \left(\frac{1 - v_x v_y}{E_y}\right)\frac{\tau_y}{h_p} \qquad (2\text{-}10)$$

or

$$\frac{d^2\tau_y}{dy^2} - A^2\tau_y = 0 \qquad (2\text{-}11)$$

where

$$A^2 = \frac{1}{R}\left(\frac{1 - v_s^2}{E_s\,h_s} + \frac{1 - v_x\,v_y}{E_y\,h_p}\right) \qquad (2\text{-}12)$$

From Eq. (2-11), τ_y can be solved, with appropriate boundary conditions. Once τ_y is obtained, the remainder of the variables, σ_{sy}, σ_{py}, v_s and v_p can all be solved for.

The solution of Eq. (2-12) with the symmetry boundary condition $\tau_y = 0$ at $y = 0$ [see Fig. 2-2], is given by:

$$\tau_y = C\,sinh\,(Ay) \qquad (2\text{-}13)$$

From the equilibrium equation [Eq (2-11)], one can then derive:

$$\sigma_{sy} = \frac{C}{A\,h_s}\,cosh\,(Ay) + C_1 \qquad (2\text{-}14)$$

34

$$\sigma_{py} = \frac{-C}{A\,h_p}\cosh\,(Ay) + C_2 \tag{2-15}$$

The boundary conditions are [Figure 2-2]:

$$\sigma_{sy} = \sigma_0 \qquad \text{at} \qquad y = H \tag{2-16}$$

and
$$\sigma_{py} = 0 \qquad \text{at} \qquad y = H \tag{2-17}$$

Using (2-16) and (2-17) in (2-14) and (2-15), one obtains:

$$\sigma_{sy} = \sigma_0 - \frac{C}{Ah_s}[\cosh\,(AH) - \cosh\,(Ay)] \tag{2-18}$$

and
$$\sigma_{py} = \frac{C}{Ah_p}[\cosh\,(AH) - \cosh\,(Ay)] \tag{2-19}$$

Using these stresses in the stress-strain relations [Eqs. (2-2) and (2-3)] one can obtain the expressions for strains ε_{sy} and ε_{py}. Integrating these strains, one may obtain the displacements, thus:

$$v_s = \int_0^y \varepsilon_{sy}\,d\eta = \int_0^y \frac{\left(1 - v_s^2\right)}{E_s}\sigma_{sy}\,d\eta \tag{2-20}$$

$$= \frac{\left(1 - v_s^2\right)}{E_s}\left[\sigma_0\,y - \frac{C}{Ah_s}\left(y\cosh\,(AH) - \frac{1}{A}\sinh\,(Ay)\right)\right] \tag{2-21}$$

$$v_p = \int_0^y \varepsilon_{py}\,d\eta = \int_0^y \left(\frac{\left(1 - v_x v_y\right)}{E_y}\right)\sigma_{py}\,d\eta$$

and
$$= \left(\frac{\left(1 - v_x v_y\right)}{E_y}\right)\left[\frac{C}{Ah_p}\left(y\cosh\,(AH) - \frac{1}{A}\sinh\,(Ay)\right)\right] \tag{2-22}$$

Note that the constant C is as yet undetermined in the expressions for τ_y [Eq. 2-13]; v_s [Eq. 2-21] and v_p [Eq. 2-22]. This can be determined from the compatibility relation:

$$\tau_y = \frac{v_s - v_p}{R} \tag{2-23}$$

From Eq. (2-23), upon substituting for τ_y, v_s and v_p from Eqs. (2-13), (2-21) and (2-22), respectively, one finds that:

$$C = \frac{\left(1 - v_s\right)^2 \sigma_0}{R\,E_s\,A\cosh\,(AH)} \tag{2-24}$$

Thus, the expressions for the stresses τ_y, σ_{sy} and σ_{py} are:

$$\tau_y = \frac{\left(1 - v_s^2\right)\sigma_0}{R\,E_s\,h_a\,A\cosh\,(AH)}\sinh\,(Ay) \tag{2-25}$$

$$\sigma_{sy} = \sigma_0 - \frac{\left(1 - v_s^2\right)\sigma_0}{R\,E_s\,h_s\,A^2\cosh\,(AH)}[\cosh\,(AH) - \cosh\,(Ay)] \tag{2-26}$$

35

and

$$\sigma_{py} = \frac{\left(1 - v_s^2\right)\sigma_0}{R\,E_s\,h_a\,A^2\,cosh\,(AH\,)}\,sinh\,(Ay)$$

(2-27)

When $cosh\,(AH)\,>>\,1$, the stresses on the plane $x = 0$ can be expressed as:

$$\sigma_{sy} = \sigma_0 - \frac{\left(1 - v_s^2\right)\sigma_0}{R\,E_s\,h_s\,A^2}$$

(2-28)

$$\sigma_{py} = \frac{\left(1 - v_s^2\right)\sigma_0}{R\,E_s\,h_p\,A^2}$$

(2-29)

and $\tau_y = 0$.

(2-30)

Thus, the solution for Problem A is completed.

Problem B of   Figure 2-3 can be broken up into two components: (i) the metal sheet alone [Figure 2-4];   and (ii) the orthotropic patch alone   [Figure 2-5]. The enforcement of appropriate compatibility and traction reciprocity conditions on   problems in Figures 2-4 and 2-5, would lead to a solution of the problem in Figure 2-3.
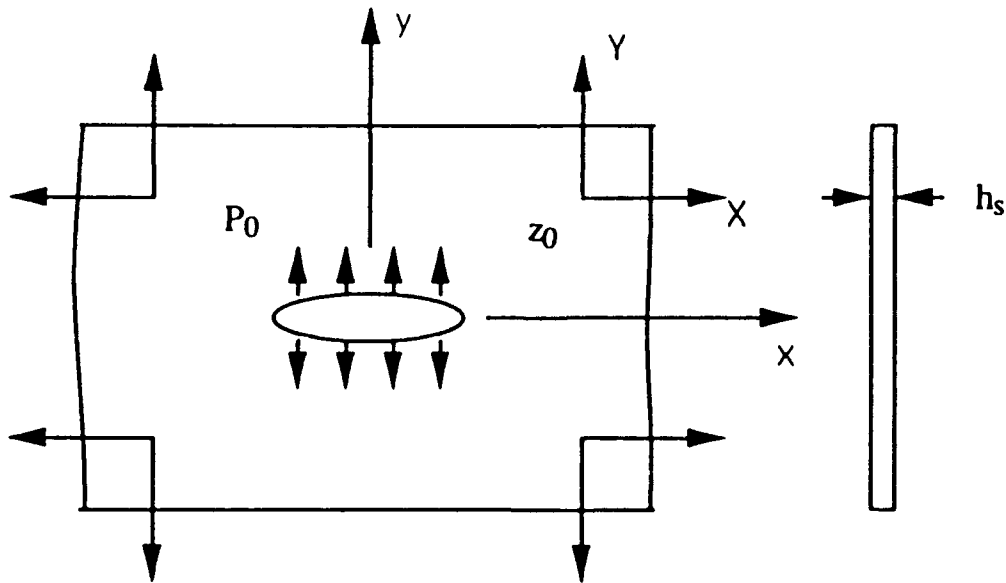
FIGURE 2-4. CRACKED METAL SHEET WITH CRACK-FACE PRESSURE AND BODY FORCES τ_{xz} AND τ_{yz} DUE TO THE ADHESIVE LAYER
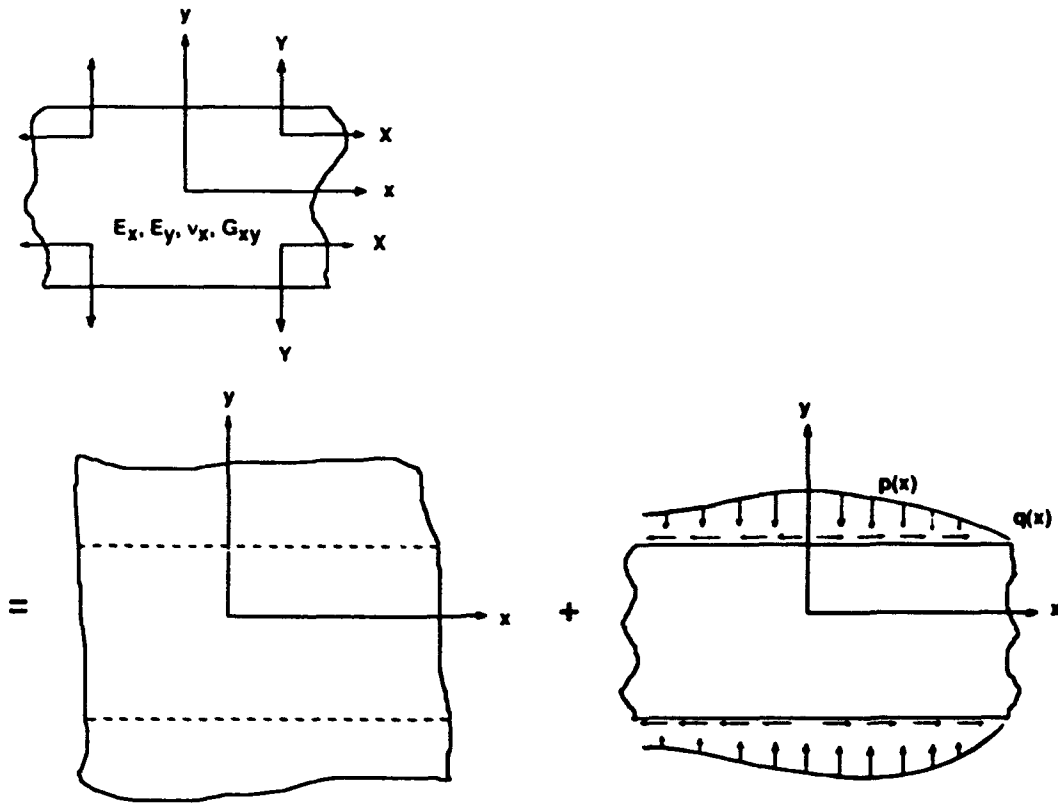
FIGURE 2-5. GREEN'S FUNCTION SOLUTION FOR A FINITE SIZED ORTHOTROPIC PLATE

2.1.2 Green's Function for the Isotropic Metal Sheet:

Using the complex variable method [10,11], the solutions for displacements due to uniform crack-surface pressure P_0 [Figure 2-4] are obtained as:

$$u(x,y) = \frac{P_0}{4G}\left\{(k-1)Re\left[(z^2-a^2)^{1/2}\right] - 2y\,Im\left[\frac{z}{(z^2-a^2)^{1/2}}\right] + (1-k)x\right\} \equiv P_0 f_1(x,y)$$

(2-31)

$$v(x,y) = \frac{P_0}{4G}\left\{(k+1)Im\left[(z^2-a^2)^{1/2}\right] - 2y\,Re\left[\frac{z}{(z^2-a^2)^{1/2}}\right] + (1-k)y\right\} \equiv P_0 f_2(x,y)$$

(2-32)

where, $z = x + iy$, and $k = (3 - v)/(1 + v)$.

The solutions for concentrated forces X and Y acting at z_0 [Figure 2-4] can also be obtained easily from the complex-variable formulation [for further details, see Erdogan [12], and for a more convenient form, Roderick [13]]. These are given by:

$$2G(u + iv) = s\,g(z, z_0) + \bar{s}\,g(z, \bar{z}_0)$$

(2-33)

where

$$s = \frac{X + iY}{2\pi(1 + k)\,h_s}$$

(2-34)

37

and
$$g(z, z_0) = k \{Re\, X A(z, z_0) - X C(z, z_0)\}$$
$$+ \frac{1}{2}\{k^2 X B(z, \bar{z}_0) + \overline{X B(z, z_0)}\}$$
$$+ X C(\bar{z}, z_0)$$
$$+ 2\left(\frac{z\, z_0 - \bar{z}_0\, \bar{z}}{\bar{z}^2 - z_0^2}\right) + (z - \bar{z}) B(\bar{z}, z_0)$$

(2-35)

In the above,

$$X A(z, z_0) = -\log\left|-\frac{z\, z_0 - a^2 - I(z_0) I(z)}{z\, z_0 + a^2 - I(z_0) I(z)}\right|$$

(2-36)

$$X B(z, z_0) = \log\left|\frac{z\, z_0 - a^2 - I(z_0) I(z)}{z\, z_0 + a^2 - I(z_0) I(z)}\left[\frac{z + z_0}{z_0 - z}\right]^2\right|$$

(2-37)

$$X C(z, z_0) = \frac{\bar{z}_0 - z_0}{z^2 - z_0^2}\left(z - z_0\frac{I(z)}{I(z_0)}\right)$$

(2-38)

$$B(z, z_0) = \frac{1}{2}\left(\frac{-4\,z_0}{z^2 - z_0^2} + \frac{k\,z\,\bar{z}_0}{z^2 - z_0^2} + \frac{z - \bar{z}_0}{(z - z_0)^2} - \frac{z + \bar{z}_0}{(z + z_0)^2}\right)$$
$$+ \frac{z_0 - \bar{z}_0}{2\,I(z_0) I(z)}\left(\frac{a^2 - z\,\bar{z}_0}{(z_0 - z)^2} - \frac{a^2 - z\,\bar{z}_0}{(z_0 + z)^2}\right)$$
$$- \frac{z}{I(z)}\left(\frac{I(z_0)}{z_0^2 - z^2} - \frac{k\,I(\bar{z}_0)}{\bar{z}_0^2 - z^2}\right)$$

(2-39)

$$I(z) = (z^2 - a^2)^{1/2}$$

Thus, the displacement field in the metal sheet, due to crack-face pressure P_0, and due to adhesive shear stresses τ_x and τ_y, can be expressed as:

$$u_s = P_0 f_1(x,y) - \frac{1}{h_s}\int [H_{11}(x,y;\, x_0,y_0)\, \tau_x(x_0,y_0) + H_{12}(x,y;\, x_0,y_0)\, \tau_y(x_0,y_0)] dx_0\, dy_0$$

(2-40a)

and

$$v_s = P_0 f_2(x, y) - \frac{1}{h_s}\int [H_{21}(x,y;\, x_0,y_0)\, \tau_x(x_0,y_0) + H_{22}(x,y;\, x_0,y_0)\, \tau_y(x_0,y_0)] dx_0\, dy_0$$

(2-40b)

where H_{ij} can be defined from Eq. (2-13).

To enforce the compatibility and traction reciprocity conditions between the metal sheet and the composite patch, the Green's functions for a finite-sized orthotropic sheet subject to transverse shear stresses on its surface are developed next.

2.1.3 Green's Function for an Orthotropic Plate

The displacement field due to a symmetric group of point loads acting on a finite repair patch of composite material can be obtained by linear superposition of the two problems: The first for an infinite plate; and the second for a finite plate with residual tractions from the first

38

solution acting on the boundaries of the finite plate [Figure 2-5]. The Kolosov-Mushkelishvili functions for the first problem are derived to be [see Roderick [13] or Erdogan and Arin [11] for details]:

$$\Phi(z_1) = (c_{11}X + c_{12}Y) \log(z_1 - \xi_1)$$
(2-41)

$$X(z_2) = (c_{21}X + c_{22}Y) \log(z_2 - \xi_2)$$
(2-42)

where

$$z_k = x + s_k y \ ; \quad \xi_k = x_0 + s_k y_0 \ ; \quad (k = 1,2)$$

$$z = x + i y \ ; \quad z_0 = x_0 + i y_0$$

$$C_{11} = \frac{\frac{1}{2\pi i}\left(s_2 + \bar{s}_2 + \bar{s}_1 + \bar{s}_1 s_2 \bar{s}_2 \frac{v_x E_y}{E_x}\right)}{\left[(s_1 - s_2)(s_1 - \bar{s}_1)\left(1 - \frac{\bar{s}_2}{s_1}\right)\right]}$$

$$C_{12} = \frac{\frac{1}{2\pi i}(s_2 \bar{s}_2 + \bar{s}_1 s_2 + \bar{s}_1 \bar{s}_2 + v_x)}{\left[(s_1 - s_2)(s_1 - \bar{s}_1)\left(1 - \frac{\bar{s}_2}{s_1}\right)\right]}$$

$$C_{21} = \frac{\frac{1}{2\pi i}\left(s_1 + \bar{s}_1 + \bar{s}_2 + s_1 \bar{s}_1 \bar{s}_2 + \frac{v_x E_y}{E_x}\right)}{\left[(s_2 - s_1)(s_2 - \bar{s}_2)\left(1 - \frac{\bar{s}_1}{s_2}\right)\right]}$$

$$C_{22} = \frac{\frac{1}{2\pi i}(s_1 \bar{s}_1 + \bar{s}_2 s_1 + \bar{s}_2 \bar{s}_1 + v_x)}{\left[(s_2 - s_1)(s_2 - \bar{s}_2)\left(1 - \frac{\bar{s}_1}{s_2}\right)\right]}$$

and
(2-43)

In the above, s_1 and s_2 are the roots of:

$$s^4 + \left(\frac{E_x}{G_{xy}} - 2v_x\right)s^2 + \frac{E_x}{E_y} = 0$$
(2-44)

for which, $I_m(s_k) > 0 \ ; \ k = 1, 2.$

The stresses and displacements are expressed as:

$$\sigma_{px} = 2 Re\left[s_1^2 \phi_2'(z_1) + s_2^2 X_2'(z_2)\right]$$

$$\sigma_{py} = 2 Re\left[\phi_2'(z_1) + X_2'(z_2)\right]$$

$$\tau_{pxy} = -2 Re\left[s_1 \phi_2'(z_1) + s_2 X_2'(z_2)\right]$$
(2-45)

$$u_2(z_1 z_0) = 2 Re\left[p_1 \phi_2(z_1) + p_2 X_2(z_2)\right]$$

and
$$v_2(z_1 z_0) = 2 Re\left[q_1 \phi_2(z_1) + q_2 X_2(z_2)\right]$$
(2-46)

where,

$$p_k = \frac{1}{E_x}\left(s_k^2 - v_x\right)$$

and

$$q_k = \frac{1}{s_k E_y}\left(1 - v_y s_k^2\right) \qquad k = 1, 2$$

(2-47)

Now we consider the second problem, viz., that of a finite patch, with residual tractions at its boundary [Figure 2-5]. Here, $-p(x)$ and $-q(x)$ are the normal and shear stresses acting on the $y=H$ plane. Then, $u(x, y)$ and $v(x, y)$ become odd and even functions respectively, with respect to x. Thus, the displacements u and v can be written as:

$$u(x, y) = \frac{2}{\pi}\int_0^\infty \phi(\alpha, y) \sin \alpha x \; d\alpha$$

$$v(x, y) = \frac{2}{\pi}\int_0^\infty \psi(\alpha, y) \cos \alpha x \; d\alpha$$

(2-48)

The equilibrium equations for the composite patch [Figure 2-5c] are written, in terms of displacements, as:

$$\left(\frac{v_x E_y}{1 - v_x v_y}\right)\frac{\partial^2 u}{\partial x \partial y} + \left(\frac{E_y}{1 - v_x v_y}\right)\frac{\partial^2 v}{\partial y^2} + (G_{xy})\left(\frac{\partial^2 u}{\partial x \partial y} + \frac{\partial^2 v}{\partial x^2}\right) = 0$$

and

$$\left(\frac{E_y}{1 - v_x v_y}\right)\frac{\partial^2 v}{\partial y^2} + \left(\frac{v_x E_y}{1 - v_x v_y}\right)\frac{\partial^2 u}{\partial x \partial y} + (G_{xy})\left(\frac{\partial^2 v}{\partial x^2}\right) = 0$$

(2-49)

Substituting Eqs. (2-48) in Eq. (2-49), we obtain the following ordinary differential equations for ϕ and ψ:

$$\frac{d^4\phi}{dy^4} + \alpha^2\left(\frac{-E_x}{G_{xy}} + 2v_x\right)\frac{d^2\phi}{dy^2} + \alpha^4\frac{E_x}{E_y} = 0$$

and

$$\frac{d^4\psi}{dy^4} + \alpha^2\left(\frac{-E_x}{G_{xy}} + 2v_x\right)\frac{d^2\psi}{dy^2} + \alpha^4\frac{E_x}{E_y} = 0$$

(2-50)

The general solutions of these 4th order differential equations are [Itou [14]]:

$$\phi = e_1 A_1 \cos h\beta_1 y + e_2 A_2 \cos h\beta_2 y + e_1 A_3 \sin h\beta_1 y + e_2 A_4 \sin h\beta_2 y$$

and

$$\psi = A_1 \sin h\beta_1 y + A_2 \sin h\beta_2 y + A_3 \cos h\beta_1 y + A_4 \cos h\beta_2 y$$

40

where,

$$e_k = \frac{\alpha \beta_k [v_x E_y + G_{xy}(1 - v_x v_y)]}{G_{xy}\beta_k^2(1 - v_x v_y) - \alpha^2 E_x} \; ; k = 1, 2 \tag{2-51}$$

and, β_1 and β_2 are the roots of:

$$\beta^4 - \alpha^2 \left(\frac{E_x}{G_{xy}} - 2 v_x\right)\beta^2 + \alpha^4 \frac{E_x}{E_y} = 0, \tag{2-52}$$

for which, $Re(\beta_k) > 0 \quad k = 1, 2$.

Considering the symmetry conditions,

$$u(x, y) = u(x_1 - y)$$

and $$v(x, y) = -v(x_1 - y),$$

we see that the constants A_3 and A_4 must be zero in Eq. (2-51). Using Eq. (2-51) in Eq. (2-48), we obtain:

$$u_p(x, y) = \frac{2}{\pi}\int_0^\infty \left(e_1 A_1 \cos h \, \beta_1 y + e_2 A_2 \cos h \, \beta_2 y\right) \sin \alpha x \, d\alpha$$

$$v_p(x, y) = \frac{2}{\pi}\int_0^\infty \left(A_1 \sin h \, \beta_1 y + A_2 \sin h \, \beta_2 y\right) \cos \alpha x \, d\alpha$$

and

Also, $$\tag{2-53}$$

$$\sigma_{px} = \frac{2}{\pi}\int_0^\infty \left[\left(\alpha M_1 e_1 + M_2 \beta_1\right)A_1 \cosh\beta_1 y + \left(\alpha M_1 e_2 + M_2 \beta_2\right)A_2 \cosh\beta_2 y\right] \cos \alpha x \, d\alpha$$

$$\sigma_{py} = \frac{2}{\pi}\int_0^\infty \left[\left(\alpha M_2 e_1 + M_3 \beta_1\right)A_1 \cosh\beta_1 y + \left(\alpha M_2 e_2 + M_2 \beta_2\right)A_2 \cosh\beta_2 y\right] \cos \alpha x \, d\alpha$$

and

$$\alpha_{pxy} = \frac{2}{\pi}\int_0^\infty \left[G_{12}\left(e_1 \beta_1 - \alpha\right)A_1 \sinh \, \beta_1 y + G_{12}\left(e_2 \beta_2 - \alpha\right)A_2 \sinh \, \beta_2 y\right] \sin \alpha x \, d\alpha$$

$$\tag{2-54}$$

where, $$M_1 = \frac{E_x}{1 - v_x v_y} \; ; \quad M_2 = \frac{v_y E_x}{1 - v_x v_y} = \frac{v_x E_y}{1 - v_x v_y} \quad \text{and} \quad M_3 = \frac{E_y}{1 - v_x v_y}.$$

We define $P(\alpha)$ and $Q(\alpha)$ as follows:

$$P(\alpha) = \int_0^\infty P(x) \cos \alpha x \, dx$$

$$Q(\alpha) = \int_0^\infty q(x) \sin \alpha x \, dx$$

and
<div align="right">(2-55)</div>

$$p(x) = \frac{1}{2\pi} \int_0^\infty P(\alpha) \cos \alpha x \, d\alpha$$

or

$$q(x) = \frac{1}{2\pi} \int_0^\infty Q(\alpha) \sin \alpha x \, d\alpha$$

and

In order to satisfy the boundary conditions for the finite composite patch, the following equations must be satisfied:

$$\left(\alpha M_2 e_1 + M_3 \beta_1\right)\left(\cosh \beta_1 H\right) A_1 + \left(\alpha M_2 e_2 + M_3 \beta_2\right)\left(\cosh \beta_2 H\right) A_2 = P(\alpha)$$

and
$$G_{12}\left(e_1\beta_2 - \alpha\right)\left(\sinh \beta_1 H\right)A_1 + G_{12}\left(e_2\beta_2 - \alpha\right)\left(\sinh \beta_2 H\right)A_2 = Q(\alpha) \qquad (2\text{-}56)$$

From Eq. (2-56), we can obtain A_1 and A_2 as functions of α. Then, by substituting A_1 and A_2 into Eqs. (2-53) and (2-54), we may evaluate the stresses and displacements.

Using Eqs. (2-41), (2-42) and (2-45), $p(x)$ and $q(x)$ are expressed as:

$$p(x) = -2 \, Re \, \frac{(C_{11}X + C_{12}Y)(x - x_0 + \eta(H - y_0))}{\left\{x - x_0 + \eta(H - y_0)^2 + \rho^2(H - y_0)^2\right\}} - \frac{(C_{11}X + C_{12}Y)\,\rho(H - y_0)i}{\left\{((x - x_0) + \eta(H - y_0)^2 + \rho^2(H - y_0)^2\right\}}$$

$$+ \frac{(C_{21}X + C_{22}Y)(x - x_0 + \nu(H - y_0))}{\left\{(x - x_0 + \nu(H - y_0))^2 + \delta^2(H - y_0)^2\right\}} - \frac{(C_{21}X + C_{22}Y)\,\delta(H - y_0)i}{\left\{((x - x_0) + \nu(H - y_0))^2 + \delta^2(H - y_0)^2\right\}} \qquad (2\text{-}57)$$

and

$$q(x) = 2 \, Re \, \frac{(C_{11}X + C_{12}Y)S_1(x - x_0 + \eta(H - y_0))}{\left\{(x - x_0 + \eta(H - y_0))^2 + \rho^2(H - y_0)^2\right\}} - \frac{(C_{11}X + C_{12}Y)S_1\,\rho(H - y_0)i}{\left\{((x - x_0) + \eta(H - y_0))^2 + \rho^2(H - y_0)^2\right\}}$$

$$+ \frac{(C_{21}X + C_{22}Y)S_2(x - x_0 + \nu(H - y_0))}{\left\{(x - x_0 + \nu(H - y_0))^2 + \delta^2(H - y_0)^2\right\}} - \frac{(C_{21}X + C_{22}Y)S_2\,\delta(H - y_0)i}{\left\{((x - x_0) + \nu(H - y_0))^2 + \delta^2(H - y_0)^2\right\}} \qquad (2\text{-}58)$$

where, $\qquad S_1 = \eta + i\rho \; ; \quad S_2 = \nu + i\delta \;$ and $\; i = \sqrt{-1}.$

Since $p(x) = p(-x)$ and $q(x) = -q(-x)$, we may write:

$$p(x) = \frac{1}{2}\left[p(x) + p(-x)\right] \quad \text{and} \quad q(x) = \frac{1}{2}\left[q(x) - q(-x)\right] \qquad (2\text{-}59)$$

Using Eq. (2-59) and the following identities:

$$\int_0^\infty \left[\frac{\beta}{\beta^2 + (a-x)^2} + \frac{\beta}{\beta^2 + (a+x)^2} \right] \cos \alpha x \, dx = \pi \cos(a\alpha) e^{-\beta\alpha} \quad ; \quad |Im \, \alpha| < Re \, \beta$$

$$\int_0^\infty \left[\frac{a+x}{\beta^2 + (a+x)^2} + \frac{a-x}{\beta^2 + (a-x)^2} \right] \cos \alpha x \, dx = \pi \sin(a\alpha) e^{-\beta\alpha} \quad ; \quad |Im \, \alpha| < Re \, \beta;$$

$$\int_0^\infty \left[\frac{\beta}{\beta^2 + (a-x)^2} - \frac{\beta}{\beta^2 + (a+x)^2} \right] \sin \alpha x \, dx = \pi \sin(a\alpha) e^{-\beta\alpha} \quad ; \quad Re \, \beta > 0 ; \quad \text{and}$$

$$\int_0^\infty \left[\frac{a+x}{\beta^2 + (a+x)^2} - \frac{a-x}{\beta^2 + (a-x)^2} \right] \sin \alpha x \, dx = \pi \cos(a\alpha) e^{-\beta\alpha} \quad ; \quad Re \, \beta > 0 ;$$

$$(2-60)$$

We may express $P(\alpha)$ and $Q(\alpha)$ as:

$$P(\alpha) = P_1(\alpha ; x_0, y_0, X, Y) + P_1(\alpha ; -x_0, y_0, -X, Y)$$
$$+ P_1(\alpha ; x_0, -y_0, X, -Y) + P_1(\alpha ; -x_0, -y_0, -X, -Y)$$

and
$$Q(\alpha) = Q_1(\alpha ; x_0, y_0, X, Y) + Q_1(\alpha ; -x_0, y_0, -X, Y)$$
$$+ Q_1(\alpha ; x_0, -y_0, X, -Y) + Q_1(\alpha ; -x_0, -y_0, -X, -Y)$$

$$(2-61)$$

Here,

$$P_1(\alpha ; x_0, y_0, X, Y) = -\pi \, Im \left\{ (C_{11}X + C_{12}Y) \exp[-\rho(H-y_0)\alpha + i\{\eta(H-y_0) - x_0\} \alpha] \right.$$
$$\left. + (C_{21}X + C_{22}Y) \exp[-\delta(H-y_0)\alpha + i\{v(H-y_0) - x_0\} \alpha] \right\}$$

$$Q_1(\alpha ; x_0, y_0, X, Y) = \pi \, Re \left\{ (C_{11}X + C_{12}Y) \exp[-\rho(H-y_0)\alpha + i\{\eta(H-y_0) - x_0\} \alpha] \right.$$
$$\left. + (C_{21}X + C_{22}Y) \exp[-\delta(H-y_0)\alpha + i\{v(H-y_0) - x_0\} \alpha] \right\}$$

The displacements due to the adhesive shear stresses τ_x and τ_y can be expressed as:

$$u_p = \frac{1}{h_p} \int_D [K_{11}(x, y; x_0, y_0) \, \tau_x(x_0, y_0) + K_{12}(x, y; x_0, y_0) \, \tau_y(x_0, y_0)] dx_0 \, dy_0$$

$$v_p = \frac{1}{h_p} \int_D [K_{21}(x, y; x_0, y_0) \, \tau_x(x_0, y_0) + K_{22}(x, y; x_0, y_0) \, \tau_y(x_0, y_0)] \, dx_0 \, dy_0$$

$$(2-62)$$

Here, K_{ij} $(i, j = 1, 2)$ can be evaluated from Eqs. (2-46) and (2-53) by numerical integration.

Substituting the expressions for the sheet displacements [(u_s and v_s) of Eq. (2-40), and the patch displacements (u_p and v_p) of Eq. (2-62)] into the compatibility conditions:

$$\tau_x = \frac{u_s - u_p}{R} \quad ; \quad \text{and} \quad \tau_y = \frac{v_s - v_p}{R} \tag{2-63}$$

where R is the adhesive flexibility, one obtains the following integral equations:

$$R\,\tau_x\,(x, y) + \int_D [k_{11}(x, y; x_0, y_0)\,\tau_x(x_0, y_0) + k_{12}(x, y; x_0, y_0)\,\tau_y(x_0, y_0)]dx_0dy_0 = p_0 f_1(x, y) \tag{2-64}$$

$$R\,\tau_y\,(x, y) + \int_D [k_{21}(x, y; x_0, y_0)\,\tau_x(x_0, y_0) + k_{22}(x, y; x_0, y_0)\,\tau_y(x_0, y_0)]dx_0dy_0 = p_0 f_2(x, y) \tag{2-65}$$

where,

$$k_{11} = \frac{H_{11}}{h_1} + \frac{K_{11}}{h_2}$$

$$k_{12} = \frac{H_{12}}{h_1} + \frac{K_{12}}{h_2}$$

$$k_{21} = \frac{H_{21}}{h_1} + \frac{K_{21}}{h_2}$$

and

$$k_{22} = \frac{H_{22}}{h_1} + \frac{K_{22}}{h_2} \tag{2-66}$$

once τ_x and τ_y are obtained from the solution of the integral equations (2-64) and (2-65), the stress intensity factor can be calculated from the following equation:

$$K_I = p_0 \sqrt{\pi a} + \frac{1}{h_s} \int_D [K_1(x_0, y_0)\,\tau_x(x_0, y_0) + K_2(x_0, y_0)\,\tau_y(x_0, y_0)]dx_0dy_0 \tag{2-67}$$

where K_1 (x_0, y_0) and K_2(x_0, y_0) are the stress intensity factors due the concentrated body forces X and Y respectively.

2.1.4 Analytical Formulation

By using the Buckingham's Π theorem for non-dimensional variables, it is easily shown that the normalized stress-intensity factor for the patched crack is a function of several non-dimensional parameters as shown below:

$$K_I^* = \frac{K_I}{(\sigma_0\sqrt{\pi a})} = K_I^* \left[\left(\frac{G_s}{h_s}R\right) ; \left(\frac{a}{h_s}\right) ; \left(\frac{h_p E_y}{h_s G_s}\right) ; \nu_s ; \left(\frac{E_y}{E_x}\right) ; \left(\frac{E_x}{G_{xy}}\right) ; \nu_x ; \nu_y ; \frac{H}{a} \right] \tag{2-68}$$

44

where

G_s = shear modulus of sheet

h_s = thickness of sheet

R = $\left(\dfrac{h_a}{G_a}\right) + \left(\dfrac{3h_s}{8G_s}\right) + \left(\dfrac{3h_p}{8G_p}\right)$

= adhesive flexibility parameter

h_a = thickness of adhesive

G_a = shear modulus of adhesive

a = crack length

h_p = thickness of patch

E_y = modulus of patch in the direction normal to the crack

E_x = modulus of patch in the direction parallel to the crack line

v_s = Poisson's ratio of sheet

G_{xy} = shear modulus of patch

H = height of patch normal to the crack

Thus, there are eight non-dimensional parameters that are identified. Out of these eight parameters, the effects of v_y; (E_y/E_x) ; and (E_x/G_{xy}) are very small, as shown in Figures 2-6 and 2-7. Thus, we may reduce the effective number of design parameters to five.

For given values of adhesive flexibility parameter, $(G_s R / h_s)$, and the patch stiffness parameter, $(h_p E_y / h_s G_s)$, the variation of the normalized stress-intensity factor at the *patched* crack-tip, as a function of the normalized crack length, (a / h_s), is shown in Figure 2-8a. This figure shows that for longer crack lengths, the stress intensity factor for a patched crack is substantially lower than that for the unpatched crack. Also these results reveal that for a patched crack, the actual stress-intensity factor at the patched crack-tip becomes a constant as the crack-length increases. Figure 2-8b shows the variation of the actual k-factor as the crack grows, with and without the presence of a composite patch. It is seen that without the patch, the k-factor increases as expected, but in the presence of a patch, the k-factor levels off to a constant value as the crack grows.

For given values of patch stiffness parameter $(h_p E_y / h_s G_s)$, and the crack length (a / h_s), the variation of the normalized stress-intensity factor at the patched crack-tip, as a function of the adhesive flexibility parameter, $(G_s R / h_s)$ is shown in Figure 2-9. This figure shows that for lower values of $(G_s R / h_s)$, the stress-intensity factor is substantially lowered, while it reaches a constant value as $(G_s R / h_s)$ increases. This figure thus provides guidelines in selecting the adhesive, so as to reduce the stress-intensity at the patched-crack-tip.

For given values of $(G_s R / h_s)$ and (a / h_s), the variations of the stress-intensity factor at the patched crack-tip, as functions of the patch stiffness parameter $(h_p E_y / h_s G_s)$, are shown in

Figure 2-10. This figure shows that as the modulus E_y of the patch, in the direction normal to the crack, increases the normalized stress-intensity factor at the tip of the patched crack decreases. This figure reveals thus, that the use of boron/epoxy patches on aluminum sheets is an excellent choice. The five design parameters, that are germane to the problem of composite repair of cracks in metallic sheets, have been identified to be:

$$\left(\frac{G_s R}{h_s}\right); \quad \left(\frac{a}{h_s}\right); \quad \left(\frac{h_p E_y}{h_s G_s}\right); \quad \left(\frac{H}{a}\right); \quad v_x$$
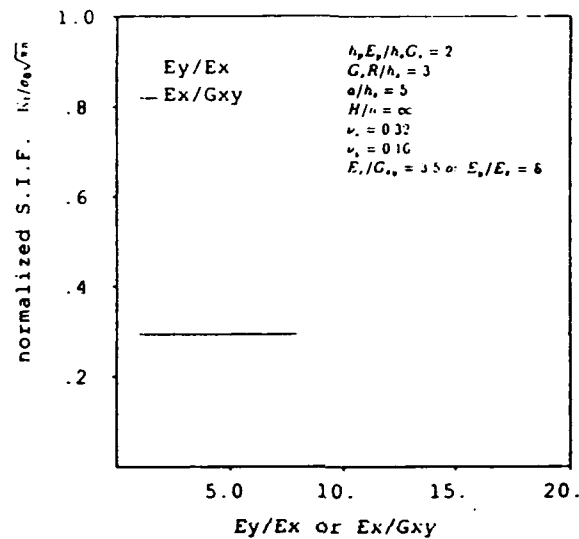
FIGURE 2-6. NORMALIZED S.I.F. FOR REPAIRED CRACK OF A GIVEN LENGTH AS A
FUNCTION OF (E_y/E_x) THE PATCH
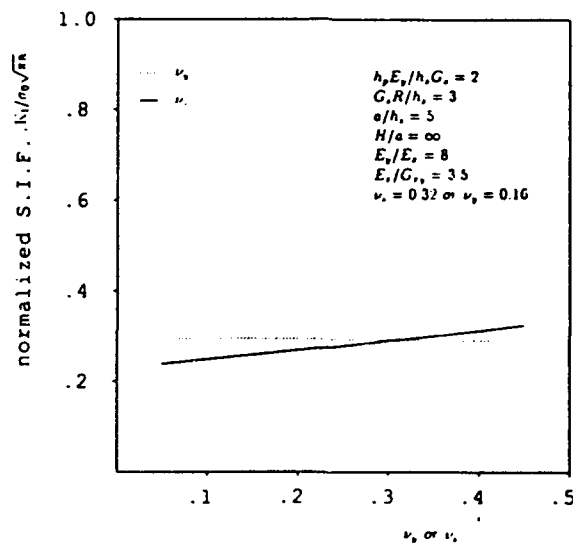
FIGURE 2-7. NORMALIZED S.I.F. FOR A REPAIRED CRACK OF A GIVEN LENGTH AS A
FUNCTION OF v_p THE PATCH

46
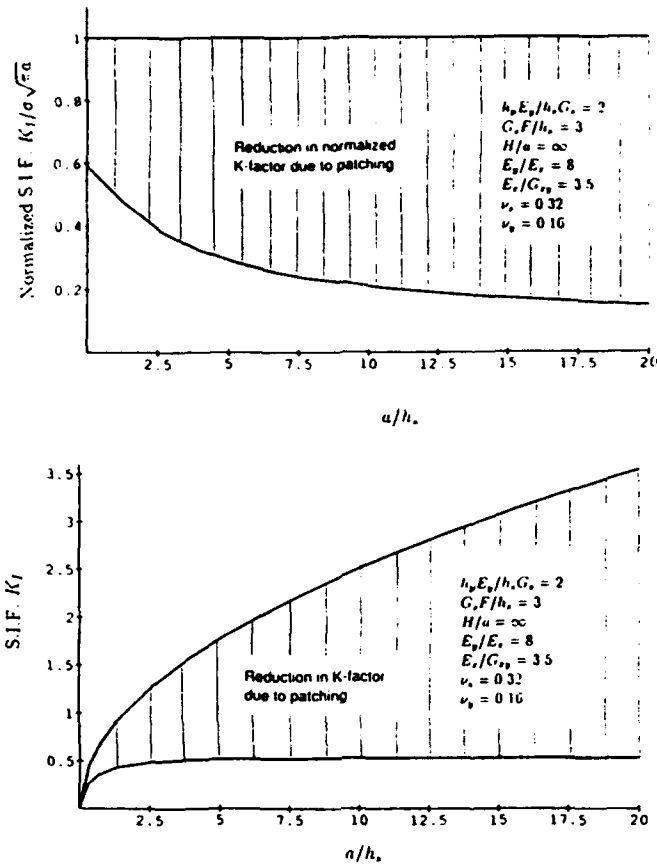
FIGURE 2-8. REDUCTION IN: (a) NORMALIZED S.I.F. DUE TO PATCHING AS A FUNCTION OF
THE CRACK LENGTH; (b) THE ACTUAL S.I.F. (FOR $\sigma_0=1$) DUE TO PATCHING AS A FUNCTION
OF THE CRACK LENGTH
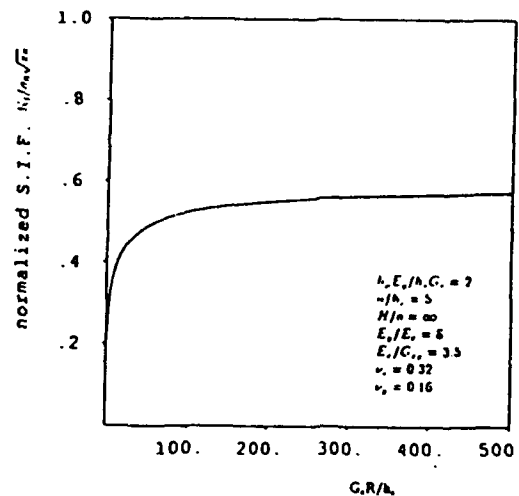
FIGURE 2-9. NORMALIZED S.I.F. FOR A GIVEN CRACK LENGTH AS A FUNCTION OF
ADHESIVE FLEXIBILITY

47
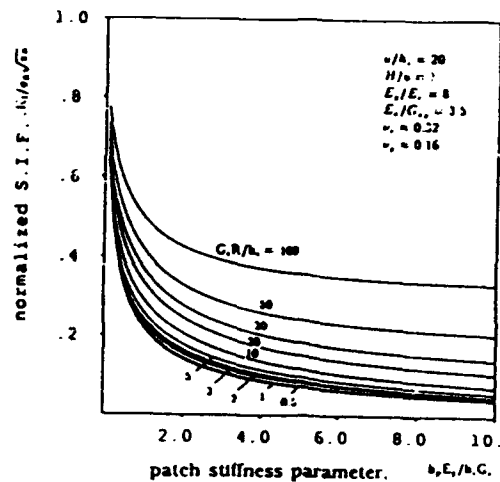
FIGURE 2-10. NORMALIZED S.I.F. FOR CRACK LENGTH AS A FUNCTION OF PATCH
STIFFNESS AND ADHESIVE FLEXIBILITY

The variation of the stress-intensity factor, stresses in the patch, and stresses in the
adhesive at the tip of repaired crack, as a function of the above five parameters has been
computed, and an ensemble of design charts have been prepared. These are shown in   Figures
2-11 to 2-25.
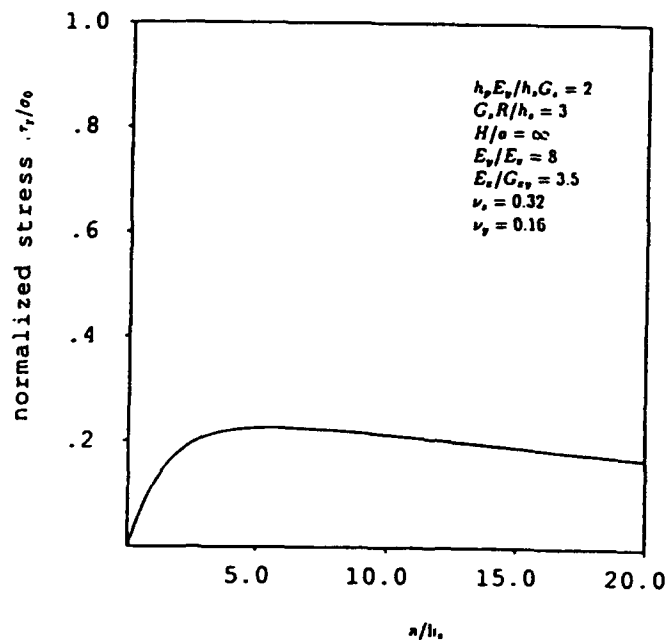
FIGURE 2-11. ADHESIVE SHEAR STRESS AT x=0, y=0 AS A FUNCTION OF THE CRACK
LENGTH
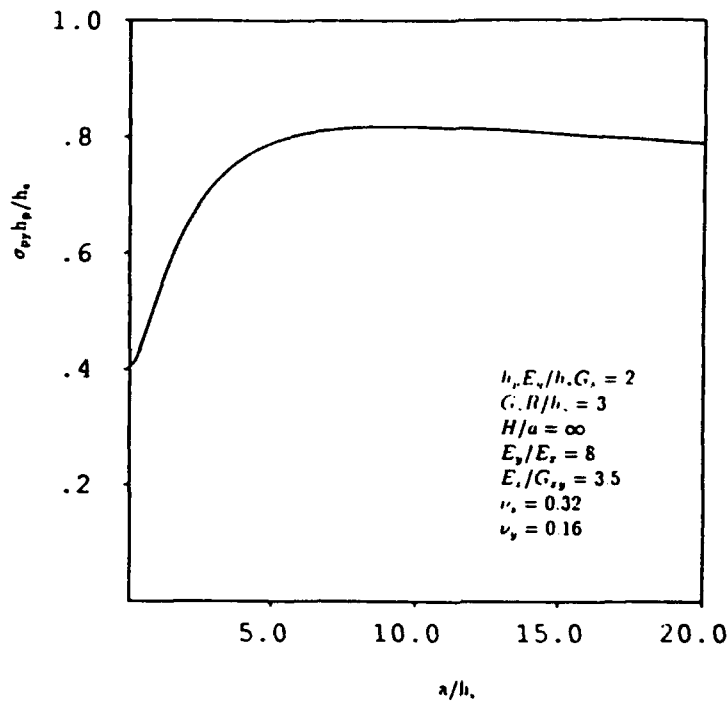
FIGURE 2-12. PATCH STRESS σ_{yy}^p (x=0,y=0) AS A FUNCTION OF THE CRACK LENGTH
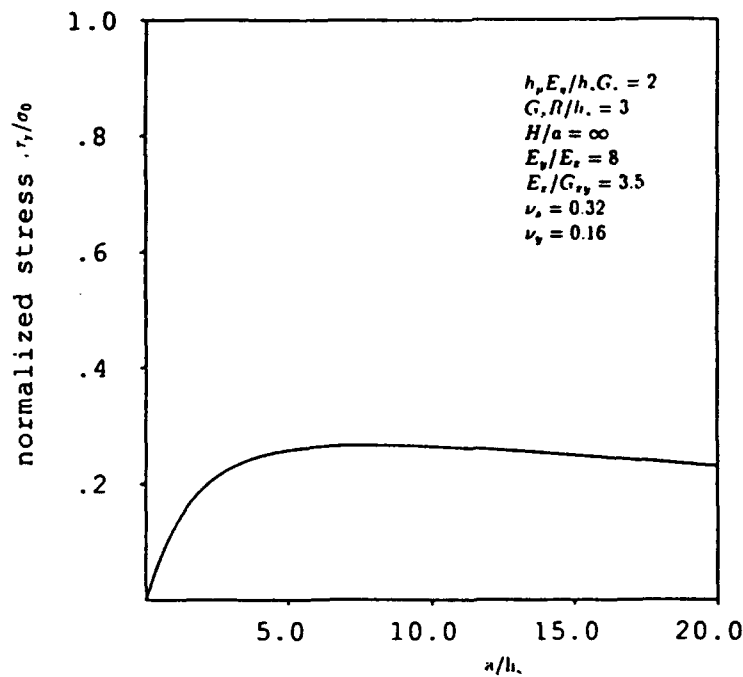
FIGURE 2-13. ADHESIVE SHEAR STRESS AT x=0, y=0, AS A FUNCTION OF THE CRACK
LENGTH
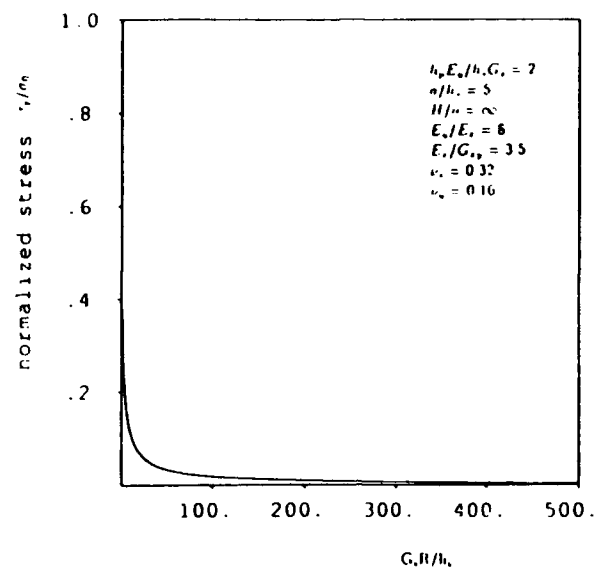
FIGURE 2-14. ADHESIVE SHEAR STRESS AT x=0, y=0 AS A FUNCTION OF ADHESIVE FLEXIBILITY
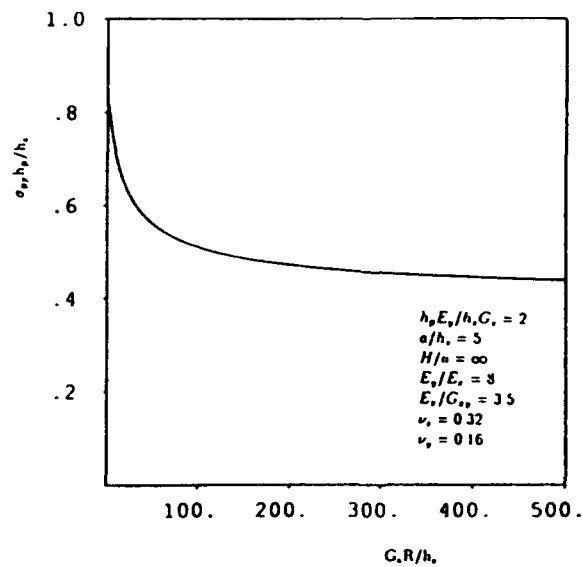
FIGURE 2-15. PATCH STRESS AT x=0, y=0 AS A FUNCTION OF ADHESIVE FLEXIBILITY
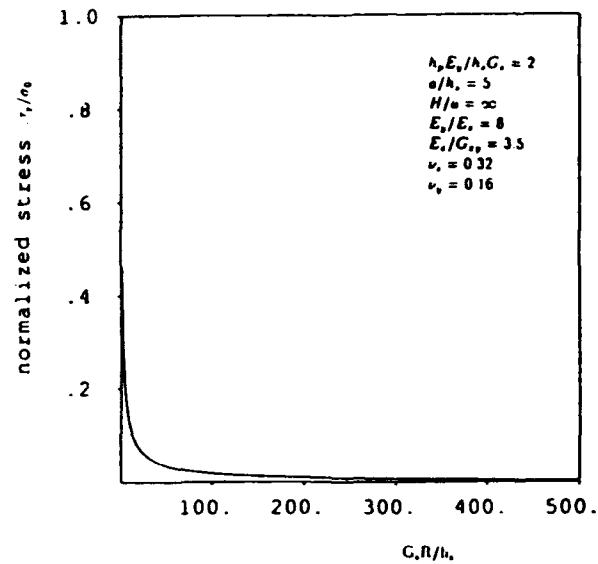
FIGURE 2-16. ADHESIVE SHEAR STRESS AT x=0, y=0 AS A FUNCTION OF ADHESIVE
FLEXIBILITY
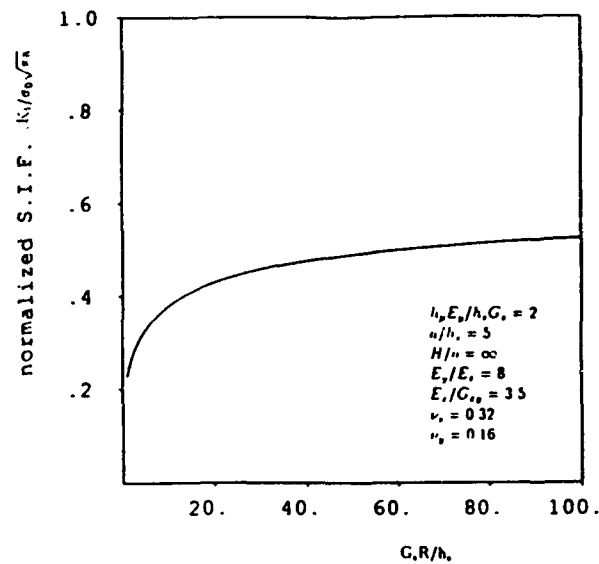
FIGURE 2-17. NORMALIZED S.I.F. FOR A GIVEN CRACK LENGTH AS A FUNCTION OF
ADHESIVE FLEXIBILITY

51
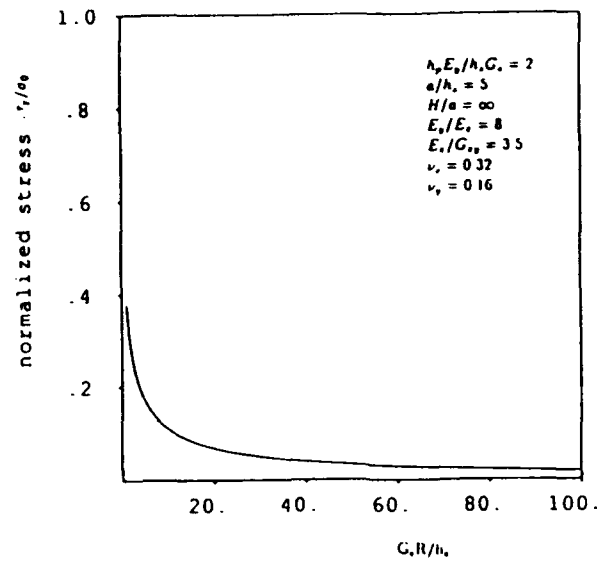
FIGURE 2-18. ADHESIVE SHEAR STRESS AT x=0, y=0 AS A FUNCTION OF ADHESIVE
FLEXIBILITY
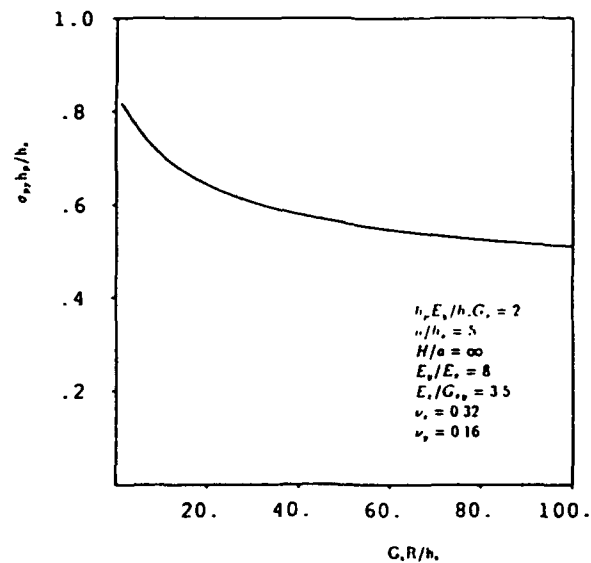
FIGURE 2-19. PATCH TENSILE STRESS AT x=0, y=0 AS A FUNCTION OF ADHESIVE
FLEXIBILITY

52
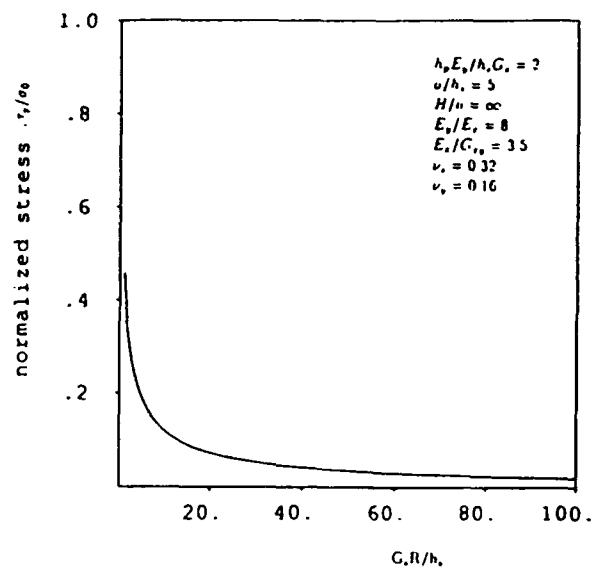
FIGURE 2-20. ADHESIVE SHEAR STRESS AS A FUNCTION OF ADHESIVE FLEXIBILITY
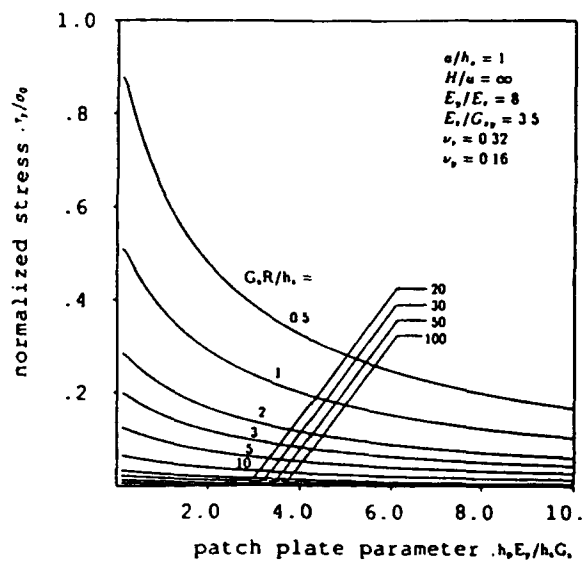
FIGURE 2-21. ADHESIVE SHEAR STRESS AT x=0, y=0 AS A FUNCTION OF PATCH
STIFFNESS AND ADHESIVE FLEXIBILITY

53
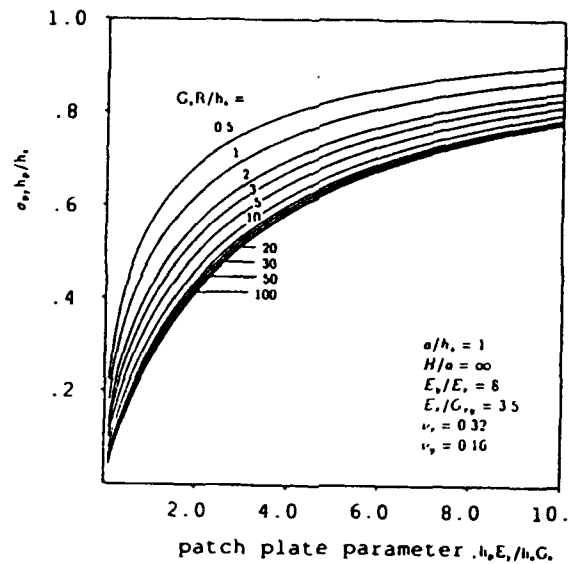
FIGURE 2-22. PATCH STRESS σ^p_{yy} AS A FUNCTION OF PATCH-STIFFNESS AND ADHESIVE FLEXIBILITY
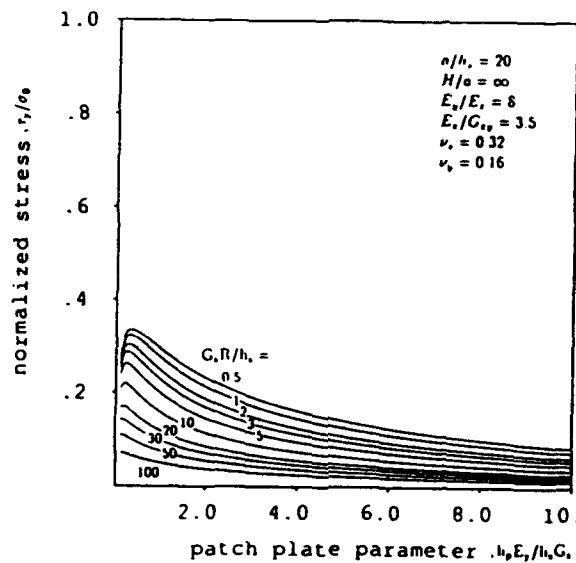
FIGURE 2-23. ADHESIVE SHEAR STRESS x=0, y=0 AS A FUNCTION OF PATCH STIFFNESS AND ADHESIVE FLEXIBILITY

54
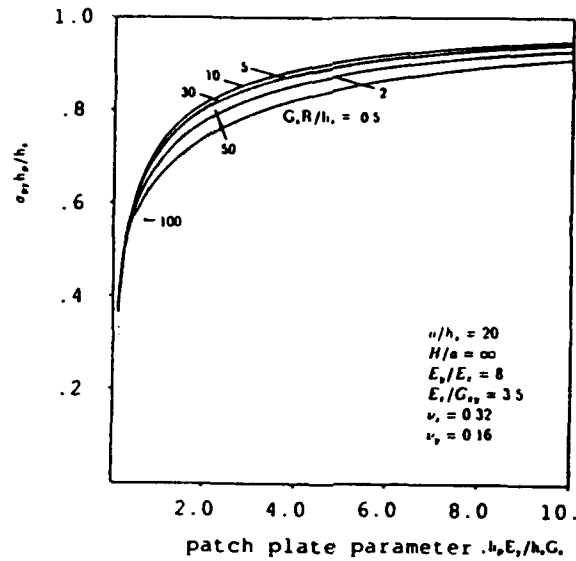
FIGURE 2-24. PATCH TENSILE STRESS AS A FUNCTION OF ADHESIVE FLEXIBILITY AND
PATCH STIFFNESS
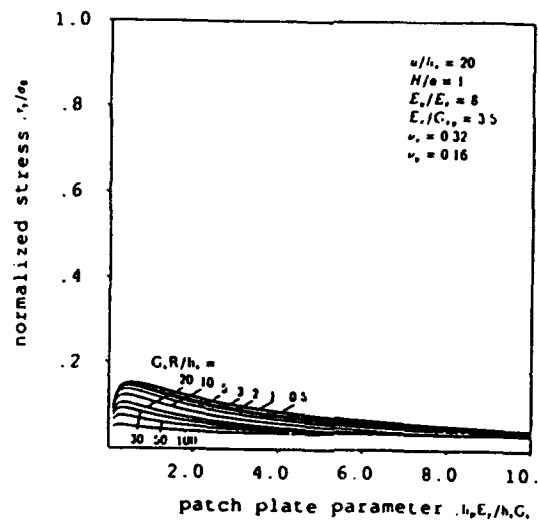
FIGURE 2-25. ADHESIVE SHEAR STRESS x=0, y=0 AS A FUNCTION OF PATCH STIFFNESS
AND ADHESIVE FLEXIBILITY

55

Further results for the variation of the stresses in the patch: adhesive shear stresses, and the stress-intensity factors at the crack-tip as functions of the above parameters have been developed. These are shown in Figures 2-26 to 2-42 in this report.
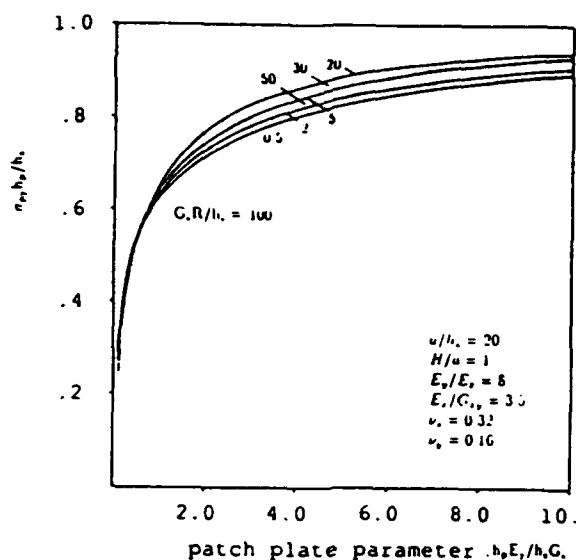
FIGURE 2-26. PATCH STRESS AS A FUNCTION OF ADHESIVE FLEXIBILITY AND PATCH STIFFNESS
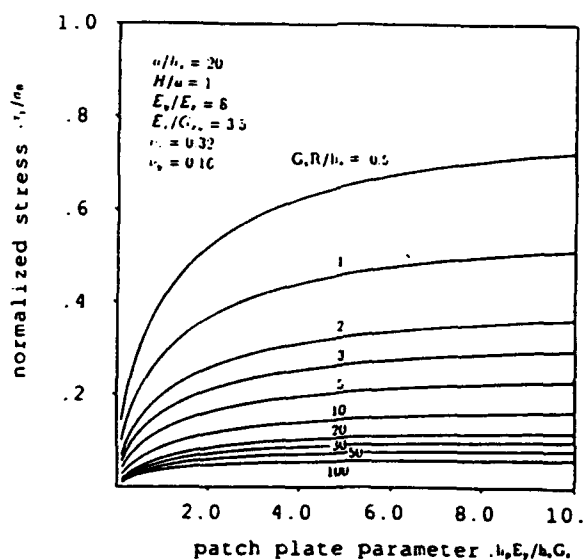
FIGURE 2-27. ADHESIVE SHEAR STRESS x=0, y=H AS A FUNCTION OF PATCH STIFFNESS AND ADHESIVE FLEXIBILITY

56
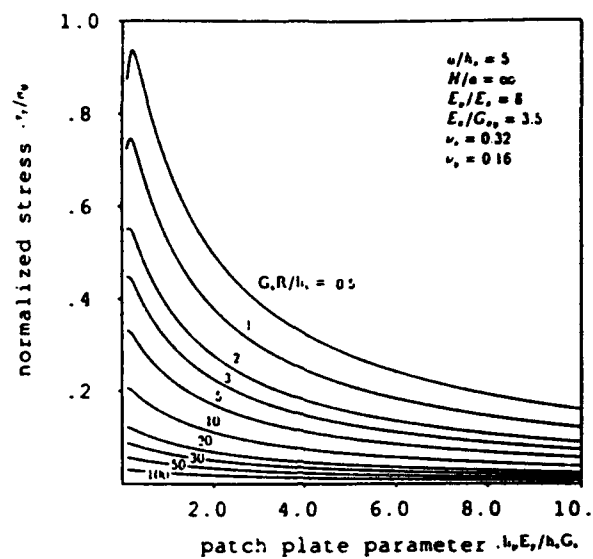
FIGURE 2-28. ADHESIVE SHEAR STRESS x=0, y=0 AS A FUNCTION OF PATCH STIFFNESS
AND ADHESIVE FLEXIBILITY
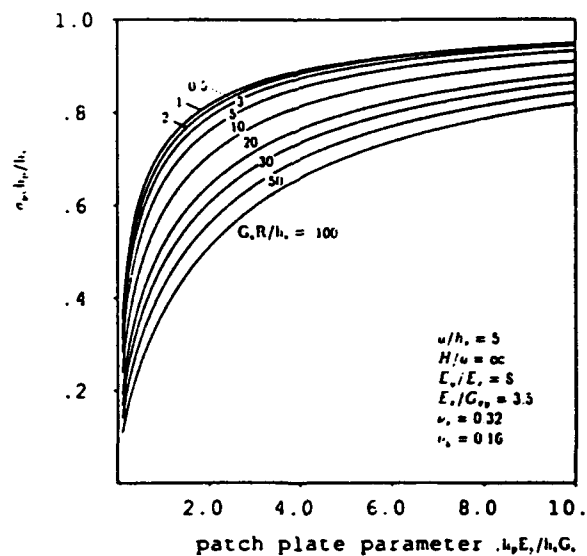
FIGURE 2-29. PATCH TENSILE STRESS AS A FUNCTION OF PATCH STIFFNESS AND
ADHESIVE FLEXIBILITY

57
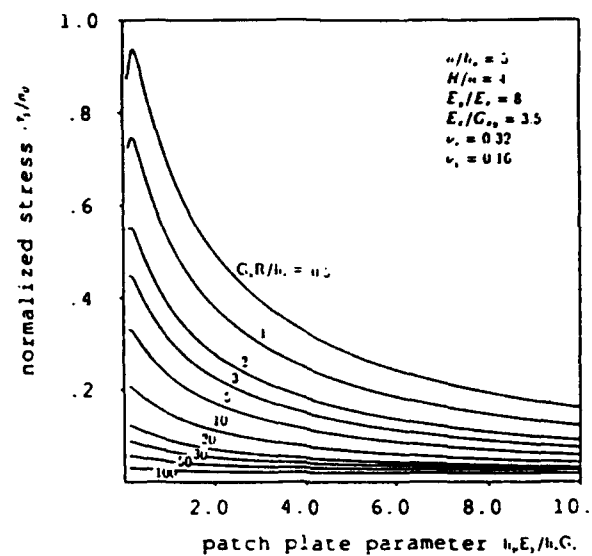
FIGURE 2-30. ADHESIVE SHEAR STRESS x=0, y=0 AS A FUNCTION OF PATCH STIFFNESS
AND ADHESIVE FLEXIBILITY
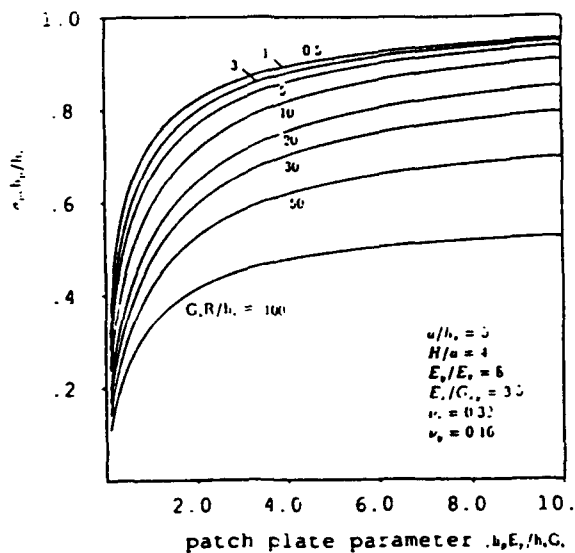
FIGURE 2-31. PATCH TENSILE STRESS AS A FUNCTION OF PATCH STIFFNESS AND
ADHESIVE FLEXIBILITY
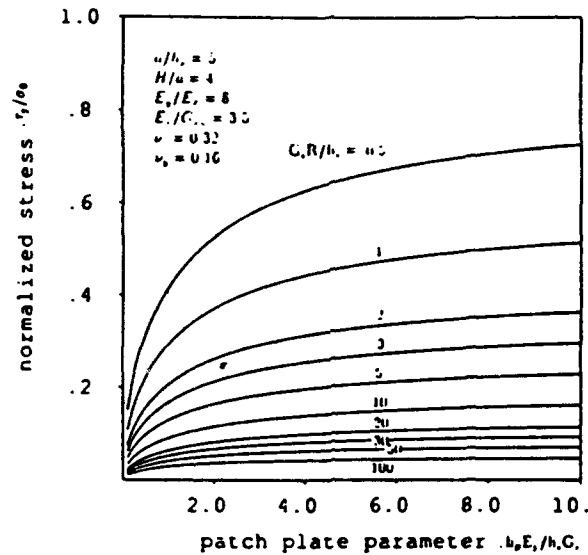
FIGURE 2-32. ADHESIVE SHEAR STRESS x=0, y=H AS A FUNCTION OF ADHESIVE
FLEXIBILITY AND PATCH STIFFNESS
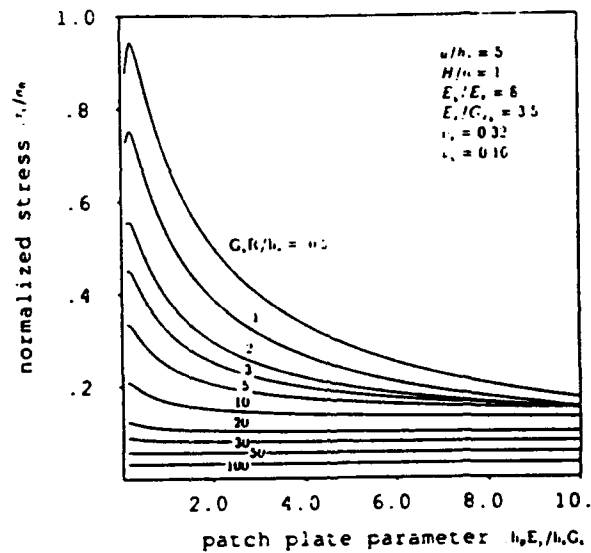
FIGURE 2-33. ADHESIVE SHEAR AT x=0, y=0 AS A FUNCTION OF ADHESIVE FLEXIBILITY
AND PATCH STIFFNESS
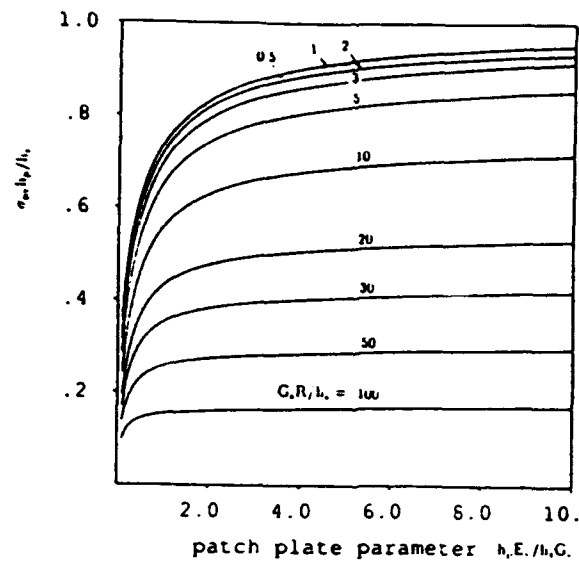
FIGURE 2-34. PATCH STRESS AS A FUNCTION OF PATCH STIFFNESS AND ADHESIVE
FLEXIBILITY
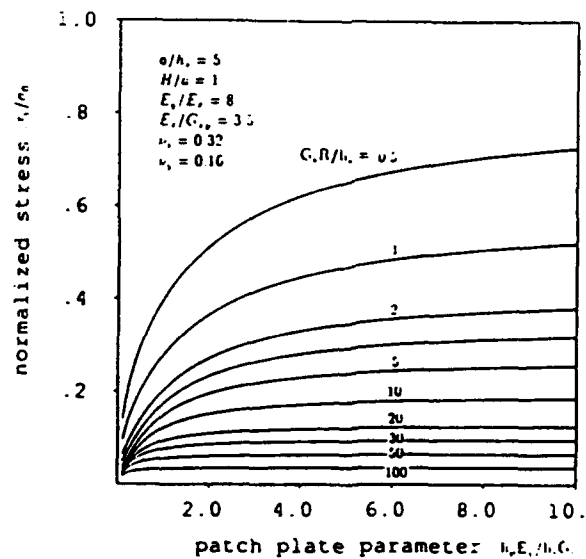
FIGURE 2-35. ADHESIVE SHEAR x=0, y=H AS A FUNCTION OF PATCH STIFFNESS AND
ADHESIVE FLEXIBILITY

60
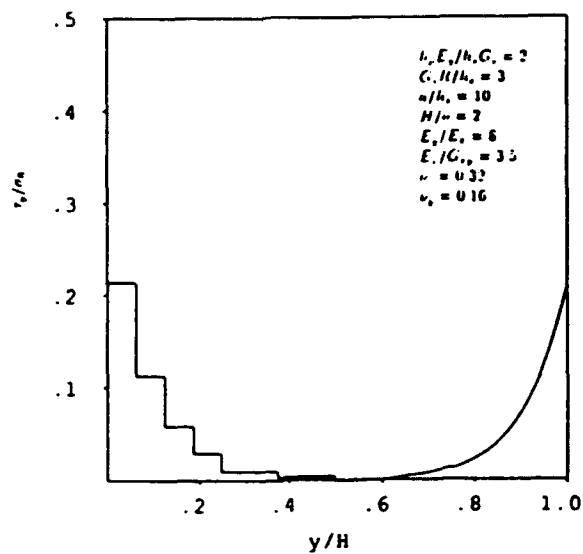
FIGURE 2-36. VARIATION OF ADHESIVE SHEAR STRESS ALONG THE HEIGHT OF THE
PATCH
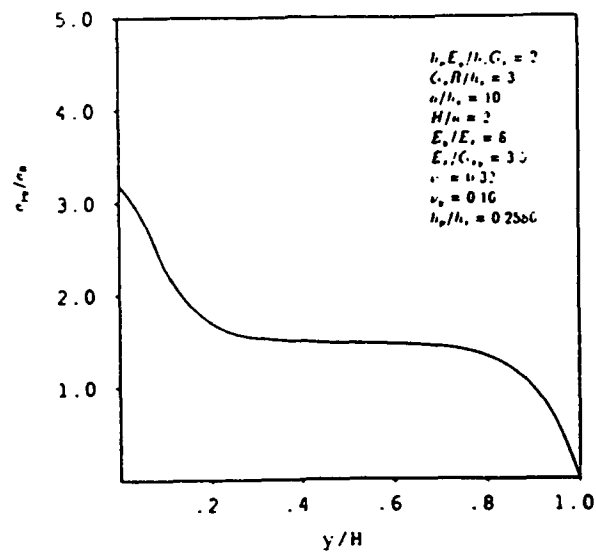
FIGURE 2-37. VARIATION OF PATCH TENSILE STRESS ALONG THE HEIGHT OF THE PATCH

61
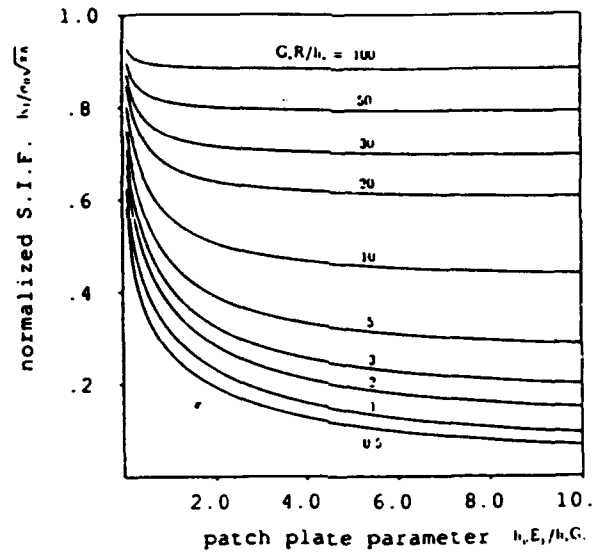
FIGURE 2-38. NORMALIZED S.I.F. FOR A GIVEN CRACK LENGTH AS A FUNCTION OF PATCH
STIFFNESS AND ADHESIVE FLEXIBILITY
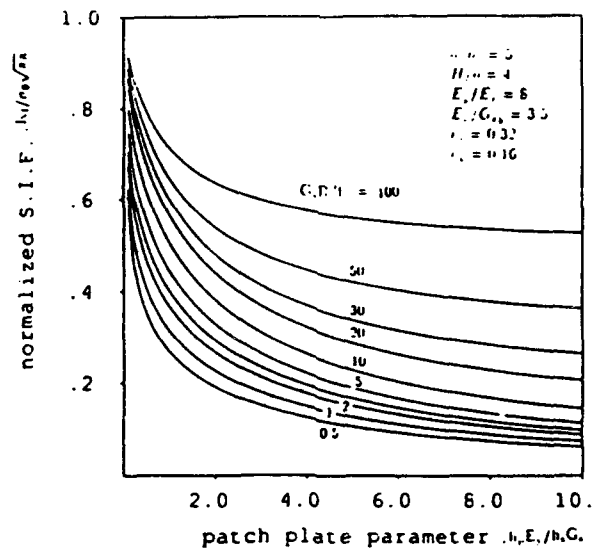
FIGURE 2-39. VARIATION OF NORMALIZED S.I.F. AS A FUNCTION OF PATCH STIFFNESS
AND ADHESIVE FLEXIBILITY
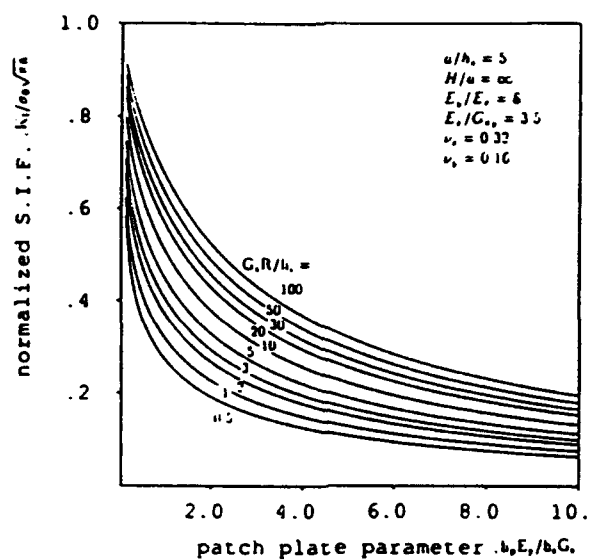
FIGURE 2-40. VARIATION OF NORMALIZED S.I.F. AS A FUNCTION OF PATCH STIFFNESS
AND ADHESIVE FLEXIBILITY
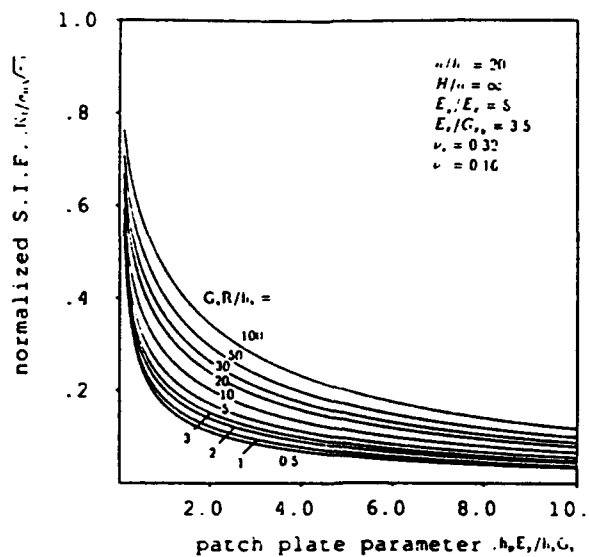
FIGURE 2-41. VARIATION OF S.I.F. AS A FUNCTION OF PATCH STIFFNESS AND ADHESIVE
FLEXIBILITY

63
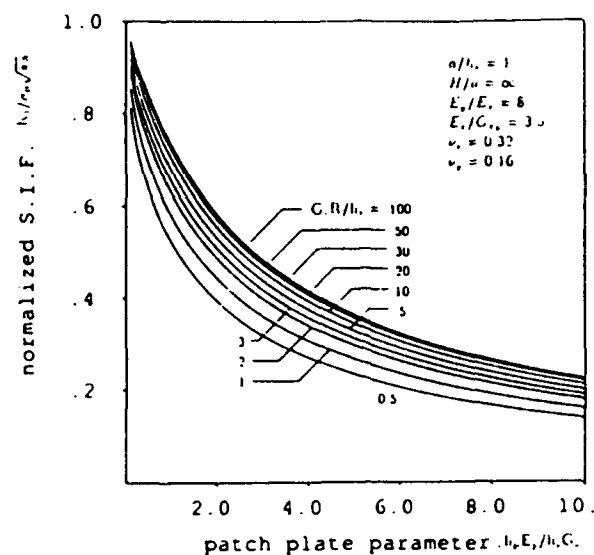
FIGURE 2-42. VARIATION OF S.I.F. AS A FUNCTION OF PATCH STIFFNESS AND ADHESIVE
FLEXIBILITY

2.1.5 Comparison of Test and Analytical Results for Edge Cracked Panels with Composite Repairs

Three different test specimens were considered. The geometrical and material property data are given below. In the test, the load point displacements and fatigue crack growth rates are measured. The fatigue crack-growth rate is assumed to be governed by the empirical power law relation as shown below. Note that since (ΔK) is raised to the power of 3.5 , any small change in ΔK tends to be magnified in the fatigue crack growth data. Also, in the analysis, a perfect bond between the metal sheet and the composite patch is assumed; and that the metal sheet is assumed to remain entirely elastic with only small scale yielding near the crack-tip. However, in reality, a small debond zone develops near the crack-tip, and in some cases, the plastic zone near the crack-tip may not be very small. It can be seen that debonding of the composite patch tends to increase the stress-intensity factor near the crack-tip in the metal sheet; while a large-scale plasticity near the crack-tip in the metal sheet tends to decrease the 'apparent' stress intensity factor. These factors have to be taken into account when comparing the analytical predictions with the test results.

64

GEOMETRY DATA

SHEET HEIGHT (HALF)		150 mm
PATCH RADIUS		75
SHEET WIDTH		160
SHEET THICKNESS		3.18
PATCH THICKNESS		0.89
ADHESIVE THICKNESS		0.19

MATERIAL DATA

SHEET	E	71.0 GPa
	NU	0.32
ADHESIVE	G	0.54
PATCH	EX	25.0
	EY	208.0
	NUX	0.0192
	NUY	0.16
	GXY	7.00

SHEET FATIGUE PROPERTY

$$da/dn = 4.3 \times 10^{-8} \times \Delta K^{3.5}$$

(mm/cycle)   (MPa$\sqrt{m}$)

In order to compare the results with test data, the effect of repairs in an edge-cracked tensile panel is analysed. The analysis of the edge-cracked specimen is entirely analogous to that of the center-cracked panel described earlier, except that the boundary conditions along the line perpendicular to the crack-axis at the center of the crack (as in the center cracked panel) are now changed to those of a traction-free boundary. While most of the experimental data is reported in Part III of this result, some experimental results on edge-cracked panels are discussed here in order (i) to compare the test data with computed results and (ii) to account for the adhesive disbond through the comparison of the computed stress intensity factors and those inferred from the fatigue crack growth data. The comparisons of the computed results for the load-point displacement with test results, for each of the three specimens, as the crack length increases, are shown in   Figures 2-43 to   2-45, respectively. In the first specimen, this comparison is excellent. In the second specimen, the test results are somewhat higher than the computed results, indicating the presence of a debond of the composite patch near the crack-tip in the metal sheet. In the third specimen, the test results are much higher than the computed results, indicating the presence of significant plasticity in the metal sheet.

Since plasticity and debonding are not accounted for in the analysis, a simple design procedure is developed to account for these effects in the analytical predictions. The fatigue crack growth data for one of the specimens appears in Figure 2-46.The 'inferred' stress-intensity factor [from the empirical power-law given above] at the crack-tip as a function of the crack-length is indicated as 'the generated SIF'[Figure 2-47].The analytically computed SIF (assuming no debonding and perfect elasticity) is also   in Figure 2-47 . The difference between the two results is due to debonding. Thus, an empirical scale-up factor is developed, which when it

multiplies the analytically predicted SIF, gives the actual SIF. This scale factor is developed from the first specimen's data [Figure 2-47], and used to compute the actual SIF in the other two specimens. Thus the computed and actual SIF are used in 'predicting' the fatigue crack growth in specimens 2 and 3. It is seen from Figures 2-48 and 2-49 that thus predicted fatigue crack growth is in excellent agreement with the test data.
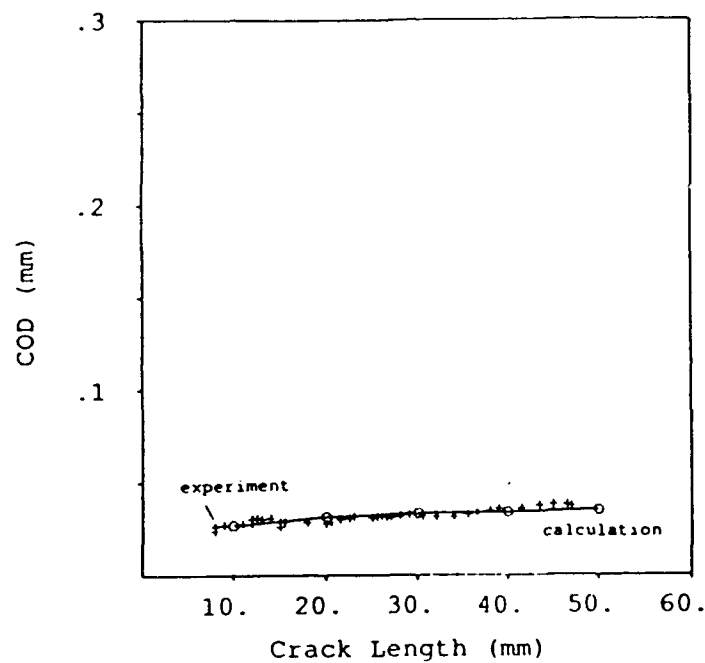
FIGURE 2-43. COMPARISON OF CALCULATED AND EXPERIMENTAL VALUES FOR COD AS A FUNCTION OF CRACK LENGTH (EXPT 1)
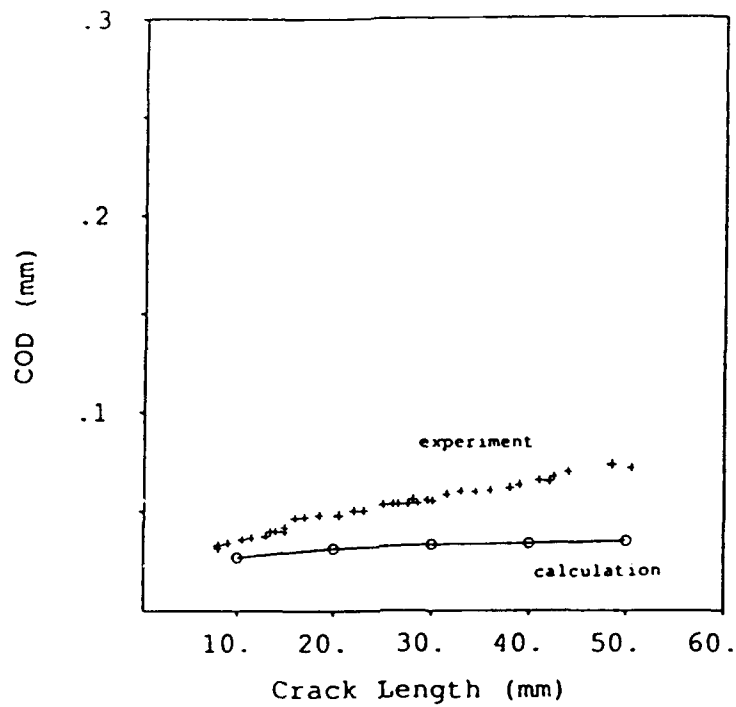
FIGURE 2-44. COMPARISON OF CALCULATED AND EXPERIMENTAL VALUE FOR COD AS A
FUNCTION OF CRACK LENGTH (EXPT 2)
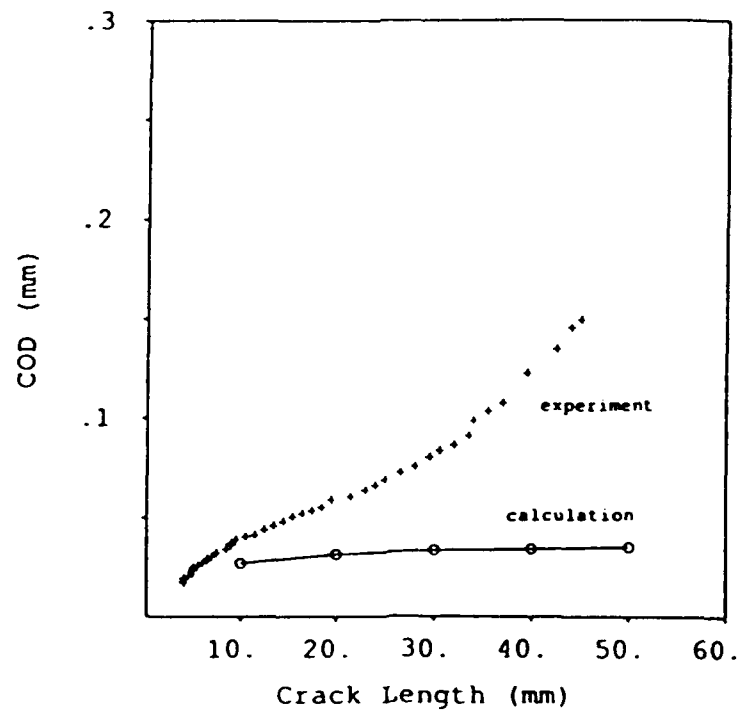
FIGURE 2-45. COMPARISON OF COD (EXPT 3) WITH CALCULATION

FIGURE 2-46. CRACK LENGTH VS. NUMBER OF CYCLES (CALCULATION VS. EXPERIMENT)

FIGURE 2-47.   DIRECTLY CALCULATED S.I.F. VS. S.I.F. INFERRED FROM FATIGUE DATA
(EXPT 1)

68

FIGURE 2-48. COMPARISON OF CALCULATED FATIGUE CRACK GROWTH HISTORY WITH EXPT 2 (CALCULATED S.I.F. ADJUSTED FOR POSSIBLE DISBONDS)

FIGURE 2-49. COMPARISON OF CALCULATED FATIGUE CRACK GROWTH HISTORY WITH EXPT 3 (CALCULATED S.I.F. ADJUSTED FOR POSSIBLE DISBOND)

2.2 THROUGH-THE-THICKNESS CRACKS IN A METAL SHEET AT A LOADED FASTENER HOLE WITH A BONDED COMPOSITE PATCH

2.2.1 Basic Formulation

As a model problem, a single pin loaded fastener hole in a metal sheet is considered. Through-the-thickness cracks are assumed to emanate from the hole. A boron/epoxy composite patch is assumed to be applied to cover the hole as well as the cracks, as shown in Figure 2-50.
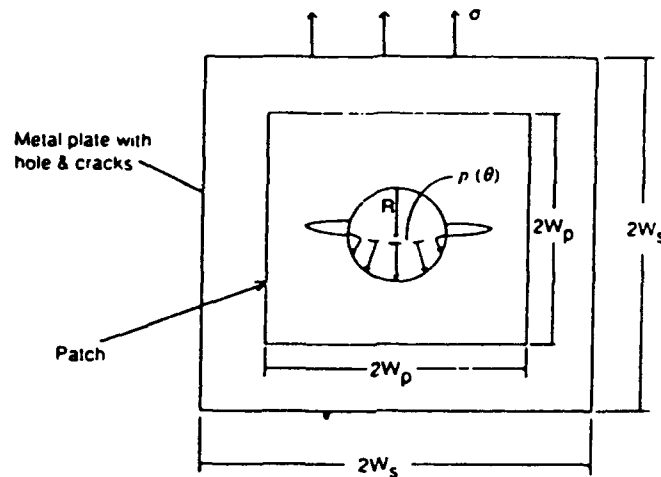
FIGURE 2-50. SCHEMATIC OF REPAIRED CRACKS EMANATING FROM LOADED HOLES

If only the mode I stress-intensity factors are considered, the solution for the above problem can be obtained from the superposition of three problems as shown in Figure 2-51.
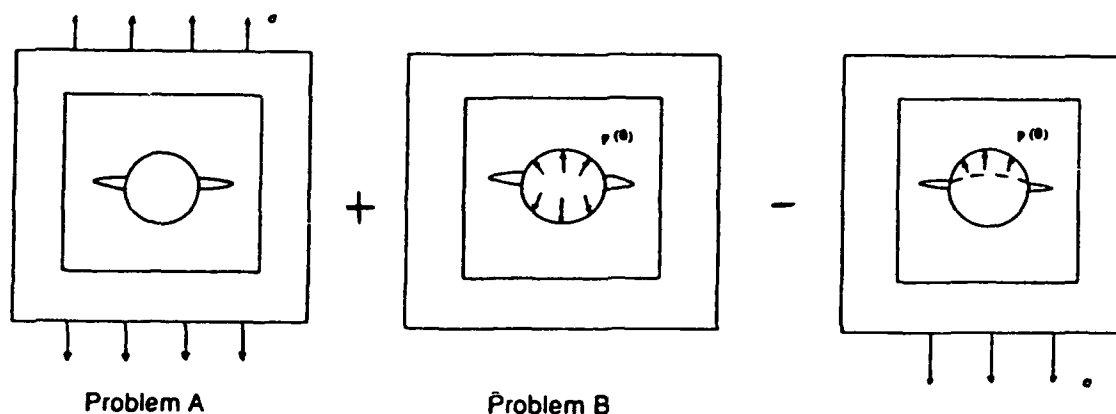
Problem A   Problem B

FIGURE 2-51. LINEAR SUPERPOSITION OF COMPONENT PROBLEMS

70

Thus, for the actual problems in Figure 2-50, the stress intensity factor is given by:

$$K_I = \frac{1}{2}[(K_I)_A + (K_I)_B]$$

wherein the subscripts A and B refer to problems 'A' and 'B' respectively, as shown above.

In order to solve the given problem in Figure 2-50, the displacement field should be obtained in the finite-sized plates in the following cases:

A. uniform stress σ applied to a finite-sized isotropic sheet with a hole and crack.

B. pin load $p(\theta)$ applied along the periphery of a hole with cracks, in an isotropic sheet.

C. point loads in the plane of the finite isotropic sheet with a hole and cracks.

D. point loads in the plane of the finite-sized orthotropic patch.

Each of the above displacement fields can be obtained from a finite-element-alternating technique. This solution technique for cases A, B and C above can be schematically described as follows:

(1)Using the analytical solution for an infinite plate with a circular hole, calculate the stresses at the location of the crack and the stresses at the location of the outer boundary.

(2) Apply the reverse of the crack-face stresses, obtained in Step (1), on the surface of a crack in an infinite plate withour a hole, and calculate the stresses at the location of the hole boundary as well as at the outer boundaries.

(3) Using the finite element analysis, obtain the stresses at the location of the crack, when the reverse of the tractions, obtained in steps (1) and (2), are applied on the boundary of the finite element model, which has the same geometry as the given problem, except for the crack.

(4) If the crack-face tractions as obtained in Step (3) are small, stop the calculation. If not, apply the reverse of the crack-location stresses on the crack surface in an infinite plate without a hole, and calculate the stresses at the location of the hole as well as at the outer boundary.

(5) Using the finite element analysis, obtain the stresses at the location of the crack, when the reverse of the tractions, obtained in Step (4) are applied on the boundary, and go back to Step (4).

(6) Add the displacement increments in each step; and

(7) Add the increments of stress and stress-intensity factors, in each step.

The solution procedure for case D above, is as follows:

(1) Using the analytical solution for an infinite orthotropic plate, calculate the tractions at the location of the boundaries of the finite orthotropic patch.

(2) Using the finite element analysis, obtain the displacements when the reverse of the tractions in Step (1) are applied on the boundary.

(3) Add the displacements in Steps (1) and (2).

Finally, employing the compatibility relations for displacements in the isotropic

sheet, and the orthotropic patch, using the properties of the adhesive, a set of integral equations for the original problem can be developed.

2.2.2 Plate with a Hole Under Uniform Stress

Figure 2-52 shows a uniformly loaded infinite plate with a hole.
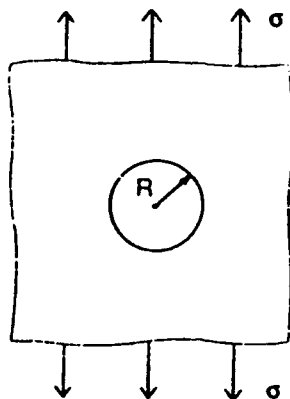
FIGURE 2-52. INFINITE PLATE, WITH A HOLE, LOADED AT INFINITY

The well-known complex-variable formulation [10] leads to:

$$\sigma_x + \sigma_y = 2\left[\ \phi(z) + \overline{\phi(z)}\ \right]$$

$$\sigma_y - i\sigma_{xy} = \phi(z) + \overline{\phi(z)} + z\ \overline{\phi\ '(z)} + \overline{\psi(z)}$$

$$2G\ (u + i\ v) = k\ \varphi(z) - z\ \overline{\varphi'(z)} - \overline{\chi(z)} \qquad\qquad (2\text{-}68)$$

It is also well known that, for this problem,

$$\phi(z) = \frac{\sigma}{4}\left(1 + \frac{2R^2}{z^2}\right)$$

$$\psi(z) = \frac{\sigma}{z}\left(1 + \frac{R^2}{z^2} + \frac{3R^4}{z^4}\right)$$

$$\varphi(z) = \frac{\sigma}{4}\left(z - \frac{2R^2}{z}\right)$$

$$\chi(z) = \frac{\sigma}{2}\left(z - \frac{R^2}{z} - \frac{R^4}{z^3}\right) \qquad\qquad (2\text{-}69)$$

72

2.2.3 Plate with a Hole Subjected to Pin Loads

Figure 2-53 shows an infinite plate with hole-face loading.
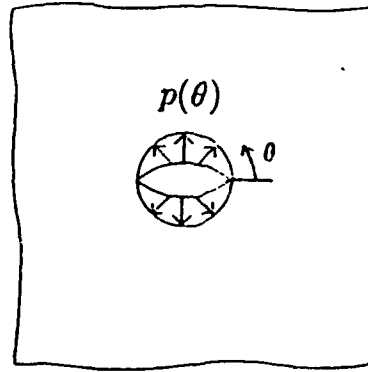
FIGURE 2-53. INFINITE PLATE, WITH A HOLE, WITH HOLE-FACE LOADING

The pin load is considered to be distributed as:

$$p(\theta) = p_m \left| \sin \theta \right|$$

Again, using the complex variable method, the boundary conditions at the periphery of the hole may be written as:

$$\sigma_{rr} - i\, \sigma_{r\theta} = N - iT$$

$$= -p_m \left| \sin \theta \right|$$

$$= \sum_{-\infty}^{\infty} A_k e^{ik\theta} \qquad (k = 0,1,2...) \qquad (2\text{-}70)$$

where:

$$A_0 = \frac{2p_m}{\pi}$$

$$A_k = 0 \ ; \ k = 1,3,5...$$

$$A_k = \frac{2p_m}{\pi\left(k^2 - 1\right)} \ ; \quad k = 2,4,6... \qquad (2\text{-}71)$$

In order to satisfy the above hole-surface boundary conditions, the stress functions must satisfy:

$$\phi(z) + \overline{\phi(z)} - e^{2i\theta}\left[\bar{z}\phi'(z) + \psi(z)\right] = N - iT \quad \text{at the hole boundary.} \qquad (2\text{-}72)$$

We assume the solutions:

$$\phi(z) = \sum_{k=0}^{\infty} a_k z^{-k} \qquad (2\text{-}73)$$

73

and

$$\psi(z) = \sum_{k=0}^{\infty} a'_k z^{-k}$$

(2-74)

Substituting these into the boundary conditions, we obtain:

$$\phi(z) = \sum_{n=1}^{\infty} a_n z^{-2n}$$

(2-75)

and

$$\psi(z) = \sum_{n=1}^{\infty} a'_n z^{-2n}$$

(2-76)

where

$$a_n = \frac{2p_m}{\pi(4n^2 - 1)} \quad ; \quad n = 1,2,3...$$

$$a'_1 = \frac{2p_m}{\pi} R^2$$

$$a'_n = \frac{4(n-1)p_m}{\pi(4n^2-8n+3)} R^{2n} \quad ; \quad n = 2,3,4...$$

(2-77)

2.2.4 Plate with a Hole Subjected to Point Loads

Figure 2-54 shows an infinite plate subjected to body forces.
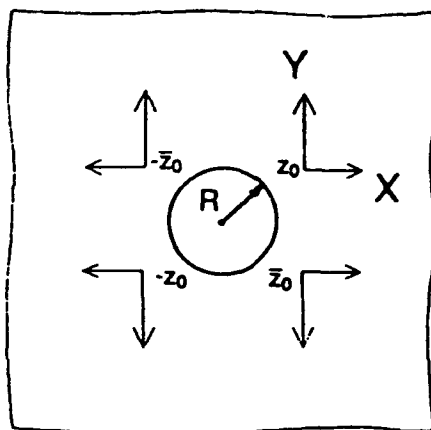
FIGURE 2-54. INFINITE PLATE WITH A HOLE, SUBJECTED TO BODY FORCES

74

First consider the problem shown in Figure 2-55, an infinite plate with a hole, subjected to body forces.
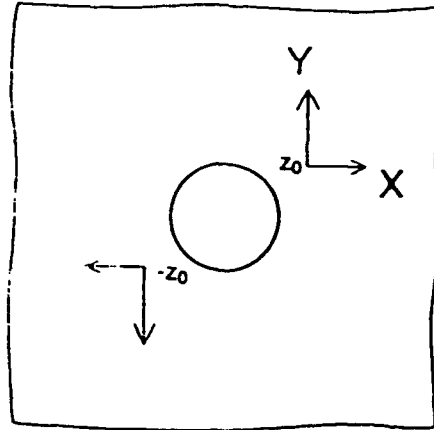
FIGURE 2-55.   INFINITE PLATE WITH A HOLE, SUBJECTED TO A
PAIR OF DIAMETRICALLY OPPOSED BODY FORCES

Once again, Mushkelishvilli's complex variable formulation is used. The relevant stress-functions can be expressed as:

$$\varphi_1(z) = -\frac{X + iY}{2\pi(1 + k)} \log(z - z_0)$$

$$+ \frac{X + iY}{2\pi(1 + k)} \log(z + z_0)$$

$$+ \varphi_1^0(z)$$

$$= -\frac{X = iY}{2\pi(1 + k)} \log\frac{z - z_0}{z + z_0} + \varphi_1^0(z) \tag{2-78}$$

and $$\psi_1(z) = -\frac{k(X = iY)}{2\pi(1 + k)} \log\frac{z - z_0}{z + z_0} + \frac{\bar{z}_0(X + iY)}{2\pi(1 + k)}\left(\frac{1}{z - z_0} + \frac{1}{z + z_0}\right) + \psi_1^0(z) \tag{2-79}$$

where φ_1^0 and ψ_1^0 are holomorphic functions.
We introduce a conformal mapping as:

$$z = R\,\zeta \tag{2-80}$$

Then, the region outside of a circle with radius R is mapped on to the region outside of a unit circle.

In the ζ plane, the stress functions are expressed as,

$$\varphi(\zeta) = -\frac{(X + iY)}{2\pi(1 + k)} \log\frac{\zeta - \zeta_0}{\zeta + \zeta_0} + \varphi_0(\zeta) \tag{2-81}$$

75

and
$$\psi(\zeta) = -\frac{k(X + iY)}{2\pi(1+k)} \log \frac{\zeta - \zeta_0}{\zeta + \zeta_0} \frac{\overline{\zeta_0}(X + iY)}{2\pi(1+k)}\left(\frac{1}{\zeta - \zeta_0} + \frac{1}{\zeta + \zeta_0}\right) + \psi_0(\zeta)$$
(2-82)

Here, $\varphi_0(\zeta)$ and $\psi_0(\zeta)$ are holomorphic functions outside a unit circle in the ζ-plane, and $R\zeta_0 = z_0$. The stress-free boundary conditions at the periphery of a unit circle in the ζ plane can be expressed as:
$$\varphi(\sigma) + \sigma\overline{\varphi'(\sigma)} + \overline{\psi(\sigma)} = 0$$
(2-83)

where σ is a generic point on the unit circle. Substituting the stress functions given above into this boundary condition leads to:
$$\varphi_0(\sigma) + \sigma\overline{\varphi_0'(\sigma)} + \overline{\psi_0(\sigma)} = f_0$$
(2-84)

where

$$f_0 = \frac{X + iY}{2\pi(1+k)} \log \frac{\sigma - \zeta_0}{\sigma + \zeta_0} - \frac{k(X+iY)}{2\pi(1+k)} \log \frac{1 - \sigma\overline{\zeta_0}}{1 + \sigma\overline{\zeta_0}} + \frac{X - iY}{2\pi(1+k)} \frac{2\sigma(\sigma^2\overline{\zeta_0} - \zeta_0)}{(1 - \sigma\overline{\zeta_0})(1 + \sigma\overline{\zeta_0})}$$
(2-85)

Also,

$$\overline{f_0} = \frac{X - iY}{2\pi(1+k)} \log \frac{1 - \sigma\overline{\zeta_0}}{1 + \sigma\overline{\zeta_0}} - \frac{k(X - iY)}{2\pi(1+k)} \log \frac{\sigma - \zeta_0}{\sigma + \zeta_0} + \frac{X + iY}{2\pi(1+k)} \frac{2(\zeta_0 - \sigma^2\overline{\zeta_0})}{\sigma(\sigma - \zeta_0)(\sigma + \zeta_0)}$$
(2-86)

Now, we discuss the solutions for the holomorphic functions φ_0 and ψ_0.

Since $\psi_0(\sigma)$ represents the boundary value of the function $\psi_0(\zeta)$, which is holomorphic outside the unit circle γ, it must satisfy the following condition:

$$\frac{1}{2\pi i} \int_\gamma \frac{\overline{\psi_0(\sigma)}}{\sigma - \zeta} d\sigma = 0 \quad \text{for all } \zeta \text{ outside } \gamma.$$

Since $\quad \varphi_0(\sigma) + \sigma\overline{\varphi_0'(\sigma)} + \overline{\psi_0(\sigma)} = f_0$,
(2-87)

the above condition leads to:

$$\frac{1}{2\pi i} \int_\gamma \frac{f_0}{\sigma - \zeta} d\sigma - \frac{1}{2\pi i} \int_\gamma \frac{\varphi_0(\sigma)}{\sigma - \zeta} d\sigma - \frac{1}{2\pi i} \int_\gamma \frac{\overline{\sigma\varphi_0'(\sigma)}}{\sigma - \zeta} d\sigma = 0$$
(2-88)

Thus,

$$\varphi_0(\zeta) = -\frac{1}{2\pi i} \int_\gamma \frac{f_0}{\sigma - \zeta} d\sigma$$

(2-89)

From Cauchy's formula,

$$\psi_0\left(\zeta\right) = -\frac{1}{2\pi i}\int_\gamma \frac{\psi_0(\sigma)}{\sigma - \zeta} d\sigma + \psi_0(\infty)$$

(2-90)

By using equation (2-87) above, and by neglecting the constant term $\psi_0\left(\infty\right)$, the function $\psi_0\left(\zeta\right)$ can be expressed as,

$$\psi_0\left(\zeta\right) = -\frac{1}{2\pi i}\int_\gamma \frac{\overline{f_0}}{\sigma - \zeta} d\sigma - \frac{1}{\zeta}\dot{\varphi}_0(\zeta)$$

(2-91)

Substituting the expressions given for f_0 and $\overline{f_0}$ in Eqs. (2-85) and (2-86), into Eqs. (2-89) and (2-91) above, we obtain:

$$\varphi_0\left(\zeta\right) = -\frac{k(X+iY)}{2\pi(1+k)}\log\frac{\zeta\overline{\zeta}_0 - 1}{\zeta\overline{\zeta}_0 + 1} + \frac{X-iY}{2\pi(1+k)}\frac{2\zeta(\zeta\overline{\zeta}_0 - 1)}{\overline{\zeta}_0(\zeta\overline{\zeta}_0 + 1)(\zeta\overline{\zeta}_0 - 1)}$$

(2-92)

and

$$\psi_0\left(\zeta\right) = \frac{(X-iY)}{2\pi(1+k)}\log\frac{\zeta\overline{\zeta}_0 - 1}{\zeta\overline{\zeta}_0 + 1} - \frac{X-iY}{2\pi(1+k)}\frac{2}{\zeta\overline{\zeta}_0}$$

$$+ \frac{k(X+iY)}{2\pi(1+k)}\frac{2\overline{\zeta}_0}{\zeta(\zeta\overline{\zeta}_0 + 1)(\zeta\overline{\zeta}_0 - 1)} + \frac{X-iY}{2\pi(1+k)}\frac{2(\zeta_0\overline{\zeta}_0 - 1)(\zeta^2\overline{\zeta}_0^2 + 1)}{\zeta\overline{\zeta}_0(\zeta\overline{\zeta}_0 + 1)^2(\zeta\overline{\zeta}_0 - 1)^2}$$

(2-93)

Next, we consider an infinite plate with a hole subjected to body forces, as shown in Figure 2-56.
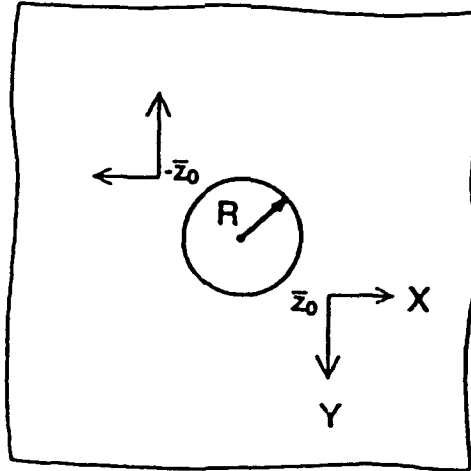
FIGURE 2-56. INFINITE PLATE WITH A HOLE, SUBJECTED TO A COMPLEMENTARY PAIR OF DIAMETRICALLY OPPOSED BODY FORCES

77

As earlier, it can be seen that:

$$\varphi(\zeta) = -\frac{(X-iY)}{2\pi(1+k)} \log \frac{\zeta - \bar{\zeta_0}}{\zeta + \bar{\zeta_0}} + \varphi_0(\zeta)$$

(2-94)

and

$$\psi(\zeta) = -\frac{k(X+iY)}{2\pi(1+k)} \log \frac{\zeta - \bar{\zeta_0}}{\zeta + \bar{\zeta_0}} + \frac{\zeta_0(X-iY)}{2\pi(1+k)}\left(\frac{1}{\zeta-\bar{\zeta_0}} + \frac{1}{\zeta+\bar{\zeta_0}}\right) + \psi_0(\zeta)$$

(2-95)

where

$$\varphi_0 = -\frac{k(X-iY)}{2\pi(1+k)} \log \frac{\zeta\zeta_0 - 1}{\zeta\zeta_0 + 1} + \frac{X+iY}{2\pi(1+k)} \frac{2\zeta((\zeta_0\bar{\zeta_0} - 1)}{\zeta_0(\zeta\zeta_0 + 1)(\zeta\zeta_0 - 1)}$$

(2-96)

and

$$\psi_0 = -\frac{X+iY}{2\pi(1+k)} \log \frac{\zeta\zeta_0 - 1}{\zeta\zeta_0 + 1} - \frac{X-iY}{2\pi(1+k)} \frac{2}{\zeta\bar{\zeta_0}}$$

$$+ \frac{k(X+iY)}{2\pi(1+k)} \frac{2\zeta_0}{\zeta(\zeta\zeta_0 - 1)(\zeta\zeta_0 + 1)} + \frac{X+iY}{2\pi(1+k)} \frac{2(\zeta_0\bar{\zeta_0} - 1)(\zeta^2\zeta_0^2 + 1)}{\zeta\zeta_0(\zeta\zeta_0 + 1)^2(\zeta\zeta_0 - 1)^2}$$

(2-97)

The stresses and displacements can be calculated using the following relations:

$$\sigma_{rr} + \sigma_{\theta\theta} = 2\left[\Phi(\zeta) + \overline{\Phi(\zeta)}\right]$$

(2-98)

$$\sigma_\theta + i\sigma_{r\theta} = \Phi(\zeta) + \overline{\Phi(\zeta)} + \frac{\zeta^2}{|\zeta|^2}\left[\bar{\zeta}\Phi'(\zeta) + \overline{\psi(\zeta)}\right]$$

(2-99)

and

$$2G(u + iv) = k\,\varphi(\zeta) - \zeta\overline{\varphi'(\zeta)} - \overline{\psi(\zeta)}$$

(2-100)

where,

$$\Phi(\zeta) = \frac{1}{R}\,\varphi(\zeta); \text{ and } \overline{\psi(\zeta)} = \frac{1}{R}\,\psi'(\zeta)$$

(2-101)

To complete the set of basic solutions needed to solve problems of a patched pin-loaded hole with cracks, the following last basic solution is developed. It concerns a crack in an infinite isotropic sheet, the faces of which are subjected to a pair of concentrated crack-opening forces as shown in   Figure 2-57.
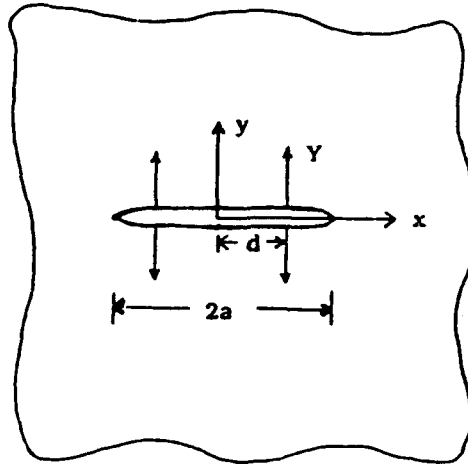
FIGURE 2-57. INFINITE PLATE WITH A CRACK, WITH POINT LOADS ON THE CRACK-FACE

The solution for this problem is standard, but the details are reported here for completeness.

Consider the general case when the crack faces are subjected to arbitrary tractions $p(t)$ and $q(t)$, defined as:

$$p(t) = \frac{1}{2}(\sigma_y^+ + \sigma_y^-) - \frac{i}{2}(\tau_{xy}^+ + \tau_{xy}^-)$$

$$q(t) = \frac{1}{2}(\sigma_y^+ - \sigma_y^-) - \frac{i}{2}(\tau_{xy}^+ - \tau_{xy}^-) \qquad (2\text{-}102)$$

where, $(\sigma_y^+$ and $\tau_{xy}^+)$ are stresses on the upper crack surface, and $(\sigma_y^-$ and $\tau_{xy}^-)$ are the stresses on the lower crack surface.

When the tractions at infinity are zero as in the present problem, the appropriate stress functions can be defined as:

$$\Phi(z) = \Phi_0(z) + \frac{C}{x(z)} \qquad (2\text{-}103a)$$

$$\Omega(z) = \Omega_0(z) + \frac{C}{x(z)} \qquad (2\text{-}103b)$$

where,

$$\Phi_0 = \frac{1}{2\pi i X(z)} \int_L \frac{X(t)\, p(t)\, dt}{t-z} + \frac{1}{2\pi i} \int_L \frac{q(t)\, dt}{t-z}$$

$$\Omega_0 = \frac{1}{2\pi i X(z)} \int_L \frac{X(t)\, p(t)\, dt}{t-z} - \frac{1}{2\pi i} \int_L \frac{q(t)\, dt}{t-z}$$

$$X(z) = \sqrt{(z-a)(z+a)} \qquad (2\text{-}104)$$

and the constant C is determined from the condition of the single-valuedness of the displacements, i.e.

$$2(K+1)\int_L \frac{C\,dt}{X(t)} + K\int_L \left[\Phi_0^+(t) - \Phi_0^-(t)\right]dt + \int_L \left[\Omega_0^+(t) - \Omega_0^-(t)\right] = 0$$

(2-105)

For the problem shown in Figure 2-57,

$$p(t) = -Y\left[\delta(x+d) + \delta(x-d)\right]$$
$$q(t) = 0$$

(2-106)

where δ denotes a Dirac function. Using (2-106) in (2-104), one obtains:

$$\Phi_0 = \frac{Y\sqrt{d^2-a^2}}{2\pi i\sqrt{z^2-a^2}}\left(\frac{1}{z+d} + \frac{1}{z-d}\right)$$

$$\Omega_0 = \frac{Y\sqrt{d^2-a^2}}{2\pi i\sqrt{z^2-a^2}}\left(\frac{1}{z+d} + \frac{1}{z-d}\right)$$

(2-107)

Using (2-107) in (2-105) we find that $C = 0$. Thus, we have:

$$\Phi(z) = \Omega(z) = \frac{Y\sqrt{d^2-a^2}}{2\pi i\sqrt{z^2-a^2}}\left(\frac{1}{z+d} + \frac{1}{z-d}\right)$$

(2-108)

If $\Phi(z) = \varphi'(z)$ and $\Omega(z) = \omega'(z)$, we find that:

$$\varphi(z) = \omega(z) = \frac{-Y}{2\pi i}\left[\log\frac{2\sqrt{d^2-a^2}\sqrt{z^2-a^2} + 2dz - 2a^2}{(z-d)} + \log\frac{2\sqrt{d^2-a^2}\sqrt{z^2-a^2} - 2dz - 2a^2}{(z+d)}\right]$$

(2-109)

The stresses and displacements are given by:

$$\sigma_x + \sigma_y = 2\left[\Phi(z) + \overline{\Phi(z)}\right]$$

$$\sigma_y - i\,\sigma_{xy} = \Phi(z) + (z - \bar{z})\,\overline{\Phi'(z)} + \Omega(\bar{z})$$

$$2\mu(u + iv) = k\,\varphi(z) - \omega(\bar{z}) - (z - \bar{z})\,\overline{\Phi(z)}$$

(2-110)

The stress-intensity factors are defined in the usual fashion, as:

$$K_I - i\,K_{II} = \lim_{z\to a} 2\sqrt{2\pi}\,(z-a)^{1/2}\,\Phi(z)$$

(2-111)

From which, we find that:

$$K_I = \frac{Y}{\sqrt{\pi a}}\left(\frac{\sqrt{a+d}}{\sqrt{a-d}} + \frac{\sqrt{a-d}}{\sqrt{a+d}}\right)$$

2.2.5 Integral Equation Formulation

Let the displacement field for case (i) above be $u = f_{1A}(x, y)$ and $v = f_{2A}(x, y)$. Let the displacement field for case (ii) above be $u = f_{1B}(x, y)$ and $v = f_{2B}(x, y)$.

In case (iii), let point loads X, Y be applied symmetrically at the points (x_0, y_0); $(-x_0, y_0)$, $(x_0, -y_0)$ and $(-x_0, -y_0)$. Let the displacement field at a point (x, y) in the plate be:

$$u(x, y) = H_{11}(x, y; x_0, y_0)X + H_{12}(x, y; x_0, y_0)Y$$ (2-112)

$$v(x, y) = H_{21}(x, y; x_0, y_0)X + H_{22}(x, y; x_0, y_0)Y$$ (2-113)

In case (iv), let point loads X, Y be applied symmetrically at the points (x_0, y_0); $(-x_0, y_0)$, $(x_0, -y_0)$ and $(-x_0, -y_0)$ in a finite orthotropic plate. Let the displacements at a point (x, y) in the plate be expressed as:

$$u_p (x, y) = K_{11} (x, y ; x_0, y_0)X + K_{12} (x, y ; x_0, y_0)Y \qquad (2\text{-}114)$$

$$v_p (x, y) = K_{21} (x, y ; x_0, y_0)X + K_{22} (x, y ; x_0, y_0)Y \qquad (2\text{-}115)$$

For the problem of a loaded hole, the total displacement in the isotropic sheet can now be written as:

$$u_s = \frac{1}{2}(f_{1A} + f_{1B}) - \frac{1}{h_s} \int\int_D [H_{11}(x, y ; x_0, y_0)\tau_x(x_0, y_0) + H_{12} (x, y ; x_0, y_0)\tau_y(x_0, y_0)]dD \qquad (2\text{-}116)$$

$$v_s = \frac{1}{2}(f_{2A} + f_{2B}) - \frac{1}{h_s} \int\int_D [H_{21}(x, y ; x_0, y_0)\tau_x(x_0, y_0) + H_{22} (x, y ; x_0, y_0)\tau_y(x_0, y_0)]dD \qquad (2\text{-}117)$$

Likewise, the total displacements in the composite patch are:

$$u_p(x, y) = \frac{1}{h_p} \int\int_D [K_{11}(x, y ; x_0, y_0)\tau_x(x_0, y_0) + K_{22} (x, y ; x_0, y_0)\tau_y(x_0, y_0)]dD \qquad (2\text{-}118)$$

The conditions of displacement compatibility between the metal sheet and the composite patch can be written as:

$$\tau_x = \frac{u_s - u_p}{F}; \quad \text{and} \quad \tau_y = \frac{v_s - v_p}{F} \qquad (2\text{-}119)$$

where F is the adhesive flexibility. By substituting (2-117) and (2-118) into Eq. (2-119), we obtain integral equations for τ_x and τ_y. Once τ_x and τ_y are evaluated, the K factors for the crack in the isotropic sheet can be computed as in Task 2.1, described earlier.

To test the accuracies of the methodologies that are developed in this research (as reported on in earlier months), first the problem of an unrepaired metallic sheet with cracks emanating from a hole that is subjected to distributed fastener stresses along the hole periphery, and far-field hoop stresses, is analyzed (Figure 2-58).

$$p (\theta) = \frac{4w_s\sigma_0}{\pi R} |\sin \theta|$$
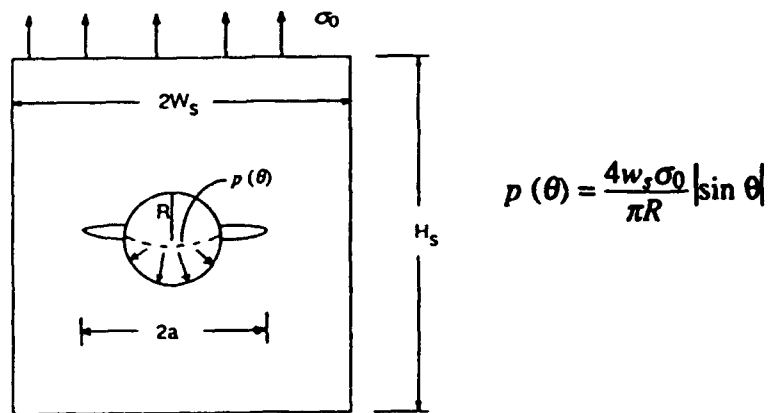
FIGURE 2-58. A FINITE PLATE WITH A HOLE, SUBJECT TO FAR-FIELD LOADING AND PIN-LOADING

In Figure 2-59, the calculated stress-intensity factors are compared with those of [15] for the case when $(H_s/W_s) = 2$; $(W_s/R) = 4$. In Figure 2-59, K_{IA} is the mode I stress intensity factor when uniform stress σ_0 is applied symmetrically on the plate; and K_{IB} is the stress-intensity factor when the bearing pressure is applied symmetrically on the hole surface, and K_I is the average of K_{IA} and K_{IB}. It can be seen
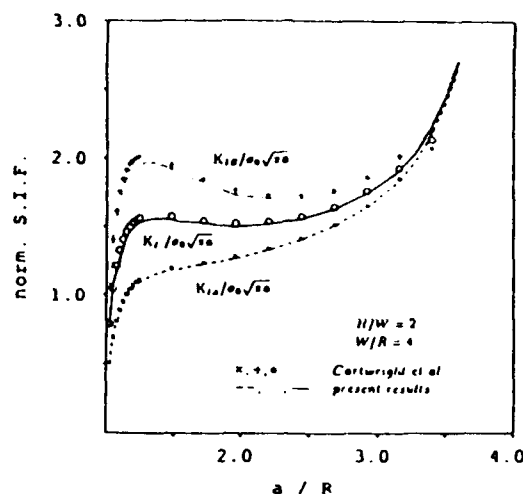
FIGURE 2-59 NORMALIZED K_I FACTOR AS A FUNCTION OF CRACK LENGTH (UNREPAIRED)

that the present values agree excellently with those of Cartwright and Parker. In the present finite-element alternating analyses, only 65 eight-noded isoparametric elements were used, and only 55 seconds of computational time was used in solving ⌐ problem, on a micro-VAX system.

Figure 60a shows the effect of patching on the stress-intensity factors when $(H/W)_s = 2$, $W_s/R) = 4$, and $(R/h_s) = 5$. The properties of the composite patch, and those of the adhesive layer, are shown (inset Figure 2-60a). Comparing Figures 2-59 and 2-60a, the substantial reduction in the stress-intensity factor due to the composite patch may be noted. When the crack length is small, this reduction is not much; but as the value of (a/R) increases, so does the effect of patching. In this problem we assumed that $H_s = H_p = H$, and $W_s = W_p = W$.

From Figure 2-59 it is seen that as the crack approaches the boundary of the plate, the stress-intensity factor increases rapidly. Figure 2-60a shows no such increase in the stress intensity factor as the crack length increases, in the presence of the patch. This is because the presence of the composite patch prevents the rapid increase of bending stresses in the uncracked ligament.

Figure 2-60b shows the effect of a patch on the actual stress intensity factor, as the crack length increases, for given geometrical and material parameters as identified in the inset of Figure 2-60b.

82
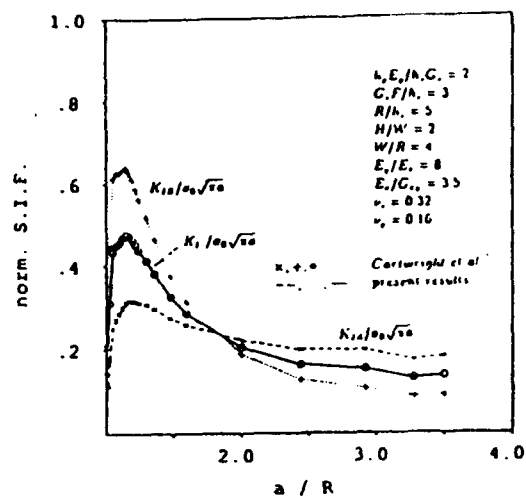
FIGURE 2-60a. VARIATION OF NORMALIZED STRESS INTENSITY FACTORS AS A
FUNCTION OF CRACK LENGTH (REPAIRED)
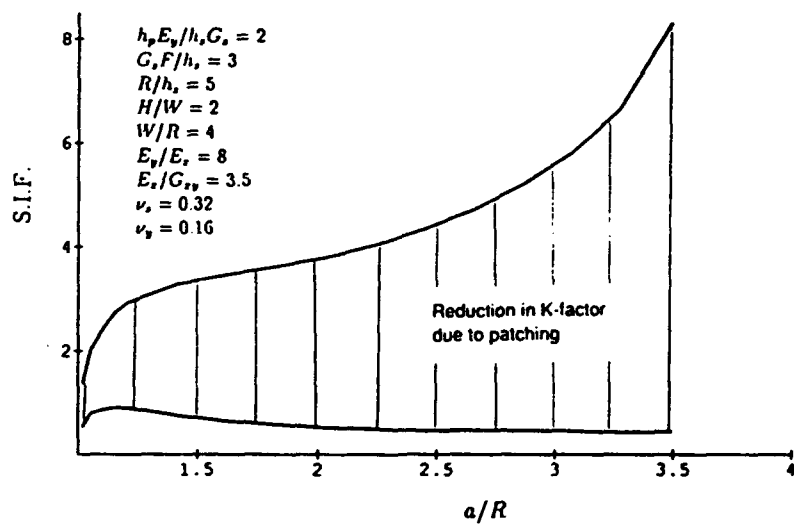
FIGURE 2-60b. REDUCTION IN K-FACTOR (σ_0=1) DUE TO REPAIR FOR CRACKS EMANATING
FROM A LOADED FASTENER HOLE

83

Figure 2-61 shows the effect of (R/h*) on the normalized stress intensity factors. When the hole radius R is much smaller than the thickness of the base plate, the effect of patching is also small. However, as R increases, the effect of patching also increases. Note that in this figure, (a/R) = 2.
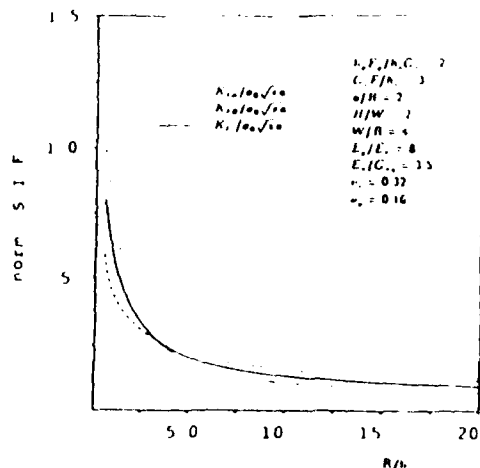
FIGURE 2-61. VARIATION OF NORMALIZED S.I.F. FOR A GIVEN CRACK, AS A FUNCTION OF HOLE RADIUS

Figure 2-62 shows the effect of the adhesive flexibility parameter and the patch stiffness parameter on the normalized stress-intensity factors K_{IA}. Figure 2-63 shows similar results for K_{IB}. If results of Figures 2-62 and 2-63 are compared, they show nearly the same trends when the
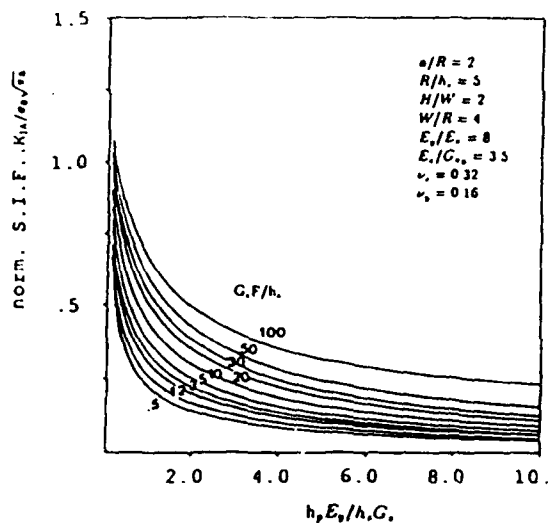
FIGURE 2-62. VARIATION OF NORMALIZED K-FACTOR AS A FUNCTION OF PATCH STIFFNESS, ADHESIVE FLEXIBILITY

84
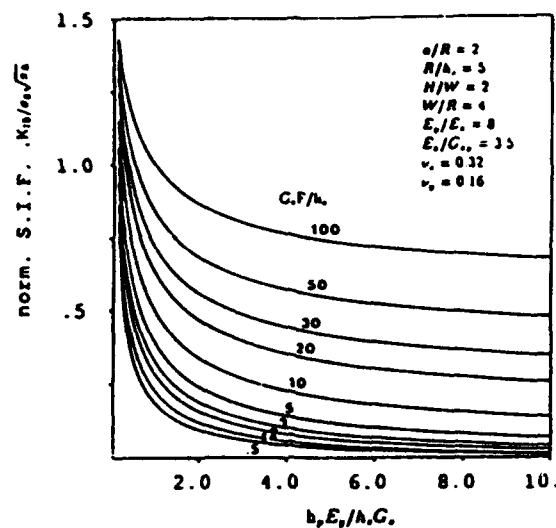
FIGURE 2-63. S.I.F. AS FUNCTION OF PATCH STIFFNESS & ADHESIVE FLEXIBILITY

adhesive flexibility parameter is small. But, as the adhesive flexibility increases, K_{IB} increases more rapidly than K_{IA}. In the case of uniform loading on the patched plate, the reduction in stress intensity factor is achieved by the adhesive shear stresses near the end of the patch plate (near $y = H_p$) and the adhesive shear stresses near the crack and the hole. The effect of the shear stresses near the end of the patch is less sensitive to the properties of the adhesive layer. On the other hand, the effect of the adhesive shear stresses near the crack and the hole are sensitive to the properties of the layer. Since, in the case of pin loading, the reduction in the stress intensity factor is achieved only by the adhesive shear stresses near the hole and the crack, the stress intensity factors are very sensitive to adhesive layer parameters. Figure 2-63 shows the effect of adhesive flexibility parameters and the patch stiffness parameters on the overall stress intensity factor [= $(K_{IA} + K_{IB})/2$].

2.3 SURFACE CRACK IN A THREE-DIMENSIONAL PLATE WITH A BONDED COMPOSITE PATCH

Consider the problem of a base plate with a surface crack, with a composite patch, as shown [Figure 2-64]. We assume that the sizes of the base plate and patch are infinite. This assumption is reasonable as long as the widths and lengths of the plate as well as the patch are about five times the length of the semi-major axis of the elliptical surface flaw. [Figure 2-64], but that the thicknesses of the base plate as well as the patch are finite. Let the thicknesses of the base plate and the patch be h_a and h_p, respectively. The loading is assumed to be far-field tension, as in Figure 2-64.

This problem now can be solved by using the superposition principle as shown in

Figure 2-65. Here, the displacement fields of the basic problems as in Figure 2-66 need to be solved for.
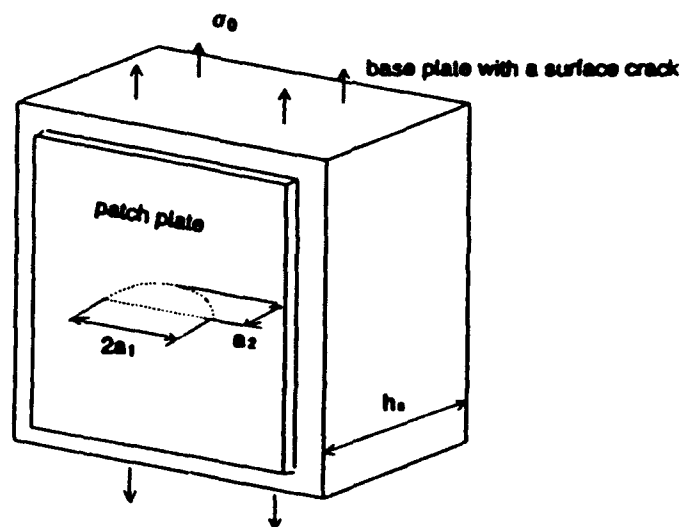
FIGURE 2-64. SCHEMATIC OF A PATCHED SURFACE FLAW IN A PLATE

(A)   **(B)**
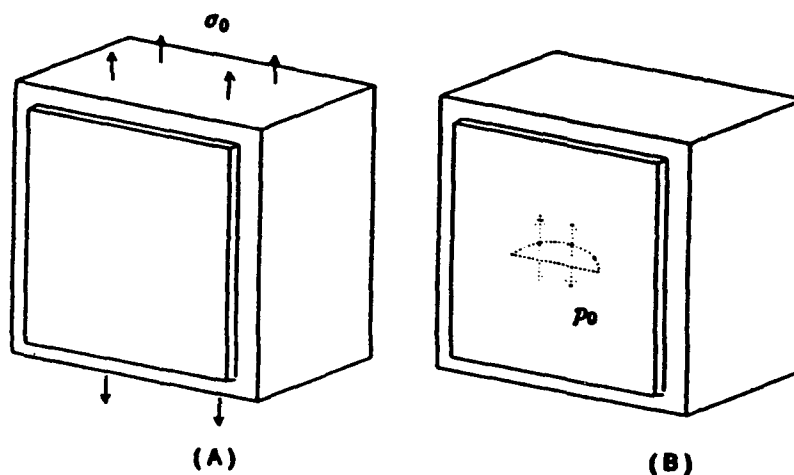
FIGURE 2-65. LINEAR SUPERPOSITION OF TWO PROBLEMS

Figure 2-66a is the case wherein uniform stress σ_0 is applied on the crack-surface. The displacement field for this problem is generated by using an analytical alternating technique, wherein the analytical solution for an infinite body containing an embedded elliptical flaw, subjected to arbitrary crack-face tractions, is employed. This analytical solution has been previously obtained by Atluri [16].
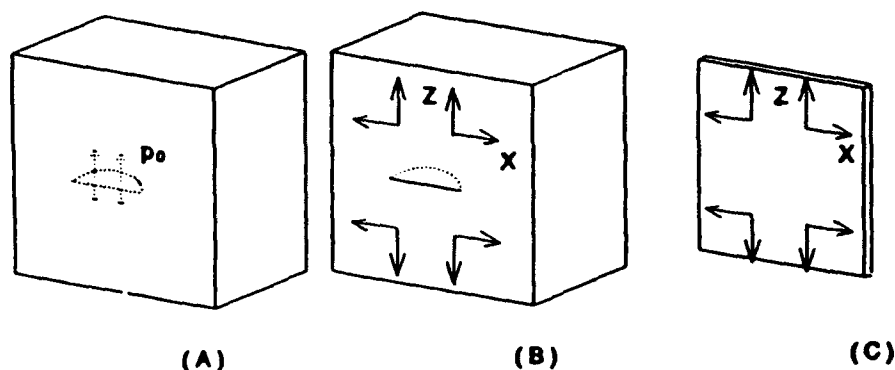
FIGURE 2-66. BASIC PROBLEMS TO BE SOLVED FOR IN ANALYZING THE PROBLEMS OF
,FIGURE 2-65

Figure 2-66b shows the problem wherein point loads x, z are applied symmetrically at the points (x_0, z_0), $(x_0, -z_0)$, $(-x_0, z_0)$ and $(-x_0, -z_0)$ on the plate with a semi-elliptical surface crack. Let the displacements at a point (x, z) on the front surface $(y = 0)$ be expressed as:

$$u = H_{11} (x, z; x_0, z_0) X + H_{12} (x, z; x_0, z_0) Z$$

$$w = H_{21} (x, z; x_0, z_0) X + H_{22} (x, z; x_0, z_0) Z$$

Figure 2-66's problem   is one wherein point loads X, Z are applied symmetrically on an infinite orthotropic plate. This solution has been reported on previously. Let the displacements at a point (x, z) for this problem be expressed as:

$$u_p = K_{11} (x, z; x_0, z_0) X + K_{12} (x, z; x_0, z_0) Z$$

$$w_p = K_{21} (x, z; x_0, z_0) X + K_{22} (x, z; x_0, z_0) Z$$

Let the displacements u_s and w_s denote the total displacements from problems 2-66a and b. The compatibility conditions between the base plate and the composite patch are expressed as:

$$\tau_x = \frac{u_s - u_p}{F}$$

and

$$\tau_y = \frac{w_s - w_p}{F}$$

where F is the adhesive flexibility, defined as earlier, as:

$$F = \frac{h_a}{G_a} + \frac{3h_p}{8G_p}$$

By using these compatibility conditions, integral equations are derived as earlier in this

report, for τ_x and τ_y. Once these are solved for, the stress intensity factors are obtained in a manner described in section 2.2.5.

Figure 2-67 shows the effect of the thickness of the base plate on the normalized stress-intensity factors for both the unrepaired and repaired cases. When the base plate thickness is small, about 50% reduction in stress intensity factor is obtained. As the base plate becomes thicker, however, the effect of the patch is reduced (to about 40%), and the stress intensity factor converges to a constant value. Note that in the case of the surface-flaw, the stress intensity factor that is considered is at the intersection of the crack-front with the front face of the base plate. From Figure 2-67 note also that if one uses a stiff patch, a better reduction in the stress intensity factor is obtained. However, a stiff patch may increase the adhesive shear stresses.
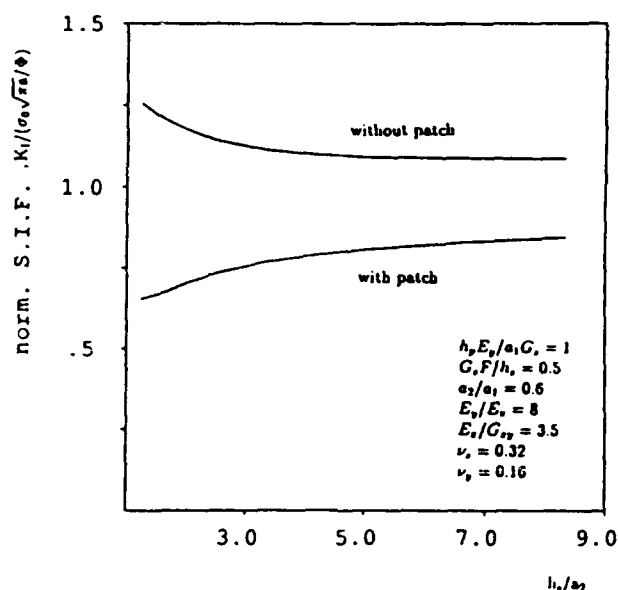
FIGURE 2-67. NORMALIZED S.I.F. AT THE DEEPEST POINT WITH AND WITHOUT REPAIRS

Figure 2-68 shows the effect of patch-stiffness parameters and adhesive flexibility parameters on the normalized stress intensity factors.

Figure 2-69 shows effect of patch stiffness and adhesive flexibility on the adhesive shear stresses, τ_z/σ_0 at $x = 0$, $y = 0$ and $z = 0$. Finally Figure 2-70 shows the effect of the patch-stiffness and adhesive flexibility on the values of σ_{pz}.
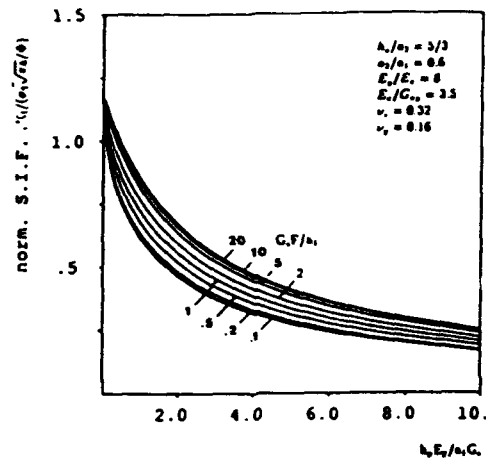
FIGURE 2-68. NORMALIZED S.I.F. AS A FUNCTION OF PATCH STIFFNESS AND ADHESIVE
FLEXIBILITY
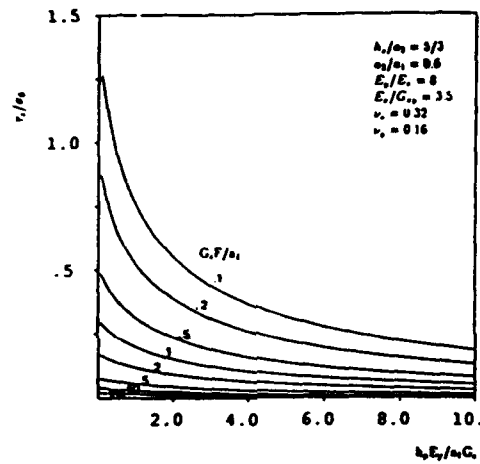
FIGURE 2-69. ADHESIVE SHEAR STRESS AS A FUNCTION OF PATCH STIFFNESS AND
ADHESIVE FLEXIBILITY
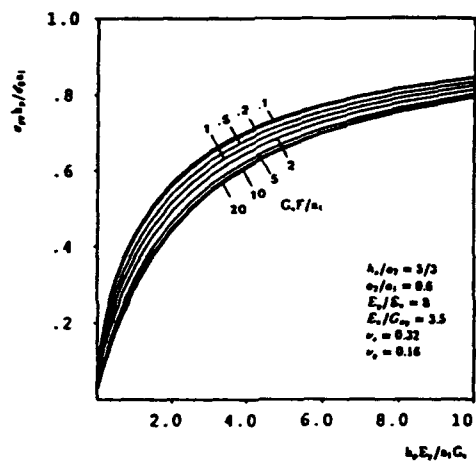
FIGURE 2-70. TENSILE STRESS IN THE PATCH AS A FUNCTION OF PATCH STIFFNESS
AND ADHESIVE FLEXIBILITY

89

2.4 SURFACE CRACK NEAR A HOLE IN A THREE-DIMENSIONAL PLATE WITH A BONDED COMPOSITE PATCH

The problem is shown schematically in Figure 2-71. To repair the crack, a patch of width $2 W_p$ and height $2H_p$ is applied, such that the center of the patch coincides with the center of the hole.

The basic component problems to be analyzed appear in Figures 2-72a, b, and c. For problem 2-72a, the displacement fields on the front surface and the stress intensity factors can be obtained by using the 3-D finite element alternating technique [16].

As for the problem in Figure 2-72b, when a point force (x,z) is applied at the point (x_0,z_0) and a symmetrical point load (x, -z) is applied at $(x_0, -z_0)$, once again the 3-D finite element alternating technique can be used.

As for problem 2-72c, the displacement field in the patch is determined as before.

The finite element mesh used for problems 2-72a and b appears in Figure 2-73. The finite element mesh used for problem 2-72c is shown in Figure 2-74.

The variations of the stress intensity factor along the crack front, with and without the repair patch, appear in Figure 2-75. Once again, the significant reduction in the crack-growth retardation, achieved by the application of the patch, is evident.
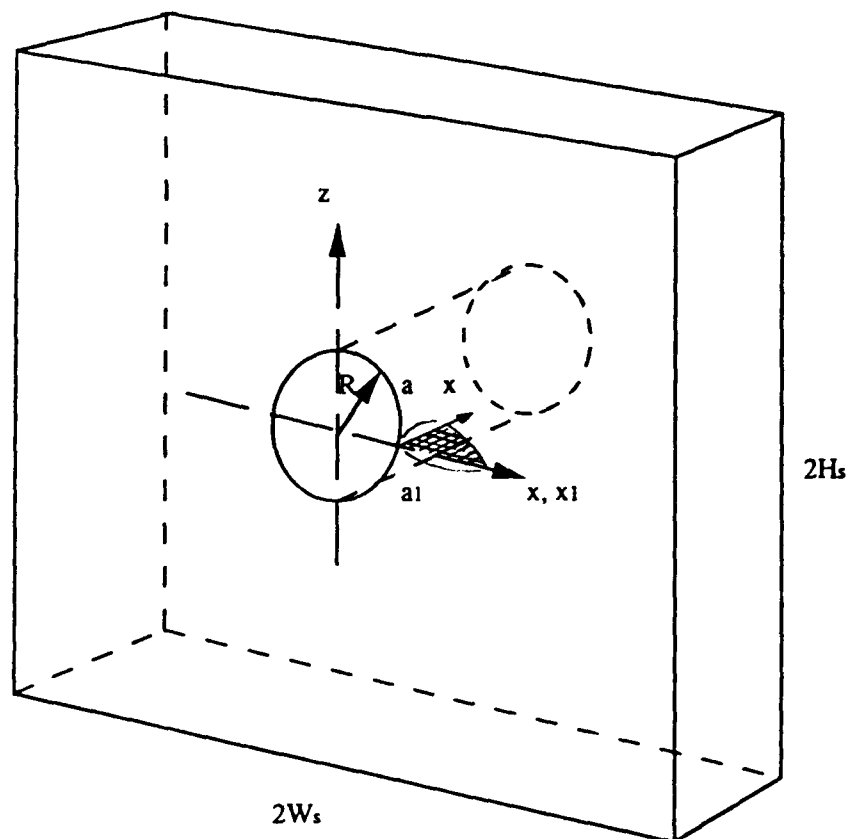
FIGURE 2-71. SCHEMATIC OF A SURFACE FLAW NEAR A FASTENER HOLE

90
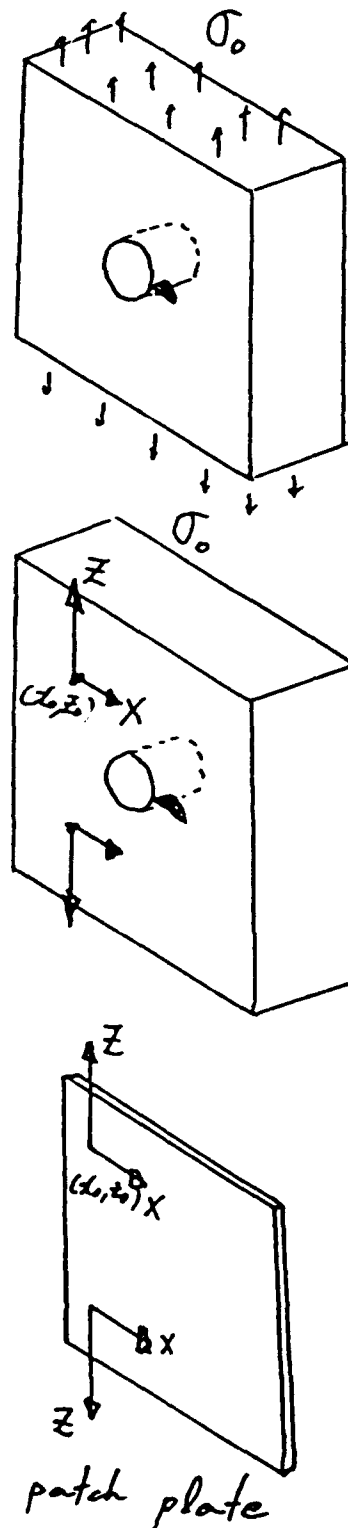
FIGURE 2-72. BASIC PROBLEMS IN THE SOLUTION FOR FIGURE 2-71
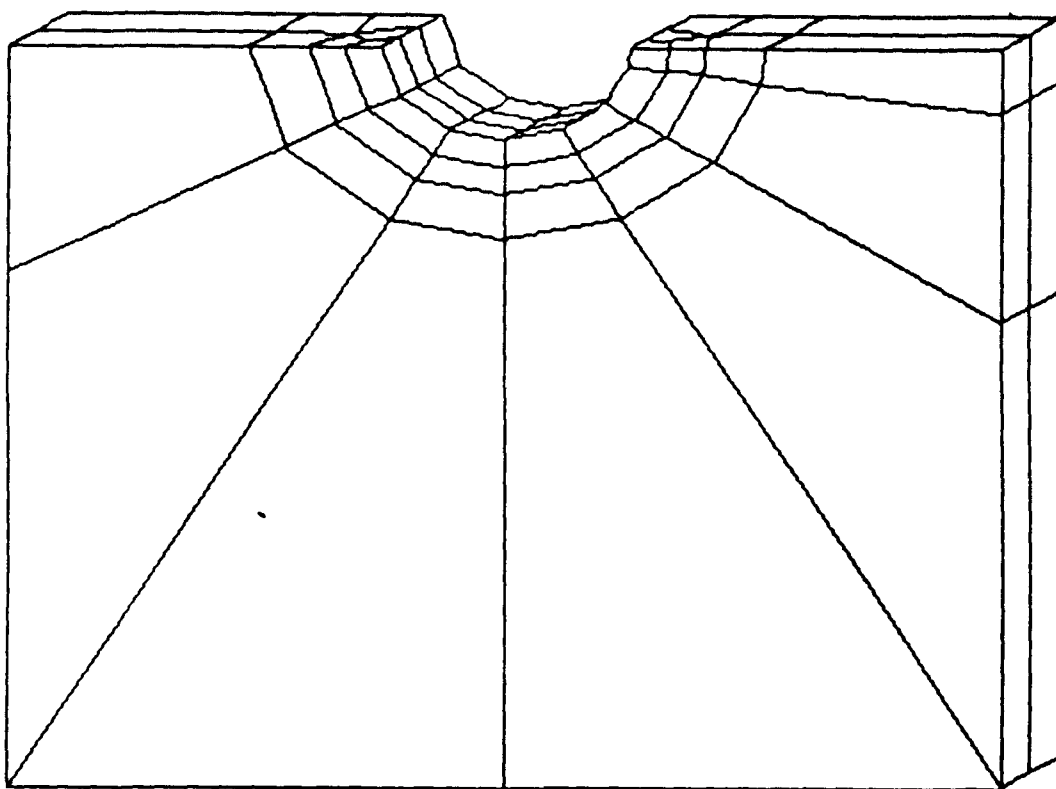
FIGURE 2-73. FINITE ELEMENT MESH FOR BASE PLATE (56 ELE., 401 NODES)
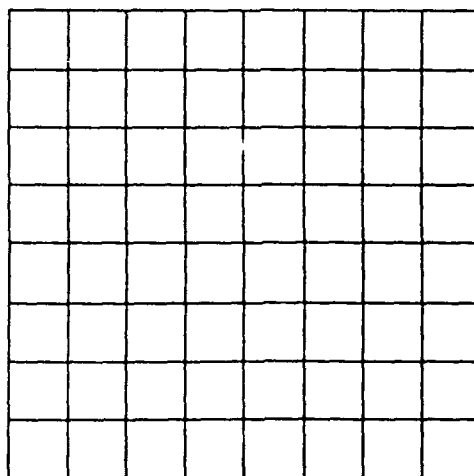
FIGURE 2-74. F.E.M. MESH FOR PATCH PLATE, 64 2-D 8 NODE ISOPARAMETRIC
ELEMENTS, 225 NODES
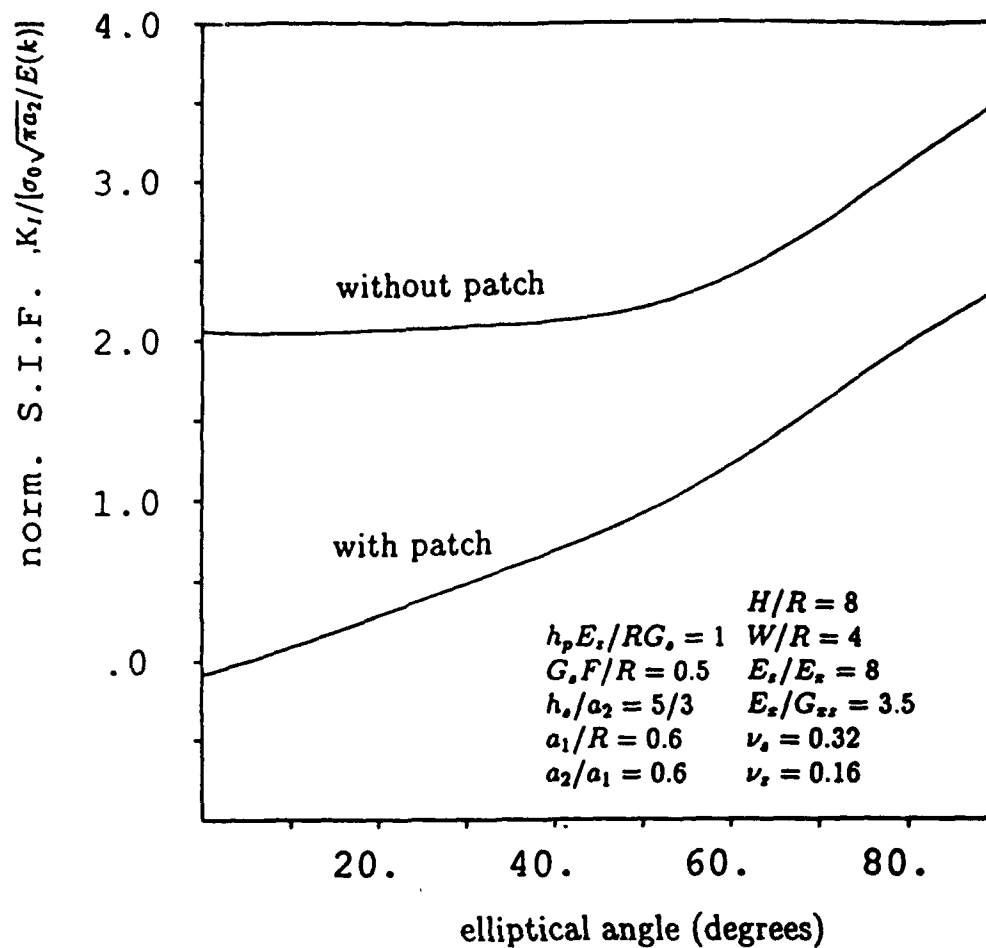
FIGURE 2-75. S.I.F. VARIATION ALONG THE CRACK FRONT WITH AND WITHOUT REPAIRS

3. FABRICATION AND TESTING OF SPECIMENS

3.1 EDGE CRACKED SPECIMENS

Additional test results have been obtained for edge cracked specimens subjected to a constant-amplitude cyclic loading. The adhesive used was FM300; the patch was a 7 layer boron-epoxy composite; the amplitude of the cyclic stress was 138 MPa; the initial crack length was about 75 mm. The tests were conducted at 20°C as well as at 100°C. The results are given in Figures 3-1 to 3-6 and Tables B1-B6 in Appendix B.

3.2 SURFACE CRACK SPECIMEN

A specimen with a surface crack 40 mm long and 5.7 mm deep in an 11.2 mm thick, 106.8 mm wide, and 304.8 mm long aluminum alloy, has been fabricated. The crack is repaired by a ten ply boron/epoxy laminate 180 mm long and 108 mm wide, with the fibers running in the direction of the load (see Figure 3-7). A number of strain gauges, all located in a line along the center of the specimen, running in the direction of the load (90 degrees to the crack front) have been installed.

To avoid obtaining unrealistically long lives for the patched specimens a small amount of crack growth was allowed prior to patching. Unfortunately, in the case of specimens 2P and 6P, the crack grew faster and hence longer than anticipated before patching, with the result that their subsequent fatigue lives were substantially reduced.

3.2.1 Constant Amplitude Testing

The reductions of the stress intensity factors obtained in previous work suggest that a significant increase in fatigue life of this specimen should occur. To confirm this prediction, a series of constant amplitude fatigue tests were performed. The testing machine employed was an INSTRON 500 kN electrohydraulic fatigue testing machine. The loads were applied such that the far field stress in the aluminum had an amplitude of 68.9 MPa with a stress ratio, R, of 0.01. The results of these tests are shown in Table 3-1. While there is a large scatter in the fatigue lives of the patched specimens, even specimen number (2P), which has the lowest life, still exhibits more than five times the mean life of the   unpatched specimens.

94
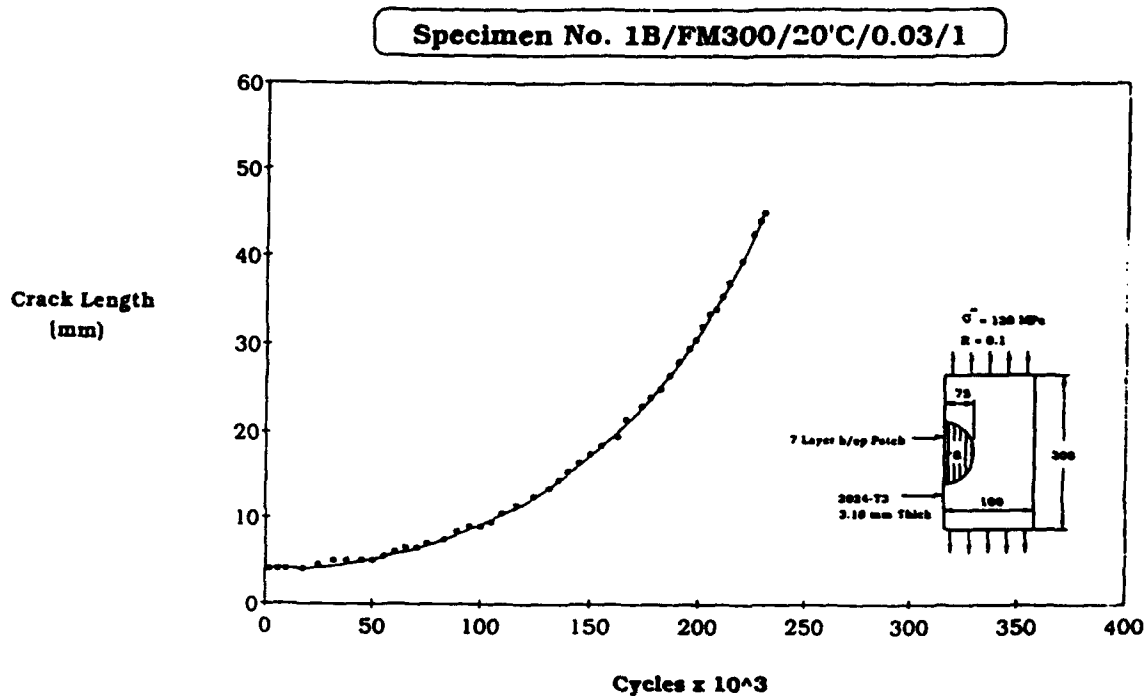
FIGURE 3-1. FATIGUE CRACK LENGTH FOR SPECIMEN 1B
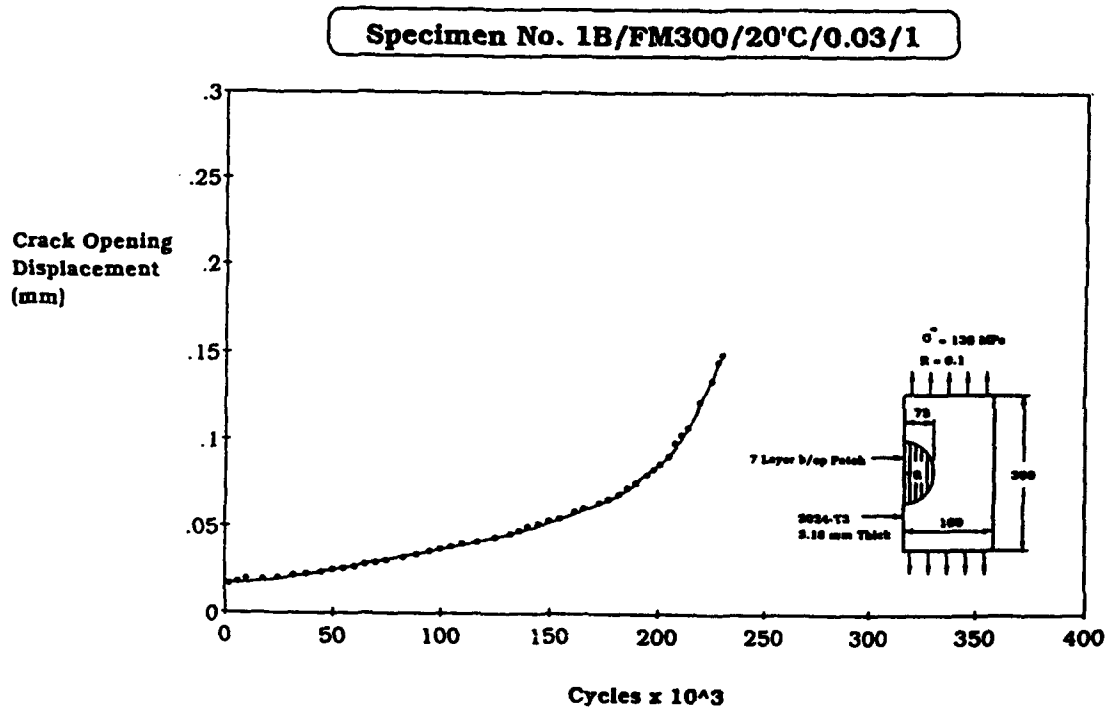
FIGURE 3-2. FATIGUE CRACK OPENING DISPLACEMENT FOR SPECIMEN 1B

95
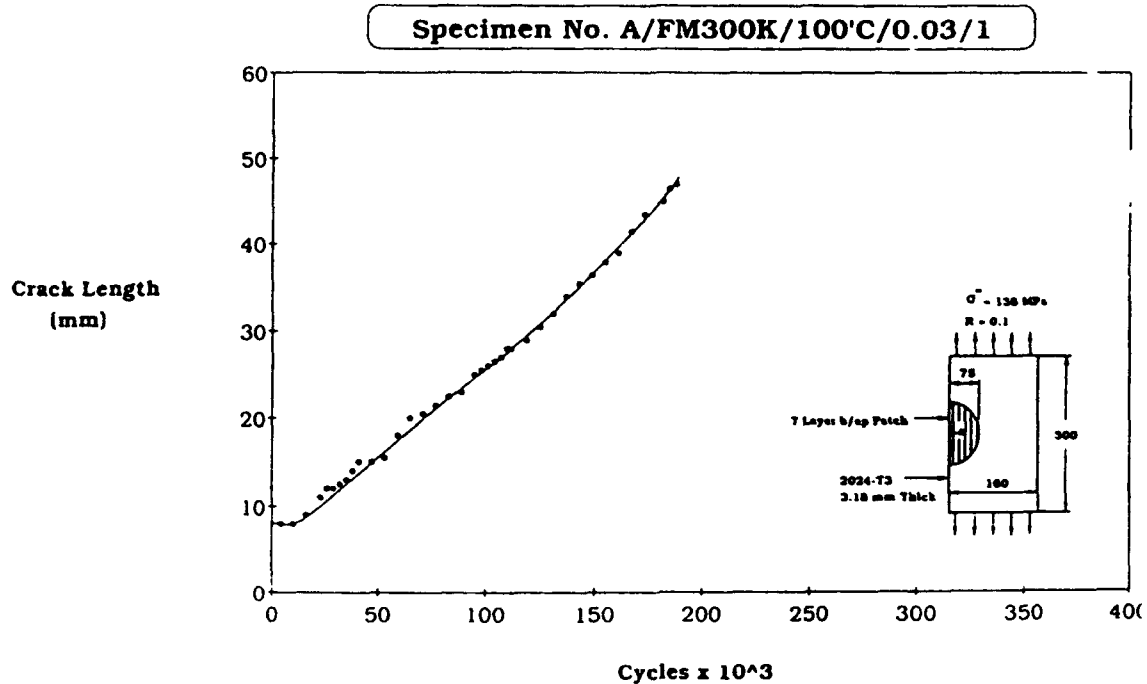
FIGURE 3-3. FATIGUE CRACK LENGTH FOR SPECIMEN A
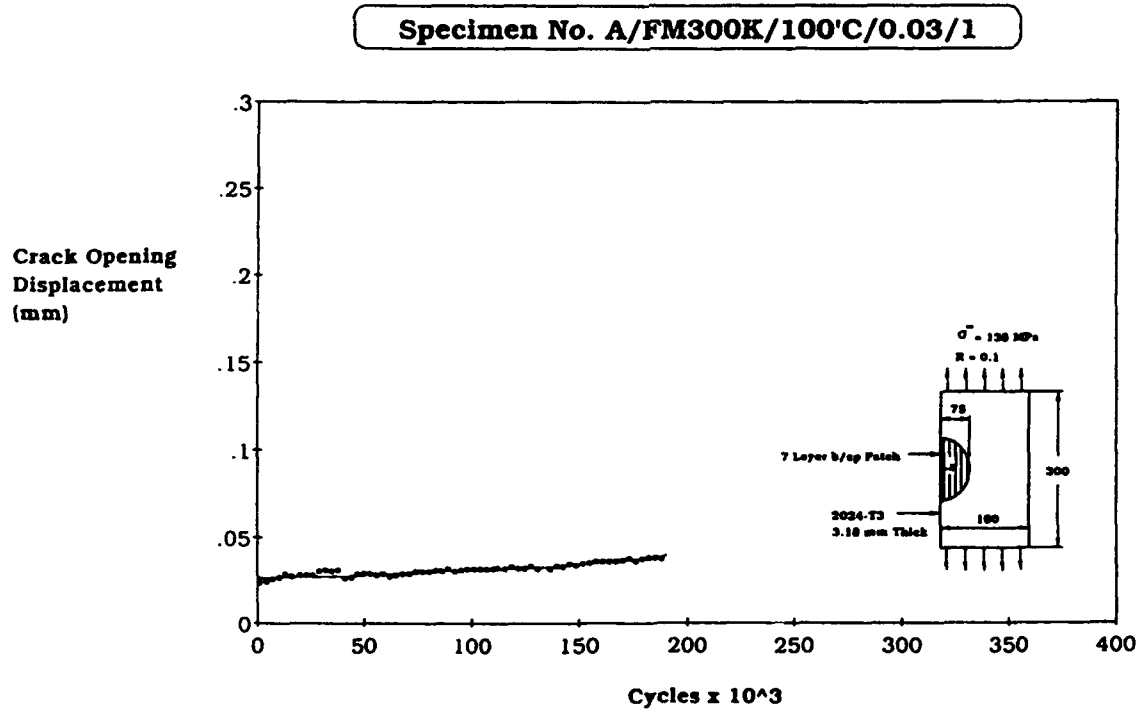
FIGURE 3-4. FATIGUE CRACK OPENING DISPLACEMENT FOR SPECIMEN A

96

Specimen No. B/FM300K/100'C/0.03/1

Crack Length (mm)

Cycles x 10^3
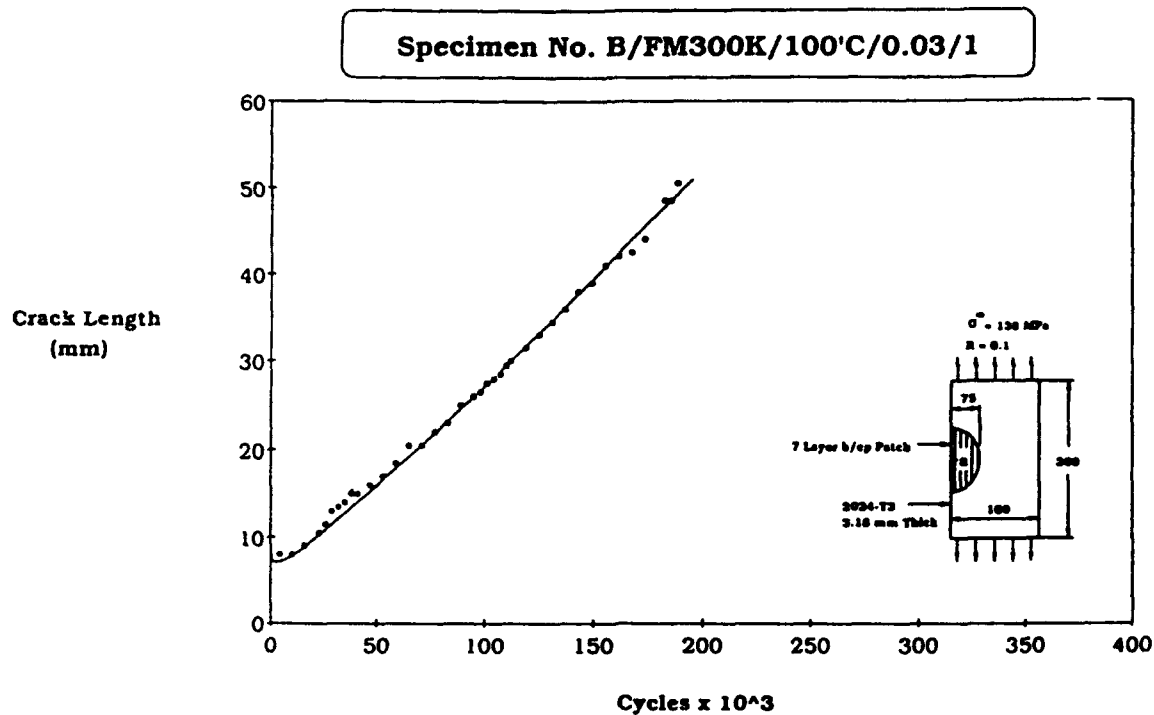
FIGURE 3-5. FATIGUE CRACK LENGTH FOR SPECIMEN B

Specimen No. B/FM300K/100'C/0.03/1

Crack Opening Displacement (mm)

Cycles x 10^3
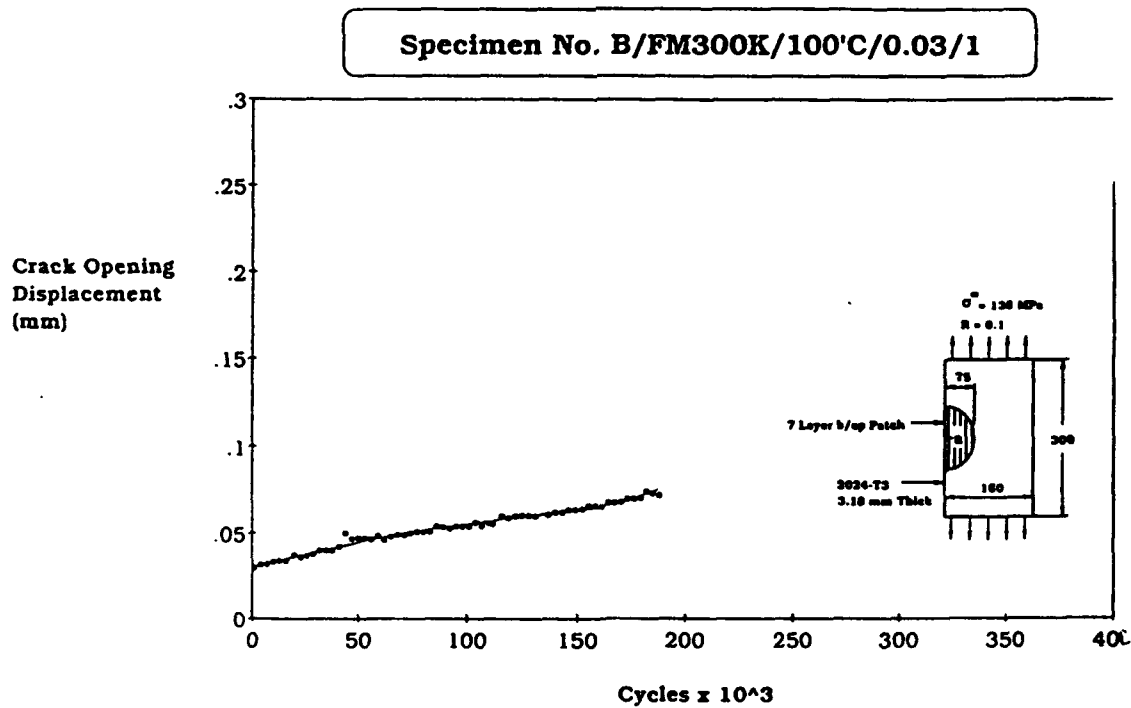
FIGURE 3-6. FATIGUE CRACK OPENING DISPLACEMENT FOR SPECIMEN B

97

All dimensions in mm
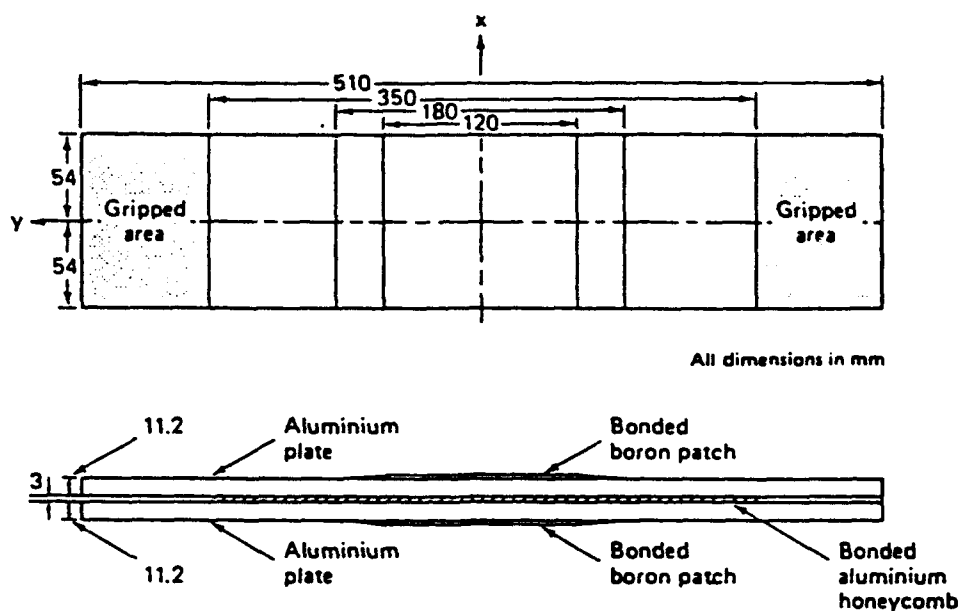
FIGURE 3-7 TEST GEOMETRY FOR THE SURFACE FLAW SPECIMEN

TABLE 3-1. FATIGUE LIVES OF PATCHED AND UNPATCHED SPECIMENS

Specimen Condition	Specimen Number	Cycles to Failure
Unpatched	1U	21,500
	2U	21,800
	3U	30,439
	4U	27,980
	5U	29,000
	mean life	26,144
Patched	1P	728,000
	2P	137,000
	3P	728,000
	4P	451,000
	5P	1,253,000
	6P	170,000
	mean life	577,000

3.2.2 FALSTAFF Fatigue Testing

Following the initial tests it was decided to perform additional test under a FALSTAFF loading sequence with a peak stress of 137.8 MPa. The patch thickness was left unchanged even though it was initially chosen so as to prevent yielding in the adhesive, at 68.9 MPa (yield stress of adhesive). The stress has been increased in an attempt to ensure that the adhesive will yield and accumulate fatigue damage, thereby enabling the damage tolerance of the repair to be evaluated. In this series of tests particular attention will be paid to whether:

1) large disbonds can be tolerated without failure of the patch

2) large disbonds negate the reduction in crack growth rate which results from patching. The ability of a bonded patch to withstand large disbonds without failure and still provide a significant decrease in crack growth rate is central to the application of this technology to civil aircraft.

Fatigue testing was carried out at a frequency of 5 Hz using a computer controlled servohydraulic Amsler machine of 600 kN dynamic capacity. Eight specimens were subjected to FALSTAFF loading [17-19] (peak stress 137.8 MPa) under amplitude adaptive control. The remaining two specimens were subjected to constant amplitude block loading where the maximum stress was 65.5 MPa, and the stress ratio, R, was 0.1. This was followed by loading at the same maximum stress but with the stress amplitude halved. The low stress amplitude blocks were introduced in order to mark the crack front. The growth of surface cracks was monitored using plastic replicas for unpatched specimens and an eddy current technique (Elotest B1) for patched specimens.

The fatigue lives of specimens subjected to FALSTAFF loading (peak stress 137.8 MPa) are given in Table 3-2 below.

TABLE 3-2. EFFECT OF PATCHING ON FATIGUE LIFE (FALSTAFF)

Patched/unpatched	Specimen	Cycles to failure
Unpatched	9/22U	344,039
	5/6U	326,056
	3/4U	411,595
	7/8U	334,778
	mean	354,117
Patched	14/15P	1,954,783
	18/19P	2,699,357
	16/17P	1,923,680
	12/13P	1,632,406
	mean	2,052,557

These results show that the patch increased fatigue life by a factor of approximately 5.8. This is much lower than the factor of 22 obtained previously for constant amplitude testing (maximum stress=65.5 MPa, R=0.01). Thus, the remaining two specimens were tested under constant amplitude conditions similar to those used before but with additional low amplitude marker blocks. Fatigue lives of 2,061,556 and 74,878 cycles were obtained for the patched and unpatched specimens, respectively, which indicates that patching increased fatigue life by a factor of 28. This is in good agreement with the prior results and therefore the relatively poor patch performance observed in the present work for FALSTAFF loading cannot be attributed to degradation during long term storage or handling. Indeed the reduction is due to fatigue damage in the adhesive, as was the intent of these tests.

The effect of patching on the growth of surface cracks is shown in Figure 3-8, where length of surface crack from edge of 40 mm length notch (Δa) is plotted against number of FALSTAFF cycles in Figure 3-8. The shaded areas cover the data obtained for four patched and four unpatched specimens. Examination of fracture surfaces revealed that cracks grew through the plates from the base of the surface flaws before any surface crack growth was detected. It follows from Figure 3-8 that the growth of through cracks accounted for at least half the fatigue life of both patched and unpatched specimens. The beneficial effect of patching on the rate of growth of through cracks is shown in Figure 3-9 where crack growth rate (da/dN) is plotted against normalized crack length (a/b). Data are shown for three patched and three unpatched specimens where similar rates of crack growth were observed for front and back plates. The solid symbols show data obtained from fractography; crack growth rates were determined by measuring distances between crack front markings associated with level 32 loads. Constant amplitude loading results are shown in Figure 3-10; when a/b is in the range 0.4 to 0.5 the reduction in crack growth rate is more pronounced than that observed for FALSTAFF loading. Figure 3-10 also shows da/dN - ΔK data determined for the unpatched specimen (dotted line) and for a smaller center cracked 2024-T4 specimen (solid line). The smaller specimen was tested in order to obtain da/dN - ΔK data at crack growth rates as low as those observed for the patched specimen.
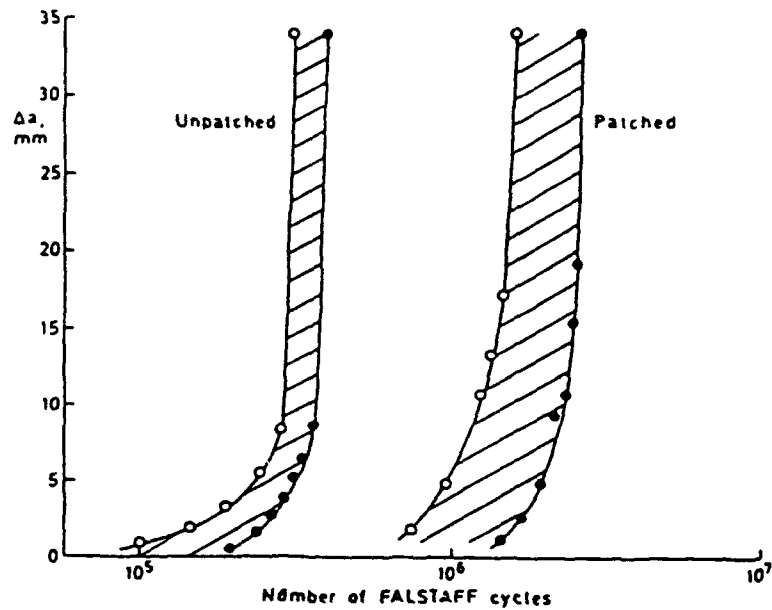
FIGURE 3-8. EFFECT OF PATCHING ON GROWTH OF SURFACE CRACKS DURING FALSTAFF
LOADING
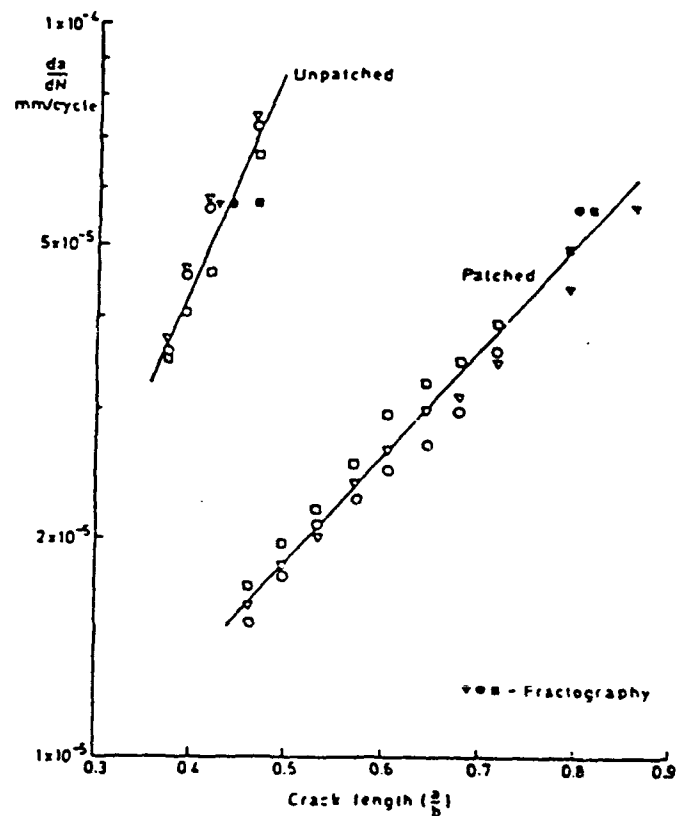
FIGURE 3-9. EFFECT OF PATCHING ON RATE OF GROWTH OF THROUGH CRACKS DURING
FALSTAFF LOADING

101
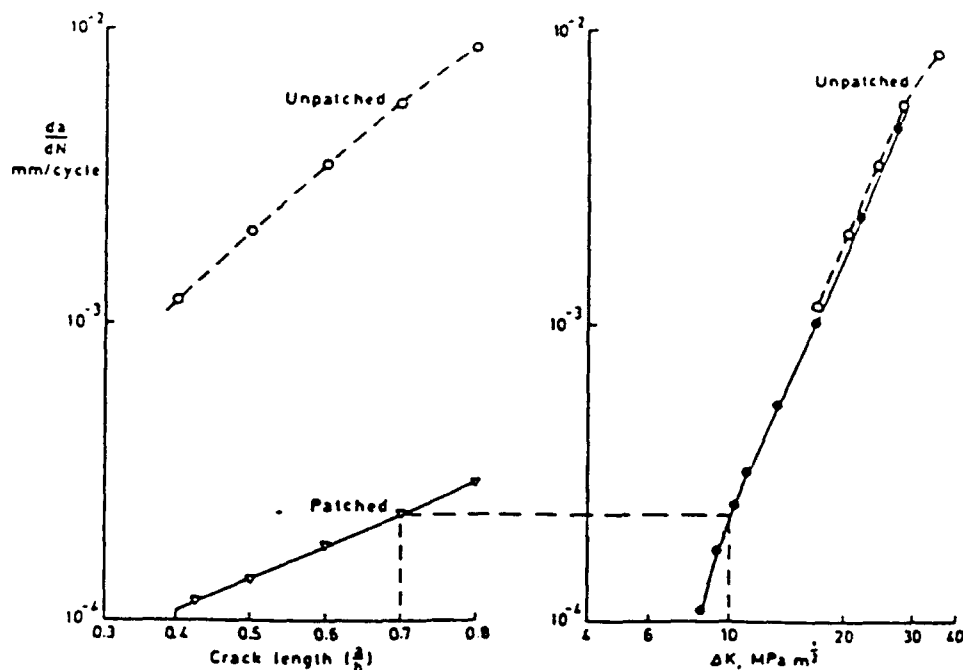
FIGURE 3-10. EFFECT OF PATCHING ON RATE OF GROWTH OF THROUGH CRACKS DURING
CONSTANT AMPLITUDE LOADING

3.2.3 SPATE Studies

SPATE (Stress Pattern Analysis by Thermal Emission) studies were carried out on selected patched specimens for two main reasons:

a) To obtain information concerning the magnitude and distribution of stresses in the surface layers of patches as a function of crack length.

b) To establish the extent to which the technique may be used to monitor the growth of cracks under patches.

In the present work a SPATE 8000 scan unit was set up normal to and 80 cm from the patch surface, which had been sprayed with matt black paint to give a surface of uniform high infrared emissivity. Patched specimens were subjected to constant amplitude sinusoidal loading (frequency 5 Hz, maximum stress 22 MPa, minimum stress 2 MPa) during SPATE scans. It was considered that intermittent loading under these conditions would not significantly affect the results of fatigue tests under FALSTAFF loading (peak stress 137.8 MPa); this was subsequently confirmed by comparing the results of tests with and without intermittent SPATE scans. Patch surface areas measuring 147 X 97 mm were scanned; 62 X 41 points approximately 1 mm in diameter, were sampled over a period of 25 minutes.

Two strain gauge rosettes were applied to the patch at positions 50 mm above and 50 mm below the center of the notch, to enable strains at 0° and 90° to the fiber direction to be measured. A full SPATE scan, as described earlier, was carried out during constant amplitude loading at 5 Hz, R=0.1 and stress range $\Delta\sigma$=20 MPa. Line scans adjacent to the strain gauges

102

·ere then carried out during constant amplitude loading at higher stress ranges. Figure 3-11 shows the average SPATE output for these line scans plotted against longitudinal stress range, as determined from strain gauge measurements and materials properties. This calibration, which accounts for mean stress effects, assumes that the relative contribution of the transverse stresses to the SPATE output was the same over the entire patch surface. Possible calibration errors associated with this assumption are believed to be relatively small. As found in the previous section the strain gauge readings indicated that the longitudinal stress contribution dominated the SPATE output (the transverse stress contribution was less than 8% of the longitudinal contribution).

Testing under FALSTAFF loading was interrupted at selected intervals and SPATE scans carried out. In order to take account of possible variations in test conditions, eg. ambient temperature, average SPATE o :tputs for 24 scan points in identical areas adjacent to the strain gauges were compared, and the SPATE outputs were normalized with respect to the corresponding data obtained before FALSTAFF loading commenced. These normalized SPATE outputs and the calibration shown in Figure 3-11 were used to determine constant longitudinal patch stress contours.

Figure 3-12 shows typical stress patterns determined from SPATE scans after various periods of FALSTAFF loading; the longitudinal stress range contours shown were obtained using SPATE 9000 software. Figure 3-12a shows the position of the 40 mm long surface flaw and the relatively low stress concentration observed in the patch over the surface flaw before FALSTAFF loading commenced. An average longitudinal stress range of approximately 40MPa was observed for most of the patch surface. Figure 3-12b shows that stress concentration in the patch was much more pronounced after 1.0×10^6 FALSTAFF cycles when a 40 mm long through crack had developed. Figure 3-12c shows the increased length of through crack (55 mm) and associated stresses in the patch which were observed after 1.5×10^6 FALSTAFF cycles; as in Figure 3-12b the positions of the crack tips correspond to 50-57 MPa longitudinal stress range contours in the patch. The stress pattern observed after 1.88×10^6 FALSTAFF cycles, shortly before failure at 1.92×10^6 cycles, is shown in Figure 3-12d. The crack tip on the right-hand side again corresponds to the 50-57 MPa contour, but the crack tip on the left-hand side was difficult to determine using the eddy current technique, owing to edge effects. The shape of the stress contours in Figure 3-12d suggested that debonding had occurred and this was confirmed by ultrasonic inspection which detected debonding in the area indicated by the dotted line. Similar SPATE results were obtained for another patched specimen, where three additional strain gauges were located at positions over the center and edge of the initial flaw and at a point midway between the edge of the initial flaw and the edge of the specimen. Longitudinal stress ranges measured from these strain gauges were in good agreement with the stress contours obtained from SPATE measurements using the calibration method described above.
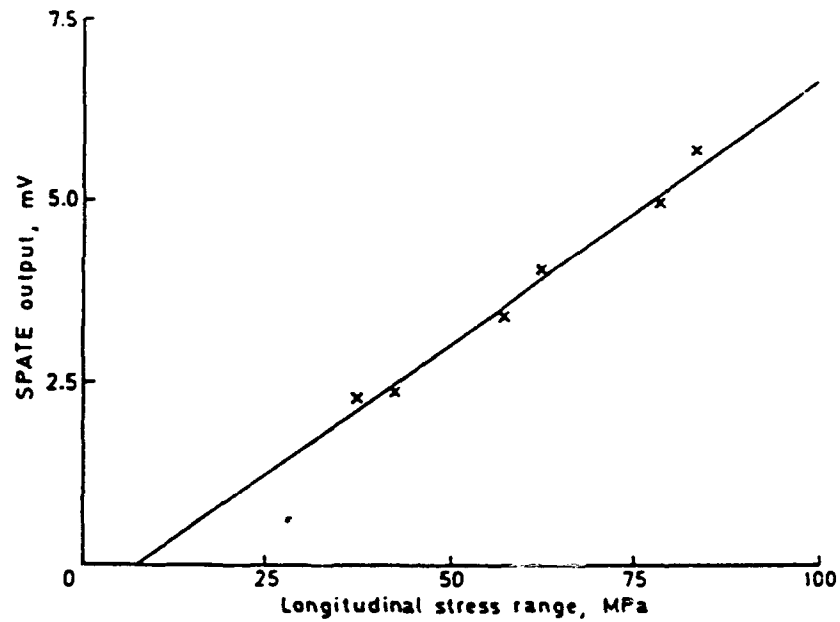
FIGURE 3-11. SPATE OUTPUT VS. STRESS RANGE IN FIBER DIRECTION IN PATCH
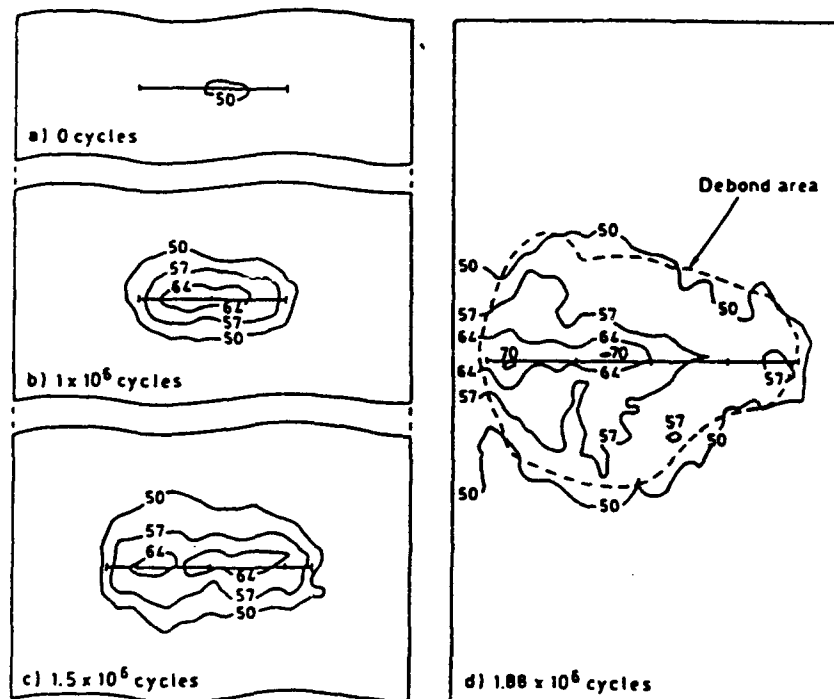
FIGURE 3-12. SPATE STRESS PATTERNS SHOWING VARIATION OF PATCH STRESSES IN
FIBER DIRECTION DURING FALSTAFF LOADING

104

3.2.4 Ultrasonic Inspection of Bondlines

In view of the debonding reported above for one specimen, it was decided to use a pulse-echo ultrasonic technique to monitor the growth of debonds during fatigue testing of the three remaining patched specimens. The technique involved the use of a hand-held 10 MHz transducer, with plastic spacer.

Extensive debonding was observed for two specimens subjected to FALSTAFF loading; typical results for one side of one specimen are shown in Figure 3-13. A detailed description and discussion of rate of growth of debonds is beyond the scope of this report. However, it was observed that the edge of the debonded area was frequently close to the crack tip position and that the shape of the debonded area tended to be elliptical. The worst case was assumed to be represented by an elliptical debond where the minor axis/major axis ratio was 0.7 and the major axis was of the same length as the through crack. In contrast to specimens tested under FALSTAFF loading, no debonding was detected in the case of the patched specimen tested under constant amplitude loading.

3.2.5 Conclusions

1. Adhesively bonded BFRP patches increased the fatigue life of 11.2 mm thick aluminum alloy plate specimens containing surface flaws by a factor of 5.8 for FALSTAFF loading (peak stress 137.8 MPa) and by a factor of approximately 28 for constant amplitude loading (R=0.1,

Debond	Cycles
1	1.00×10^6
2	1.25×10^6
3	1.50×10^6
4	1.75×10^6
5	1.88×10^6
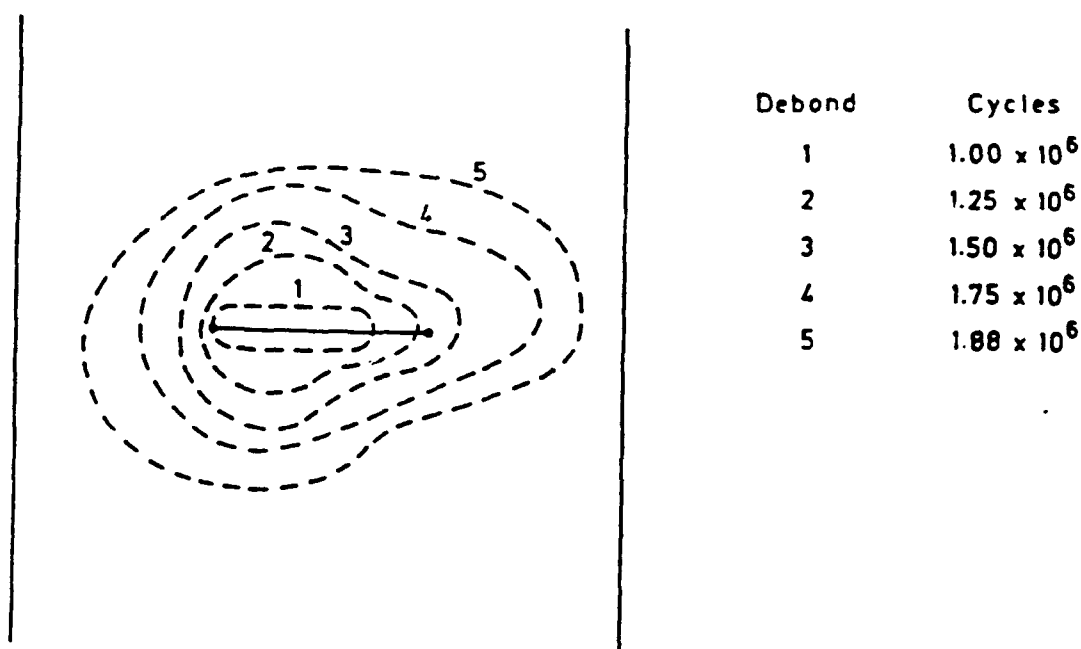
FIGURE 3-13. DEVELOPMENT OF DEBOND DURING FALSTAFF LOADING
(SPECIMEN 16/17P)

maximum stress=65.5 MPa).

2. The rate of growth of through cracks was markedly reduced by patching; the reductions in crack growth rate were greater for the constant amplitude loading than for the FALSTAFF loading.

3. Debonding occurred during the FALSTAFF loading tests but not during the constant amplitude loading tests. This observation is consistent with the better patch efficiency indicated by the constant amplituae tests.

The debonding was deliberately induced to evaluate the damage tolerance of the structure. Indeed the results show that even though there were large disbonds the doublers did not fail, and that the rate of crack growth was dramatically reduced (when compared with the unpatched case). The delamination damage was sufficiently severe so that it could be found easily using either ultra sounds or SPATE. This represents a severe test of the ability of bonded doublers to increase fatigue life, even in the presence of severe delamination damage. It is particularly severe in that the cracked component is relatively thick, ie. 11.2 mm. Further tests are to be performed in a hot-wet-salt environment.

3.3 SURFACE CRACK AT HOLE SPECIMENS

The fatigue testing of specimens with three-dimensional flaws at the edge of a fastener hole that are repaired with a bonded sleeve and/or a bonded composite patch. For convenience and repeatability of flaw geometry, the flaw used was a notch, to simulate approximately the behavior of a specimen with a crack. Significant increases in fatigue lives are anticipated. As previously mentioned the repair of these three-dimensional flaw geometries was chosen since they closely simulate the crack geometries occurring in practice.

3.3.1 Specimen and Repair Geometries

Two variations of a corner flaw specimen were considered. As shown in Figure 3-14, the two specimen geometries were basically the same, each containing a fastener hole with two diametrically opposed quadrant notches, but with one having a larger hole radius. The smaller hole and larger hole specimens are designated as specimens A and B respectively. These basic unrepaired specimens were machined from the same batch of 11.2 mm thick 2024-T4 aluminum alloy extruded plates, with the rolling direction along the length of the specimen. The notches were obtained using spark erosion methods with the notch cut being approximately 0.25 mm thick. The specimen dimensions were chosen so that the thickness, hole and flaw size were realistic representations of fastener holes in service in aircraft structures. The width of the specimen (i.e. more than 10 times the hole diameter) was chosen so that finite width effects on the stress field around the hole would be negligible.

106

(i) Specimen A   (ii) Specimen B
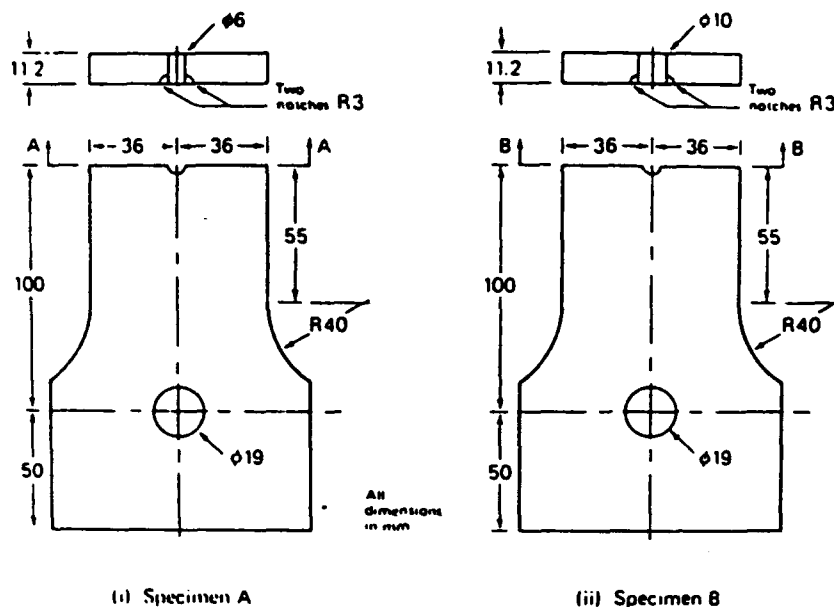
FIGURE 3-14. DIMENSIONS OF SPECIMENS A AND B

Two types of bonded repair schemes were investigated as shown in Figure 3-15. In scheme 1, a 1 mm thick steel sleeve was bonded into the hole using the toughened acrylic adhesive Permabond F241. In scheme 2, a 1 mm thick steel sleeve was bonded into the hole, using an epoxy adhesive, Hysol EA9321, and a unidirectional boron/epoxy fiber composite patch was bonded over the front face of the specimen. The patch consisted of ten layers of boron/epoxy and was bonded to the specimen using the Cyanamid film adhesive FM73. Details of the bonding procedures used in both schemes are given in Appendix C.

Bonding the patch to one side only caused the specimen to bend slightly due to the difference in the coefficients of thermal expansion of the aluminum and the boron epoxy. The amount of out of plane displacement was of the order of 0.5 mm. Hence while these patched specimens would be somewhat eccentrically stressed, the effect of the prebend on the stresses in the critical region was considered to be negligible.

The following specimen configurations are being tested:

A.   4 type A specimens without a repair

B.   4 type A specimens repaired with scheme 1

C.   4 type A specimens repaired with scheme 2

D.   1 type A specimen repaired with scheme 2, but with patch removed after 2,437,200 cycles (designate this as scheme 3)

E.   3 type B specimens without a repair

F.   4 type B specimens repaired with scheme 1

107
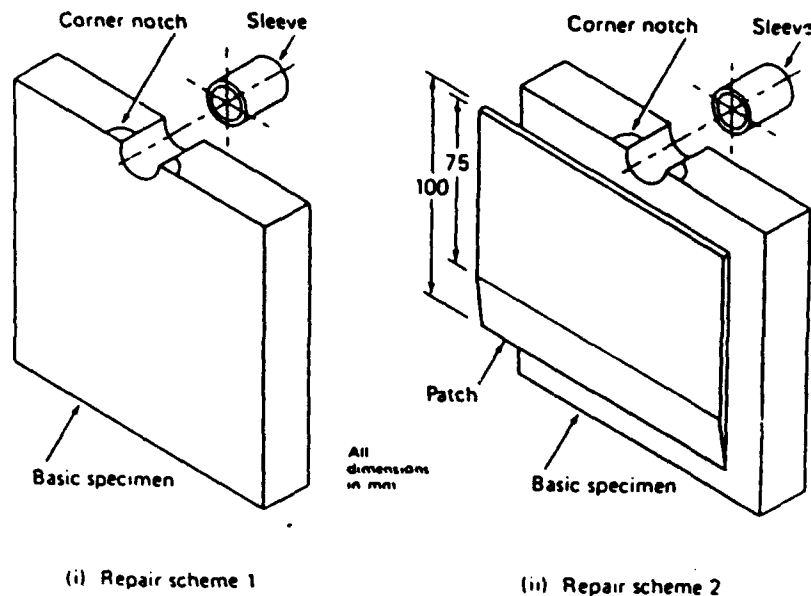
FIGURE 3-15. SPECIMEN REPAIR SCHEMES 1 AND 2

3.3.2 Testing and Results

Constant amplitude fatigue testing was carried out using an Instron 1255 servo-hydraulic testing machine with a dynamic loading range of ±250 kN. The gross area tensile stress at the notch region was 68.9 MPa with stress ratio R=0.01 for all specimens and the loading frequency was 26 Hz.

3.3.2.1 Unrepaired Specimens and Specimens Repaired with Scheme 1

While the main aim in this work was to compare final fatigue lives at failure, it was also decided to monitor the growth of the cracks on the specimen surface. A loading rig was used to provide enough room between the hydraulic grips to make use of a traveling microscope. The rig was designed with a double pin joint attached to each end of the specimen with the specimens being clamped by tightening bolts to provide a relatively uniform stress field 100 mm above and below the crack line. The microscope used had a vernier scale with a smallest unit of measure of 0.01 mm. A wooden board attached to the testing machine frame was used as a working platform for the microscope. Two light sources were used to illuminate the specimen crack tip regions.

Crack tip coordinates were thus measured at various intervals and the tip to tip distance evaluated. The fatigue crack growth results are given in Figures 3-16 and 3-17. The fatigue lives to failure are given in Tables 3-3 and 3-4.

It can be seen from Tables 3-3 and 3-4 that the fatigue lives of both specimen types A and

108

B were significantly increased by using repair Scheme 1. The increases were of the order of 70% over the unrepaired specimens. Figures 3-16 and 3-17 show that the presence of the sleeve marginally increased the time for crack initiation, but subsequently also reduced the surface crack growth rate until the crack was relatively long. This indicates that the adhesive remained effective for most of the specimen life and did not prematurely fail. As expected, the fatigue lives for the type A specimens were greater than the type B specimens.

TABLE 3-3. FATIGUE TEST RESULTS FOR SPECIMEN TYPE A

Specimen condition	Specimen Number	Fatigue Life (cycles)	Average (cycles)
Unrepaired	A-1	94,240	
	A-2	104,150	113,537
	A-3	137,830	
	A-4	117,930	
Repaired with Scheme 1	A-5	119,800	
	A-6	179,160	215,405
	A-7	277,310	
	A-8	285,351	
Repaired with Scheme 2	A-9	623,630*	
	A-10	2,347,200*	N/A
	A-11	2,253,500*	
	A-12	5,078,200@	
Repaired with Scheme 3 (specimen A-10 with patch removed)	A-13	558,920	558,920

*Specimen failed in grips, no cracking of notched hole observed
@Test stopped, no cracking of notched hole observed

TABLE 3-4. FATIGUE TEST RESULTS FOR SPECIMEN TYPE B

Specimen condition	Specimen Number	Fatigue Life (cycles)	Average (cycles)
Unrepaired	B-1	97,600	
	B-2	86,600	94,967
	B-3	100,700	
Repaired with Scheme 1	B-5	162,500	
	B-6	147,000	203,900
	B-7	258,000	
	B-8	248,100	

3.3.2.2 Specimens Repaired Using Scheme 2

The first three of these specimens, i.e. A-9, A-10 and A-11, failed in the loading grips. Specimen A-12 was removed after it had experienced more than 5,000,000 cycles (see Table 3-3). The loading method for specimen A-9 was as described above, and the specimen failed in

the grips due to a crack which initiated due to the combined effects of a surface scratch at the specimen edge and from fretting within the loading fixture.

Because of the failure of specimen A-9 in the loading fixture, subsequent specimens (i.e. A-10, A-11 and A-12) were clamped directly in the machine hydraulic grips using backing plates and 3M's 'Screenback', to minimize the likelihood of fretting. These later specimens were also polished at the edges at the grip line region to minimize crack propagation outside the gauge length. As a results of these measures specimens A-10 and A-11 did not fail at the edge, but instead failed at the edge of the hole in the grips at a much greater number of cycles than specimen A-9. Following these tests the composite patch was removed from the three specimens, A-9, A-10 and A-11 and it was found that there was no crack propagation on the front surface of the specimens. Also, the sleeve was removed from specimens A-9 and A-11, revealing that there had been no cracking along the bore of the hole.

It can be seen from Table 3-3 that no fatigue cracking was found in the region of interest for any of the type A specimens which were repaired using Scheme 2. A large fatigue life was apparent considering that the one specimen that did not fail in the loading grips achieved 5,000,000 cycles before the test was stopped, representing a 50 fold increase in fatigue life over the unrepaired specimens. It is believed that this repair scheme has reduced K around the crack front to a level below the threshold value for crack growth. This is consistent with the fact that upon removal of the patch from the three specimens it was found that there was no cracking on the specimen surfaces.
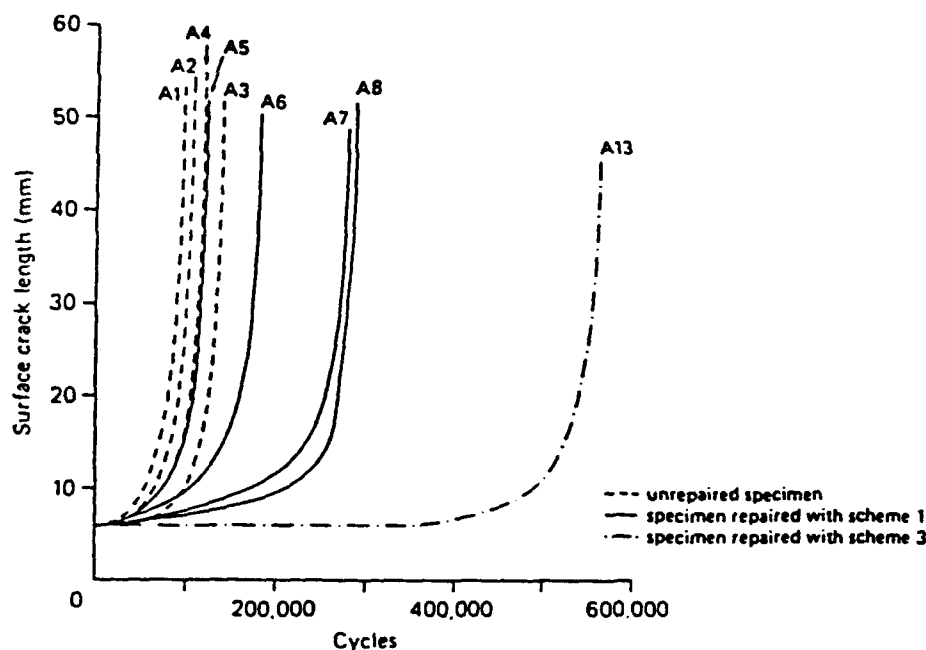
FIGURE 3-16. SURFACE CRACK LENGTH VS. CYCLES FOR TYPE A SPECIMENS WITH & WITHOUT REPAIR SCHEME 1

110
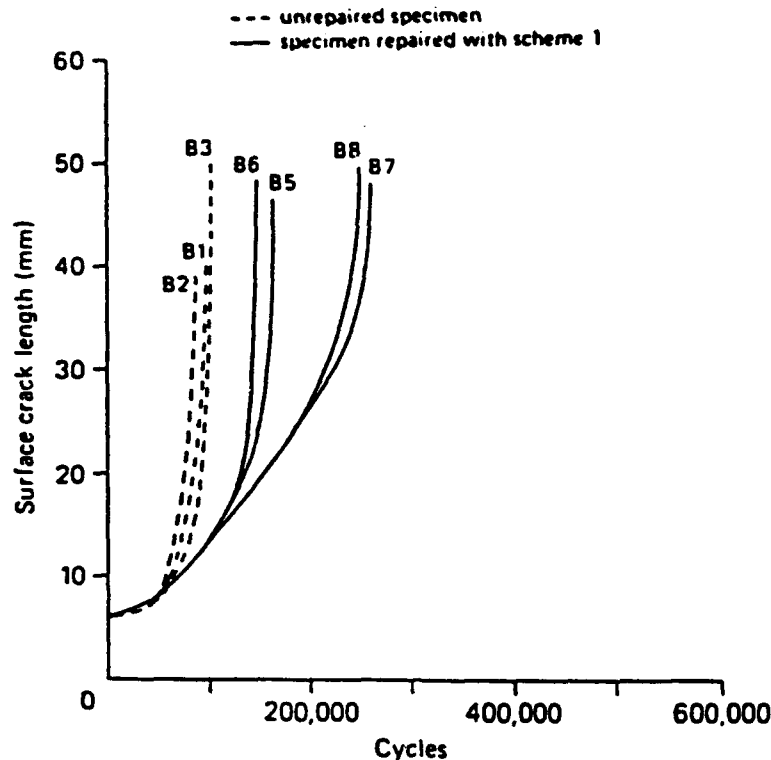
FIGURE 3-17. SURFACE CRACK LENGTH VS. CYCLES FOR TYPE B SPECIMENS WITH &
WITHOUT REPAIR SCHEME 1

3.3.2.3 Specimens Repaired Using Scheme 3

To allow an approximate comparison of the use of the two different adhesives (and associated bonding procedure) for specimens repaired with a bonded sleeve only, specimen A-10 with patch removed was retested. The top of this specimen was mounted directly into the machine grips as per the Scheme 2 specimens, while the bottom was loaded as per the Scheme 1 specimens. Since this specimen had previously been fractured across the top hole, the distance between the top machine grip and the crack line was only 50 mm, as opposed to 100 mm for previous specimens. Surface crack growth results were again obtained and are given in Table 3-3. For clarity we will call this configuration Scheme 3 and rename the specimen A-13.

The results of Table 3-3 show that there was approximately a 100% increase over the fatigue lives achieved using Scheme 1, and it should be remembered that the Scheme 3 specimen had previously been loaded for over 2,000,000 cycles before patch removal. Although only one Scheme 3 specimen was tested, the results obtained seems to indicate that the sleeve adhesive and bonding approach used in Scheme 3 is better than that of Scheme 1. Similar comments regarding crack growth rate apply to Scheme 1 specimens.

111

3.3.3 Conclusion and Recommendations

It has been shown that the stress intensity factors for three-dimensional flaws at hole edges in an aluminum alloy 2024-T4 plate are significantly reduced by bonded steel sleeves and bonded unidirectional boron/epoxy composite patches, either used separately or together. First order estimates can be obtained for the three dimensional geometries investigated by comparison with simpler finite element or handbook solutions. The K reductions obtained indicate the potential for significant increases in fatigue life for cracked fastener holes. The primary limiting factor is considered to be the level of stresses in the sleeve adhesive leading to possible yielding and/or fracture of the adhesive.

The experimental test program revealed that significant increases in the fatigue life of corner cracked fastener holes can be achieved using a bonded sleeve alone. However, using a combination of bonded patch and bonded sleeve is considerably better, increasing the fatigue life of the specimens in the present study by 1 to 2 orders of magnitude. Using a sleeve alone reduces the rate of crack growth until the crack reaches a relatively long length, whereas using both a patch and a sleeve stops the crack growth.

While the present study indicates that there is much promise in these repair approaches, it is believed that the effects of higher load levels and/or variable amplitude loading on the integrity of the sleeve adhesive should be investigated in any future studies.

It is believed that the primary limiting factor in the repair approaches described here will be the level of stresses developed in the sleeve adhesive, leading to the possibility of yielding and/or fracture of the adhesive. The present study has considered fatigue testing at one level of constant amplitude loading, and it was found that the sleeve adhesive performed well. However, it is believed that the effects of higher load levels and/or variable amplitude loading should be investigated in any future studies.

4. LAP JOINT WITH MULTIPLE SITE DAMAGE

In recent times the phenomenon of multi-site damage (MSD) in structures has received a great deal of attention. The consequence of the undetected presence of MSD was dramatically illustrated through the in-flight failure of a fuselage lap joint on an Aloha B-737 aircraft on April 28, 1988. Essentially this failure occurred due to numerous small cracks along a fastener line linking together, causing the residual strength of the fuselage to be exceeded under pressure.A test specimen representative of fuselage lap-joints used in commercial wide bodied aircraft was developed. This specimen was subsequently used to evaluate possible boron epoxy repairs for fuselage lap joints.

4.1 REPAIR OF MULTIPLE SITE DAMAGE IN PRACTICE

Current repair methods for detected cracking in fuselage lap joints involve removing the damaged material and the use of a riveted scab patch, see Figure 4-1. The concern here is that this introduces further stress concentrations, due to the increase in fastener holes, and that the close proximity of these repairs may lead to a compromise in the damage tolerance of the structure. The objective of this investigation was to evaluate a possible bonded repair or life enhancement for mechanically fastened fuselage lap joints.
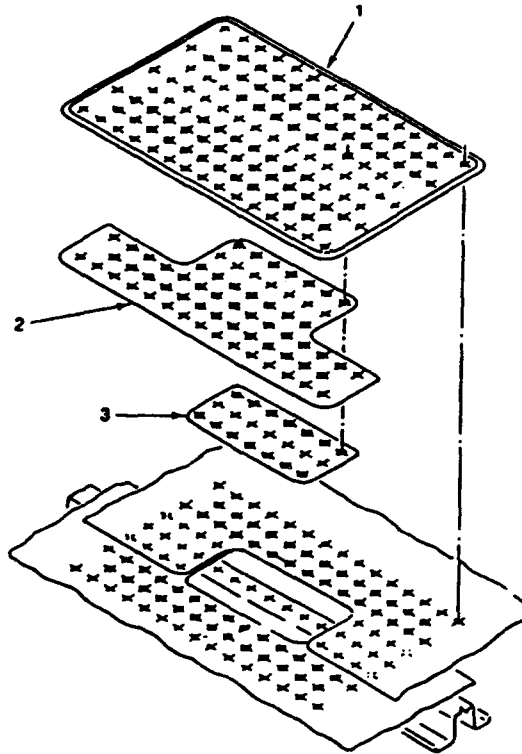
FIGURE 4-1. TYPICAL LAP JOINT FASTENED REPAIR

113

4.2 SPECIMEN DESCRIPTION

Figure 4-2 details a typical configuration of a modern wide bodied aircraft pressurized fuselage construction. For the purpose of this work attention is focused on the lap joint area. Local details of this location vary depending upon the age of the aircraft and specific manufacturers details. Figure 4-3 details a typical lap joint configuration.

It should be noted that, in many cases, in addition to fasteners the lap joints are bonded together to increase the fatigue life of the joint. In service, environmental degradation may cause this bond to become ineffective and corrosion of the mating skins could accelerate the onset of MSD. For these reasons bonded lap joints are not considered in this work.

In the present investigation, a worst case scenario was assumed, viz: a non-bonded, full depth, upper plate, counter-sunk configuration as shown in Figure 4-3. Here the counter-sunk rivet hole, if accompanied by improper rivet head seating, leads to a phenomenon known as "knife-edging". This in turn leads to a reduction in the fatigue life of the joint, relative to the case where the countersink does not fully penetrate the plate, due to the sharp corners accelerating the initiation of cracks.

The basic specimen used in this investigation consisted of two 2024-T3 clad aluminum alloy sheets 1.016mm (0.04in) thick, fastened with three rows of BACR15CE-5, 100° shear head countersunk rivets, 3.968mm (5/32in) diameter, as shown in Figure 4-4. The width of the specimen was chosen to coincide with the typical distance between tear straps of a typical transport aircraft.

The upper row of rivet holes contained initial cracks induced by means of the electrical spark erosion technique. The cracks were on either side of the hole and were nominally 1.2mm long, see Figures 4-5 and 4-6. This length was chosen so that the defect was obscured by the fastener head, which is representative of possible undetectable flaws. These flaws were achieved by drilling the rivet holes undersize (ie. drill gauge #24, 3.85mm diameter), spark eroding the initiation sites to 1.225mm, and then machining the counter-sunk (using drill gauge #21, 4.039mm to achieve the required hole diameter). The accuracy to which the latter was performed determined the final configuration of the defects. In some cases the defects only remained on one side of the hole, the other being removed by the tool. Following this the fasteners were inserted.

After pre-cracking   cycles   , a bonded doubler was applied over the joint. The doubler used was a multi-segmented unidirectional boron/epoxy laminate, containing ten plies at the greatest thickness. The laminate, (203.2 long by 203.2 mm wide), was bonded over the joint with one segment butting up against the skin step, to provide an alternative load path for each row of fasteners.

Two different methods were used to bond the boron/epoxy doubler. Both a cold-setting adhesive (Flexon 241), and a hot-curing adhesive (FM-73) were investigated. Doublers were applied both as a reinforcement, (specimens with short cracks emanating from rivet heads),

114

and as a repair (specimens completely cracked through).
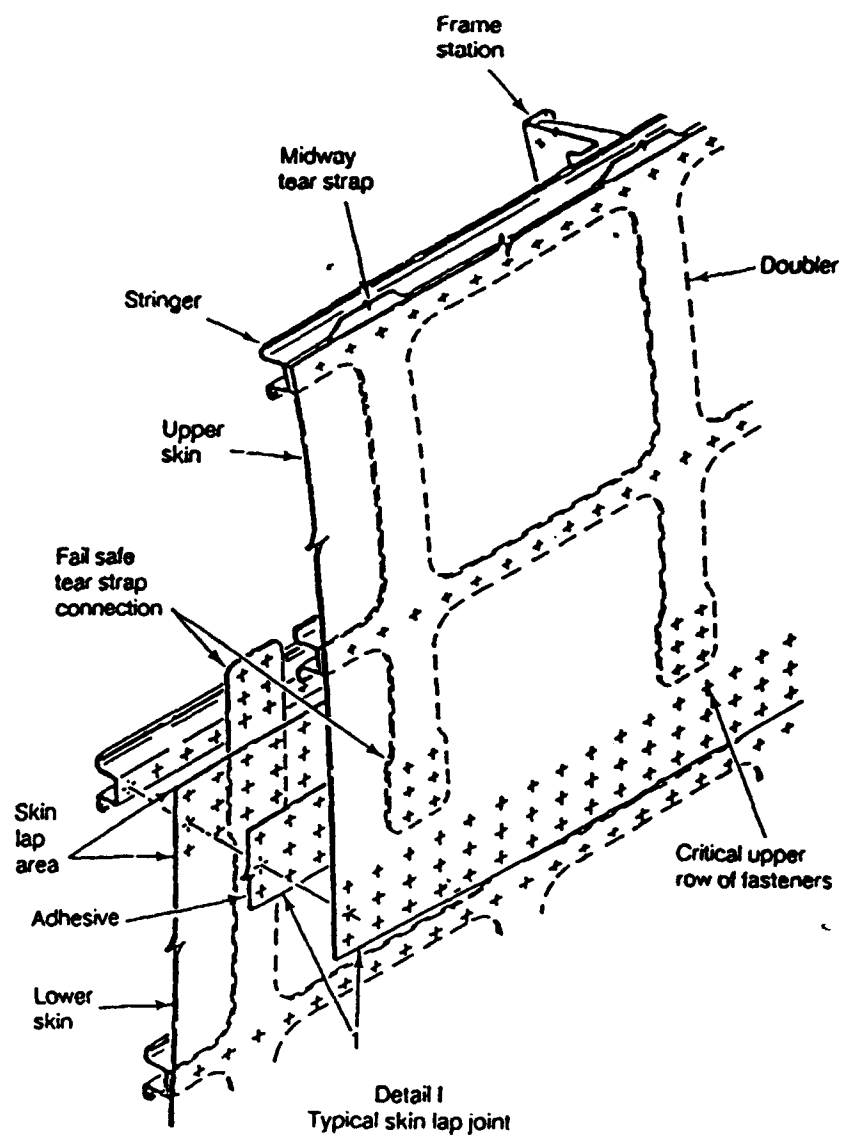
FIGURE 4-2. TYPICAL FUSELAGE CONSTRUCTION

Joint description configuration

Base line
3 rows - 5/32" Csk. Rivets
1.13" space
.04" to .04"
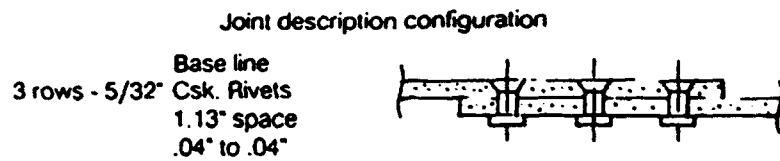
FIGURE 4-3. TYPICAL FUSELAGE LAP JOINT CONFIGURATION
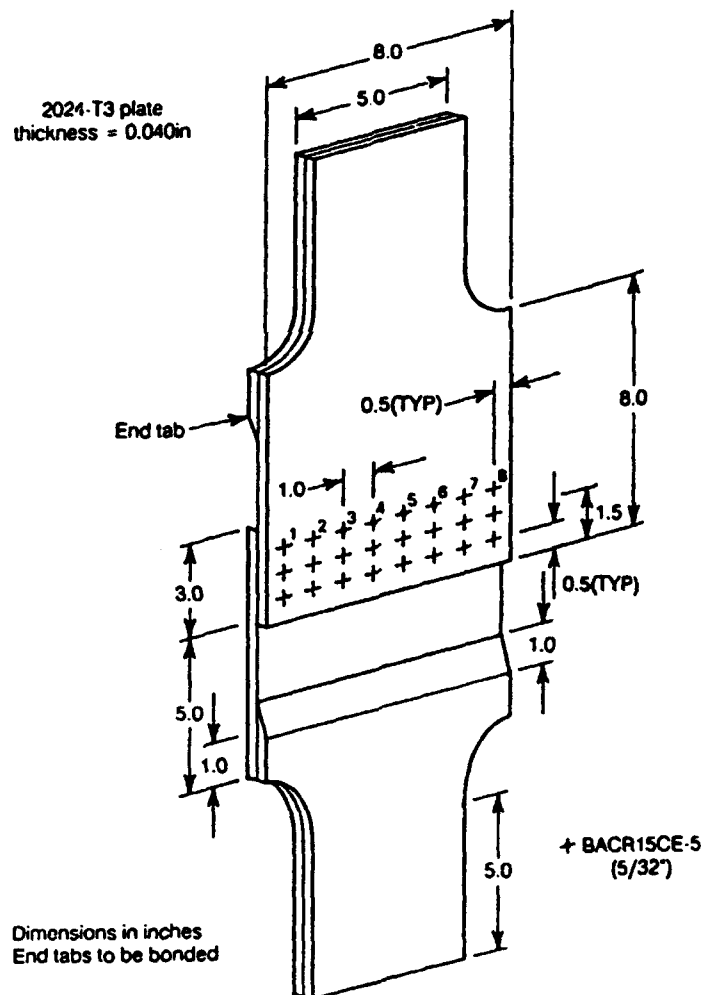
FIGURE 4-4. UNIAXIAL FUSELAGE LAP JOINT SPECIMEN
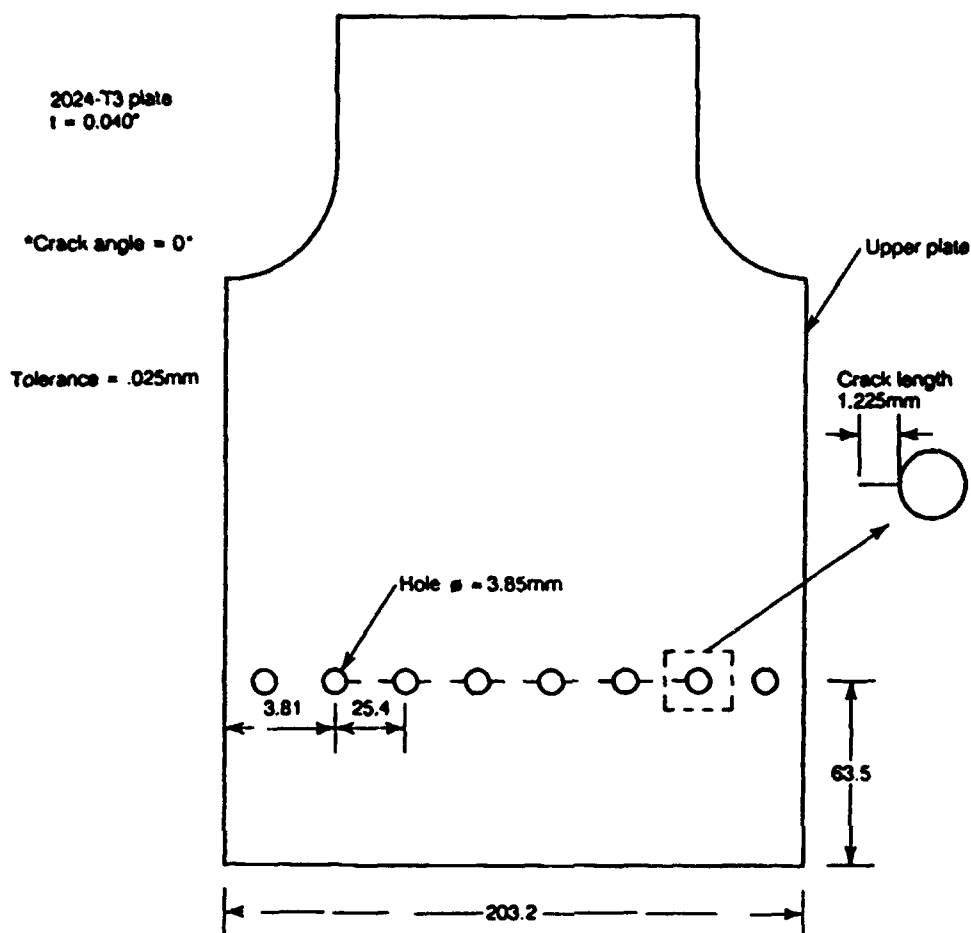
FIGURE 4-5. DETAILS OF SPARK ERODED CRACK STARTERS

The specimens were manufactured by Australian Airlines (Drawing No: B27M53-31-15), from material supplied by them, to aircraft standard. End tabs (see Figure 4-4) were bonded to the base specimen to ensure failure would not initiate from the specimen ends.

Since the amount of out-of-plane bending due to fuselage curvature, in a typical fuselage joint was unknown the local bending was prevented by testing the specimens bonded back-to-back and separated by a 12.5mm thick honeycomb core.

One drawback of this method of testing is that the failure of one face (ie. base specimen) terminates further testing of the other. The over-riding advantage of this technique is that, due to symmetry, a heat cured repair can be applied to the base specimens without including extensive bending due to the thermal expansion mismatch of the parent material and that of the repair. A view of the assembled test specimen is given in Figure 4-7.

117
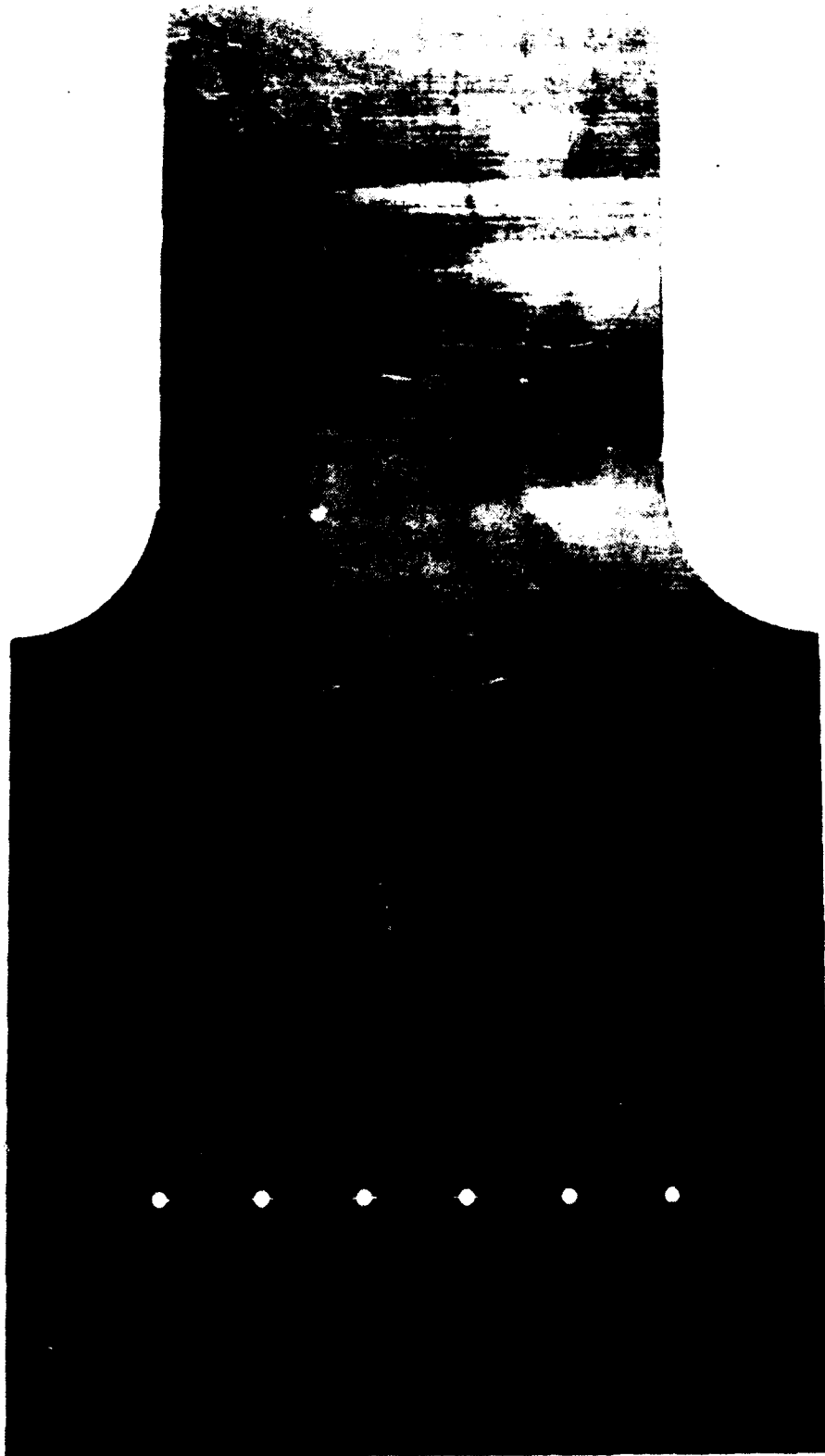
FIGURE 4-6. UTTER PLATE CONTAINING SPARK ERODED NOTCHES
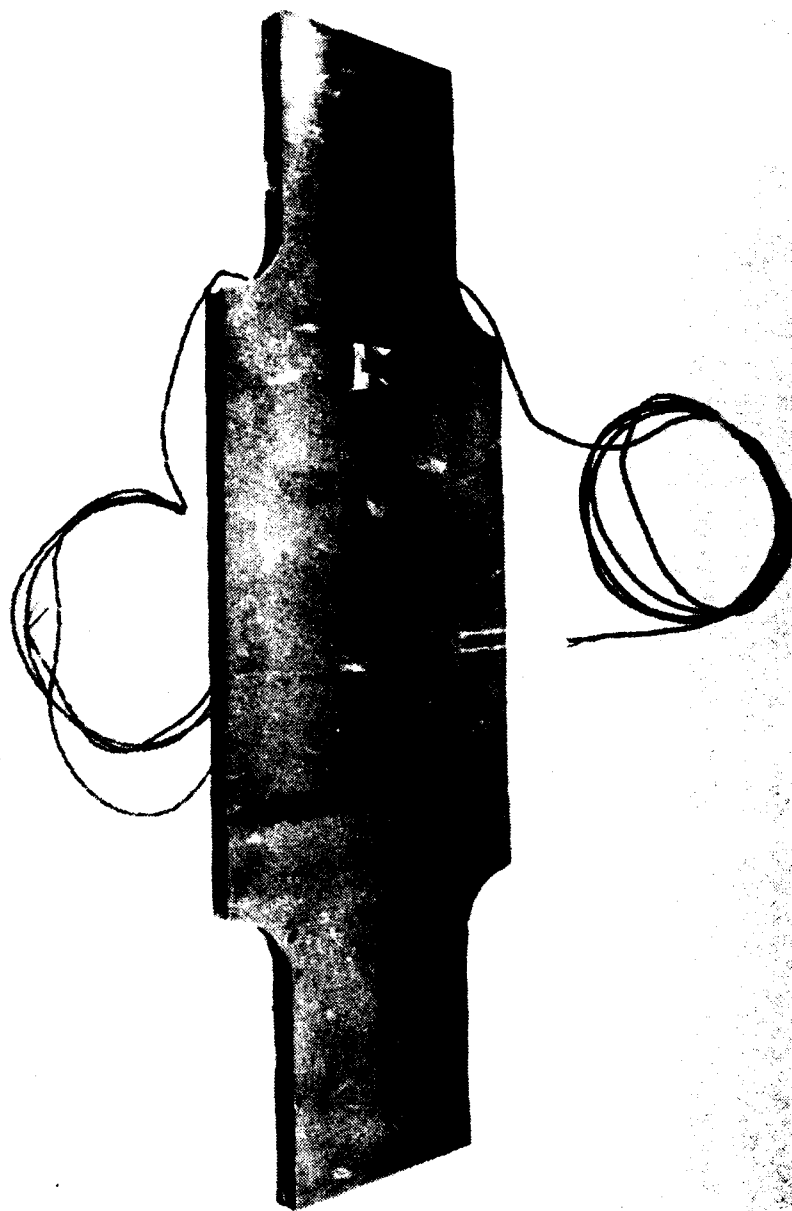
FIGURE 4-7. BACK-TO-BACK BONDED LAP JOINT SPECIMENS

The bonded doubler used in this investigation was a multi-segmented unidirectional boron/epoxy laminate. containing ten plies at the greatest thickness. The laminate (203.2mm long by 203.2mm wide), was bonded over the joint, with one segment butting up against the skin step, to provide an alternative load path for each row of fasteners. (see Figure 4-8). The doubler was applied after the specimens had been pre-cracked. In order to evaluate the fail-safe nature of the repair,specimens were repaired following complete failure of the upper row of fasteners (ie. link up of upper row fastener hole cracks).

FIGURE 4-8. REINFORCED LAP JOINT SPECIMEN

4.3 FATIGUE TESTING

The specimens were tested in various capacity servo-hydraulic test machines. The specimens were loaded in tension to give a remote plate stress of 92 MPa (13.4 ksi). The applied constant amplitude loading had a maximum load of 40.0 kN with a stress ratio, R, of 0.05 and a frequency range between 2.5 and 3 Hz. This loading represents the hoop stress induced in the fuselage skin due to pressurization.

Crack growth was monitored optically using a traveling microscope, with a magnification factor of 40. For the unreinforced specimen, the tests were terminated when the upper row of fasteners had completely failed (ie. all cracks linked).

Ten unreinforced specimens have been tested (see Table 4-1). It should be noted that in the initial process used to bond specimens A1 to A4 to the honeycomb, adhesive flowed between the two aluminum sheets and across the upper row of fasteners. This was detected subsequent to the failure of specimen A1/A2. This in effect, enhanced the fatigue life of the upper row of fasteners, as can be seen from Table 4-1. This specimen failed (i.e., two cracks linking) within 140,000 cycles of the last inspection, at which no damage was detected. The failure of A2, although probably influenced by the final failure of A1, occurred through the inner plate at the lower fastener row, in contrast to all other specimens. This may indicate a possible danger in lap joint modifications which consider only the upper row. This is of concern since damage occurring at the lower fastener is only detectable from the interior of the aircraft. To rectify the seepage of adhesive into the lap joint, a teflon strip was placed over the skin step.

During the cycling of the specimens periodic crack measurements were made. A mean life to failure of approximately 59,000 cycles was obtained. It was observed that in each case, the initial linking of two adjacent cracks occurred when the remaining ligament was approximately 2mm long.

Figures 4-9 to 4-14 present crack growth data for the five specimens which suffered total failure. In these figures only data for the most significant cracks occurring on a specimen were plotted. In each figure the two curves corresponding to the least number of cycles, were the cracks which first linked. It should be noted that for specimen A5, data were obtained subsequent to the failure and repair of specimen A6.

Figures 4-15 to 4-18 present views of the failure surfaces. These failures may be seen to reflect the nature of in-service crack growth. A small bonded repair was placed in the vicinity of fastener column 1. This was used to repair a notch in the upper plate, between fastener rows 1 and 2, which occurred during the fabrication of specimen A13. After 5000 cycles a 1 mm crack was detected at this notch. Once a boron/epoxy patch was applied, no further growth was detected. Prior to the application of the patch, the notched area was filled with plastic putty and smoothed. From observations, the remaining fasteners are not affected by this procedure.

TABLE 4-1. UNREINFORCED FUSELAGE LAP JOINT FATIGUE PROGRAM

Specimen	Status	Precracking Cycles at 17.8 ksi	Cycles to Failure at 13.4 ksi	Ligaments Joined (Top Row)	Longest Crack mm
A1*	Unpatched	—	977,600[a]	Yes	
A2*	Unpatched	—	977,600[a]	No[b]	9.0
A5	Unpatched	5,000	--	No	1.8
A6	Unpatched	5,000	25,000	Yes	—
A9	Unpatched	—	---	No	7.1
A10	Unpatched	—	105,700	Yes	—
A11	Unpatched	—	---	No	2.4
A12	Unpatched	—	67,000	Yes	—
A5+	Unpatched	n/a	41,000	Yes	—
A6/2●	Patched	n/a	see below	prior	—
A13	Unpatched	—	57,370	Yes	—
A14	Unpatched	—	---	No	0.7

*	Adhesive seepage occurred across top fastener row (enhanced fatigue life)
a	No crack detected at 837,000 cycles
b	Failed lower fastener row
+	Continuation of specimen test
●	Repaired after complete failure, using room temperature curing adhesive
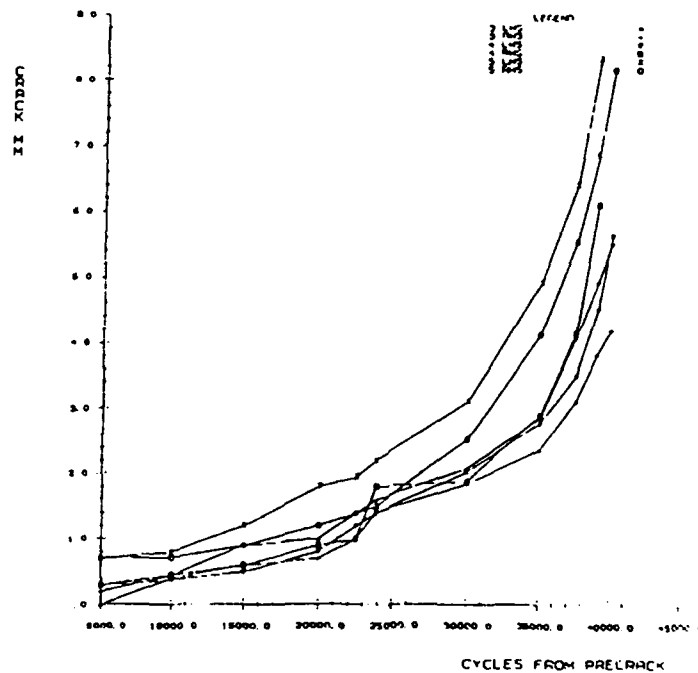
FIGURE 4-9. SPECIMEN A5 CRACK GROWTH DATA

122
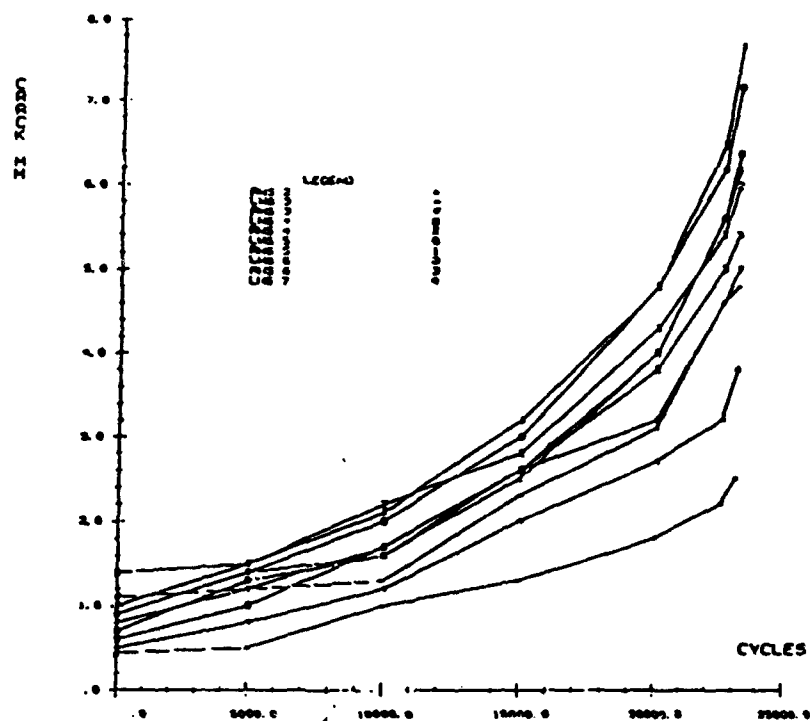
FIGURE 4-10. SPECIMEN A6 CRACK GROWTH DATA
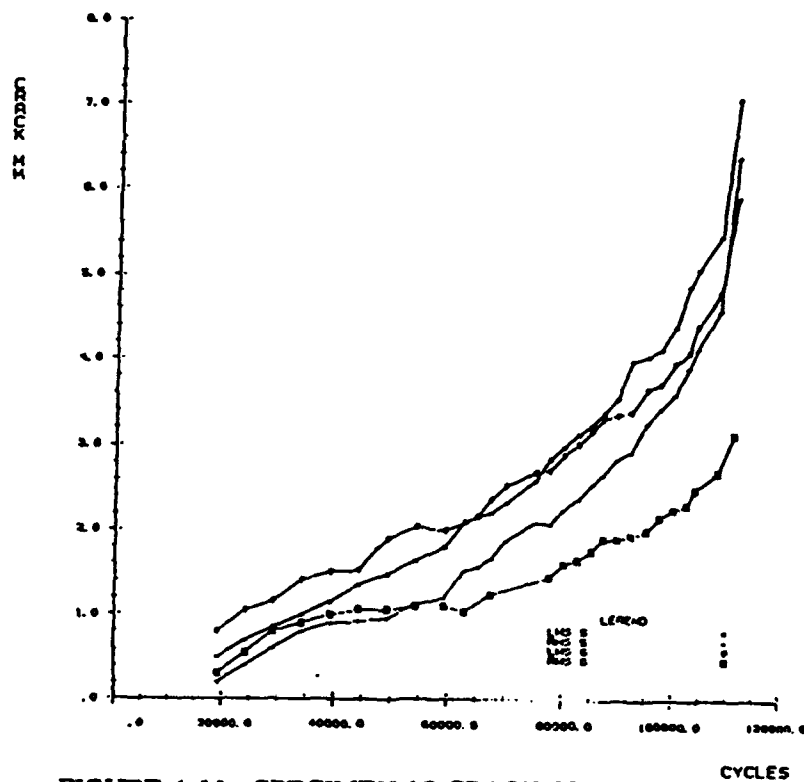
FIGURE 4-11. SPECIMEN A9 CRACK GROWTH DATA

123
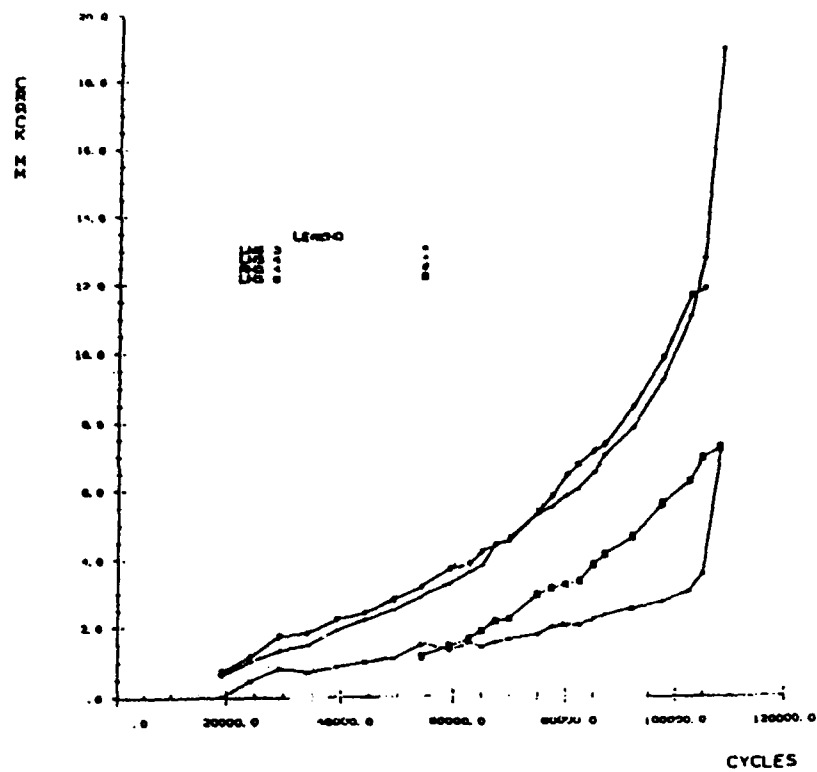
FIGURE 4-12. SPECIMEN A10 CRACK GROWTH DATA
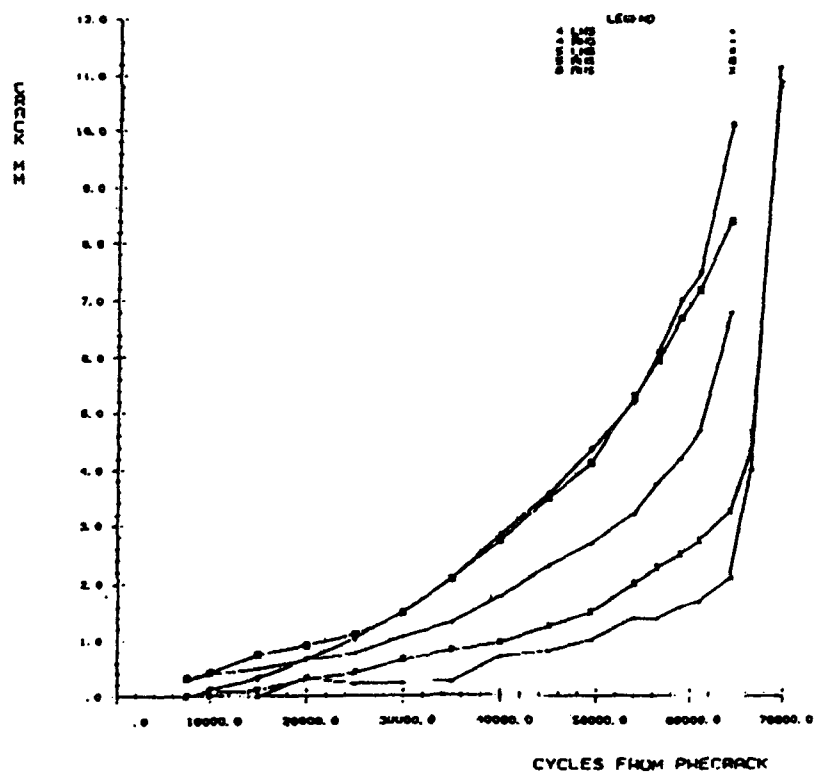
FIGURE 4-13. SPECIMEN A12 CRACK GROWTH DATA

124
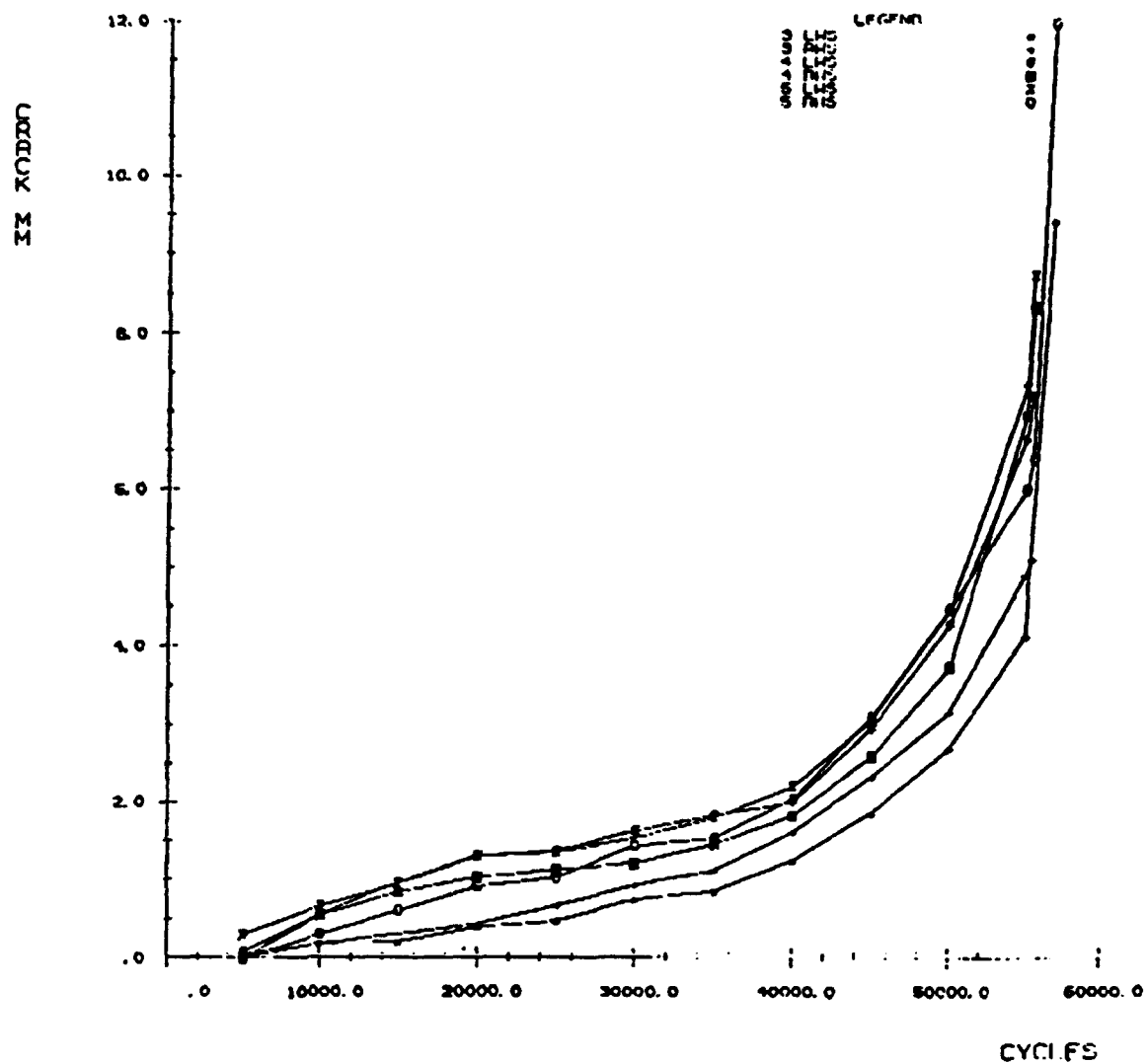
FIGURE 4-14. SPECIMEN A15 CRACK GROWTH DATA

125
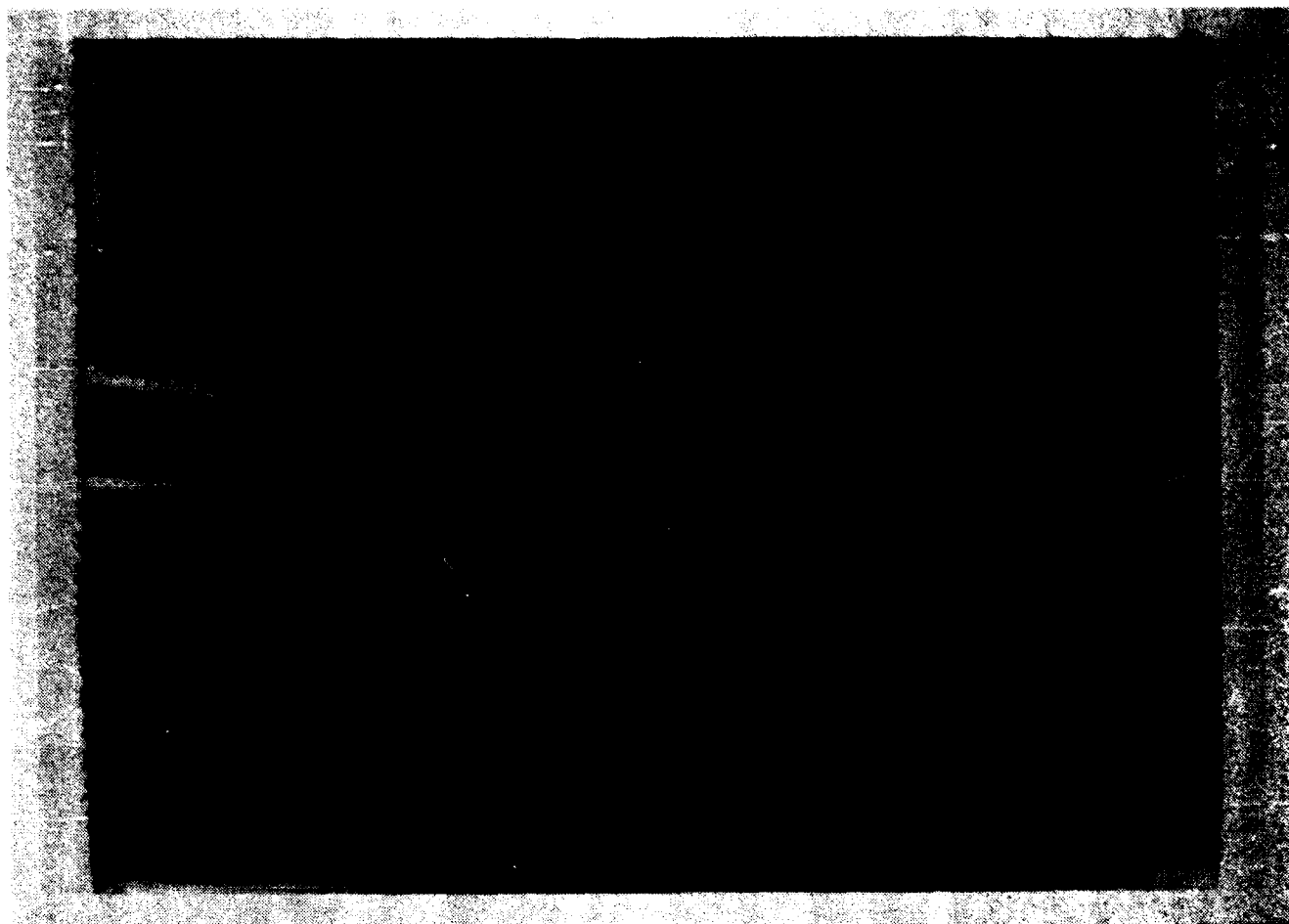
FIGURE 4-15. FAILURE OF SPECIMEN A6
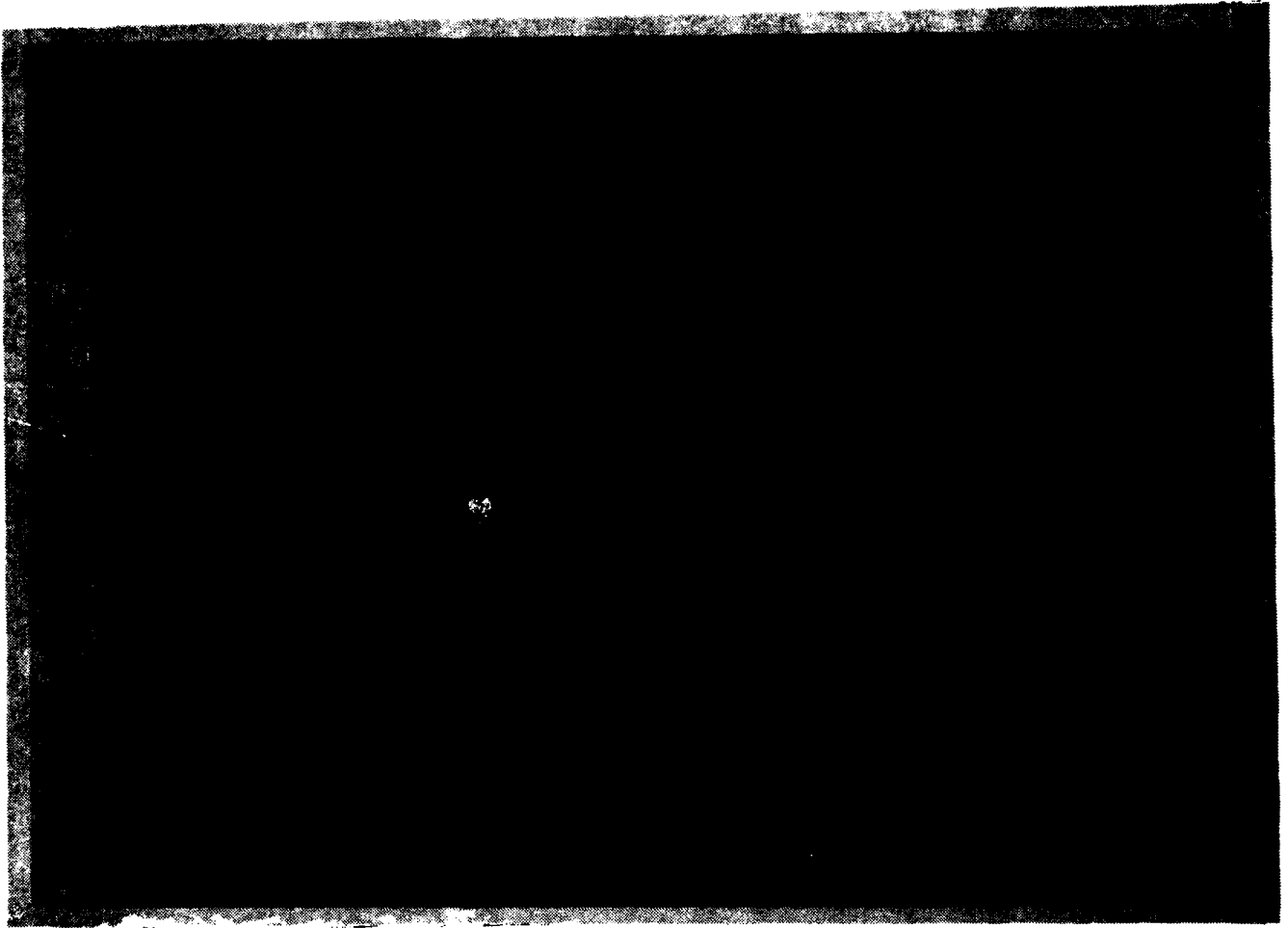
FIGURE 4-16. FAILURE OF SPECIMEN A10
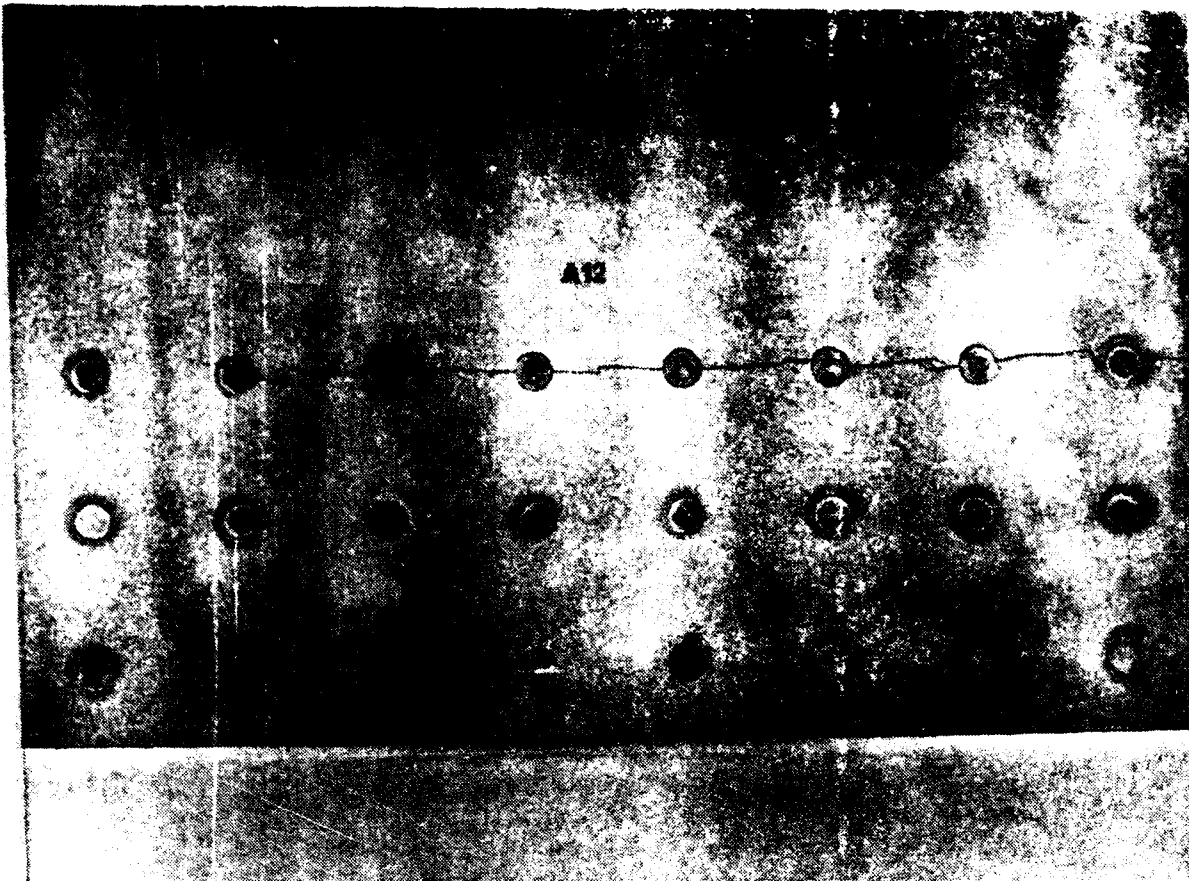
FIGURE 4-17. FAILURE OF SPECIMEN A12

4.4 REINFORCED SPECIMENS

From Table 4-2, it can be seen that the use of a bonded boron/epoxy doubler lead to an order of magnitude increase in the fatigue life of the basic specimens.

Once the failure of the specimen A6 occurred, it was repaired using the boron/epoxy doubler, and testing continued until failure of specimen A5 occurred. Because of the increased stiffness due to the repair, the loading was increased in order to maintain a 92 KN stress range for A5. This was based on strain gauge data obtained at a location on the plate away from the fasteners. The maximum loading used for this case was 43 kN with a stress ratio of 0.047. Subsequent to the failure of A5, it was also repaired with a doubler and fatigue testing continued. Test data to date on reinforced specimens is reported in Table 4-2.
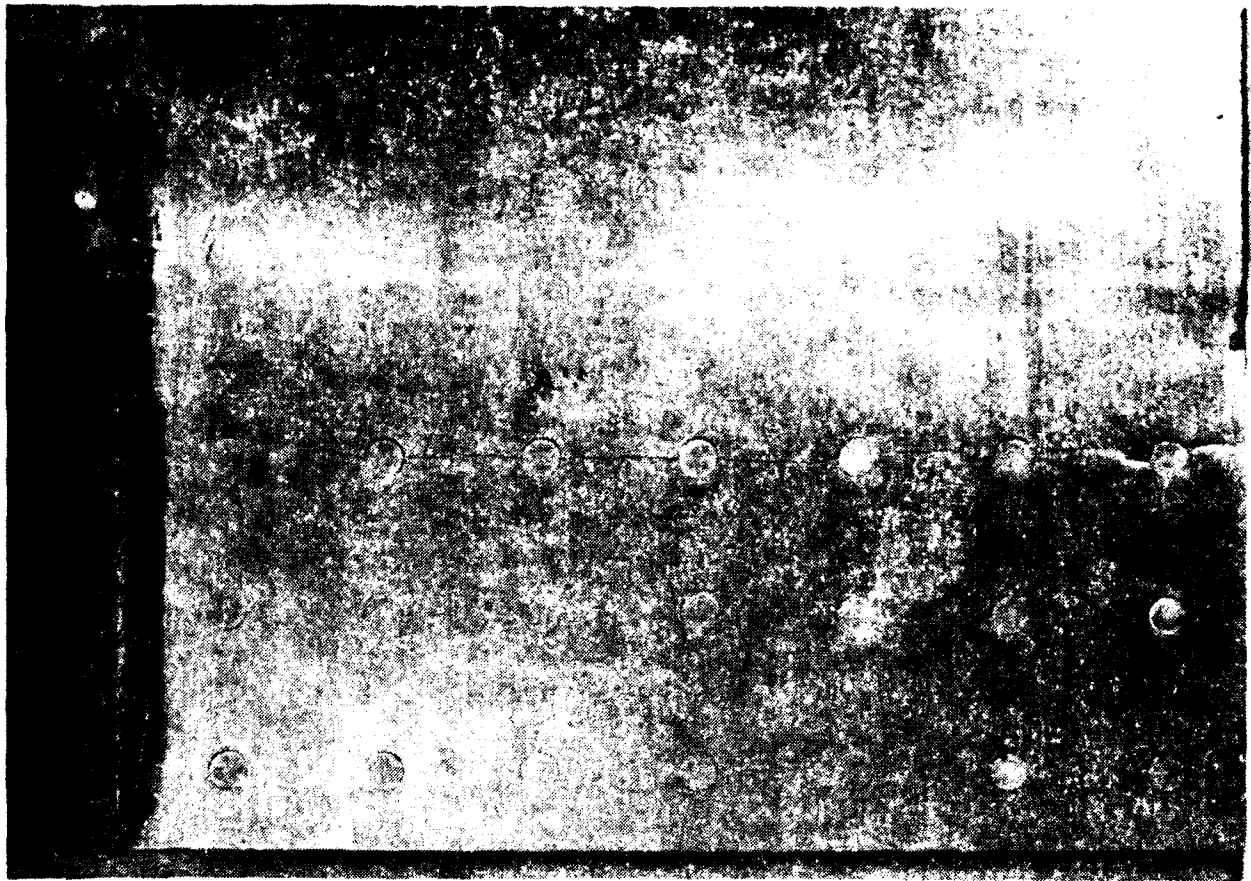
Note: repair of initial notch

FIGURE 4-18. FAILURE OF SPECIMEN A13

Pre-cracking of some specimens was acomplished at a maximum load of 50.0 kN with a stress ratio of 0.024 and a frequency of 2.5 Hz. With this loading. cracks were initiated within 5000 cycles. Patch degradation and possible failure in the reinforced specimens was monitored by eye. Eddy current techniques were used to monitor crack growth beneath the doublers.

TABLE 4-2. REINFORCED FUSELAGE LAP JOINT FATIGUE PROGRAM

Specimen	Status	Precracking Cycles at 17.8 ksi	Cycles to Failure at 13.4 ksi	Ligaments Joined (Top Row)	Longest Crack mm
A1*	Unpatched	---	977,600#	Yes	
A2*	Unpatched	---	977,600#	No$	9.0
A3*	Patched	178,400	>2,155,500	—	4.5
A4*	Patched	178,400	>2,155,500	—	—
A3	Conditioned	---	>2,700,000	No	—
A4	Conditioned	---	>2,700,000	No	—
A5	Unpatched	5,000	41,400	Yes	—
A6	Unpatched	5,000	25,000	Yes	—
A5/2@	Patched	---	>1,300,000%	prior	—
A6/2@	Patched	---	>1,316,400%	prior	—
A7	Patched	5,000	4,001,460+	No	1.0
A8	Patched	5,000	4,001,460+	No	1.0
A7	Conditioned	---	>5,500,000	No	—
A8	Conditioned	---	>5,500,000	No	—
A9	Unpatched	---	110,030	Yes	—
A10	Unpatched	---	105,700	Yes	—
A9/2@	Patched	---	1,000,000	prior	—
A10/2@	Patched	---	1,116,000	prior	—
A11	Unpatched	---	---	No	2.4
A12	Unpatched	---	70,850	Yes	—
A13	Unpatched	---	57,370	Yes	—
A14	Unpatched	---	---	No	0.7

*   Adhesive seepage occurred across top fastener row (enhanced fatigue life)
\#   No crack detected at 837,000 cycles
$ Failed lower fastener row
%   Failed in grip area of A5
+   Continuation of specimen test
@   Repaired after complete failure, using room temperature curing adhesive

4.5 ENVIRONMENTAL CONDITIONING AND TESTING

The initial testing of the reinforced and unreinforced specimens demonstrated that the bonded composite reinforcement significantly increased the fatigue life of fuselage lap joints with MSD. As can be seen in Table 4-2 all reinforced specimens did in excess of 1 million cycles with no patch degradation, and one specimen (A7/A8) did in excess of 4 million cycles

without failure of either the boron patch or the adhesive bond.

To further demonstrate the validity of the bonded repair scheme, environmental conditioning of the reinforced specimens was conducted. Table 4-3 details the processes applied to each specimen.

TABLE 4-3   FUSELAGE LAP JOINT ENVIRONMENTAL FATIGUE PROGRAM

Specimen	Status	Precondition in distilled water	Precondition in NaCl	Cycles at 13.4 ksi	Test temp. °C	All Ligaments Joined?
A3*	Patched	NO	NO	>2,155,550	20	NO
A4*	Patched	NO	NO	>2,155,550	20	NO
A3	Patched	7 days	—	> 522,000♦	60	NO
A4	Patched	60°C	—	> 522,000♦	60	NO
A3	Patched	7 days	—	> 550,000ᵅ	60	NO
A4	Patched	60°C 5%NaCl	—	> 550,000ᵅ	60	NO
A7	Patched	NO	—	>4,001,000	20	YES
A8	Patched	NO	—	>4,001,000	20	NO
A7	Patched	1 week	—	> 503,000♦	60	YES
A8	Patched	60°C	—	> 503,000♦	60	NO
A7	Patched	1 week	—	> 1,000,000ᵅ	60	YES
A8	Patched	60°C 5%NaCl	—	> 1,000,000ᵅ	60	NO

*   Adhesive seepage occurred across top fastener row (enhanced fatigue life)
♦   Testing not completed, specimen failed in grip.
ᵅ   Test stopped.

4.5.1 Hot/Wet Conditioning

Specimens A3/A4 and A7/A8 were first soaked in a water bath for a minimum of seven days, with the temperature held constant at 60°C. One week was considered sufficient time to thoroughly soak the boron doubler and the adhesive. Water temperature was monitored throughout this time.

On removal from the water bath the specimens were wrapped in plastic and sealed to retain their moisture content (Figure 4-19). They were then immediately placed in the testing machine and wrapped in 10" by 10" heater blankets. The blankets were fixed directly to each side of the specimen, then covered with insulating material. Temperature was controlled by a single thermocouple, and monitored by another four thermocouples. The temperature controller maintained a uniform temperature distribution of 60 C ± 4 C over the specimen area throughout the test. Figure 4-20 shows specimen set-up in the machine.

Specimens were then cycled at the stated load levels, for a minimum of 500,000 cycles, without failure and with no visible damage to the doubler system.

4.5.2 5% NaCl Aqueous

Following testing under hot/wet conditions, the specimens were then exposed to a more corrosive environment. They were wrapped in aluminum tape to minimize corrosion in the grip area, and placed in a water bath containing a 5% NaCl aqueous solution. The temperature was maintained at 60°C, and specimens were immersed for seven days (minimum). Figure 4-21 shows the typical condition of the specimen after removal from the salt bath.

Testing was then continued, under the conditions described above, with the temperature maintained at 60°C, and the moisture content retained.

4.5.3 Environmental Fatigue Test Results

A summary of the fatigue test program to date is given in Table 4-2 which also includes the results of the initial test program. This table details the different specimen configurations - the unpatched lap joint, the lap joint reinforced with a heat-cured composite doubler, and the failed lap joint repaired with a cold-setting adhesive bonded doubler.

4.5.3.1 Unreinforced Specimens

Ten unreinforced specimens were tested (see Table 4-2). A mean life to failure of approximately 59,000 cycles was obtained. It was observed that in each case, the initial joining of two adjacent cracks occurred when the ligament between the crack tips was approximately 2 mm long. Final failure subsequently occurred after relatively few additional cycles. Table 4-4 details the distances between cracks prior to linking. Comparing the experimentally obtained crack growth rates, in Figure 4-22, to the crack growth rates obtained from fleet data, we see

132

good agreement. The experimental crack growth data is bounded, both above and below, by the crack growth data obtained from service aircraft.
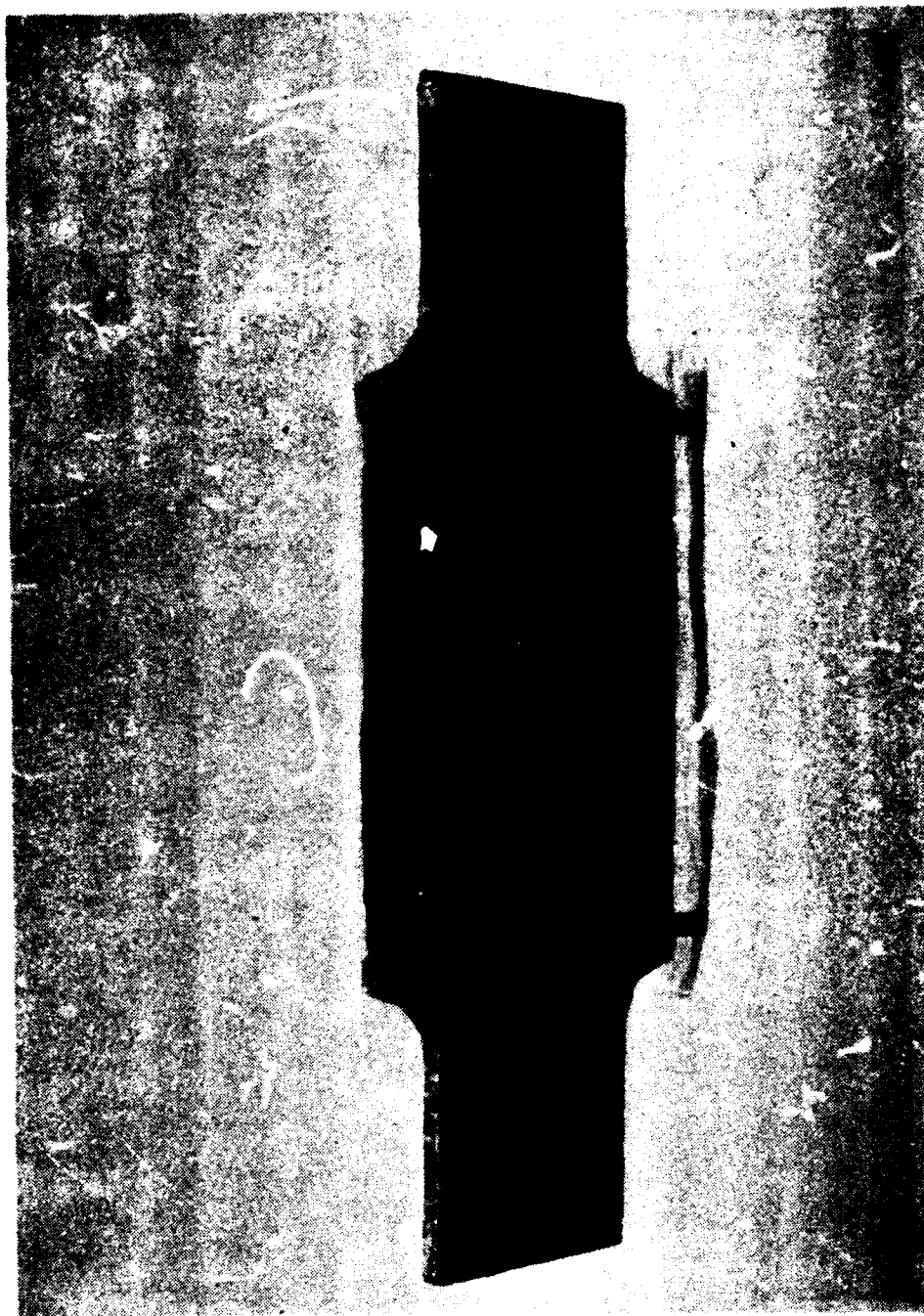
FIGURE 4-19. REINFORCED LAP JOINT SEALED TO RETAIN MOISTURE
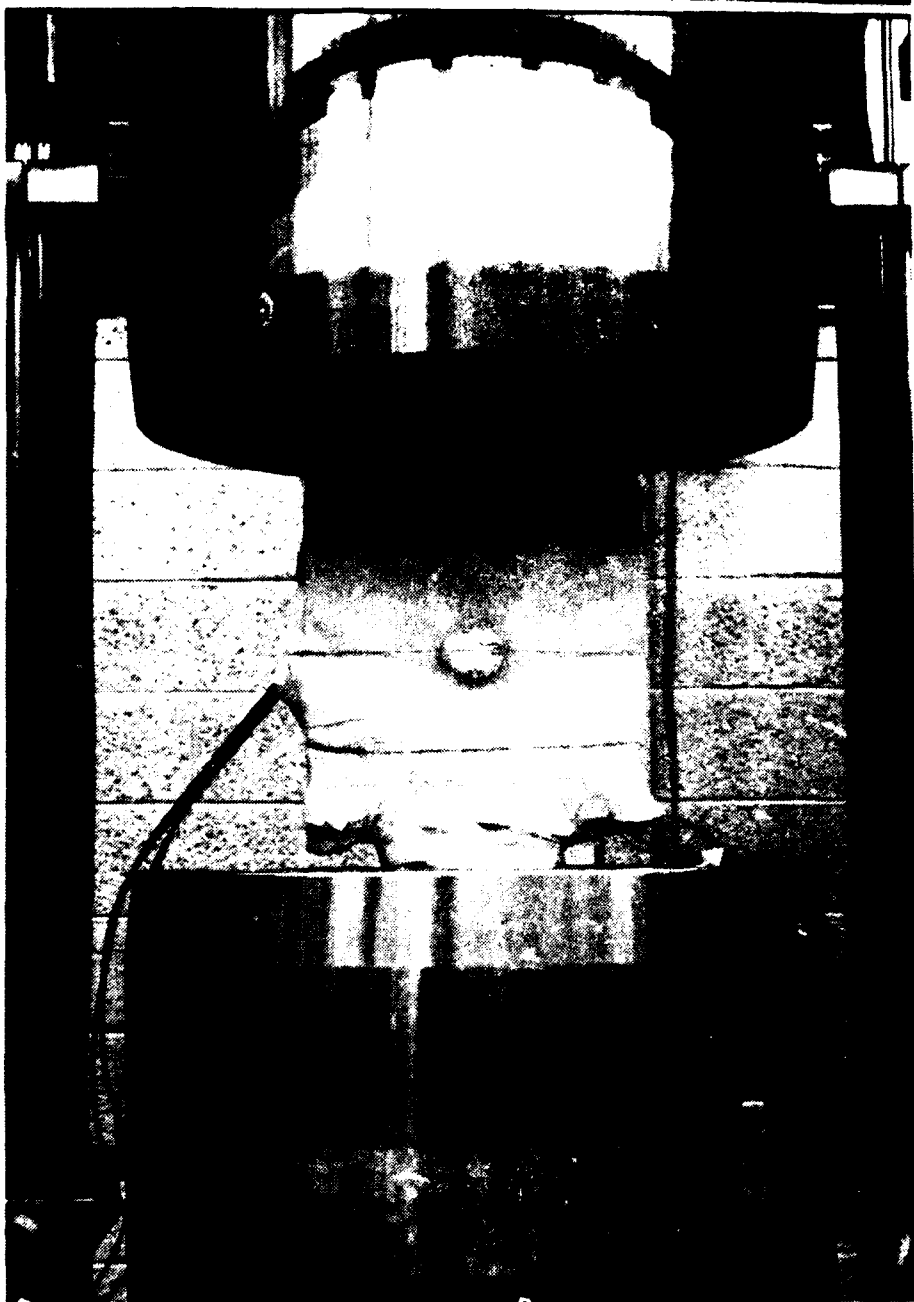
FIGURE 4-20. ENVIRONMENTAL TEST SET-UP

134
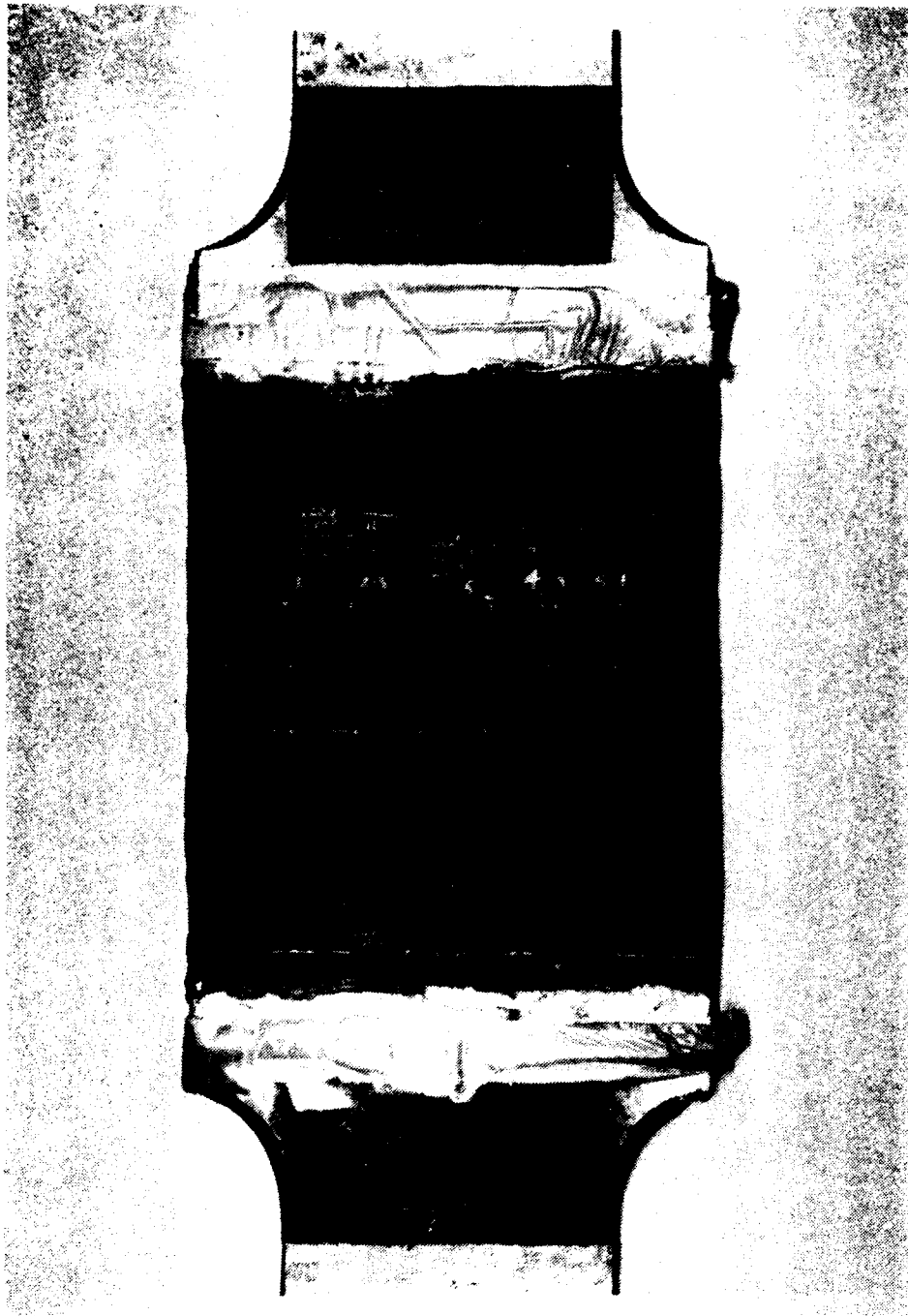
FIGURE 4-21. SPECIMEN AFTER REMOVAL FROM 5% NaCl SOLUTION
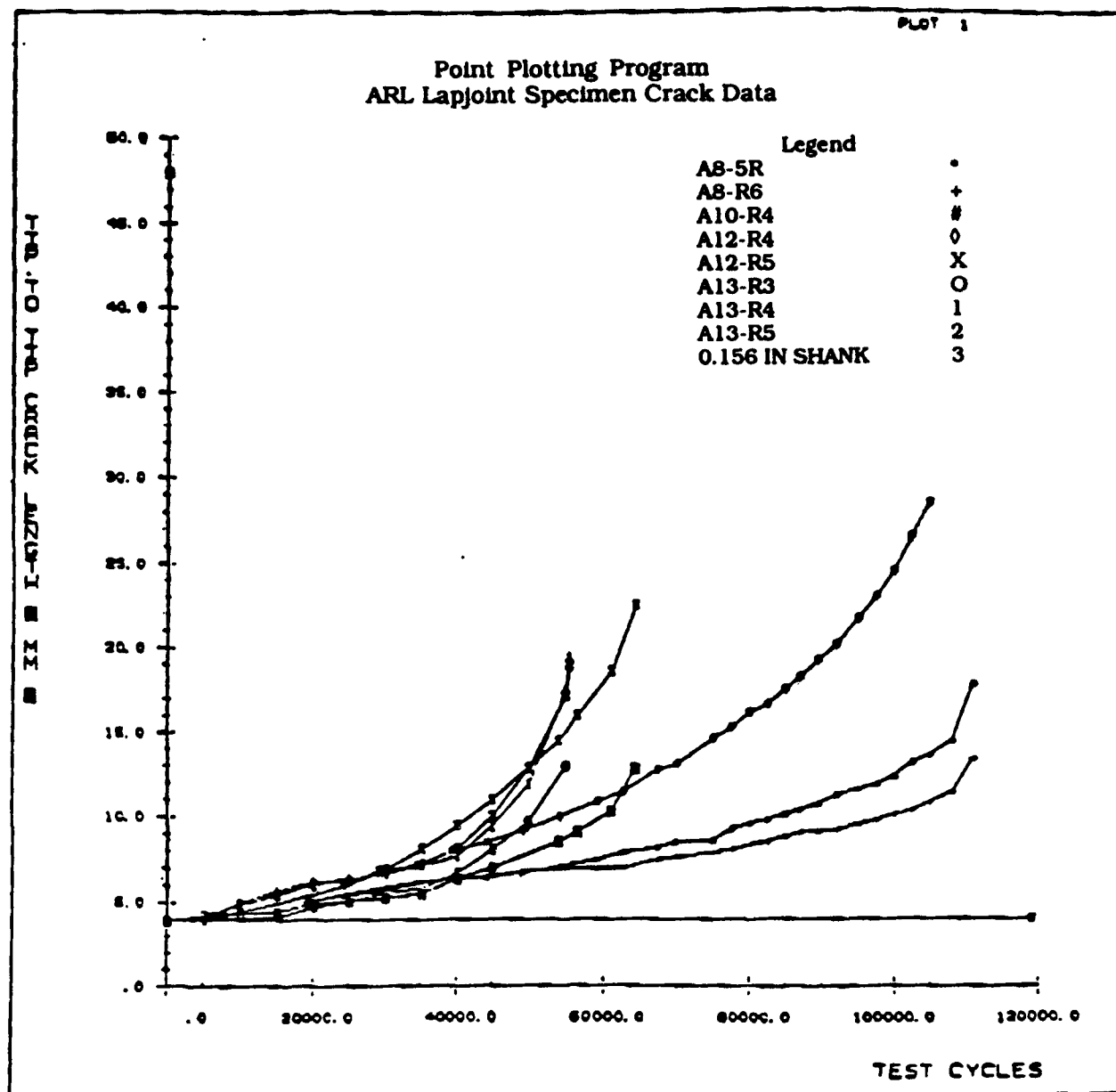
FIGURE 4-22. TEST CRACK GROWTH DATA

136

TABLE 4-4. DISTANCE BETWEEN CRACK TIPS (LIGAMENT FAILURE)

Specimen	Rivets	Distance Between Crack Tips (mm)	Cycles to Failure
A5	R4-R5	1.8	1
	R6-R7	4.9	140*
	R3-R4	4.6	960
A6	R4-R5	6.6	240
	R5-R6	9.3	360
	R3-R4	3.4	10
A9	R5-R6	8.0	1910
	R4-R5	12.5	870
	R6-R7	17.0	1700
	R3-R4	19.8	1820
	R7-R8	21.0	1980
	R2-R3	19.9	2000
A10	R3-R4	2.0	120
	R4-R5	5.2	1520
	R2-R3	13.6	2780*

* Crack tips overran each other

Note: Final failure of ligaments was usually observed by eye. Distance between crack tips was observed to be approx. 2 mm and cycles to failure approx. 100.

4.5.3.2 Reinforced Specimens

Initial testing was conducted in a laboratory environment, i.e., room temperature and dry. In this case it was found that the use of a bonded boron/epoxy doubler leads to an order of magnitude increase in the fatigue life of the basic specimens (see Table 4-3).

Specimens A3/A4 and A7/A8 were then examined, prior to environmental testing, using eddy current techniques. The results are in Figure 4-23a and b for specimens A3 and A7 respectively. Specimen A3 had small cracks emanating from some rivets, while A4 had no detectable cracking. It is interesting to note that specimen A3 also has a crack emanating from a rivet in the second row. There was significant crack growth in specimens A7 and A8. However, it must be noted that these specimens had experienced more than 4,000,000 cycles. Each specimen has experienced a large number of additional cycles without failure of either the specimen or the repair. In the case of specimens A7 and A8 the crack lengths were such that, unrepaired, the specimen would have failed after relatively few additional cycles.

Following the environmental conditioning and testing, the specimens were reexamined. There was no growth for specimens A3/A4. However, crack growth has occurred in specimens A7/A8. In both specimens the lefthand side crack from rivet 2(R2) has increased significantly in

137

(1) At 178,420 cycles - Prior to doubler application
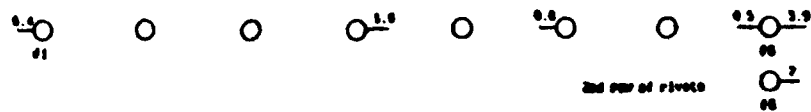
(2) At 2,155,550 cycles - Prior to environmental exposure
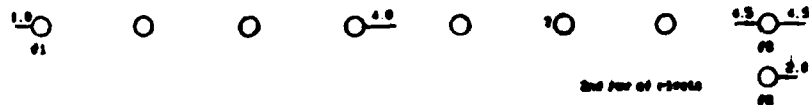
(3) At 2,717,950 cycles - After immersion in water and salt
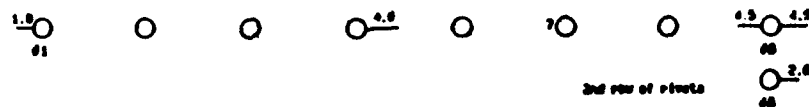
FIGURE 4-23a. CRACK GROWTH IN SPECIMEN A3

(1) At 5,000 cycles - Prior to doubler application
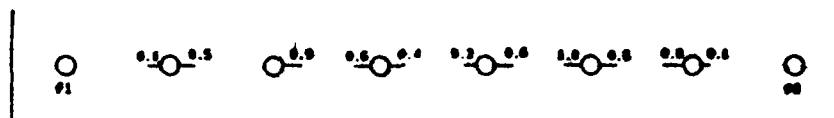
(2) At 4,001,460 cycles - Prior to environmental testing
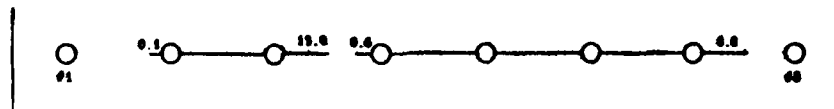
(3) At 5,504,590 cycles - After immersion in water and salt
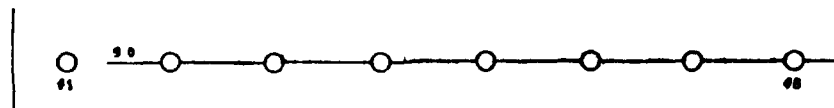
FIGURE 4-23b. CRACK GROWTH IN SPECIMEN A7

138

length. The cracks from R3 and R4 have joined, as have those from R7 and R8. All cracks have joined in specimen A8, except those from rivets 1 and 2. If cycling had continued it could be expected that these specimens would be cracked completely through the aluminum section. However, as has been demonstrated previously, the doubler is more than capable of carrying the entire load. Testing is still continuing for both specimens, with the cracks being periodically monitored. To date, none of the reinforced or repaired specimens have experienced failure in the test section.

After more than 550,000 cycles of testing in a hot wet salt environment the doublers show no sign of degradation or failure. This is in contrast to a fatigue life of 59,000 cycles for failure of the unreinforced specimens.

4.6 EXPERIMENTAL & ANALYTICAL STRESS INVESTIGATION OF LAP SPECIMEN

The basic specimen geometry used in this study is shown in Figure 4-24, and coincides with that used in previous work where it was shown that the resultant crack growth rates compare favorably with those found in service aircraft. The specimens, which contain a full depth counter sink hole, were manufactured, to aircraft industry standards, by staff at Australian Airlines. To simulate a worst case condition the upper and lower skins were left unbonded.

The specimen was placed in an Instron electrohydraulic fatigue testing machine and cycled at 8Hz with a load range of 13kN to 2 kN and thermal emission scans of various regions were then performed using a SPATE 8000 infra-red camera located approximately 55 cm from the specimen. (Thermal emission techniques rely on the coupling between thermal and mechanical energies and under adiabatic conditions the observed signal is proportional to the sum of the three principal stresses, often referred to as the bulk stress. Since, in this case, the stress normal to the surface is zero the bulk stress on the surface is equa' to the sum of the principal inplane stresses).

The three regions scanned were as follows: Region 1: A scan encompassing all three rows of rivets as well as regions in both the upper and lower skins. The area of the specimen scanned was 113 mm by 98 mm. The scan generated an array of 114 by 105 data points. Region 2: A scan encompassing three rivets in the first (i.e. critical) row of rivets. The area of the specimen scanned was 88mm by 47mm generating an array of 116 by 67 data points. Region 3: A scan of a rivet in the first row. The area of the specimen scanned was 15mm by 15mm generating an array of 82 by 80 data points. In each case the scan region was sprayed matt black to achieve a uniformly high infra-red emissivity.

The location of these regions is shown in Figure 25 and the resultant scans of regions 1-3 are shown in Figures 4-25 to 4-27 respectively. In each case the scan region is surrounded by masking tape, which can be seen around the edges of each scan and is readily identified as areas where the signal is very low.

FIGURE 4-24. UNIAXIAL FUSELAGE LAP JOINT SPECIMEN

Figure 4-25 clearly shows the load path taken in the specimen. There are three distinct zones, in each of which the bulk stress is relatively uniform. The first zone is the region up to and including the first row of rivets. At the line of the rivets there is a rapid decrease in the bulk stress to a second relatively constant value. This decrease reveals the load transferred at the first line of rivets. An analysis of this data reveals that approximately 45% of the load is transferred by this row of rivets.

The bulk stress undergoes another decrease at the second line of rivets. At this scale the stress concentration, in the bulk stress, at the first row of rivets is not apparent.

Figure 4-26 presents a more detailed view of the bulk stress field around the first row of rivets. This confirms the rapid decay in the load at the first row, due to load transfer to the lower skin. At this scale, the stress concentration in the bulk stress is still not apparent. This reveals the rapid decay of the stress concentration on the upper surface of the upper skin.

Analysis of the data also confirmed that approximately 45% of the load is transferred by the first row of rivets.

140

FIGURE 4-25. SCAN OF ALL THREE ROWS OF RIVETS. UNCALIBRATED STRESS UNITS

141
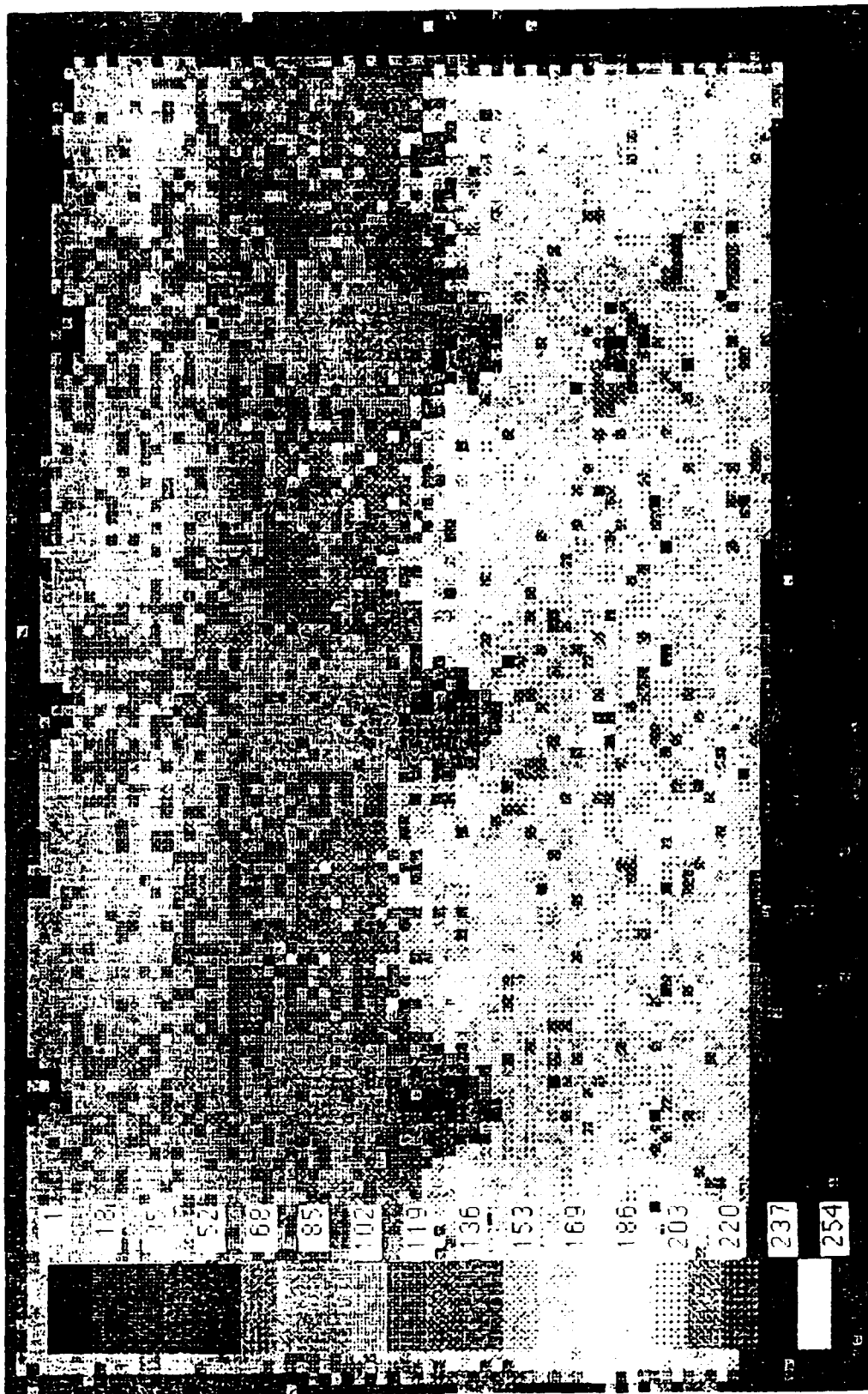
FIGURE 4-26. SCAN OF FIRST ROW OF RIVETS. UNCALIBRATED STRESS UNITS

142

Figure 4-27 presents a more detailed picture of the stress field around a fastener in the first row of rivets. Even at this scale the stress concentration, in the bulk stress, is not apparent. This highlights the role that the full depth countersink plays in making the first row of rivets a fracture critical location. Unfortunately the lower surface of the upper skin is not observable with standard thermal emission techniques.

The lack of a bond between the upper and lower skins results in the major load transfer occurring at the first row of rivets. This will exacerbate the stress concentration effect of full depth countersink holes at the lower surface of the upper plate, even though the stress concentration on the upper surface is particularly localized. Indeed, the stress concentration on the upper surface of the upper skin cannot be observed even with a fine resolution scan.

Now, a three dimensional finite element analysis of the specimen was undertaken to confirm these results. The finite element model contained 4296 nodes and had 10680 degrees of freedom with the rivets being modeled separately as three-dimensional isoparametric elements, as   in Figure   4-28. This analysis confirmed the rapid decay of the stress concentration in the bulk stress. The load transfer at the first row of rivets was also consistent with experimental measurements.

In fatigue tests performed on the lap joint specimens, linking of adjacent cracks appeared to occur when the remaining distance between the crack tips was approximately 2 mm. The 3-D elastic-plastic finite element analysis was performed to determine if this failure was due to the net section failure of the remaining 2 mm ligament between the crack tips, or due to ductile fracture. The basic finite element model is   in Figure   4-29. However, this model was significantly refined and includes two equal length cracks approaching each other from two adjacent fastener holes,   (Figures 4-29 and 4-30).   The stress/strain curve is elastic-plastic, taken from the MIL-Handbook-SE.
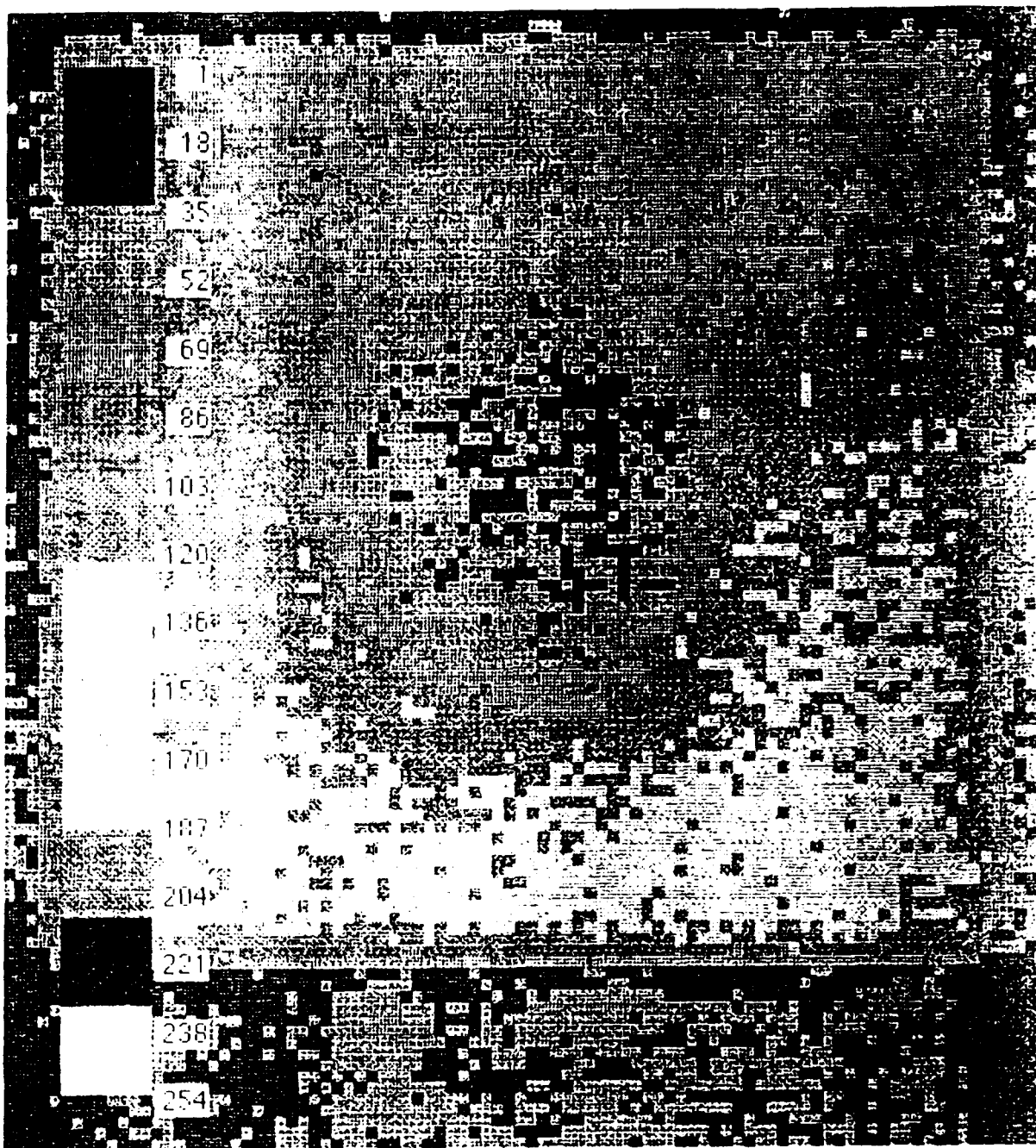
FIGURE 4-27.   SCAN OF RIVET IN THE FIRST ROW. UNCALIBRATED STRESS UNITS

144
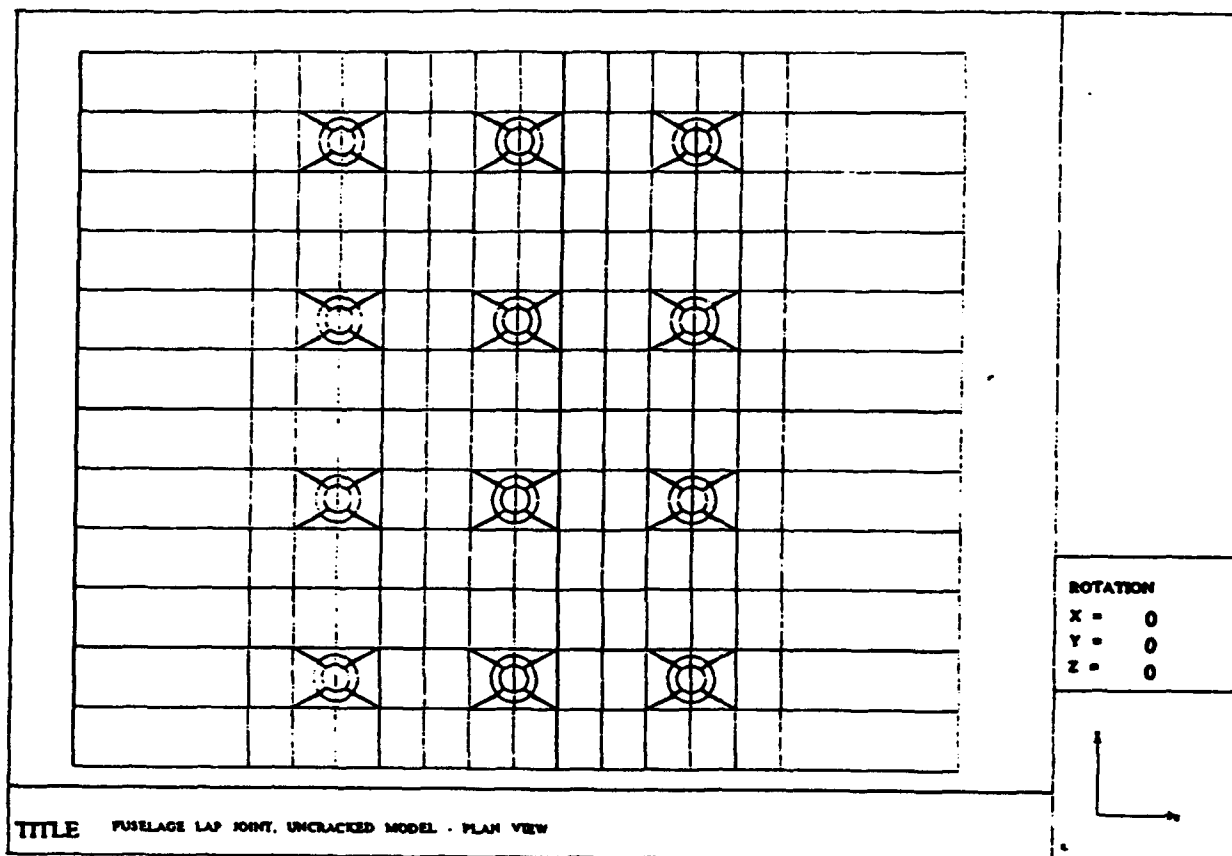
FIGURE 4-28. FINITE ELEMENT MODEL OF THE STRUCTURE

145
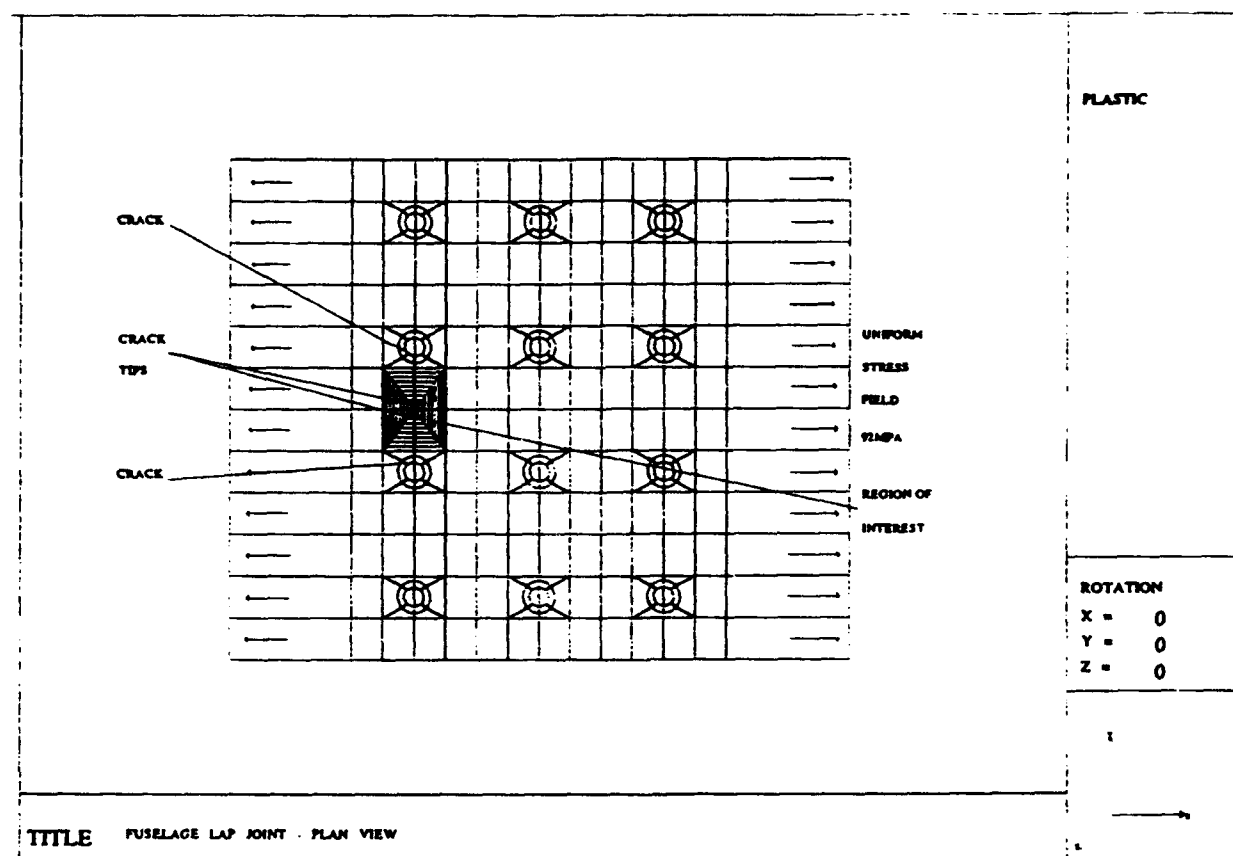
FIGURE 4-29.   FINITE ELEMENT MODEL OF THE CRACKED STRUCTURE

For mechanically fastened structures with multiple load paths, the commonly used J integral is path dependent, even for monotonic loading. To overcome this shortcoming, the path-independent integral T* [20] was calculated along a number of separate paths for remote stresses up to 13.4 ksi, which was the maximum stress applied to the specimen in the fatigue test. At the peak load the equivalent stress intensity factor, K, which we define, as in linear elastic fracture, in terms of T* and E (Young's modulus), as

$$K = (ET *)^{1/2}$$

was found to be approximately 23.9 MPa $\sqrt{M}$, which is well below the fracture toughness of the material. However, the von Mises equivalent stress was found to exceed its ultimate permissible

146

value for more than 0.5 mm of the 2.0 mm between the crack-tips. This implies that failure of the ligament, which was a precursor to total failure of the specimen, was due to net section failure. This result was consistent with earlier experimental work, where it was found that, regardless of the length of the cracks emanating from two adjacent fastener holes, linking of these cracks was always observed when the remaining ligament was approximately 2 mm.
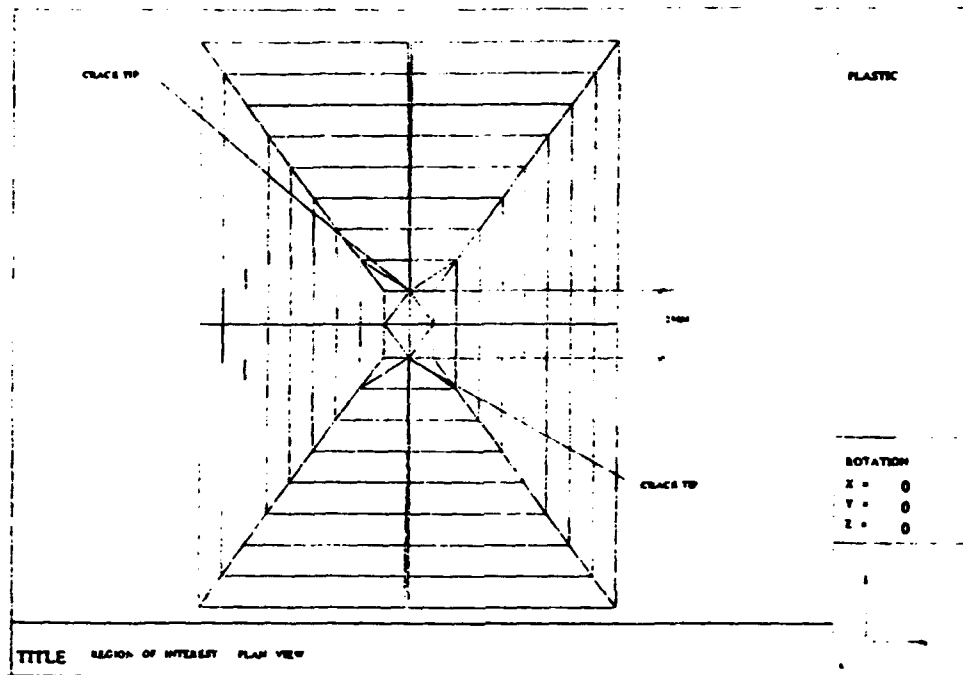
FIGURE 4-30. LOCAL DETAIL OF THE CRACKED REGION

4.7 DISCUSSION AND CONCLUSION

The variation in the fatigue lives of the unreinforced lap joint specimens was partially due to the nature of the cracking. In general, short life occurred when the largest cracks in a specimen grew towards each other from adjacent fastener holes. A longer life occurred when cracks initiated and grew from widely separated holes. Before the initial failure of a specimen (i.e., two cracks linking), the remaining ligament length was consistently of the order of 2 mm. It was also apparent that the 'knife-edging' phenomena was the dominant factor determining crack initiation. In each case the number of cycles required to achieve initial failure did not differ significantly from that to final failure of the unreinforced specimen.

After the application of a bonded doubler, it was observed that, although the cracks did continue to grow, the rate of growth was dramatically less. It was difficult to determine if the hot/wet or salt environment increased the rate of crack growth. In this case specimens A7/A8

were almost completely failed prior to environmental testing, while specimen A3/A4 obviously had no significant increase in crack growth rate.

This test program has shed some light on the phenomena of multiple site damage in typical wide-bodied aircraft pressurized fuselage lap joints. The crack growth data generated may assist in assessing the criticality of in-service cracks, and in the determination of the relevant inspection intervals.

It was demonstrated that, with the present specimen design, failure consistently occurred in the upper fastener row, as this location experiences the highest stress level and the effect of a full-depth counter-sunk in the upper plate. However, crack growth can also occur in the inner skin at the lower fastener row. This is far more difficult to detect in-service. Consequently any proposed repair should be applicable to both locations and preferably increase the required inspection interval for all fastener holes.

This report has demonstrated that an externally bonded composite reinforcement can significantly increase the fatigue life of fuselage lap joints containing multi-site damage, even under a hot wet salt environment. Although this work was generic in nature, the results obtained should be directly applicable to current operation aircraft. Future work will consider biaxial stress states, as encountered at certain locations on the perimeter of pressurized fuselages, and assess the effect of impact damage on the doubler.

5. FLIGHT DEMONSTRATOR PROGRAM

A visit was conducted to Qantas Jet Base, Sydney, Australia, to apply advanced composite doublers to a Boeing 747-300 aircraft in service with Qantas Airways. The goal was to demonstrate the durability of composite doublers in actual service.

5.1 DOUBLER LOCATIONS

Doubler locations were chosen on the following criteria:

A. If patch failure occurs, it should not affect the function of the aircraft, ie., it should not impinge on control surfaces, intakes, profiles, etc.

B. The doublers should experience harsh environmental exposure, including high velocity air, vibration, runway debris, oil, etc.

C. The doublers should be positioned in areas which have a known high probability of damage.

Since this was a demonstrator program, the doublers were not applied to any damaged locations. The chosen doubler locations of the aircraft can be seen in Figure 5-1 and were as follows:

a. The external fuselage skin longitudinal lap joint located at BS 2050 at stringer 46L ('L' for left side of aircraft when viewed from the rear).

b. Left hand side inboard trailing edge midflap. Located on the upper, aft midspar panel 12 inches from outboard edge and 6 inches aft of the teflon rubbing strip.

c. Left hand side inboard trailing edge midflap. Located on the lower forward midspar panel 18 inches from the outboard edge and 6 inches aft of the forward edge.

d. Number 2 engine pylon aft fairing on the hydraulic bay access door 6 inches forward of the aft edge.

e. The fixed leading edge nose of the left hand side wing located at inboard leading edge station 395.

f. The lower leading edge skin panel of the left hand side horizontal stabilator, station 397, 12 inches forward of the front spar.

g. The leading edge nose skin panel of the left horizontal stabilator, station 390.

h. The thrust reverser cowl translating sleeve number 2 engine serial number 12758, located outboard at the 8 o'clock position (looking forward), on the external skin, at the aft edge of the sleeve.

i. The thrust reverser cowl translating sleeve number 2 engine serial number 12758, located inboard at the 4 o'clock position (looking forward) on the external skin at the aft edge of the sleeve.

The selected locations provide a variety of environments that are ideal for demonstrating the versatility and adaptability of bonded composite repairs. Locations 'e' and 'g' are in high

velocity airflow regions; locations 'd', 'h' and 'i' are subject to exposure from engine oil and hydraulic fluid; and locations 'a', 'b', 'c' and 'f' are subject to damage from runway debris on land and take-off. These locations also experience a high frequency of service damage from bird strikes, and collision by baggage. At locations 'e' and 'g', on the leading edge of the wing and the horizontal stabilator, the radius of curvature of the nose section was small, and the boron fibers could not accommodate such a tight radius. Consequently, patches were applied just aft of the leading edge. However, a graphite/epoxy patch could have been employed as an alternative repair.

Further details of the flight demonstrator program for composite patches are given below.
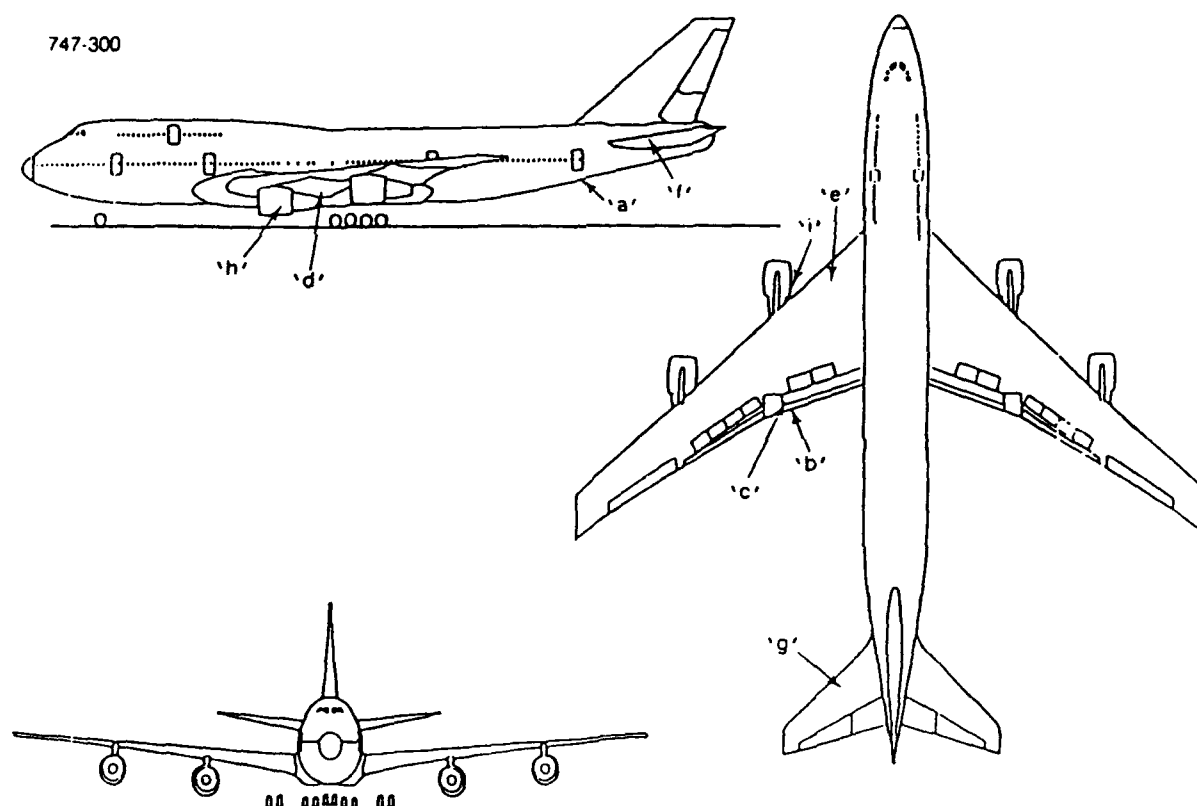
FIGURE 5-1. DOUBLER LOCATIONS ON B747-300

5.2 DOUBLER DESCRIPTIONS

All demonstrator doublers were square, with the size depending upon the particular location. A typical boron doubler, excluding the fuselage lap joint, can be seen in Figure 5-2. For each doubler location, Table 5-1 shows the adhesive type, cure time, cure temperature, dimension 'A' (see Figure 5-2) and number of plies. Each ply is stepped out by 3 mm to improve load transfer. All doublers were laid up with the fibers oriented in the free air stream direction as cracks normally appear perpendicular to the air flow. Pictures of each doubler, some at various stages of preparation, can be located by using Table 5-1 to determine the relevant figure numbers.

The doubler applied to the fuselage lap joint was the ARL standard multi-site damage repair with one modification. Boeing 747-300 aircraft have round head rivets in the upper row of the lap joint. As a result of these protruding rivets, 12 mm diameter holes were shear-punched into the 'B' staged doubler prior to application, see Figure 5-3.

In order to demonstrate the damage tolerant capability of the lap joint repair, a teflon film (25 mm x 12 mm, rounded at the corners), was inserted to simulate an adhesive void. This film was placed in the center of the lower section, close to the step, see Figure 5-4.

Upon heating the lap joint doubler, it was found that the upper side was only achieving a temperature of 80°C and therefore the standard cure time of 1 hour was extended to 8 hours to ensure complete cure of the patch and adhesive.
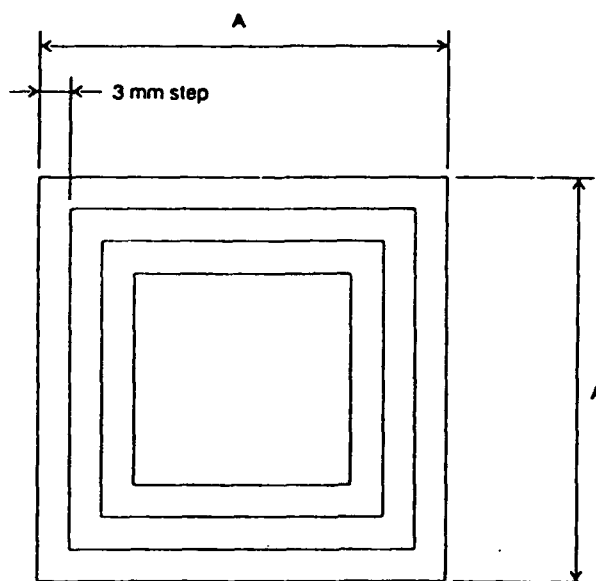
FIGURE 5-2. TYPICAL BORON/EPOXY DOUBLER

TABLE 5-1. DOUBLER INFORMATION

Repair Location	Adhesive Type	Cure Time (Hours)	Cure Temperature (° C)	Size 'A' (mm)	Plies	Figures Numbers
a	FM73	8	80	200	12/4	6, 7, 8
b	FM73	8	80	100	4	9, 10
c	V201	1	RT	150	4	11, 12
d	V201	1	RT	150	4	13, 14
e	FM73	1	120	200	4	15, 16, 17
f	V201	1	RT	146	4	18
g	FM73	1	120	100	4	19, 20
h	FM73	1	120	110	3	21, 22
i	V201	1	RT	110	3	23, 24

RT - Room Temperature
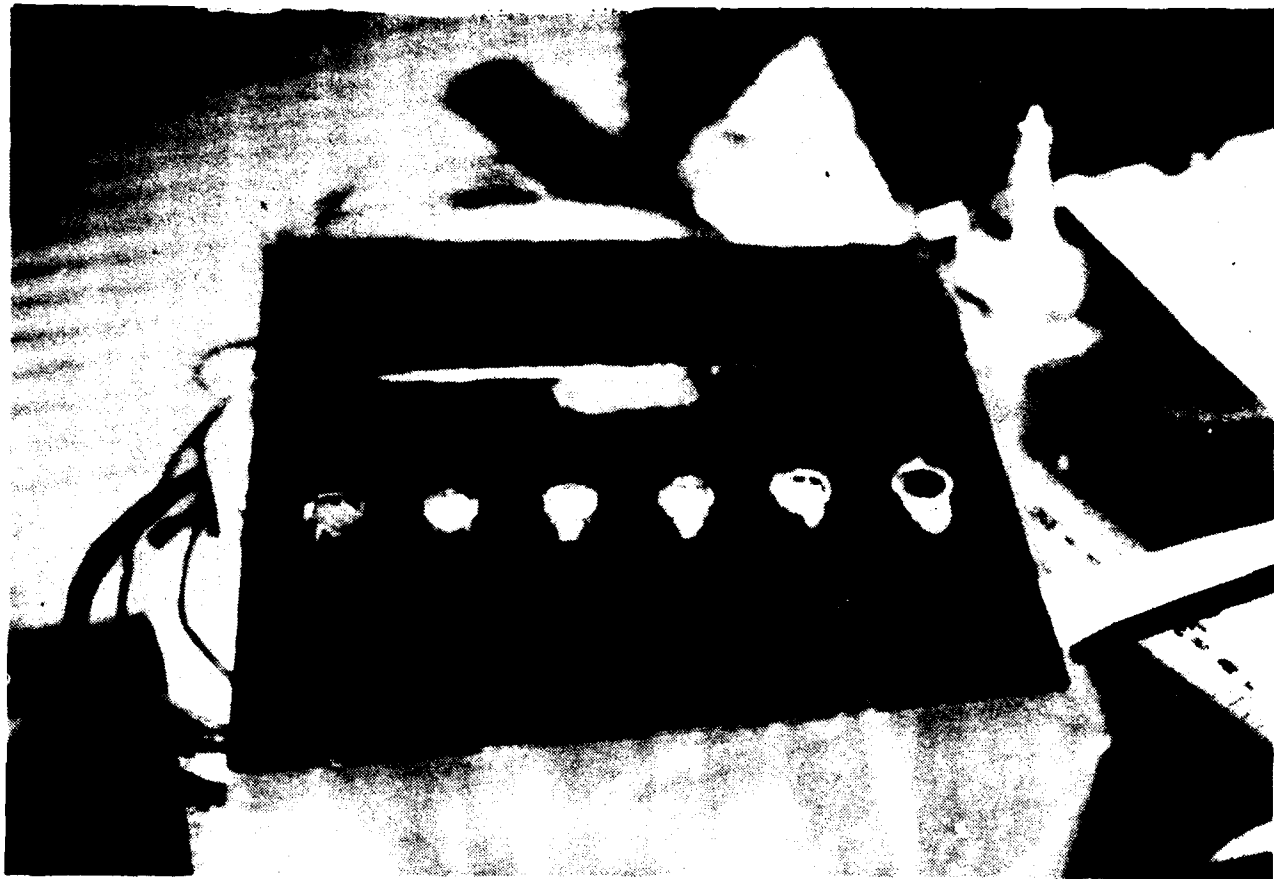
FIGURE 5-3. LAP JOINT DOUBLER SHOWING SHEAR PUNCHED HOLES

FIGURE 5-4. LAP JOINT DOUBLER TEFLON INSERT

It was intended that the repair to location 'f', on the stabilator, have an 80°C, 8 hour cure, but on performing the thermal survey the skin was found to bulge. If this cure had gone ahead the skin would have been permanently deformed, therefore a cold setting adhesive was used. This is a common problem when heating thin skins with no stiffeners in the region to stop out-of-plane deformation.

It is interesting to note that the wing leading edge doubler, location 'e', was near where Qantas maintenance staff started work on a corrosion problem 3 meters away. They were placing a metallic repair over a joint after removing some corrosive material. After two days, the repair had not been completed, but the full circumstances are presently unknown. Previous experience at ARL has shown that a saving in manhours of up to five to one was possible when compared to a metallic repair.

5.3 DOUBLER APPLICATION AND SURFACE TREATMENTS

Qantas stressed that they saw the main advantage of bonded composite repairs, over mechanical doublers, as a time-saving temporary repair that could be applied while the aircraft was at a terminal or away from a major maintenance base. They were interested in a bonding technique that was simple and could be applied quickly under field conditions. We therefore decided to apply the demonstrator doublers using four different techniques, to illustrate the versatility of bonded composite repairs.

Based on structural specifications, supplied by Qantas, all but three patches at locations 'f', 'h' and 'i', were designed and fabricated at ARL. The doublers were made from a boron/epoxy prepreg manufactured by Textron.

The adhesives used were Cyanamid FM73, an epoxy structural film adhesive, and Versilok 201 with accelerator No. 17 (V201), a two-part acrylic structural paste adhesive. The recommended cure for FM73 is at 120°C at 100 kPa for one hour, and for V201 room temperature (24°C) at 100 kPa for one hour. In this case, full strength is reached in 23 hours. It should be noted that for FM73 the cure cycle can be modified to 80°C at 100 kPa for 8 hours (see Figure 5-5), and that for V201, 90% of the ultimate strength is achieved after two hours of the cure cycle.
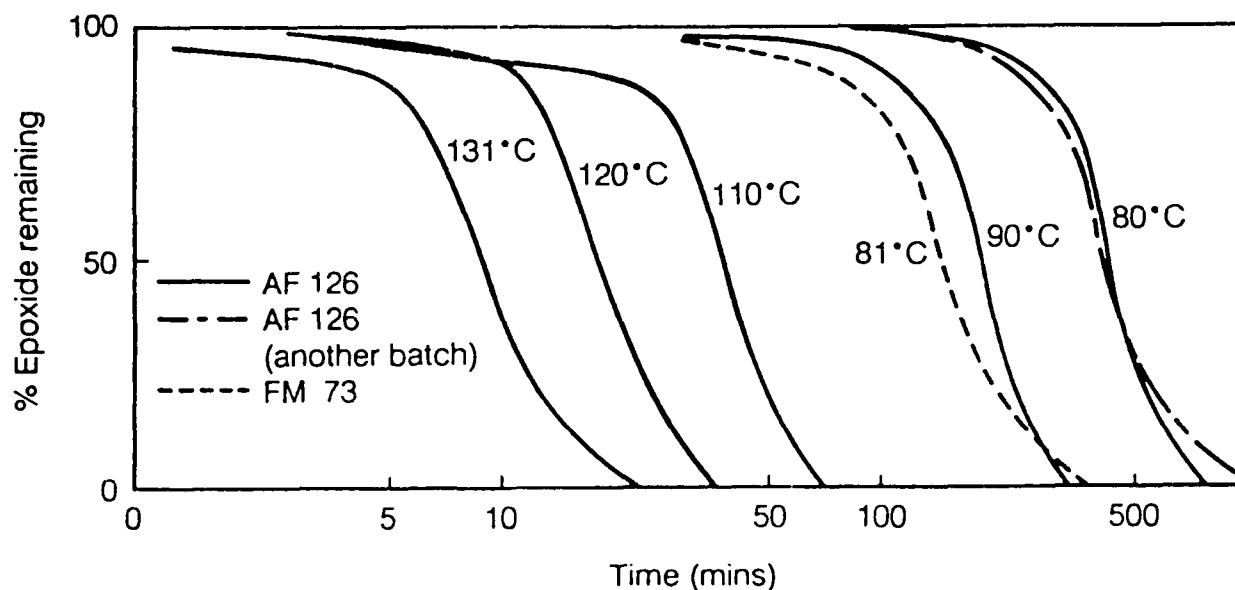
FIGURE 5-5. RATE OF EPOXIDE CONSUMPTION FROM INFRARED STUDIES AT VARIOUS TEMPERATURES FOR ADHESIVES AF126 AND FM73

The environment, parent material and structural configuration of the doubler location, determined the design of the doubler and the adhesive system used. The doubler groups are as follows:

a. A boron/epoxy patch pre-cured at 120°C at 280 kPa for one hour; bonded with FM73.

b. A boron/epoxy patch co-cured with one layer of FM73 at 120°C at 280 kPa for one hour; then bonded with an additional layer of FM73.

c. A boron/epoxy patch 'B' staged (patch partially cured and retains flexibility to accommodate curvature in parent structure) with one layer of FM73 at 80°C at 280 kPa for one hour; bonded with an additional layer of FM73.

d. A boron/epoxy patch designed and fabricated under field conditions.

The patch can be either:

1. pre-cured under vacuum bag at 120°C at 100 kPa for one hour; bonded with FM73 or V201, or

2. co-cured with FM73 under vacuum bag at 120°C at 100 kPa for one hour onto the parent structure.

The standard ARL surface preparation was used to treat the parent structure prior to bonding. This included a thorough abrade with Scotch brite, wipe clean with solvent, a light g_it blast, treatment with a one percent aqueous silane solution, and a surface priming treatment.

In all cases vacuum bags were used to apply pressure to the doublers, and heating if required was accomplished using heater blankets, which were controlled by analog heater control units. Prior to each hot bond application, a thermal survey was carried out to ensure cure temperature could be achieved at the doubler location.

The bonding cure cycle was dependent upon the parent material and sub-structure. Heating of a region, during the doubler application process, can cause local buckling which should be avoided. This occurred at location 'f' when the thermal survey was performed and as a result, a cold-setting adhesive was used. When repairing honey-comb structures care must be taken not to exceed the boiling temperature of water as the pressure buildup could cause the skin to delaminate. To avoid this problem, locations 'b', 'c' and 'd' were cured at 80°C for eight hours.

The surface treatment procedure is an important step of any adhesive bonding process. Ideally, the procedure should be easy to apply under field conditions and yet still be able to provide a high level of bond strength and durability. ARL has developed a standard surface-treatment which was used to prepare all repair locations prior to bonding:

a. The surface is wiped clean with a strong solvent (methyl ethyl ketone) to remove traces of oil and grease.

b. The surface is abraded with Scotch brite pads soaked with solvent to remove primers, paint, oxide films and any shallow scratches.

c. Disposable tissues wet with solvent are used to thoroughly clean the surface until no contamination remains.

155

d. The surface is lightly grit-blasted using 50 micron alumina grit. Compressed dry nitrogen is used as the propellant gas to prevent oil contamination (compressed air often carries oil from compressor systems) and to reduce surface oxidation by displacing oxygen during grit-blasting.

e. The surface is wet with a one percent by volume silane solution in distilled water for 15 minutes. The silane acts as a coupling agent and improves the bond durability between the adhesive and the metal. The surface is then air-dried for 15 minutes.

f. A surface priming treatment is then applied. This is a new step in the process, and laboratory results, see Figure 5-6, show a marked improvement in bond durability after application.

g. On pre-cured patches only, the patch surface is thoroughly cleaned with solvent and lightly grit-blasted.

(Painted surfaces must have the paint removed in accordance with standard aircraft practice.)

After completion of each doubler, the excess adhesive was removed and the area cleaned. Qantas required all doublers to be painted with their standard surface treatment and paint. ARL staff requested that heavy sanding of the boron doubler be avoided. A light sand prior to painting is permissible.
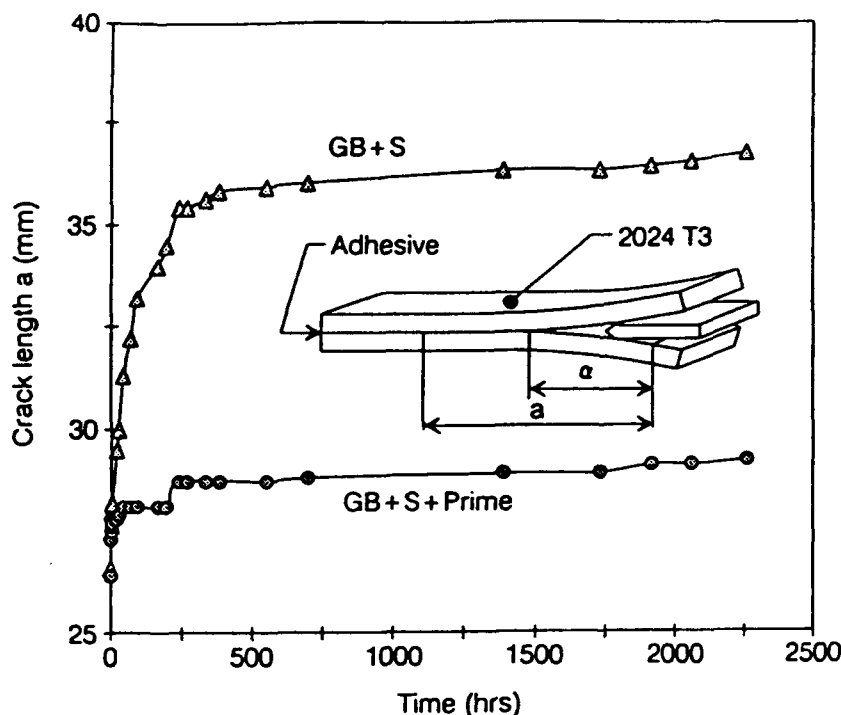
FIGURE 5-6. PLOTS OF CRACK LENGTH VS. TIME FOR WEDGE TEST SPECIMEN

156

5.4 SUMMARY AND CONCLUSION

Over a three and a half day period, nine boron/epoxy doublers were bonded to the Boeing 747-300 aircraft in service with Qantas airways. The demonstrator doublers were placed at strategic locations to provide the greatest probability for service damage and environmental conditioning. Various doubler configurations were chosen depending upon the structural configuration of the area, environment and doubler location. These doublers will be monitored by ARl and Qantas on a regular basis to assess their durability.

Of the demonstrator programs that are flying on civilian aircraft, to date, there have been no reported failures attributed to the bonded composite repair technology. The application of the doublers to the Qantas B747 aircraft is a further step towards demonstrating the durability and performance of bonded repairs. It is envisaged that as confidence is gained in the technique by the regulatory authorities, aircraft manufacturers and operators, certification of the technology will follow.

While attention has been focused on the use of a boron/epoxy repair scheme the basic specimen geometry may also be useful in evaluating other mechanically fastened repairs or alternate joint design methodologies. However, before other joint configurations can be evaluated the failure mechanisms of the existing structure must be understood. To do this a detailed understanding of the stress field in the vicinity of the joint is required. In the present report this stress field will be obtained experimentally using thermal emission techniques.

An elastic-plastic stress analysis of the unrepaired specimen will also be presented and it will be shown that failure occurs as a results of net section failure rather than by ductile fracture.

REFERENCES

1. Baker, A.A., Boron Fibre Reinforced Plastic Patching for Cracked Aircraft Structures, Aircraft, Sept. 1981.

2. Atluri, S.N., Kathiresan, K., Stress Analysis of Typical Flaws in Aerospace Structural Components Using 3-D Hybrid Displacement Finite Element Method, 19th AIAA/ ASME/SAE Structures, Structural Dynamics & Materials Conf., Bethesda, MD, pp 340351, 1978.

3. Rose, L.R.F., An Application of the Inclusion Analogy for Bonded Reinforcements, Int. J. Solids Structures, 17, 827-838,1981.

4. Baker, A.A., Fibre Composite Repair of Cracked Metallic Aircraft Components-Practical and Basic Aspects, AGARD Specialists Meeting, oslo, April 1986.

5. Baker, A.A., Roberts, J.D., Rose, L.R.F., Experimental Study of overlap Joint Parameters Relevant to the K Reduction Due lo Crack Patching, Proc. 28th National SAMPE Symposium, Azusa, 627-639, 1983.

6. Baker, A.A., Evaluation of Adhesives for Fibre Composite Reinforcement of Fatigue Cracked Aluminum Alloys, SAMPE Journal, Mar/Apr 1979.

7. Pearson, C.E. (Ed.) Handbook of Applied Mathematics, Prentice Hall, 1974.

8. Jones, R, Callinan, R.J., Finite Element Analysis of Patch Cracks, J. Struct. Mech., 7, 107-130, 1979.

9. Mitchell, RA., Wooley, R.M., Chivirut, D.J., Analysis of Composite Reinforced Cutouts and Cracks, AIAA J., 13, 744-749, 1975.

10. Muskhelishvili, N.I., Some Basic Problems of Mathematical Theory of Elasticity, P. Noordhoff, Groningen, 1953.

11. Erdogan, F., Arin, K., A Sandwich Plate with a Part-Through and a Debonding Crack, Eng. Fract. Mech., 4, 449-458, 1972.

12. Erdogan, F., on the Stress Distribution in Plates with Collinear Cuts Under Arbitrary Loads, Proc. 4th US Nat. Cong. Appl. Mech., ASME, 1962.

13. Roderick, G.L., Green Functions for Stresses, Stress Intensity Factors, and Displacements in a Cracked, Infinite, Isotropic Sheet under Symmetric Loads, Engg. Frac. Mech., 13, 95-105,1980.

14. Itou, S., Dynamic Stress Intensity Factors Around Two Co-planar Griffith Cracks in an orthotropic Layer Sandwiched Between Two Elastic Half-Planes, Engg. Frac. Mech. 34, 1085-1095, 1989.

15. Cartwright, D.J., Parker, A P., opening Mode Stress Intensity Factors for Cracks in PinLoads Joints, Int'l. Journal of Fracture, Vol. 18, pp 65-78, 1982.

16. Atluri, S.N., Nishioka, T., Analytical Solution for Embedded Elliptical Cracks, and Finite Element Alternating Methods for Elliptical Surface Cracks Subjected to Arbitrary Loads, Engg. Frac. Mech., Vol. 17, pp 247-268, 1983.

17. Lowak, H., Huck, M., Schutz, D., Schutz, W., Standardisiertes Einzelflugprogramm fur Kampfflugzeuge FALSTAFF, LBF-Bericht Nr. 3045 (1976).

18. Branger, J., Phomberg, H., Influence of Load Sequence and Ground Load Variations of FALSTAFF, Proc. of the 8th ICAF Symposium, Lausanne, Switzerland, June 1975.

19. van Dijk, G.M., de Jonge, J.B., Instroduction to a Fighter Aircraft Loading STAndard for Fatigue Evaluation FALSTAFF, NLR MP 75017 U, May 1975.

20. Atluri, S.N., *Computational Methods in the Mechanics of Fracture*, 1986.

APPENDIX A

Gel Preparation

1. Gel should be prepared 48 hours in advance.

2. All utensils should be cleaned with MEK prior to use.

3. Add 75 ml phosphoric acid to 500 ml distilled water, stirring continuously. DO NOT ADD WATER TO ACID. Make up to 1 liter.

4. Add 200 g AEROSIL 200, stirring continuously until thick. Add more if gel is too thin. Mix well.

5. Allow to stand in sealed container for 48 hours minimum.

6. Do not agitate.

7. Shelf life of 6 months.

8. If too thick, agitate slightly during use.

Power Cycle.

1. Apply 1 Volt.

2. Increase power by 1 Volt each minute to 6 Volts.

3. Hold at 6 Volts for 10 minutes.

4. Turn off power and wash surface immediately.

APPENDIX B
Crack Data

TABLE B-1. FATIGUE CRACK GROWTH DATA - 1B (EARLY)

Specimen No. 1B/FM300/20'C/0.03/1

Cycles N x 10^3	Crack Length (mm)	Clip Gauge uE (White)	Clip Gauge mm (/2513)
2 0	4.0	42	.0167130919
6.0	4 0	45	.0179068842
10 0	4.0	49	.0194986072
18.0	4.0	48	.0191006765
25.0	4.5	51	.0202944688
32.0	5.0	54	.021488261
38.0	5.0	56	.0222841226
45.0	5.0	59	0234779148
50.0	5.0	62	.0246717071
55.0	5.5	64	.0254675686
60.0	6.0	67	.0266613609
65.0	6.5	70	.0278551532
70.0	6.5	73	0290489455
75 0	7.0	76	0302427378
83.0	7.5	80	0318344608
89 0	8 5	85	0338241146
95 0	9 0	90	0358137684
100 0	9 0	93	0370075607
105 0	9.5	97	.0385992837
110.0	10 5	101	0401910068
117 0	11.5	103	0409868683
125 0	12 5	110	.0437723836
132 0	13.5	115	0457620374

TABLE B-2. FATIGUE CRACK GROWTH DATA - 1B (LATE)

Specimen No. 1B/FM300/20'C/0.03/1

Cycles N x 10^3	Crack Length (mm)	Clip Gauge uE (White)	Clip Gauge mm (/2513)
136.0	14.5	120	.0477516912
140.0	15.5	126	.0501392758
145.0	16.5	130	.0517309968
150.0	17.5	134	.0533227218
155.0	18.5	138	.0549144449
162 0	19.5	148	.0588937525
166.0	21.5	152	0604854755
173.0	23.0	160	.0636689216
177.0	24.0	166	.0660565062
182.0	25.0	173	.0688420215
186.0	26.5	182	.0724233983
190 0	28.0	190	.0756068444
195.0	29.5	202	.0803820135
198.0	30.5	210	.0835654596
201.0	32.0	217	.0863509749
205.0	33.5	229	.0911261441
208.0	34.0	248	.0986868285
211.0	35.5	260	.1034619976
214.0	37.0	270	.10744:3052
220.0	39.5	307	.1221647433
225.0	42.5	338	.1345005969
228.0	44.0	365	.1452447274
230	45.0	375	.149224035

TABLE B-3. FATIGUE CRACK GROWTH DATA - A (EARLY)

Specimen No. A/FM300K/100°C/0.03/1

Cycles N x 10^3	Crack Length (mm)	Clip Gauge uE (Black)	Clip Gauge mm (/3344)
1.0	.	79	.0236244019
4.0	8.0	80	.023923445
7.0	.	85	.0254186603
10.0	8.0	88	.0263157895
13.0	.	95	.0284090909
16.0	9.0	90	.0269138756
20.0	.	93	.0278110048
23.0	11.0	93	.0278110048
26.0	12.0	93	.0278110048
29.0	12.0	101	.0302033493
32.0	12.5	103	.0308014354
35.0	13.0	101	.0302033493
38.0	14.0	103	.0308014354
41.0	15.0	87	.0260167464
44.0	.	89	.0266148325
47.0	15.0	96	.028708134
50.0	.	96	.028708134
53.0	15.5	96	.028708134
56.0	.	93	.0278110048
59.0	18.0	96	.028708134
62.0	.	90	.0269138756

TABLE B-4. FATIGUE CRACK GROWTH DATA - A

Specimen No. A/FM300K/100°C/0.03/1

Cycles N x 10^3	Crack Length (mm)	Clip Gauge uE (Black)	Clip Gauge mm (/3344)
65.0	20.0	93	.0278110048
68.0	.	96	.028708134
71.0	20.5	96	.028708134
74.0	.	100	.0299043062
77.0	21.5	100	.0299043062
80.0	.	100	.0299043062
83.0	22.5	102	.0305023923
86.0	.	101	.0302033493
89.0	23.0	105	.0313995215
92.0	.	100	.0299043062
95.0	25.0	103	.0308014354
98.0	25.5	105	.0313995215
101.0	26.0	105	.0313995215
104.0	26.5	105	.0313995215
107.0	27.0	104	.0311004785
110.0	28.0	105	.0313995215
112.0	28.0	107	.0319976077
116.0	.	106	.0316985646
119.0	29.0	109	.0325956938
122.0	.	106	.0316985646
125.0	30.5	106	.0316985646

TABLE B-5. FATIGUE CRACK GROWTH DATA - A (LATE)

Specimen No. A/FM300K/100'C/0.03/1

Cycles N x 10^3	Crack Length (mm)	Clip Gauge uE (Black)	Clip Gauge mm (/3344)
128.0	.	110	0328947368
131.0	32.0	105	0313995215
137.0	34.0	105	0313995215
140.0	.	110	0328947368
143.0	35.5	109	.0325956938
146.0	.	115	.0343899522
149.0	36.5	112	.033492823
152.0	.	115	.0343899522
155 0	38.0	116	0346889952
15b 0	.	120	.0358851675
161.0	39.0	120	0358851675
164.0	.	120	0358851675
167.0	41.5	120	0358851675
170 0	.	121	.0361842105
173.0	43.5	125	.0373803828
176 0	.	120	.0358851675
179 0	.	124	0370813397
182 0	45.0	127	0379784689
185 0	46.5	126	0376794258
188 0	47.0	124	.0370813397

TABLE B-6. FATIGUE CRACK GROWTH DATA - B

Specimen No. B/FM300K/100'C/0.03/1

Cycles N x 10^3	Crack Length (mm)	Clip Gauge uE (White)	Clip Gauge mm (/2513)
1.0	.	74	.0294468762
4.0	8.0	79	.03143653
7.0	.	80	.0318344608
10 0	8.0	83	.0330282531
13.0	.	85	.0338241146
16.0	9.0	85	.0338241146
20 0	.	93	0370075607
23 0	10.5	90	0358137684
26 0	11.5	92	.0366096299
29 0	13.0	94	.0374054914
32 0	13.5	100	.039793076
35.0	14.0	100	.039793076
38.0	15.0	100	.039793076
41 0	15 0	105	0417827298
44 0	.	125	049741345
47 0	16.0	117	0465578989
50 0	.	118	0469558297
53.0	17.0	118	0469558297
56 0	.	116	.0461599682
59 0	18 5	121	.048149622
62 0	.	115	0457620374

Raw Crack Length Data For Fatigue Tests on Corner Flaw Specimens

TABLE B-7. SURFACE CRACK GROWTH RESULTS FOR SPECIMEN A-1.

Fatigue cycles	X position of surface point (mm)				Crack lengths (mm)		
	Left side crack tip	Left side hole edge	Right side hole edge	Right side crack tip	Left side	Right side	Total length
0	63.14	65.99	72.02	75.02	2.85	3.00	5.85
10,000	63.12	65.98	72.02	75.03	2.86	3.01	5.87
20,000	63.12	65.98	72.02	75.03	2.86	3.01	5.87
30,000	63.12	65.98	72.02	75.03	2.86	3.01	5.87
40,000	62.13	65.74	71.77	75.57	3.61	3.80	7.41
50,000	61.42	65.89	71.89	76.51	4.47	4.62	9.09
60,000	60.20	65.88	71.89	77.48	5.68	5.59	11.27
70,000	59.18	65.89	71.94	79.47	6.71	7.53	14.24
77,000	56.91	65.88	71.88	80.63	8.97	8.75	17.72
82,000	55.08	65.88	71.90	81.99	10.80	10.09	20.89
87,000	52.30	65.88	71.87	84.84	13.58	12.97	26.55
89,000	50.71	65.85	71.85	86.55	15.14	14.70	29.84
90,000	49.72	65.87	71.87	87.70	16.15	15.83	31.98
91,000	48.83	65.91	71.91	88.90	17.08	16.99	34.07
92,000	47.80	65.93	71.93	90.01	18.13	18.08	36.21
93,000	45.56	65.94	71.95	92.08	20.38	20.13	40.51
93,500	44.53	65.95	71.97	93.52	21.42	21.55	42.97
94,000	42.47	65.77	71.79	96.01	23.30	24.22	47.52
94,240							

TABLE B-8. SURFACE CRACK GROWTH RESULTS FOR SPECIMEN A-2

Fatigue cycles	X position of surface point (mm)				Crack lengths (mm)		
	Left side crack tip	Left side hole edge	Right side hole edge	Right side crack tip	Left side	Right side	Total length
0	63.10	66.03	72.07	74.94	2.93	2.87	5.80
10,000	63.10	66.03	72.07	74.94	2.93	2.87	5.80
20,000	63.10	66.03	72.07	74.94	2.93	2.87	5.80
30,000	63.10	66.03	72.07	74.94	2.93	2.87	5.80
40,000	62.89	66.03	72.06	75.43	3.14	3.37	6.51
50,000	62.41	66.03	72.06	75.77	3.62	3.71	7.33
60,000	61.76	66.04	72.05	76.61	4.28	4.56	8.84
70,000	60.83	66.04	72.05	77.79	5.21	5.74	10.95
80,000	59.25	66.02	72.02	79.23	6.77	7.21	13.98
87,000	58.03	66.05	72.06	80.97	8.02	8.91	16.93
92,000	55.79	66.07	72.07	82.71	10.28	10.64	20.92
94,000	54.89	66.04	72.05	83.70	11.15	11.65	22.80
96,000	54.32	66.03	72.03	84.65	11.71	12.62	24.33
98,000	53.02	66.05	72.06	86.08	13.03	14.02	27.05
99,000	52.07	66.05	72.06	86.94	13.98	14.88	28.86
100,000	50.75	66.08	72.11	87.64	15.33	15.53	30.86
101,000	49.77	66.10	72.12	88.75	16.33	16.63	32.96
102,000	48.36	66.14	72.18	90.21	17.78	18.02	35.80
103,000	46.28	66.14	72.14	91.84	19.86	19.70	39.50
103,500	43.34	65.89	71.92	92.98	22.55	21.06	43.61
104,000	40.63	65.95	71.92	95.84	25.35	23.92	49.24
104,150							

TABLE B-9. SURFACE CRACK GROWTH RESULTS FOR SPECIMEN A-3

Fatigue cycles	X position of surface point (mm)				Crack lengths (mm)		
	Left side crack tip	Left side hole edge	Right side hole edge	Right side crack tip	Left side	Right side	Total length
0	59.62	62.31	68.52	71.53	2.69	3.01	5.70
10,000	59.62	62.31	68.52	71.53	2.69	3.01	5.70
20,000	59.62	62.31	68.52	71.53	2.69	3.01	5.70
30,000	59.62	62.31	68.52	71.53	2.69	3.01	5.70
40,000	59.62	62.31	68.52	71.53	2.69	3.01	5.70
50,000	59.62	62.31	68.52	71.81	2.69	3.29	5.98
60,000	59.63	62.30	68.52	71.84	2.67	3.32	5.99
70,000	59.66	62.28	68.50	72.11	2.62	3.61	6.23
80,000	59.30	62.42	68.65	72.91	3.12	4.26	7.38
90,000	58.78	62.48	68.65	73.11	3.70	4.46	8.16
100,000	57.91	62.36	68.61	74.12	4.45	5.51	9.96
110,000	56.86	62.33	68.61	75.33	5.47	6.72	12.19
117,000	55.71	62.36	68.63	76.85	6.65	8.22	14.87
124,000	53.05	62.37	68.59	79.13	9.32	10.54	19.86
127,000	52.18	62.32	68.48	79.91	10.14	11.43	21.57
130,000	50.23	62.36	68.50	81.77	12.13	13.27	25.40
132,000	48.91	62.32	68.51	83.29	13.41	14.78	28.19
133,000	48.05	62.50	68.65	84.20	14.45	15.55	30.00
134,000	47.07	62.46	68.64	84.95	15.39	16.31	31.70
135,000	46.57	62.43	68.62	86.95	15.86	18.33	34.19
136,000	44.63	62.36	68.57	87.81	17.73	19.24	36.97
137,000	42.66	62.41	68.59	90.53	19.75	21.94	41.69
137,500	41.71	62.31	68.59	92.81	20.60	24.22	44.82
137,830							

TABLE B-10. SURFACE CRACK GROWTH RESULTS FOR SPECIMEN A-4

Fatigue cycles	X position of surface point (mm)				Crack lengths (mm)		
	Left side crack tip	Left side hole edge	Right side hole edge	Right side crack tip	Left side	Right side	Total length
0	60.33	63.22	69.22	72.30	2.89	3.08	5.97
10,000	60.33	63.22	69.22	72.30	2.89	3.08	5.97
20,000	60.33	63.22	69.22	72.30	2.89	3.08	5.97
30,000	60.33	63.22	69.22	72.30	2.89	3.08	5.97
40,000	60.33	63.22	69.22	72.30	2.89	3.08	5.97
50,000	59.96	63.22	69.22	73.08	3.76	3.86	7.62
60,000	59.17	63.16	69.15	73.43	3.99	4.28	8.27
70,000	58.67	63.11	69.11	73.91	4.44	4.80	9.24
77,000	58.15	63.14	69.15	74.45	4.99	5.30	10.29
84,000	57.43	63.12	69.12	75.07	5.69	5.95	11.64
91,000	56.86	63.11	69.12	76.38	6.25	7.26	13.51
98,000	55.64	63.14	69.12	78.12	7.50	9.00	16.50
102,000	54.67	63.14	69.14	79.68	8.47	10.54	19.01
105,000	53.55	63.14	69.11	80.71	9.59	11.60	21.19
108,000	51.51	63.17	69.14	82.34	11.66	13.20	24.86
110,000	50.50	63.13	69.12	83.71	12.63	14.59	27.22
112,000	48.83	63.17	69.17	85.43	14.34	16.26	30.60
113,000	47.65	63.14	69.12	86.32	15.49	17.20	32.69
114,000	46.55	63.15	69.14	87.31	16.60	18.17	34.77
115,000	44.95	63.13	69.14	88.50	18.18	19.36	37.54
115,700	43.32	63.14	69.09	89.84	19.82	20.75	40.57
116,200	42.39	63.08	69.08	90.91	20.69	21.83	42.52
116,600	40.72	63.02	69.03	92.05	22.30	23.02	45.32
116,800	39.40	63.04	69.03	93.13	23.64	24.10	47.74
117,800	38.19	63.01	69.01	94.17	24.82	25.16	49.98
117,930							

TABLE B-11. SURFACE CRACK GROWTH RESULTS FOR SPECIMEN A-5

Fatigue cycles	X position of surface point (mm)				Crack lengths (mm)		
	Left side crack tip	Left side hole edge	Right side hole edge	Right side crack tip	Left side	Right side	Total length
0	64.67	-	-	76.47	2.90	2.90	5.80
10,000	64.67	-	-	76.47	2.90	2.90	5.80
20,000	64.67	-	-	76.85	2.90	3.28	6.18
30,000	64.67	-	-	77.04	2.90	3.47	6.37
40,000	63.93	-	-	77.27	3.64	3.70	7.34
50,000	63.79	-	-	77.50	3.78	3.93	7.71
60,000	63.45	-	-	78.05	4.12	4.48	8.60
80,000	62.50	-	-	79.35	5.07	5.78	10.85
100,000	60.48	-	-	82.42	7.09	8.85	15.94
110,000	57.88	-	-	85.23	9.69	11.66	21.35
115,000	54.10	-	-	88.32	13.47	14.75	28.22
119,800							

TABLE B-12. SURFACE CRACK GROWTH RESULTS FOR SPECIMEN A-6

Fatigue cycles	X position of surface point (mm)				Crack lengths (mm)		
	Left side crack tip	Left side hole edge	Right side hole edge	Right side crack tip	Left side	Right side	Total length
0	62.35	-	-	74.21	2.93	2.93	5.86
10,000	62.35	-	-	74.21	2.93	2.93	5.86
20,000	62.35	-	-	74.21	2.93	2.93	5.86
30,000	62.18	-	-	76.62	3.10	3.34	6.44
40,000	61.80	-	-	74.89	3.48	3.61	7.09
50,000	61.35	-	-	74.89	3.93	3.61	7.54
60,000	61.23	-	-	75.14	4.05	3.86	7.91
70,000	61.22	-	-	75 37	4.06	4.09	8.15
80,000	60.75	-	-	75.81	4.53	4.53	9.06
90,000	60.34	-	-	75.81	4.94	4.53	9.47
100,000	59.60	-	-	75.95	5.68	4.67	10.35
110,000	59.62	-	-	76.06	5.66	4.78	10.44
120,000	58.94	-	-	76.50	6.34	5.22	11.56
130,000	58.70	-	-	77.33	6.58	6.05	12.63
140,000	58.33	-	-	78.76	6.95	7.48	14.43
150,000	56.91	-	-	80.21	8.37	8.93	17.30
154,000	56.60	-	-	80.90	8.68	9.62	18.30
158,000	56.20	-	-	81.80	9.08	10.52	19.6
162,000	55.51	-	-	82.76	9.77	11.48	21.25
166,000	54.39	-	-	84.12	10.89	12.84	23.73
170,000	53.57	-	-	85.78	11.71	14.50	26.21
174,000	51.35	-	-	88.41	13.93	17.13	31.06
176,000	50.40	-	-	89.79	14.88	18.51	33.39
178,000	47.65	-	-	93.10	17.63	21.82	39.45
179,000	44.98	-	-	97.14	20.30	25.86	46.16
179,160							

TABLE B-13. SURFACE CRACK GROWTH RESULTS FOR SPECIMEN A-7

Fatigue cycles	X position of surface point (mm)				Crack lengths (mm)		
	Left side crack tip	Left side hole edge	Right side hole edge	Right side crack tip	Left side	Right side	Total length
0	63.20	66.12	72.12	75.05	2.92	2.92	5.85
10,000	63.20	-	-	75.05	2.92	2.92	5.85
20,000	63.20	-	-	75.05	2.92	2.92	5.85
30,000	63.20	-	-	75.05	2.92	2.92	5.85
40,000	63.20	-	-	75.05	2.92	2.92	5.85
50,000	62.84	-	-	75.26	3.28	3.13	6.42
60,000	62.73	-	-	75.51	3.39	3.38	6.78
70,000	62.74	-	-	75.72	3.38	3.59	6.98
90,000	62.53	-	-	75.93	3.59	3.80	7.40
110,000	62.39	-	-	76.20	3.73	4.07	7.81
130,000	62.05	-	-	76.50	4.07	4.37	8.45
170,000	61.40	-	-	77.20	4.72	5.07	9.80
190,000	60.71	-	-	77.76	5.41	5.63	11.05
210,000	60.49	-	-	78.16	5.63	6.03	11.67
230,000	58.73	-	-	79.07	7.39	6.94	14.34
250,000	56.93	-	-	80.67	9.19	8.54	17.74
270,000	51.13	-	-	84.75	14.99	12.62	27.62
277,310							

TABLE B-14. SURFACE CRACK GROWTH RESULTS FOR SPECIMEN A-8

Fatigue cycles	X position of surface point (mm)				Crack lengths (mm)		
	Left side crack tip	Left side hole edge	Right side hole edge	Right side crack tip	Left side	Right side	Total length
0	62.46	65.39	71.39	74.32	2.93	2.93	5.86
10,000	62.46	65.39	71.39	74.32	2.93	2.93	5.86
20,000	62.46	65.39	71.39	74.32	2.93	2.93	5.86
30,000	62.26	-	-	74.61	3.13	3.22	6.35
50,000	62.16	-	-	74.90	3.23	3.51	6.74
60,000	62.05	-	-	74.87	3.34	3.48	6.82
70,000	61.93	-	-	74.98	3.46	3.59	7.05
80,000	61.93	-	-	75.26	3.46	3.87	7.33
100,000	61.71	-	-	75.29	3.68	3.90	7.58
140,000	61.69	-	-	75.59	3.70	4.20	7.90
180,000	61.19	-	-	75.75	4.20	4.36	8.56
200,000	60.64	-	-	76.10	4.75	4.71	9.46
220,000	60.48	-	-	77.06	4.91	5.67	10.58
240,000	60.00	-	-	77.67	5.39	6.28	11.67
260,000	57.82	-	-	78.63	7.57	7.24	14.81
280,000	50.95	-	-	85.88	14.44	14.49	28.93
284,000	46.37	-	-	92.52	19.02	21.13	40.15
285,310							

TABLE B-15. SURFACE CRACK GROWTH RESULTS FOR SPECIMEN A-13

Fatigue cycles	X position of surface point (mm)				Crack lengths (mm) ·		
	Left side crack tip	Left side hole edge	Right side hole edge	Right side crack tip	Left side	Right side	Total length
0	63.60	66.43	72.48	75.54	2.83	3.06	5.89
30,000	63.60	66.43	72.48	75.54	2.83	3.06	5.89
60,000	63.60	66.43	72.48	75.54	2.83	3.06	5.89
90,000	63.60	66.43	72.48	75.54	2.83	3.06	5.89
120,000	63.60	66.43	72.48	75.54	2.83	3.06	5.89
150,000	63.60	66.43	72.48	75.54	2.83	3.06	5.89
180,000	63.60	66.43	72.48	75.54	2.83	3.06	5.89
210,000	63.60	66.43	72.48	75.54	2.83	3.06	5.89
240,000	63.60	66.43	72.48	75.54	2.83	3.06	5.89
320,000	63.60	66.43	72.48	75.54	2.83	3.06	5.89
370,410	63.60	66.43	72.48	75.54	2.83	3.06	5.89
370,410	63.18	66.03	72.05	75.15	2.85	3.05	5.90
430,410	62.22	66.03	72.05	75.66	3.81	3.61	7.42
470,410	60.94	-	-	76.05	5.09	4.00	.9.09
510,410	60.30	-	-	77.32	5.32	5.27	11.00
550,410	53.15	66.03	72.05	83.86	12.88	11.81	24.69
558,490	42.30	66.03	72.05	94.30	23.73	22.25	45.98
558,920							

TABLE B-16. SURFACE CRACK GROWTH RESULTS FOR SPECIMEN B-1

Fatigue cycles	X position of surface point (mm)				Crack lengths (mm)		
	Left side crack tip	Left side hole edge	Right side hole edge	Right side crack tip	Left side	Right side	Total length
0	63.88	66.70	76.80	79.93	2.82	3.13	5.95
10,000	63.72	66.63	76.68	79.81	2.91	3.13	6.04
20,000	63.71	66.60	76.71	79.82	2.89	3.11	6.00
30,000	63.71	66.60	76.71	79.82	2.89	3.11	6.00
40,000	63.72	66.65	76.72	80.47	2.93	3.75	6.68
50,000	63.25	66.65	76.72	81.43	3.40	4.71	8.11
60,000	62.74	66.65	76.72	83.22	3.91	6.50	10.41
70,000	61.99	66.65	76.72	84.64	4.66	7.92	12.58
80,000	60.32	66.65	76.72	87.10	6.33	10.38	16.71
90,000	57.60	66.65	76.72	91.32	9.05	14.6	23.65
97,560							

TABLE B-17. SURFACE CRACK GROWTH RESULTS FOR SPECIMEN B-26

Fatigue cycles	X position of surface point (mm)				Crack lengths (mm)		
	Left side crack tip	Left side hole edge	Right side hole edge	Right side crack tip	Left side	Right side	Total length
0	65.89	68.95	79.00	81.82	3.06	2.82	5.88
10,000	65.89	68.95	79.00	81.82	3.06	2.82	5.88
20,000	65.89	68.95	79.00	81.82	3.06	2.82	5.88
40,000	65.12	68.95	79.00	81.82	3.83	2.82	6.65
50,000	64.57	68.92	79.00	82.64	4.35	3.64	7.99
60,000	62.77	68.92	78.98	83.92	6.15	4.94	11.09
70,000	60.38	68.87	79.00	86.60	8.49	7.60	16.09
75,000	58.73	68.88	78.98	88.26	10.15	9.3	19.45
78,000	56.94	68.84	78.95	89.56	11.90	10.61	22.51
80,000	55.94	68.81	78.92	90.63	12.87	11.71	24.58
82,000	54.85	68.83	78.90	92.34	13.98	13.42	27.40
84,000	52.10	68.86	78.94	94.29	16.76	15.35	32.11
86,000	48.28	68.85	78.85	97.43	20.57	18.58	39.15
86,550							

TABLE B-18. SURFACE CRACK GROWTH RESULTS FOR SPECIMEN B-3

Fatigue cycles	X position of surface point (mm)				Crack lengths (mm)		
	Left side crack tip	Left side hole edge	Right side hole edge	Right side crack tip	Left side	Right side	Total length
0	60.76	63.70	73.75	76.92	2.94	3.17	6.11
10,000	60.76	63.70	73.75	76.92	2.94	3.17	6.11
19,000	60.76	63.70	73.75	76.92	2.94	3.17	6.11
29,000	60.55	63.70	73.75	76.92	3.15	3.17	6.32
29,000	64.14	67.21	77.31	80.44	3.07	3.13	6.20
39,000	63.67	67.26	77.35	80.53	3.59	3.18	6.77
49,000	63.18	67.20	77.27	81.71	4.02	4.44	8.46
56,000	62.91	67.22	77.27	81.71	4.31	4.68	8.99
63,000	62.65	67.23	77.28	82.65	4.58	5.37	9.95
70,000	62.10	67.22	77.30	83.21	5.12	5.91	11.03
77,000	61.50	67.24	77.31	83.83	5.74	6.52	12.26
84,000	60.40	67.23	77.30	85.30	6.83	8.00	14.83
89,000	59.29	67.24	77.30	86.77	7.95	9.47	17.42
91,000	58.60	67.24	77.32	87.75	8.64	10.43	19.07
93,000	57.40	67.24	77.31	88.65	9.84	11.34	21.18
95,000	56.36	67.24	77.31	90.09	10.88	12.78	23.66
97,000	54.65	67.29	77.34	92.16	12.64	14.81	27.45
98,000	53.66	67.39	77.45	93.30	13.73	15.85	29.58
99,000	52.14	67.39	77.46	95.16	15.25	17.70	32.95
100,000	50.00	67.39	77.42	97.74	17.39	20.32	37.71
100,500	48.08	67.44	77.47	100.27	19.36	22.80	42.16
100,720							

TABLE B-19. SURFACE CRACK GROWTH RESULTS FOR SPECIMEN B-5

Fatigue cycles	X position of surface point (mm)				Crack lengths (mm)		
	Left side crack tip	Left side hole edge	Right side hole edge	Right side crack tip	Left side	Right side	Total length
0	57.38	60.47	70.42	73.06	3.09	2.64	5.73
10,000	57.38	60.47	70.42	73.06	3.09	2.64	5.73
20,000	57.38	60.47	70.42	73.06	3.09	2.64	5.73
30,000	57.38	60.47	70.42	73.06	3.09	2.64	5.73
40,000	57.38	60.47	70.42	73.06	3.09	2.64	5.73
50,000	56.74	60.47	70.42	75.09	3.73	4.67	8.40
60,000	56.07	60.28	70.23	75.20	4.21	4.97	9.18
70,000	55.54	60.35	70.23	76.16	4.81	5.93	10.74
80,000	55.00	60.24	70.19	76.48	5.24	6.29	11.53
90,000	54.44	60.32	70.25	77.31	5.88	7.06	12.94
100,000	53.97	60.28	70.18	77.49	6.31	7.31	13.62
110,000	53.29	60.33	70.19	78.61	7.04	8.42	15.46
120,000	52.88	60.40	70.29	79.77	7.52	9.48	17.00
130,000	51.90	60.36	70.27	80.77	8.46	10.50	18.96
140,000	50.84	60.30	70.27	82.15	9.46	11.88	21.34
150,000	50.06	60.34	70.28	83.70	10.28	13.42	23.70
160,000	46.33	60.37	70.28	88.62	14.04	18.34	32.38
162,000	43.48	60.30	70.29	91.72	16.82	21.43	38.25
162,530							

TABLE B-20. SURFACE CRACK GROWTH RESULTS FOR SPECIMEN B-6

Fatigue cycles	X position of surface point (mm)				Crack lengths (mm)		
	Left side crack tip	Left side hole edge	Right side hole edge	Right side crack tip	Left side	Right side	Total length
0	55.90	58.87	68.89	71.69	2.97	2.80	5.77
10,000	55.90	58.87	68.89	71.69	2.97	2.80	5.77
20,000	55.90	58.87	68.89	71.69	2.97	2.80	5.77
30,000	55.90	58.87	68.89	71.69	2.97	2.80	5.77
40,000	55.18	58.87	68.89	72.14	3.69	3.25	6.94
50,000	54.32	58.95	68.90	72.71	4.63	3.81	8.44
60,000	54.22	58.96	68.97	73.36	4.74	4.39	9.13
70,000	53.73	58.96	68.97	73.82	5.23	4.85	10.08
80,000	52.99	59.00	69.02	74.16	6.01	5.14	11.15
90,000	52.21	59.03	69.03	75.11	6.82	6.08	12.90
100,000	51.87	59.04	69.06	75.54	7.17	6.48	13.65
110,000	51.33	59.09	69.10	76.35	7.76	7.25	15.01
120,000	50.76	59.10	69.13	77.35	8.34	8.22	16.56
130,000	49.68	59.10	69.12	79.11	9.42	9.99	19.41
140,000	47.54	59.06	69.06	82.76	11.52	13.70	25.22
143,000	45.54	59.06	69.04	85.02	13.52	15.98	29.50
144,000	44.66	59.06	69.06	85.98	14.40	16.92	31.32
145,000	43.98	59.00	68.88	87.06	15.02	18.18	33.20
146,000	41.79	58.97	68.94	88.30	17.18	19.36	36.54
147,000	37.67	58.83	68.83	93.88	21.16	25.05	46.21
147,020							

TABLE B-21. SURFACE CRACK GROWTH RESULTS FOR SPECIMEN B-7

Fatigue cycles	X position of surface point (mm)				Crack lengths (mm)		
	Left side crack tip	Left side hole edge	Right side hole edge	Right side crack tip	Left side	Right side	Total length
0	57.2	59.95	69.95	73.16	2.75	3.21	5.96
10,000	57.2	59.95	69.95	73.16	2.75	3.21	5.96
20,000	56.74	59.95	69.95	73.16	3.21	3.21	6.42
30,000	56.32	60.03	69.97	73.36	3.71	3.39	7.10
40,000	55.97	59.99	70.00	73.97	4.02	3.97	7.99
50,000	55.16	.	.	74.4	4.83	4.40	9.23
60,000	54.33	.	.	75.00	5.66	5.00	10.66
70,000	54.11	.	.	75.68	5.88	5.68	11.56
80,000	53.44	.	.	75.79	6.55	5.79	12.34
90,000	53.15	.	.	76.00	6.84	6.00	12.84
100,000	52.39	.	.	76.63	7.60	6.63	14.23
110,000	51.79	.	.	77.16	8.20	7.16	15.36
120,000	51.60	.	.	77.60	8.39	7.60	15.99
130,000	51.22	.	.	78.36	8.79	8.36	17.15
140,000	50.67	.	.	79.08	9.32	9.08	18.40
150,000	49.68	.	.	79.41	10.31	9.41	18.72
170,000	48.50	.	.	80.15	11.49	10.15	21.64
180,000	47.71	.	.	81.25	12.28	11.25	23.53
190,000	47.44	. .	.	82.00	12.55	12.00	24.55
200,000	46.06	.	.	83.11	13.93	13.11	27.04·
210,000	45.57	.	.	83.72	14.42	13.72	28.14
220,000	44.64	.	.	84.36	15.35	14.36	29.71
230,000	43.81	.	.	85.15	16.18	15.15	31.33
240,000	42.00	.	.	85.75	17.99	15.75	33.74
250,000	39.08	.	.	86.12	20.91	16.12	37.03
255,000	37.20	.	.	87.22	22.79	17.22	40.01
258,080							

TABLE B-22. SURFACE CRACK GROWTH RESULTS FOR SPECIMEN B-8

Fatigue cycles	X position of surface point (mm)				Crack lengths (mm)		
	Left side crack tip	Left side hole edge	Right side hole edge	Right side crack tip	Left side	Right side	Total length
0	59.32	62.45	72.57	75.40	3.13	2.83	5.96
10.000	59.32	62.45	72.57	75.40	3.13	2.83	5.96
20,000	59.32	62.45	72.57	75.40	3.13	2.83	5.96
30,000	59.32	62.45	72.57	75.40	3.13	2.83	5 96
40,000	58.41	.	.	76.33	4.04	3.76	7.80
60,000	57.63	.	.	77.39	4.82	4.82	9.64
80,000	56.95	.	.	78.24	5.80	5.67	11.47
100,000	56.13	.	.	79.31	6.32	6.74	13.06
120,000	55.17	.	.	80.50	7.28	7.93	15.21
140,000	54.71	.	.	80.82	7.74	8.25	15.99
160,000	52.49	.	.	82.68	9.96	10.11	20.07
170,000	52.21	.	.	82.73	10.24	10.16	20.40
180,000	50.64	.	.	83.60	11.81	11.03	22.84
190,000	49.65	.	.	84.15	12.90	11.58	24.48
200,000	48.47	.	.	85.16	13.98	12.59	26.57
210,000	46.94	.	.	86.21	15.51	13.64	29.15
220,000	45.67	.	.	87.20	16.78	14.63	31.41
230,000	44.10	.	.	88.41	18.35	15.84	34.19
240,000	41.10	.	.	89.67	21.35	17.10	28.45
245,000	39.02	.	.	90.49	23.43	17.92	41.35
248,130							

APPENDIX C
Bonding Procedures

C.1 Bonding procedures for scheme 1 specimens

The aluminum alloy specimens were vapor degreased in 1-1-1-trichloroethane and then the bonding surfaces were wiped using fresh tissues soaked with AR grade Butanone (also known as methyl ethyl ketone) until there was no discoloration of the tissues. This was followed by grit blasting with non-recycled 50 micron alumina grit. Bonding of the similarly treated steel bushes was effected promptly using Permabond F241 acrylic adhesive cured for 24 hours at room temperature.

C.2 Bonding procedures for scheme 2 specimens

Preparation of the 2024-T4 dog-bone shaped specimens followed a systematic procedure to ensure maximum reliability of the various components. Each specimen consists of three parts. Each part was pretreated before it was adhesively bonded.

The aluminum alloy specimens were vapor degreased in 1-1-1-trichloroethane and then the bonding surfaces were wiped using fresh tissues soaked with AR grade Butanone (also known as methyl ethyl ketone) until there was no discoloration of the tissues. This was followed by grit blasting with non-recycled 50 micron alumina grit. The surface was blown clean with dry nitrogen, and a 1% aqueous silane treatment applied for ten minutes. The specimens were dried in warm air (i.e. 60°C) for ten minutes taking care to avoid staining.

The pre-cured 10-layer unidirectional boron patch was grit blasted and assembled to the specimen with one layer of Cyanamid's FM 73 film adhesive. The four specimens were cured in an autoclave for one hour at 120°C at 380 kPa. A light press fit teflon plug was used to prevent adhesive flowing into the hole of the sleeve. These plugs were removed after the boron patch was bonded. The hole was grit blasted, silane treated and dried, and the similarly treated steel bushes were bonded into place using Hysol EA9321, which is a two-part room temperature curing paste adhesive. Careful attention was paid to the fit of the steel sleeves in the hole in order to control the bond line dimensions. The hole was reamed to size and the sleeve machined to leave a radial gap of 0.18 mm.

After initial curing at room temperature (i.e. 22°C) for three days, the specimens were heated to 50°C for 24 hours to complete the cure. Except for polishing the metal face and sides and radiusing the edges, the specimens were tested in the as-bonded state, thus the small adhesive fillet present at the bottom of the hole and in the notches was not removed. It was considered that these small amounts of adhesive were unlikely to influence the results whereas their removal may have initiated debonding, either mechanically or by introducing an abrupt sectional change at the bottom of the hole. This technique was also more representative of aircraft repair practice.